LBL-8581
UC-41
CONF-7809164

Lawrence Berkeley Laboratory
UNIVERSITY OF CALIFORNIA

WORKSHOP ON THE RADIATION ENVIRONMENT OF THE SATELLITE POWER SYSTEM

September 15, 1978

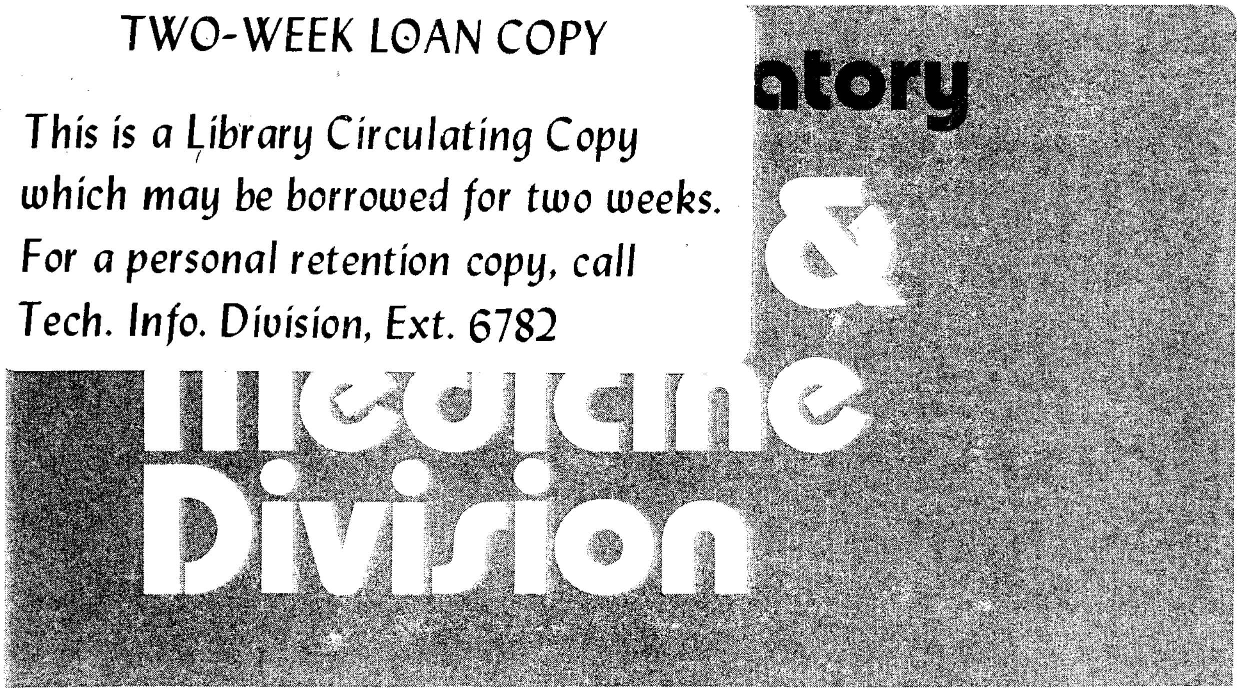

Prepared for the U. S. Department of Energy
under Contract W-7405-ENG-48

WORKSHOP ON THE RADIATION ENVIRONMENT
OF THE SATELLITE POWER SYSTEM

September 15, 1978

Lawrence Berkeley Laboratory

Walter Schimmerling and Stanley B. Curtis, Editors

Biology and Medicine Division
Lawrence Berkeley Laboratory
Berkeley, CA 94520

CONTENTS

INTRODUCTION

The need to develop long-term energy sources has resulted in an extensive search for economically competitive alternatives to our limited supplies of fossil fuels. In order to be productive, such a search must seriously consider the widest possible range of technologies. Satellite-based solar power generation is one such imaginative possibility. A proper evaluation of its merits depends on basic knowledge acquired in a large number of scientific and engineering fields. Satellite power systems (SPS) are thus a truly multidisciplinary challenge to our ingenuity, and it is fitting that the Lawrence Berkeley Laboratory, which pioneered a multi-disciplinary approach to science, should host a workshop on problems posed by the SPS.

The environment in which satellite power systems must be built and operate is characterized, among other properties, by the presence of substantial fluxes of high-energy electrons, protons, neutrons, and atomic nuclei. It is convenient to classify this radiation into three categories: (a) the electrons and protons trapped by the earth's magnetic field in the Van Allen belts, (b) the protons, helium nuclei, and, to a lesser extent, heavier nuclei, originating in the sun, and (c) the protons, helium, and heavier nuclei comprising galactic cosmic rays.

Each of these categories of radiation constitutes a hazard of different magnitude at different stages of SPS operation. The trapped protons of the Van Allen belts are of greatest concern during operations in low earth orbit. The widely varying fluxes of trapped electrons are important both during transfer to and in geostationary orbit.

Galactic cosmic rays are a low-level, continuous source of exposure to man and materials. The heavy galactic nuclei are of concern here because of the possible accumulation of biological damage over extended exposure periods. Finally, solar radiation is subject to violent and unpredictable variations in magnitude. Solar storms can drastically alter the near earth space radiation environment. Geostationary personnel must be warned in time to reach adequately shielded shelters in order to avoid lethal exposures from the large solar particle fluxes which often accompany such solar storms.

The Lawrence Berkeley Laboratory has sponsored pure and applied research into space radiation for many years. Knowledge obtained from the study of cosmic rays has stimulated scientific work in other fields at LBL, from the discovery of the antiproton to the development of heavy-ion beams for cancer therapy. Research into the biological effects of radiation, carried out at the Donner Laboratory of LBL, has led naturally to a long standing interest in the evaluation of radiation hazards in space. In 1965, C.A. Tobias, faculty senior scientist at LBL, was instrumental in arranging a Workshop Conference on Space Radiation Biology.[1] This conference, sponsored by the Office of Advanced Research and Technology of the National Aeronautics and Space Administration (NASA), was held on the campus of the University of California at Berkeley with active participation by many scientists of the Donner Laboratory. A comprehensive review of the emerging field of space radiation biology was published in 1974, under the direction

---

[1] P.E. Schambra, G.E. Stapleton and N.F. Barr, eds. Proceedings of a Workshop on Space Radiation Biology. Radiat. Res. Suppl. 7, 1967.

of the American Institute of Biological Sciences, for the Office of Information Services, United States Atomic Energy Commission. The monograph, entitled "Space Radiation Biology and Related Topics"[2] was edited by C.A. Tobias and P. Todd. Todd, who is now on the faculty of Pennsylvania State University, wrote his doctoral dissertation at Donner Laboratory.

It is clear that satellite-based solar power generation presents a series of problems in radiation environment definition, dosimetry, and hazard assessment (both archival and predictive) that need careful attention. This "Workshop on the Radiation Environment of the Satellite Power System (SPS)" was organized to review the present state of information on the radiation environment to be experienced by space workers on SPS. In order to focus our attention on a well-defined area of inquiry, the scope of the workshop was restricted to exclude nonionizing radiation (e.g., microwaves) and radiation effects on materials. The workshop was held at the Donner Laboratory of LBL on September 15, 1978, with the participation of a broad spectrum of active workers in the field drawn from industry, government and universities. In preparation for the conference, Professor Richard Madey of Kent State University was invited to spend three weeks at LBL to study the present status of research on the SPS radiation environment.

The program for the workshop comprised three parts. A morning session was intended to provide the participants with a broad perspective of pertinent topics. System definition and radiation protection studies

---

[2] C.A. Tobias and P. Todd, eds. Space Radiation Biology and Related Topics. New York: Academic Press, 1974.

for the space transportation system were reviewed by R. Hoffman of the Lyndon B. Johnson Space Center (NASA). J. Wilson of the Langley Research Center (NASA) reviewed the geophysical environment of the SPS, and J. Wefel of the Enrico Fermi Institute (University of Chicago) discussed the state of the art of radiation detection and particle identification. The afternoon session provided a forum for informal discussions of our present knowledge and of unsolved problems. A rapporteur's summary by Professor Madey concluded this part of the workshop. The participants then gathered in the evening to hear an entertaining as well as enlightening talk on space radiation biology by Professor Tobias, and to participate in a final discussion period.

The present collection of papers unfortunately cannot convey the stimulating atmosphere of a deliberately informal conference. However, we hope that the contents, consisting of the texts of the three invited talks by R. Hoffman, J. Wilson, and J. Wefel, the detailed report of calculations of environmental definition by E. G. Stassinopoulos of the Goddard Space Flight Center (NASA), and the rapporteur's summary review, will be of use to all researchers in the field. The program of presentations and the list of participants have also been included for completeness.

The logistics of this meeting were efficiently and enthusiastically handled by Sandy Sanford. Susan Proctor and Grace Walpole contributed their considerable secretarial talents. The task of compiling and editing the manuscripts for this report was efficiently handled by M.C. Pirruccello. We also wish to thank LBL Associate Director Earl Hyde for his support and encouragement.

This Conference was made possible by funding from the Satellite Power System Project Office, Office of Energy Research, U.S. Department of Energy. The funding was arranged and administered by Margaret R. White, Task Director Health and Safety, Other Effects, Satellite Power System. This financial support is gratefully acknowledged.

W. Schimmerling
S.B. Curtis

Berkeley
February 1979

Workshop on The Radiation Environment of the Satellite Power System (SPS)

September 15, 1978

Lawrence Berkeley Laboratory

PARTICIPANTS

Name	Affiliation
Barr, Nathaniel	Department of Energy
Benton, Gene	University of San Francisco
Blakely, Eleanor	Lawrence Berkeley Laboratory
Cassou, Ronald	University of San Francisco
Chatterjee, Aloke	Lawrence Berkeley Laboratory
Fabrikant, Jacob	Lawrence Berkeley Laboratory
Frank, Allan	University of San Francisco
Hanley, Gerard	Rockwell International
Heinrich, Wolfgang	University of San Francisco
Henke, Richard	University of San Francisco
Hildebrand, Dietmar	University of San Francisco
Hoffman, Rudy	NASA Johnson Space Center
Huesman, Ron	Lawrence Berkeley Laboratory
Hyde, Earl	Lawrence Berkeley Laboratory
Kast, John	Lawrence Berkeley Laboratory
Kraft, Lisbeth	NASA Ames Research Center
Lindstrom, Peter	Lawrence Berkeley Laboratory
Lyman, John	Lawrence Berkeley Laboratory
Madey, Richard	Kent State University
Magee, John	Lawrence Berkeley Laboratory

Malachowski, Mike	NASA Ames Research Center
Philpott, Delbert	NASA Ames Research Center
Schimmerling, Walter	Lawrence Berkeley Laboratory, Program Chairman
Stassinopoulos, E.G.	NASA Goddard Space Flight Center
Tobias, Cornelius	Lawrence Berkeley Laboratory
Wefel, John	The University of Chicago
White, Margaret	Lawrence Berkeley Laboratory
Wilkinson, Maurice	Boeing Aerospace Company
Wilson, John	NASA Langley Research Center
Woodcock, Gordon	Boeing Aerospace Company
Yang, Tracy	Lawrence Berkeley Laboratory

The Radiation Environment of the Satellite Power System (SPS)

AGENDA

Friday, September 15, 1978

Morning Session -- Invited Reports
Chairman: W. Schimmerling

8:30 AM -- Registration

9:00 AM -- Welcoming Remarks
M. White, Task Director, Health & Safety (Nonmicrowave), SPS

9:15 AM -- Invited Talk: Space Transportation System: Operations and Projected Radiation Exposures. R. Hoffman, NASA Johnson Space Center

10:10 AM -- Coffee Break

10:25 AM -- Invited Talk: Environmental Geophysics and SPS Shielding. J. Wilson, NASA Langley Research Center

11:20 AM -- Invited Talk: Instrumentation for Radiation Measurement in Space. J. Wefel, Enrico Fermi Institute, University of Chicago

12:15 PM -- Lunch

Afternoon Session -- Discussion and Contributed Reports

2:00 PM -- Invited Talk: A Preliminary Evaluation of the Ionizing Radiation Environment of the Satellite Power System. R. Madey, Kent State University

3:00 PM -- Instrumentation
Chairman: P. Lindstrom, Lawrence Berkeley Laboratory

4:00 PM -- Rapporteur's Summary
R. Madey, Kent State University

6:30 PM -- Cash bar

7:30 PM -- Dinner
Guest Speaker: Professor C.A. Tobias, Lawrence Berkeley Laboratory. Topic: Space Radiobiology

SPACE TRANSPORTATION SYSTEM: OPERATIONS AND PROJECTED RADIATION EXPOSURES

Rudolf A. Hoffman

NASA Johnson Space Center
Houston, Texas 77058

This workshop entitled "The Radiation Environment of the Satellite Power System (SPS)" will address what we know of that environment and what we still need to find out. Specifically we will address what instrumentation is available for further radiation environment definition and what we need to develop. The DOE concern for the above areas stems from the recent involvement by DOE in a joint venture with the NASA in exploring the feasibility of an SPS. More specifically, the concern pertains to the radiological health considerations of construction workers and maintenance personnel in space. NASA has, of course, been concerned with the space radiation exposure of astronauts for some time, and quite frankly we are pleased to share this concern now for the proposed SPS activities. Since my activities at the Johnson Space Center are directly involved with the operational aspects of the space radiation problem, my brief talk today will focus on our past manned space flight experience, our current approach to managing the space radiation exposures, and a few projections regarding radiation exposures in several flight modes, e.g., space transportation system (STS)--Spacelab.

Manned space flights to date have been of such duration and/or location to result in relatively low doses as shown in Table 1. Also,

TABLE 1

Previous Mission Exposure History

Mission	Range (mrad/day)	Average (mrad/day)
Mercury	27	27
Gemini	4-303	40
Apollo	10-141	44
SL2	58-65	62
SL3	62-71	67
SL4	81-95	88
ASTP	10-15	13

TABLE 2

NASA Radiation Exposure Limits

Constraints (rem)	Bone (5 cm)	Skin (0.1 mm)	Eye (3 mm)	Testes (3 cm)
1 year average daily rate	0.2	0.6	0.3	0.1
30 day max	25	75	37	13
Quarterly max	35	105	52	18
Yearly max	75	225	112	38
Career limit	400	1200	600	200

because of the very small population involved and because of the relatively high risks of other aspects of space flight, the current space exposure limits have been set (Table 2) considerably higher than allowed for terrestrial occupational exposures (Table 3). For these reasons, it has not been necessary to be extremely precise in identifying the LET spectrum of radiation contributing to the dose equivalent. Instead, a rather conservative quality factor (QF) has been applied in order to err on the safe side. However, with more frequent and longer exposures to the space environment by space workers as is projected in a project such as the SPS, a more accurate assesssment of exposures will be required. This will be true if the current NASA exposure limits are applied, but may become of even more concern if there is a reduction of these limits as is deemed likely. There is pressure from many areas to reduce the terrestrial exposure limits and it is not unreasonable to assume that with more personnel exposed to space flight and with other space flight risks reduced there will be a similar trend to reduce the space exposure limits. But whatever the governing limits will be, it is our expectation that remaining within those limits will pose a significant operational problem and will require judicious budgeting of worker time in space coupled with the most accurate dosimetry practicable to enable us to avoid the practice of overestimating exposure as is presently done.

Some recent calculations have been made (Getschmann, 1977) regarding the radiation dose rate at various locations within the spacelab at various orbital altitudes and inclinations. Figures 1, 2, 3, and 4 depict some of the results of these calculations. Although the

TABLE 3

Occupational Radiation Exposure Limits (NRC & OSHA)*

Constraints (rem)	Active Blood Forming Organs	Skin	Lens of Eye	Gonads
One year average daily rate	.014	.082	.014	.014
Quarterly max	3	7.5	3	3
Yearly max	5	30	5	5
Career limit	5 (N-18)			

*The accumulated occupational dose equivalent to the whole body shall not exceed 5 (N-18) rems, where "N" equals the individual's age in years.

TABLE 4

Mission Length to Exceed Quarterly Eye Dose Equivalent Limit (52 rem) with 2.0 and 5.0 g/cm^2 Shielding for 0^o and 30^o Inclination Orbits*

Altitude (N.Mi.)	Mission Length (days)			
	2.0 g/cm^2 shield		5.0 g/cm^2 shield	
	0^o Inc.	30^o Inc.	0^o Inc.	30^o Inc.
200	600	140	600	520
300	420	70	600	200
400	140	28	500	100
500	56	14	104	50

*Hardy, 1978.

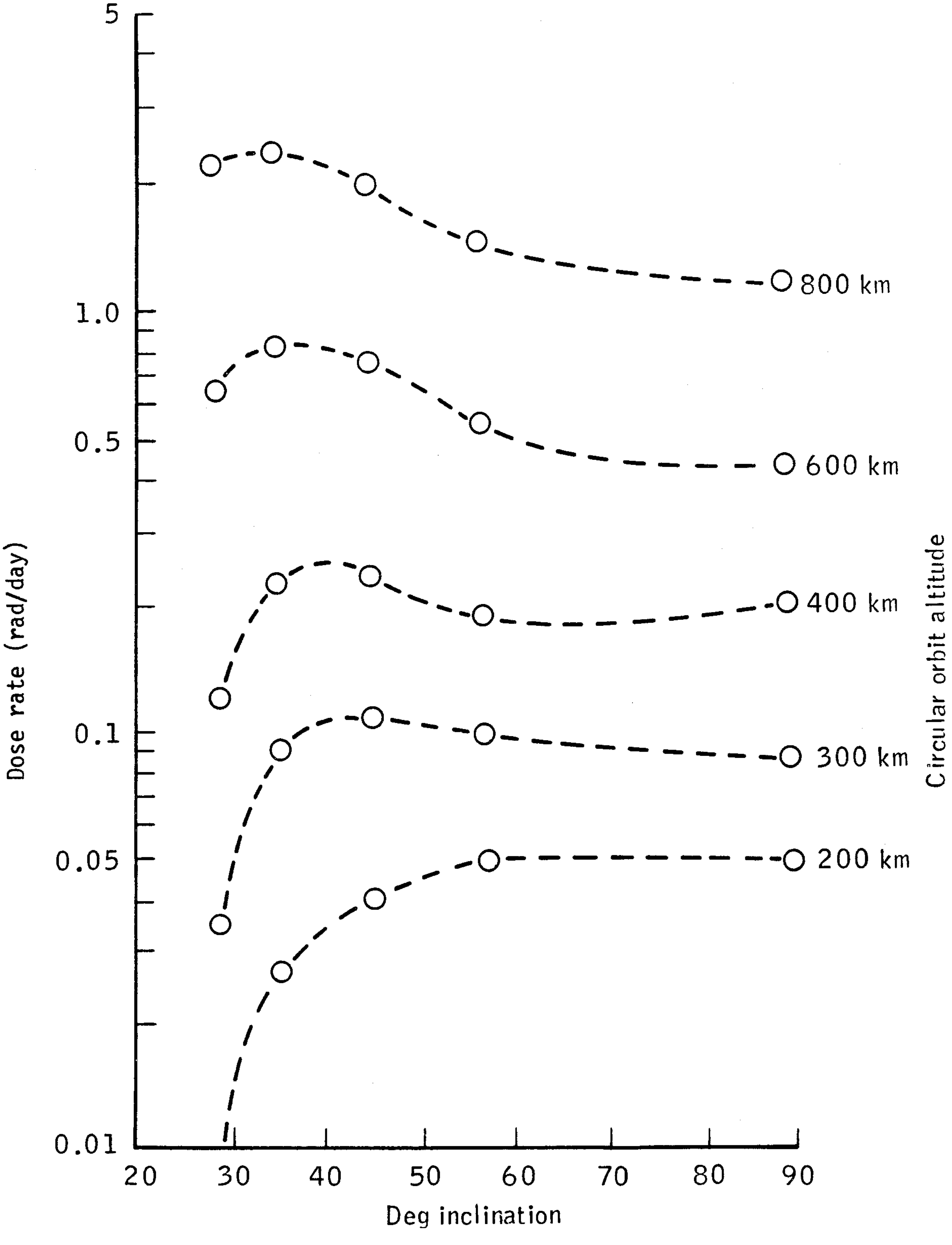

Figure 1: Daily dose (rad) versus orbit parameters for dose point 0.0.0 (no body shielding) (Getzschmann, 1977).

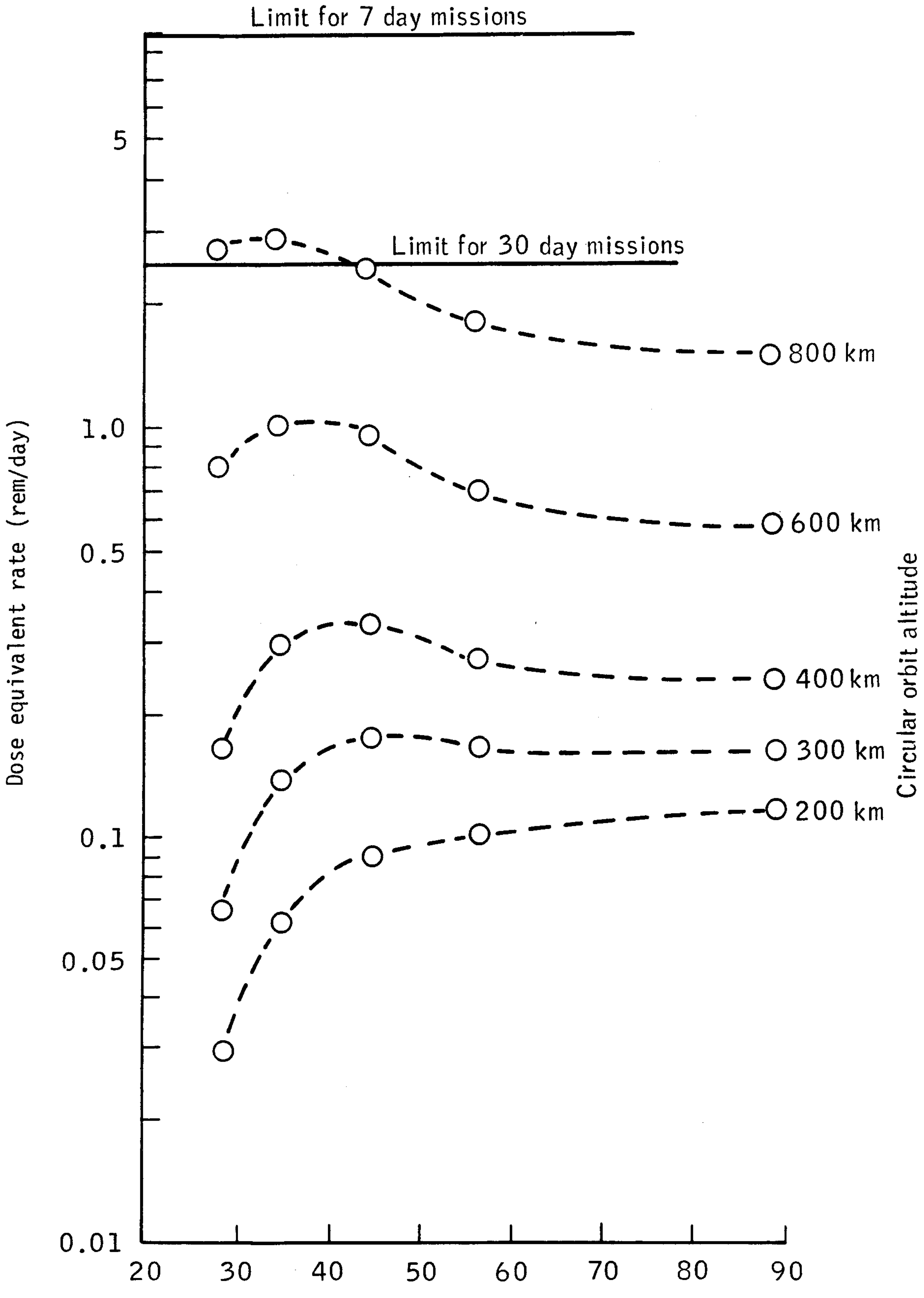

Figure 2: Daily dose equivalent (rem) versus orbit parameters for skin, dose point 0.0.0 (Getzschmann, 1977).

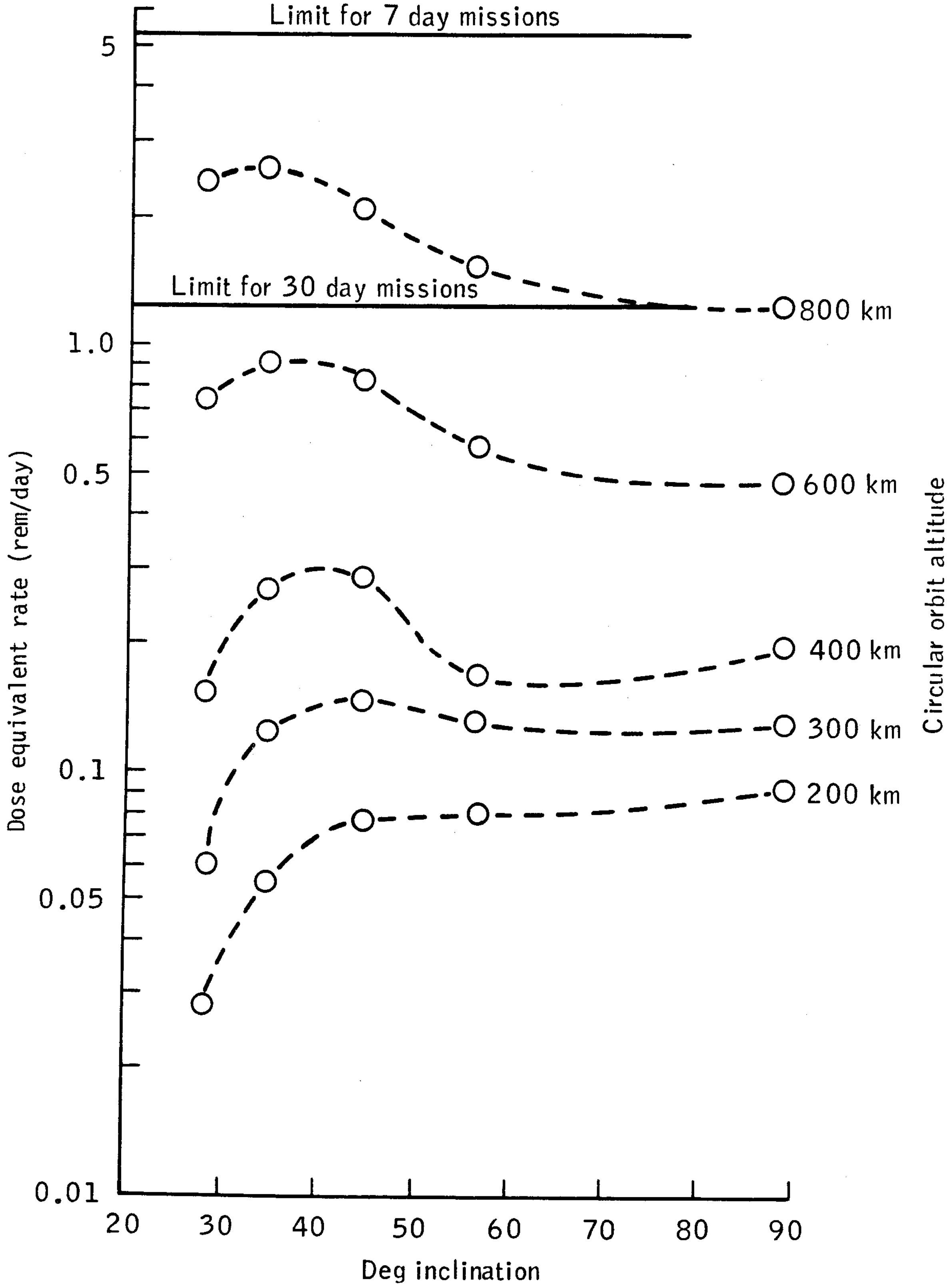

Figure 3: Daily dose equivalent (rem) versus orbit parameters for lens of eye, dose point 0.0.0 (Getzschmann, 1977).

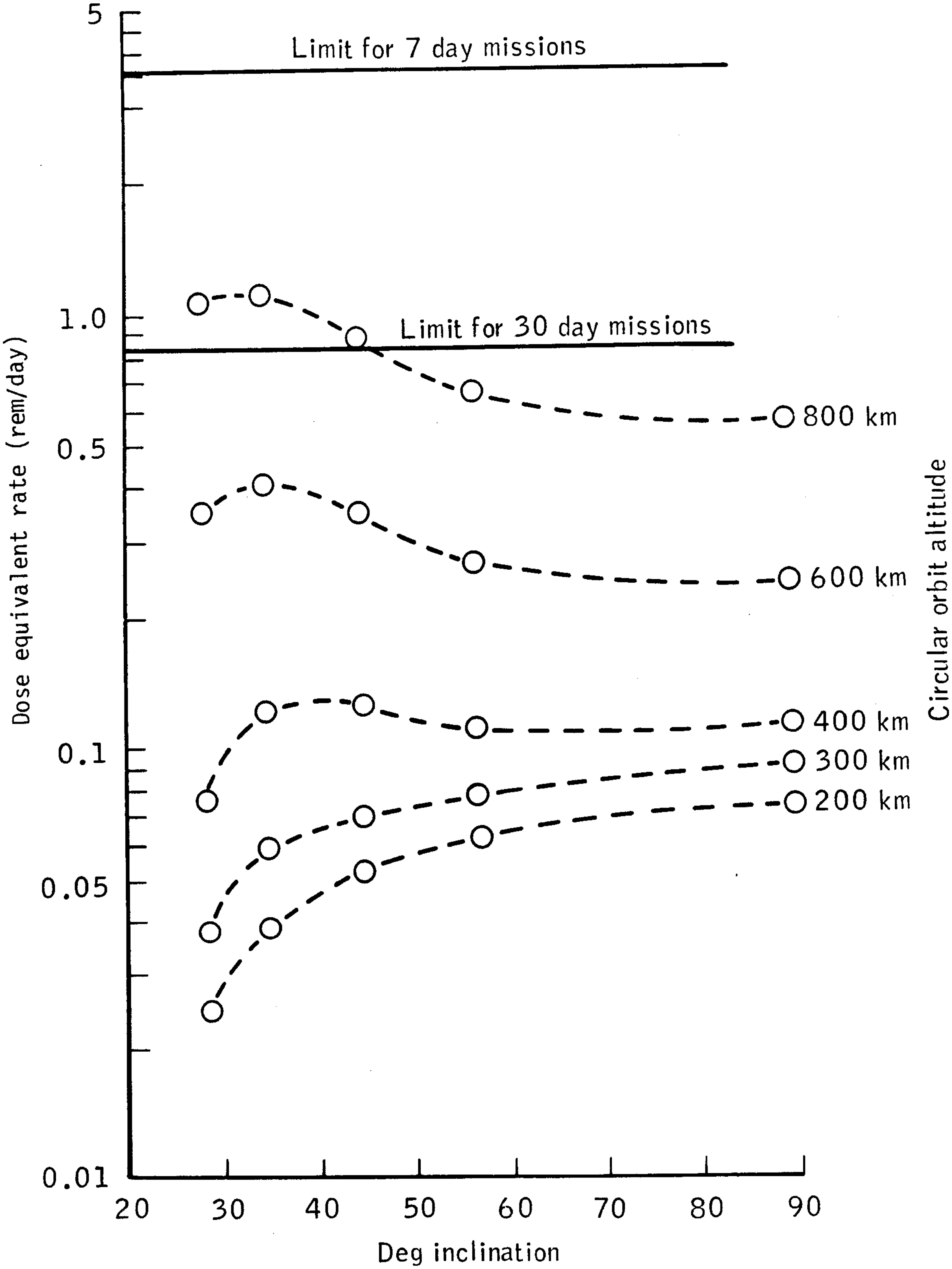

Figure 4: Daily dose equivalent (rem) versus orbit parameters for bone marrow, dose point 0.0.0 (Getzschmann, 1977).

dose rate within the Spacelab varies with location within the vehicle because of shielding variations, the data for dose point 0.0.0. shown in these figures are representative. The limit values shown on the figures are those currently in effect for 7 and 30 day missions. For example, the current allowable bone marrow dose for a 30 day exposure is 25 rem or approximately 0.8 rem/day. Referring to Figure 4, one can see that for orbital altitudes below 800 km the projected dose would be less than that allowed. However, for orbits at 800 km altitude and at inclinations below about 45^{o} the allowable dose would be exceeded. From these calculations one can also determine what orbital characteristics result in exceeding the average daily limits for selected stay times--for example 90 days. These kinds of calculations serve only as relatively gross guides at this time. Nevertheless, it is this type of approach that is necessary to define the nature of the radiation exposure problem inherent in the projected SPS activity and to define the implication of these radiation exposures in the design of structures and in the planning of radiation budgeting.

Figures 5 and 6 show the contribution of various radiation components to the total dose for various altitudes at 35^{o} and 90^{o} inclination. One can see that in most instances, trapped protons represent the primary source of radiation. However, there are certainly instances where this is not the case; for example, low altitude polar orbits where the skin dose is primarily from electrons, and the bone marrow dose from galactic cosmic radiation. In geosynchronous orbit, especially under light shielding conditions, electrons and bremsstrahlung are expected to constitute a significant exposure source. Further, if higher quality

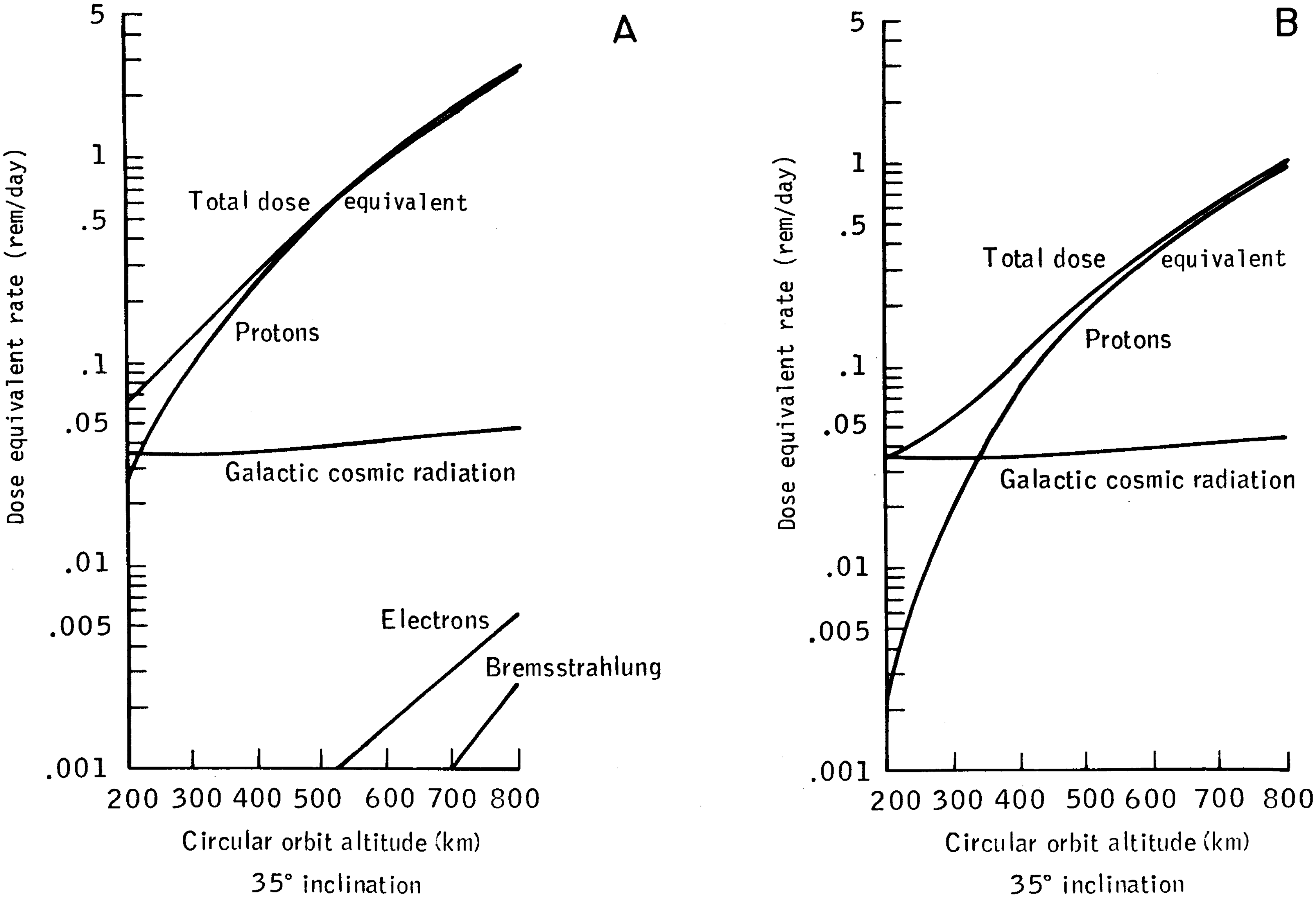

Figure 5: (A) Dose equivalents caused by different radiation sources for skin (Getzschmann, 1977).
(B) Dose equivalents caused by different radiation sources for bone marrow (Getzschmann, 1977).

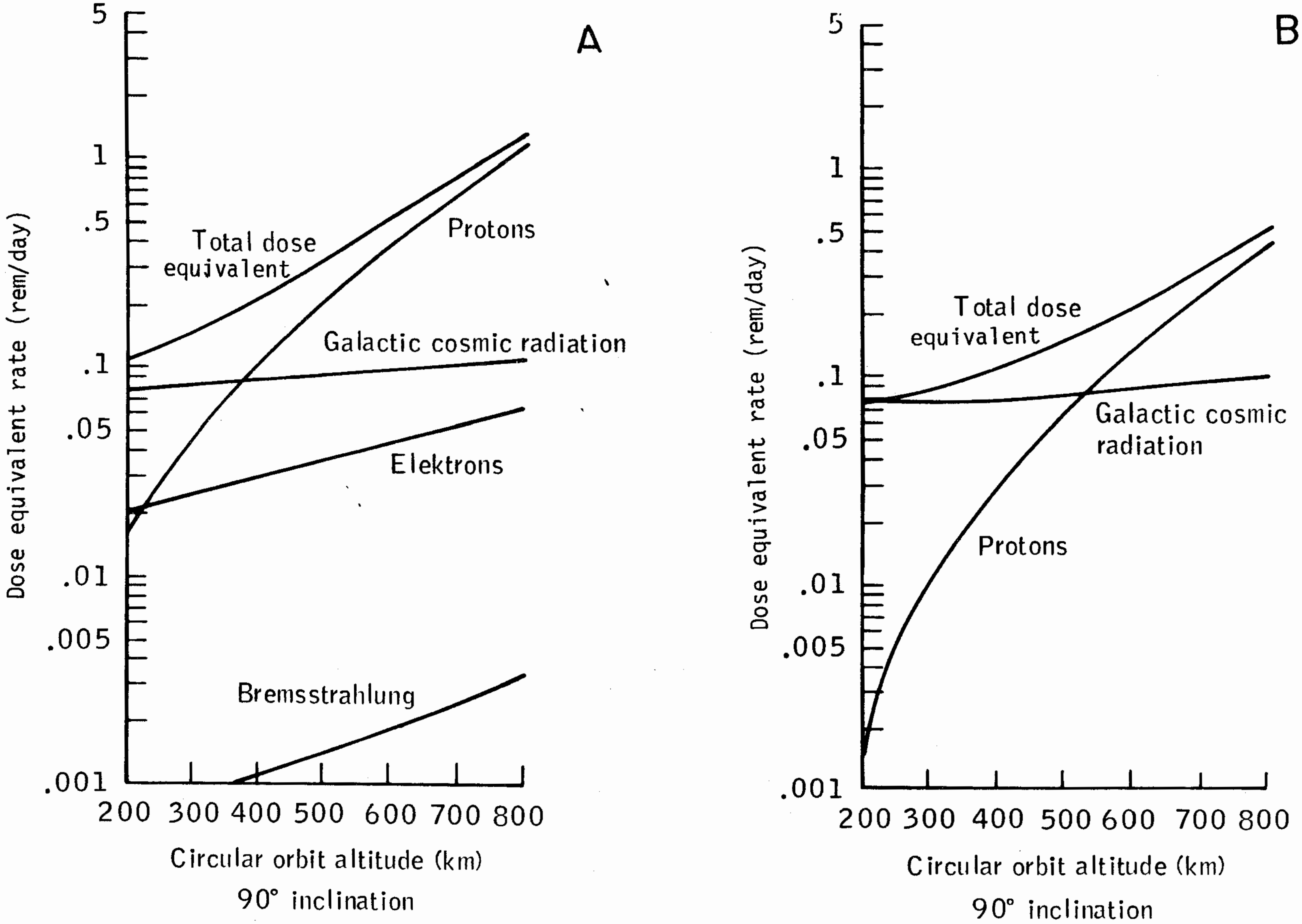

Figure 6: (A) Dose equivalents caused by different radiation sources for skin (Getzschmann, 1977).
(B) Dose equivalents caused by different radiation sources for bone marrow (Getzschmann, 1977).

factors now being considered for low dose and low dose-rate exposures to high LET radiation do indeed become law, then the contribution of the galactic component and secondary neutrons to the rem dose will undoubtedly increase.

Figure 7 (Hardy, 1978) depicts the scope of exposure expected in transferring from a relatively near earth orbit (500 km) to geosynchronous orbit. Flight transfer mechanics result in more exposure when starting from 0^o inclination than from 30^o. This is because more time is spent in radiation belts when starting at 0^o. A large contribution to dose is from low energy protons and from electrons as is evident from the dose reduction effected by only 2 or so g/cm^2 aluminum equivalent shielding. A similar large reduction in dose from only minimal shielding at geosynchronous orbit is shown in Figure 8. It can be seen from this figure that rather large doses, primarily to the skin, could result from extravehicular activity at geosynchronous orbit if the only shielding is that afforded by a space suit with little effective shielding ($0.1\ g/cm^2$). For this reason, little such extravehicular activity is planned. Most of the construction activity will be by remote manipulators controlled from within construction modules.

Figure 9 through 14 and Table 4 present additional calculations and different ways of assessing allowable on-orbit stay times under differing conditions.

Solar flares have not posed a problem for our previous manned flights because our missions have fortuitously occurred during periods with no significant solar particle events. We cannot expect to avoid

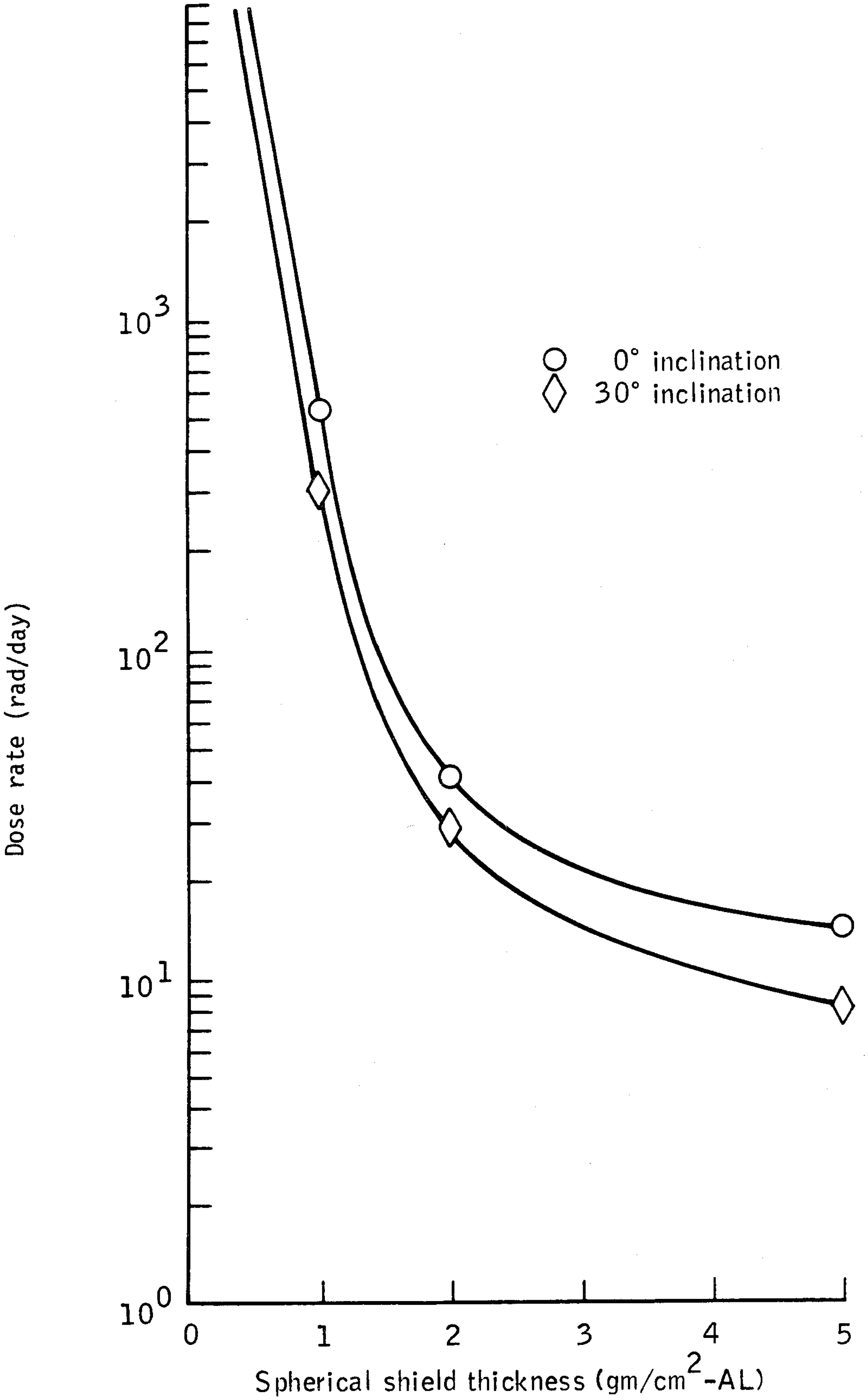

Figure 7: Total proton and electron dose per day of transfer time as a function of aluminum shield thickness for low thrust transfer from 500 N.Mi. to synchronous orbit (Getzschmann, 1977).

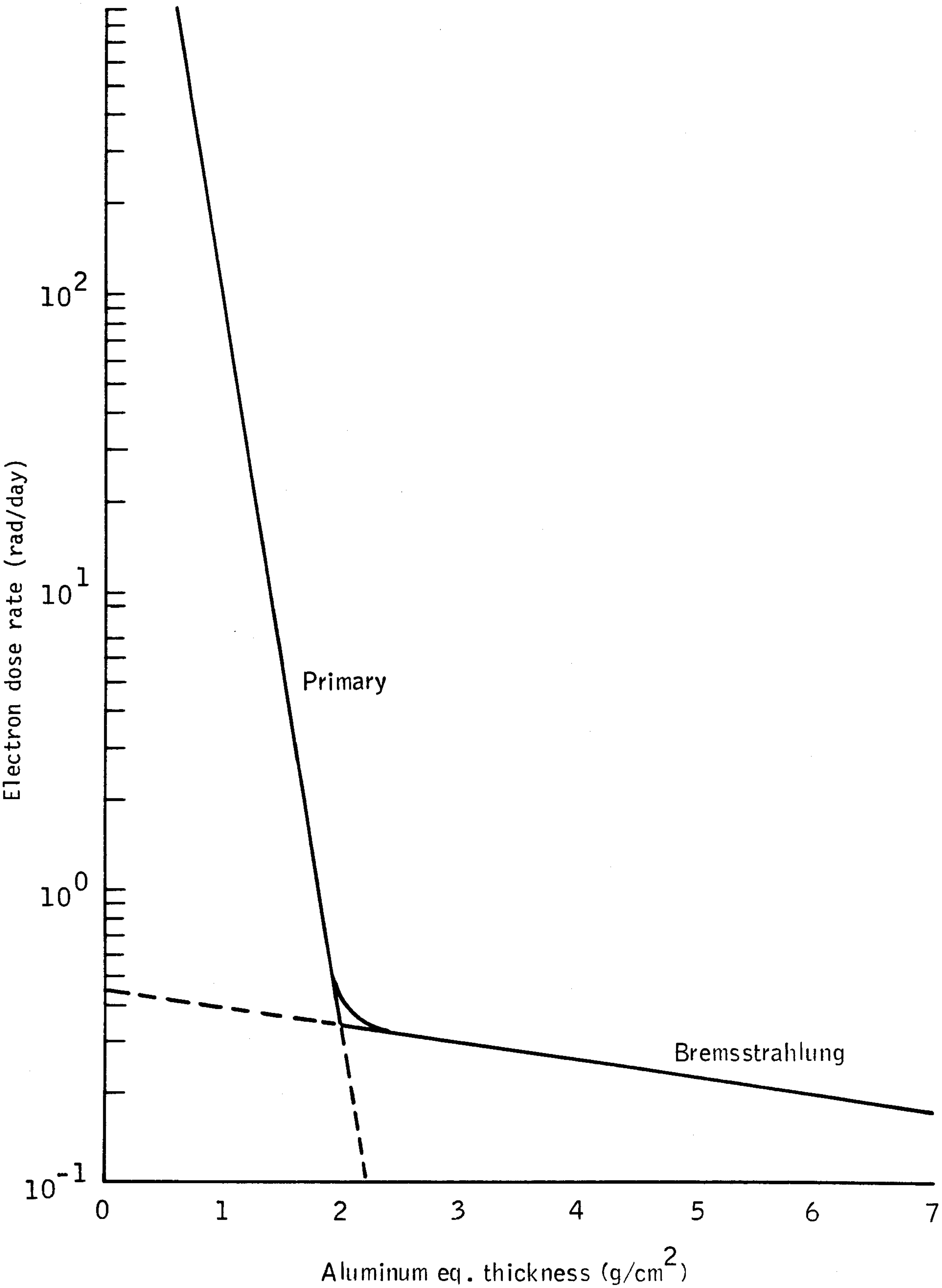

Figure 8: Synchronous orbit average daily electron dose (rad/day) versus aluminum shell thickness (g/cm^2) for solar maximum conditions (Getzschmann, 1977).

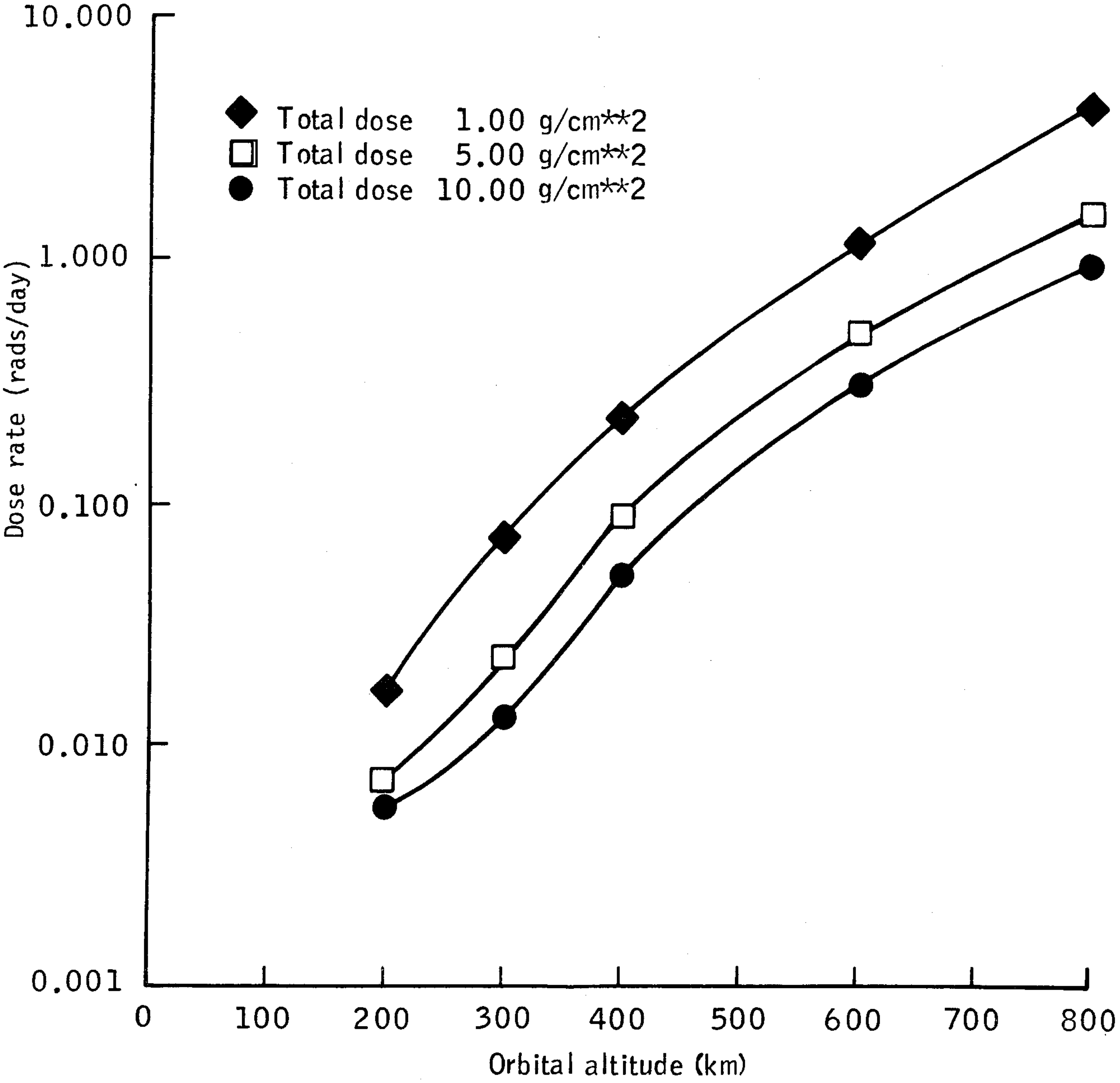

Figure 9: Dose rate (rad/day) behind a spherical aluminum shell shield versus altitude for various shield thicknesses and 28.5° inclination (Watts and Wright, 1976).

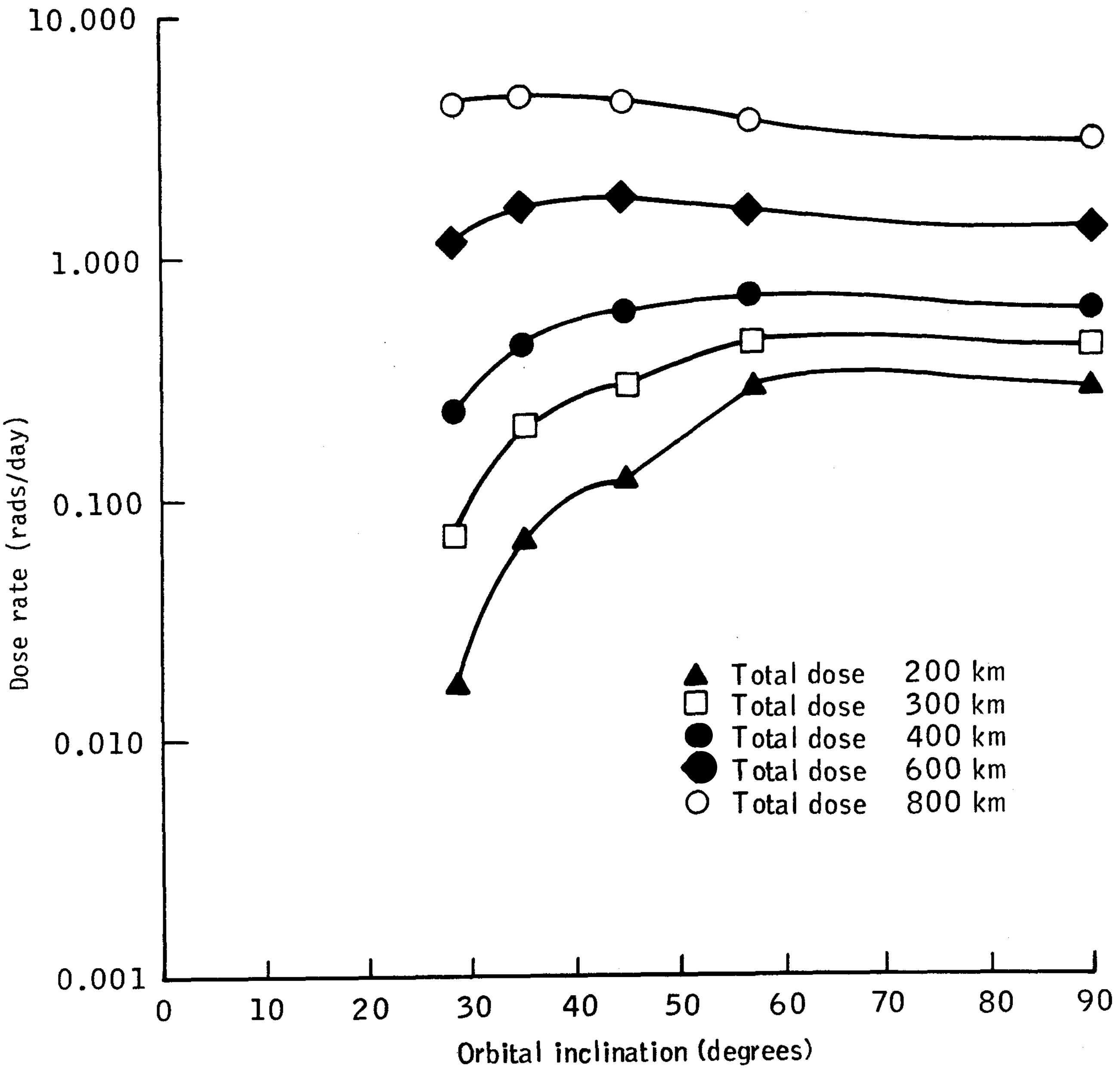

Figure 10: Dose rate (rad/day) behind a 1.0 g/cm^2 spherical aluminum shell shield versus inclination for various altitudes (Watts and Wright, 1976).

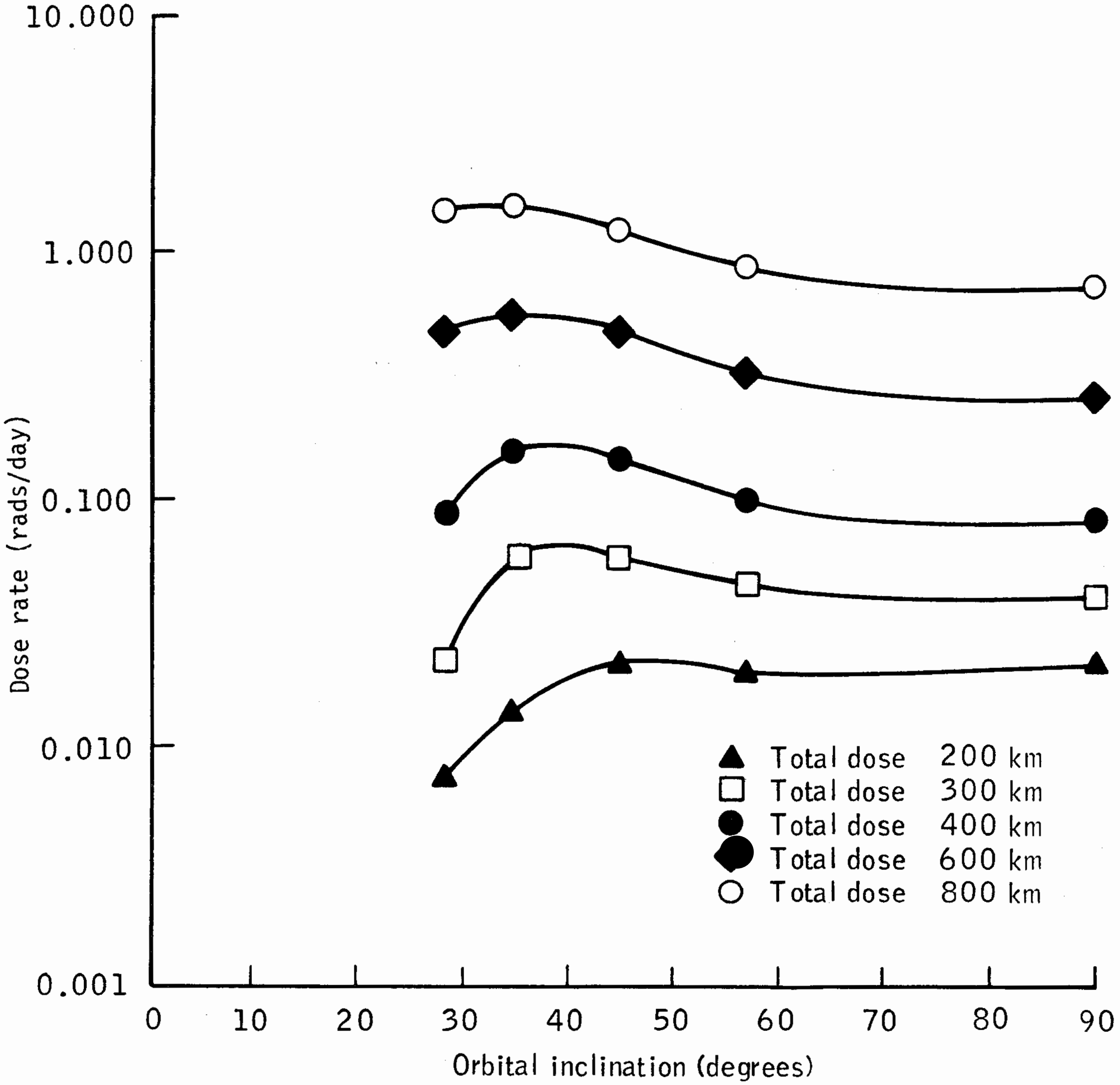

Figure 11: Dose rate (rad/day) behind a 5.0 g/cm^2 spherical aluminum shell shield versus inclination for various altitudes (Watts and Wright, 1976).

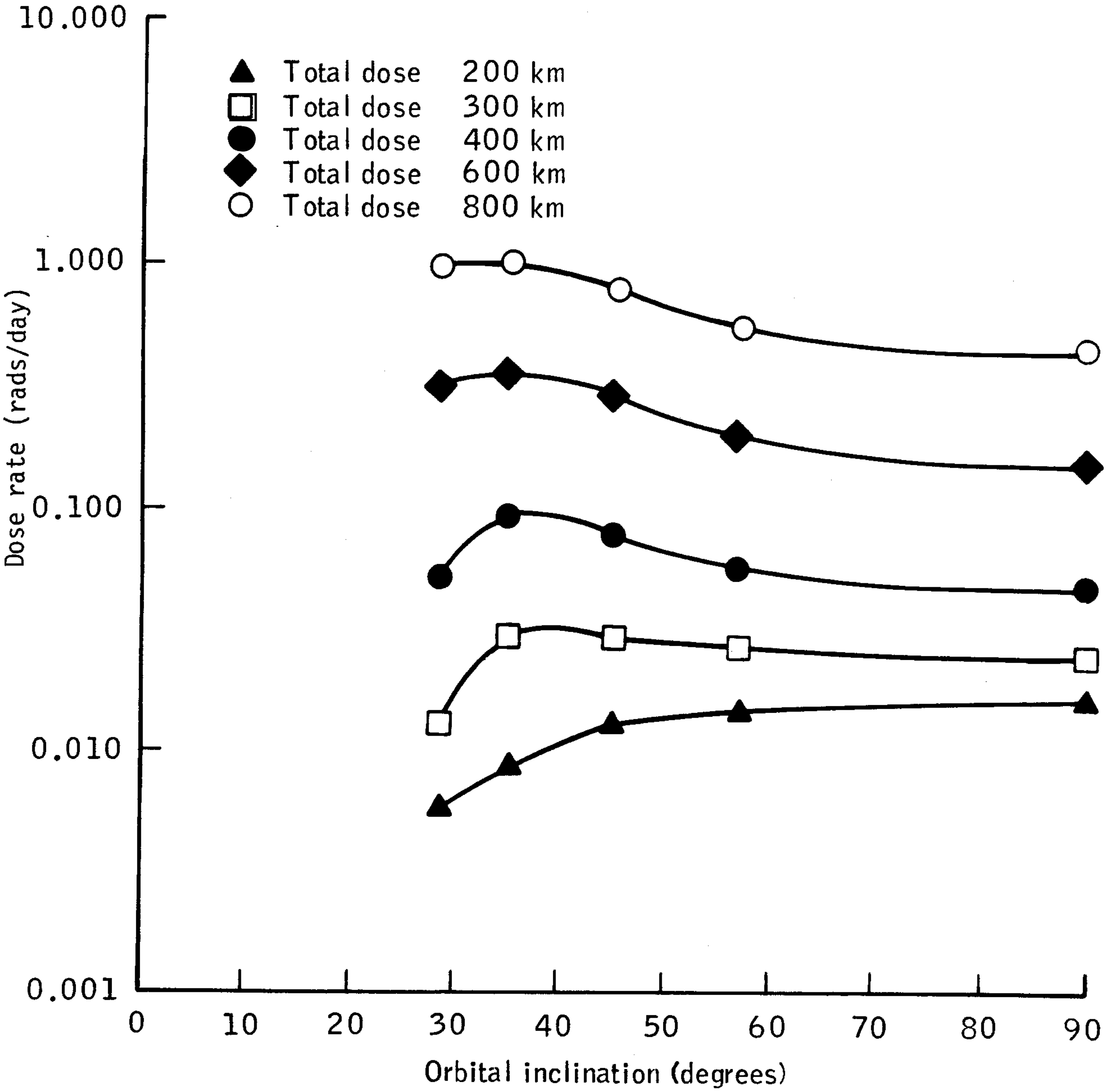

Figure 12: Dose rate (rad/day) behind a 10.0 g/cm^2 spherical aluminum shell shield versus inclination for various altitudes (Watts and Wright, 1976).

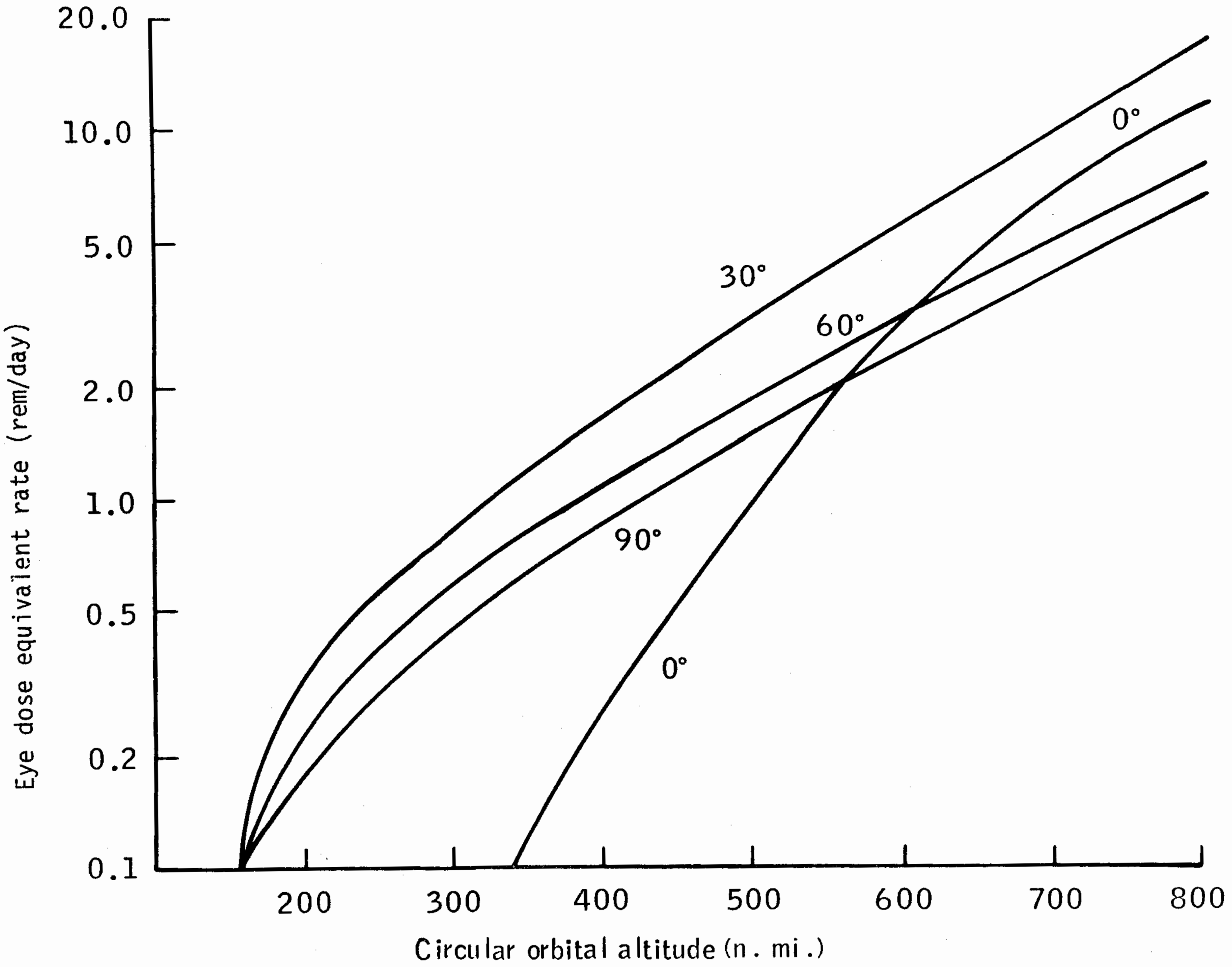

Figure 13: Eye dose equivalent rate (rem/day) behind 2.0 g/cm^2 shielding as a function of altitude of circular orbits with 0, 30, 60, and 90 degree inclination--self-shielding included (Hardy, 1978).

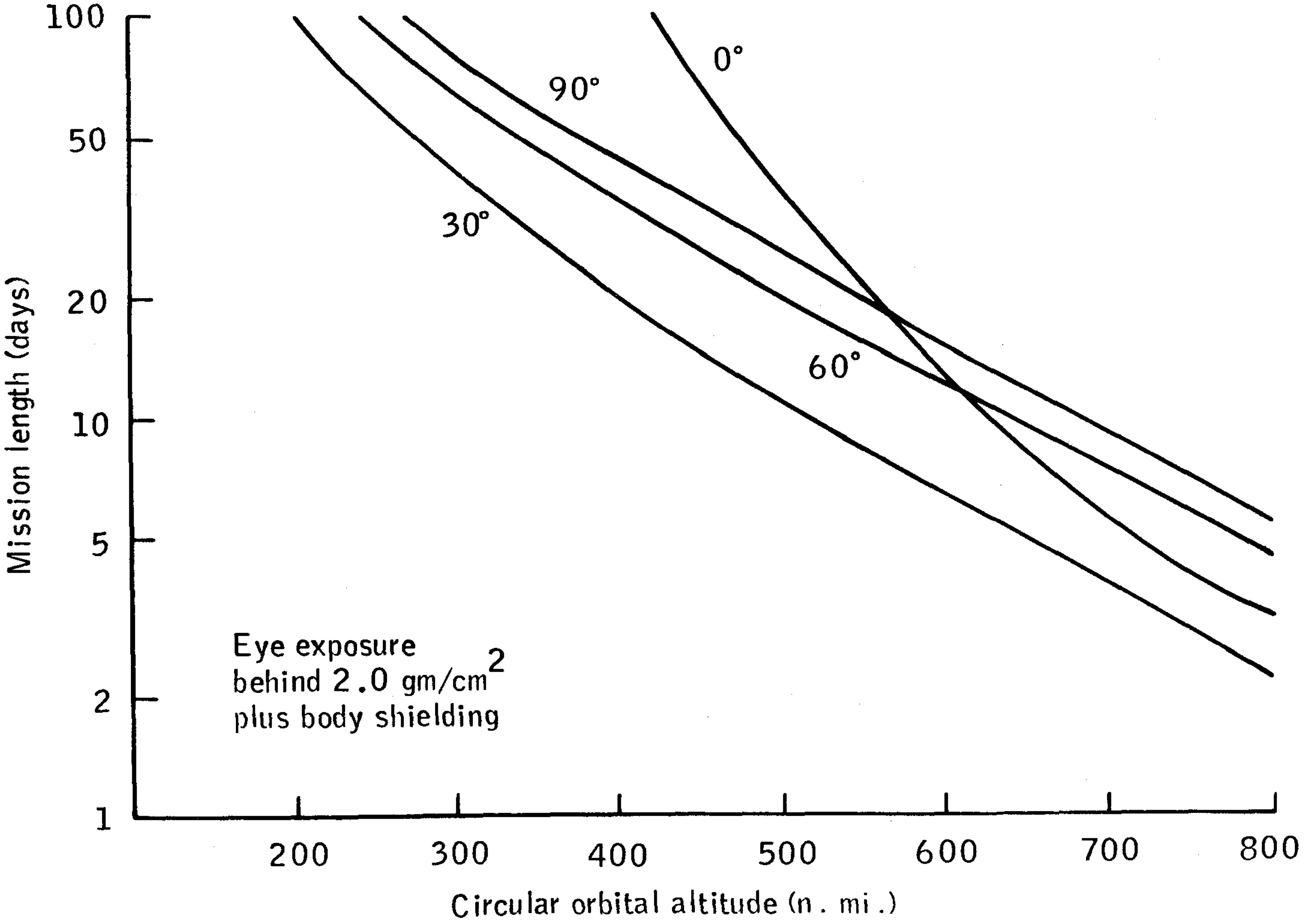

Figure 14: Maximum allowable mission length to receive eye dose equivalent limit of 37 rem (30 day limit) as a function of circular orbital altitude for orbital inclinations (Hardy, 1978).

the occurrence of solar flares in a large SPS type of activity. Consequently we must calculate the expected impact of solar flares and design and plan accordingly. Table 5 presents the results of some calculations regarding the doses resulting from a "representative" solar flare. There is of course great variation in the severity of flares and the resulting hazard to space residents. Certainly some protection will have to be provided, perhaps in the form of a "storm cellar" approach. But the question remains as to how much protection is reasonable to provide. For example, one might plan for protection from the average flare and accept higher exposure from the unusual larger events, fully realizing this would mean the possibility of removing from the space work force those individuals so exposed because they would have "used up" an excessive portion of their annual or career exposure budget.

The preceding has dealt primarily with what our past manned space flight radiation exposure experience has been and with what some projected exposures are expected to be for selected flight characteristics. But now let us compare for a moment the scope of the past manned space experience with that projected for such projects as SPS. We must compare our radiobiological requirements of the past with those appropriate for expanded space activities. In this way we can determine where our emphasis should be placed in radiobiological research, space radiation environment definition, and dosimetry instrumentation development. To reiterate an earlier statement, our past radiological health approach and that being used for the early space transportation system is based on a small space worker population engaged in flights of

TABLE 5

Solar Proton Event Dose behind Various Aluminum Absorber Thicknesses (200-N.Mi. altitude)*

Thickness	Dose (rad/flare) at Inclination		
(g/cm^2)	28.5°	57°	90°
0.1	0	4560	9960
0.25		1752	4080
0.5		768	1920
0.75		456	1140
1.0		312	780
1.5		192	480
2.0		126	324
3.0		76.8	186
4.0		48	120
5.0		33.6	85.2
6.0		25.2	63
8.0		15.6	39
10.0		10.1	25.2
15.0		4.08	10.2
20.0		2.0	5.6
25.0		1.2	3.0
30.0		0.72	1.8
40.0		0.336	0.84
50.0		0.168	0.42

*Getzschmann, 1977.

relatively short duration (Skylab flights may be considered an exception) spending very little time in regions where appreciable radiation dose is accrued. Additionally, the exposure limits were (and still are) set much higher than allowable terrestrial limits because of the small population exposed and because of the other relatively high risks associated with space flight. Because of these factors our dosimetry and the resolution of radiation components contributing to the dose need not be as accurate as they must be in the projected SPS activities. With increasing populations planned for space exposure and with the likelihood that exposure limits will be reduced, we must improve the accuracy of our dosimetry, and we must improve our understanding of the long-term biological effects of exposure to the complex radiation environment. To improve specificity of dose projections we must continually update our knowledge of the space radiation environment and improve our programs for calculating doses through various shielding configurations. Dosimetry instrumentation must be such that depth-dose information is provided. Additionally, we must be able to identify the portion of the total dose attributable to radiation components with differing LET, thus enabling appropriate conversion of absorbed dose (in rad) to equivalent dose (in rem). We recognize that it is no small task to provide such dosimetry and still have a feasible, practical approach. Nevertheless, we must strive for nothing less. And in the radiobiological area, we must continue to acquire data relevant to chronic low dose rate exposure to high LET radiation. We are currently emphasizing this in our NASA program and expect to continue.

In summary, it should be evident that while we in NASA have had no space radiation exposure problems in the past, the contrasting programs for the future require a new approach if we are to assure that no excessive risks are incurred by the space residents and yet not unnecessarily constrain the engineering and management aspects of those future endeavors. We hope that the NASA and the DOE will work closely together in supporting a well-conceived and implemented research and development program to provide the required information.

REFERENCES

Hardy, A.C. 1978. Johnson Space Center, personal communication.

Getzschmann, A. 1977. Radiation analysis. Part 1. Radiation impact on crew. VFN-Fokker Erno Report, RP-ER-0055.

Watts, J.W. and Wright, J.J. 1976. Charged particle radiation environment for the spacelab and other missions in low earth orbit - Revision A. NASA TMX-73358, November 29, 1976, Marshall Space Flight Center.

ENVIRONMENTAL GEOPHYSICS AND SPS SHIELDING

John W. Wilson

NASA Langley Research Center
Hampton, Virginia 23665

The types of particle radiations that occur in space are summarized in Figure 1. Of course there are both temporal as well as spatial variations. For example, trapped particles exist only in the geomagnetosphere, the solar wind can really only be seen out of the magnetosphere, the auroral electrons are seen only in polar regions, solar cosmic rays are rare transient events, and so on. The radiations with energies below 100 keV and the protons below 10 MeV are mainly important only from a materials point of view, e.g., thermal control coatings, and are considered biologically unimportant. The radiations that are important for biological consideration are the trapped protons in the inner zone, the trapped electrons in both the inner and the outer zone, and solar flare protons. Of course, galactic cosmic rays are also biologically important. They are of low intensity but many questions surround them because of their particular composition, and their biological action is potentially hazardous and not well understood experimentally. Data are taken from Noll and McElroy (1975), Foelsche (1963), McDonald (1963), Divine (1975), and Johnson (1965).

Looking at the impact of radiation on earth orbital operations (Figure 2), we see that imposed limits are very restrictive in some

SPACE RADIATION ENVIRONMENT

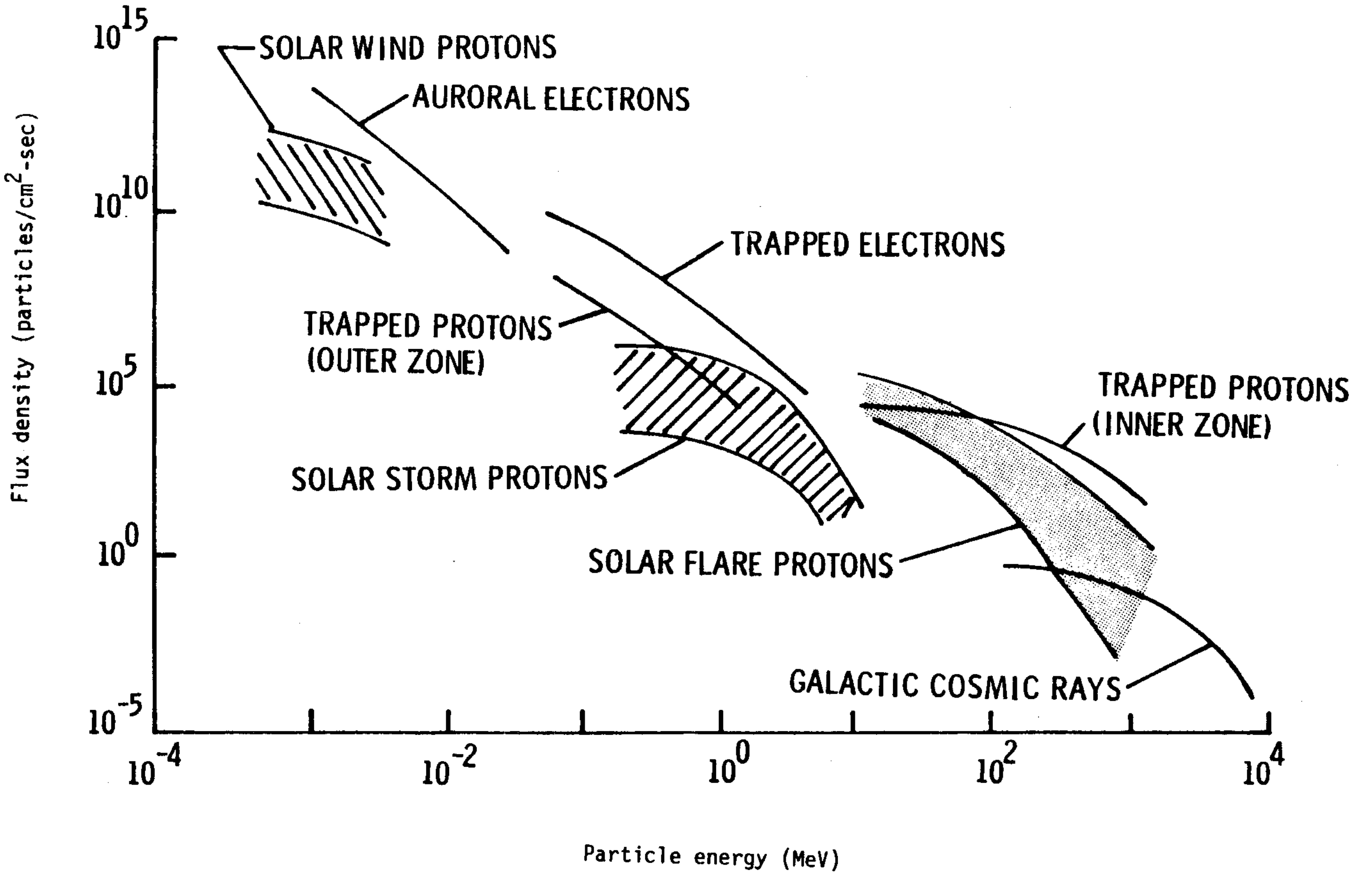

Figure 1

regions of space. Within the inner zone below 400 nautical miles are mostly protons and electrons. Behind the 2 g/cm^2 of shield only about 22 days are required to reach the quarterly exposure limit at the maximum altitude. The limiting biological factor is the testes which could be protected by personal shielding. As for the outer zone, which is important to the space solar power satellites, the radiation is primarily electrons and a shield on the order of 6.7 g/cm^2 is required to reach the quarterly exposure limits in 90 days. The biologically limiting factor is again the testes. If the bremsstrahlung is eliminated by putting a high Z material on the inner side of the wall, the shield could be reduced quite a bit. A shield thickness of only 1.4 g/cm^2 is required to meet the quarterly exposure limit in 90 days and the limiting factors are skin, lens, and the blood forming organs (BFO). This 1.4 g/cm^2 shield is, of course, an absolute minimum shield because there is no personal shielding that is practical for the organs involved. The solar cosmic rays consist mostly of protons and alphas with fewer other particles. Behind 5 g/cm^2, only about six hours are required to reach exposure limits, and the limiting factors are listed in the figure. For a shield of 10 g/cm^2, it takes about half a day to reach exposure limits for the lens and testes, which can be protected by using personal shielding. The galactic cosmic rays contain a little bit of everything, and the type of shielding required and the number of days to reach exposure limits are presently in question. Most probably the hazard will be associated with nonregenerative tissues which also have a unique function. Galactic heavy ions will probably be the ultimate limiting factor

IMPACT OF RADIATION ON OPERATIONS IN EARTH ORBIT

Source	Composition	Aluminum Shielding	Number of days*	Limiting factor
Inner Zone (h < 400 n.mi)	protons electrons	2 g/cm^2	22	Testes
Outer Zone (h > 19,000 n.mi)	electrons	6.7 g/cm^2 1.4 g/cm^2	90 90	Testes Skin, Lens, BFO+
Solar Cosmic Rays	proton alpha	5 g/cm^2 10 g/cm^2	0.25 0.5	Lens, Testes, Skin, BFO Lens, Testes
Galactic Cosmic Rays	proton alpha carbon : iron	?	?	Nonregenerative tissues with unique function?

* Number of days to reach quarterly exposure limit

\+ Assuming personal shielding for testes

Figure 2

in space operations, but all of these points are still open for debate. Conclusions are drawn from data taken from Burrell and Watts (1968), Wilson and Denn (1976), Wilson and Denn (1977a, 1977b), and NAS (1973).

Figure 3 shows how the abundance of galactic cosmic rays falls off as the higher atomic numbers are reached (Simpson and Garcia-Munoz, 1970). The dose is proportional to the charge squared. The relative dose contribution is more nearly the same for different particle types; it doesn't follow that the less abundant types are necessarily negligible.

The galactic cosmic rays are affected by interaction with the earth's magnetic field (Figure 4). Mainly the low rigidity particles are excluded from equatorial regions at low altitudes whereas near the poles the particles may come in freely at all altitudes. Although the particles with low rigidity are seen at low altitude mainly near the polar region, the heavy ions are by far the most rigid particles of the galactic beam. Consequently, mostly protons are lost in the equatorial region.

Most space radiations are affected by solar activity in one way or the other, either as their source or in some secondary effect. Figure 5 shows the annual smoothed sunspot numbers for the past couple of hundred years. The main thing to notice is that to my estimation the concept of a "typical" solar cycle is uncertain. It is clearly illustrated that cycle 19 is one of the most extreme cycles in terms of sunspot number that we have ever seen (last full cycle at right). Cycle 20, shown in part just to the right of cycle 19, was pretty close to an average cycle and we should keep that in mind when we discuss solar cosmic rays later. These data were taken from Sleeper (1972).

GALACTIC HEAVY ION INTENSITIES

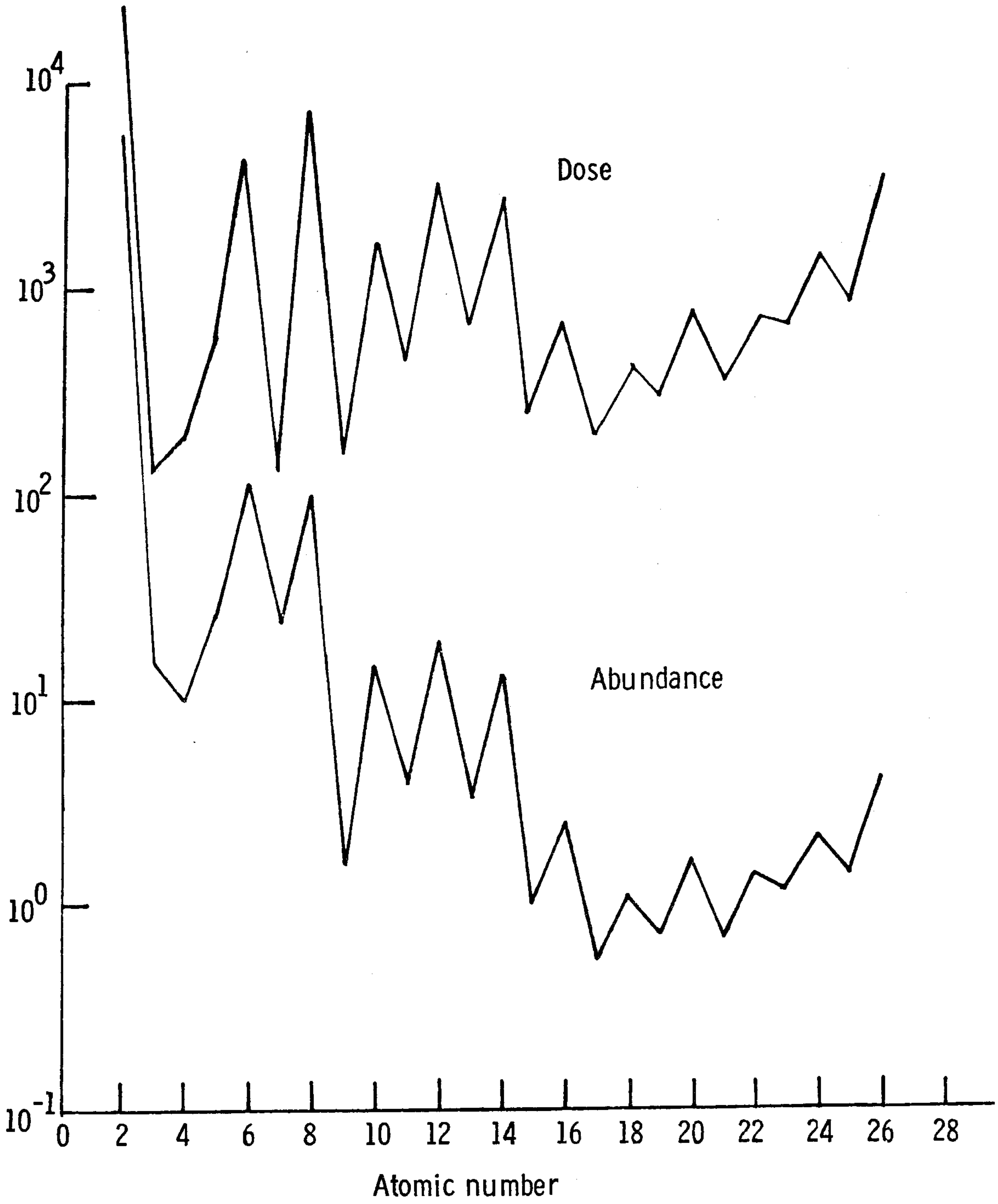

Figure 3

GALACTIC COSMIC RAY INTERACTION WITH GEOMAGNETIC FIELD

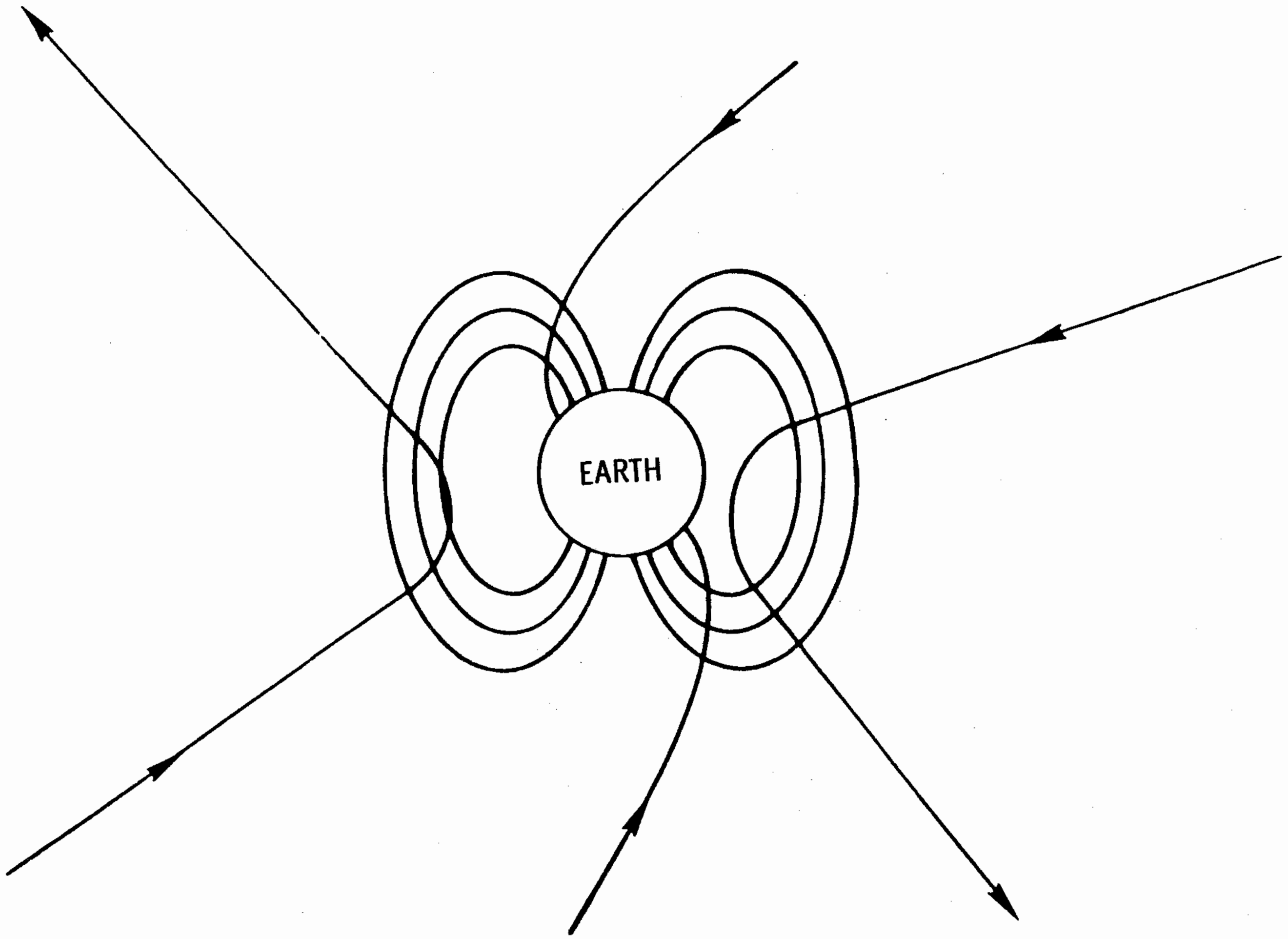

Figure 4

ANNUAL SMOOTHED SUNSPOT NUMBERS

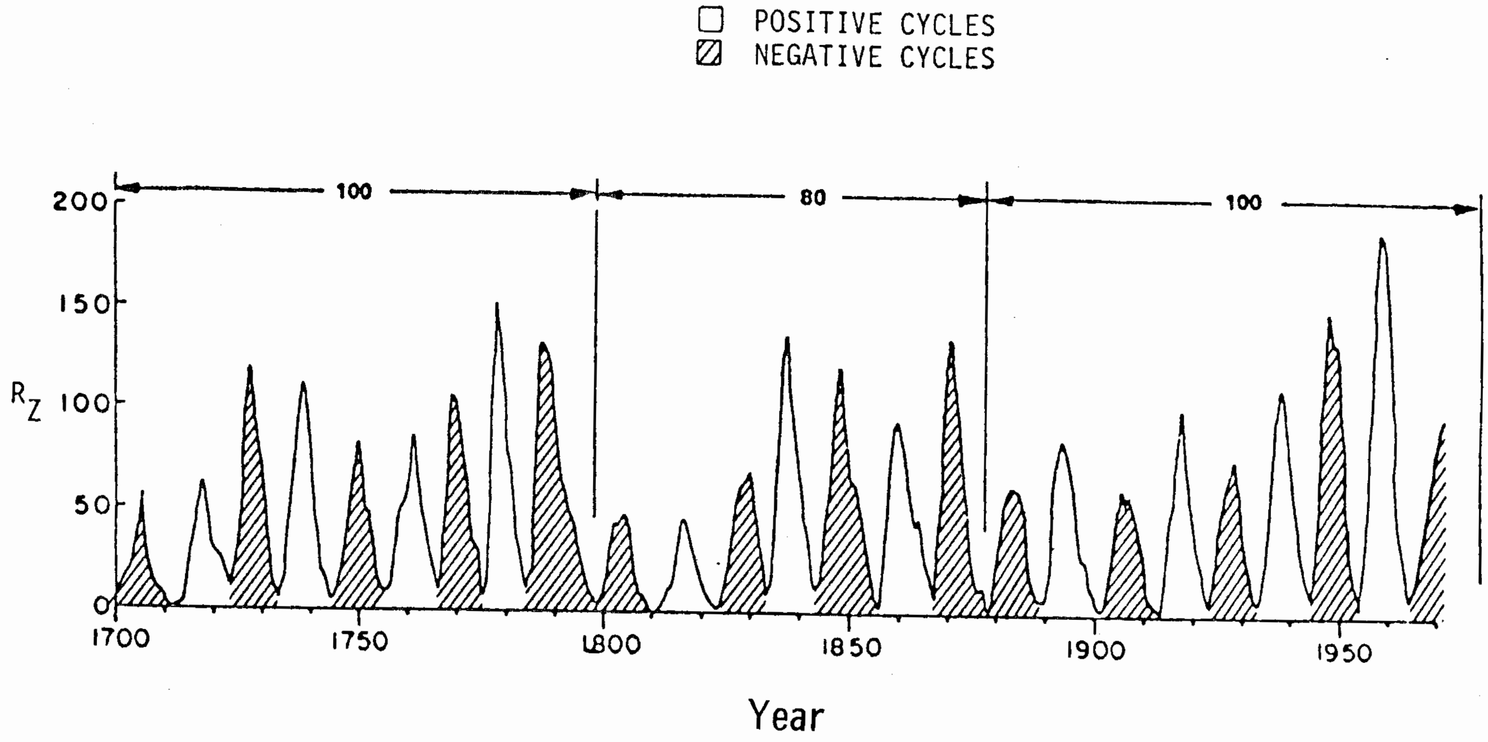

Figure 5

One of the effects observed during solar activity is the fluctuation of the expanding solar corona during the changes in solar activity. The galactic cosmic rays coming in from galactic space interact with this plasma and slow down. In Figure 6 we plotted the amount of energy that the particles lose coming in from galactic space to earth orbit represented as a potential function. It correlates very well with sunspot number which is related to solar activity. These data were taken from O'Brien (1972).

Occasional solar flares are associated with the sun and solar activity. There are a large number of optical flares in which radio bursts and plasma are ejected. During some of these flares (actually very few of them), there are particles that are ejected at high energy into interplanetary space. These high energy particles are able to escape the solar magnetic fields only if the lines are open to the interplanetary region. The data shown in Figure 7 were taken from Slutz et al. (1971), King (1974), and Blizard (1969). This figure shows the sunspot numbers during cycles 19 and 20, and plots of the proton fluence greater than 30 MeV. This is the total fluence of each individual particle event as a function of time. There is a rough correlation between the number of particles and the degree of solar activity. Generally there are anywhere from one to perhaps five of them which might be called major events during any particular cycle.

Some details of what happened during cycles 18, 19, and 20 can be found in Figure 8. Here we show just the major events that occurred during these particular cycles; notice that, in general, the largest events happened during the ascending or descending phase of the solar

GALACTIC COSMIC RAY MODULATION PARAMETER AND SOLAR ACTIVITY

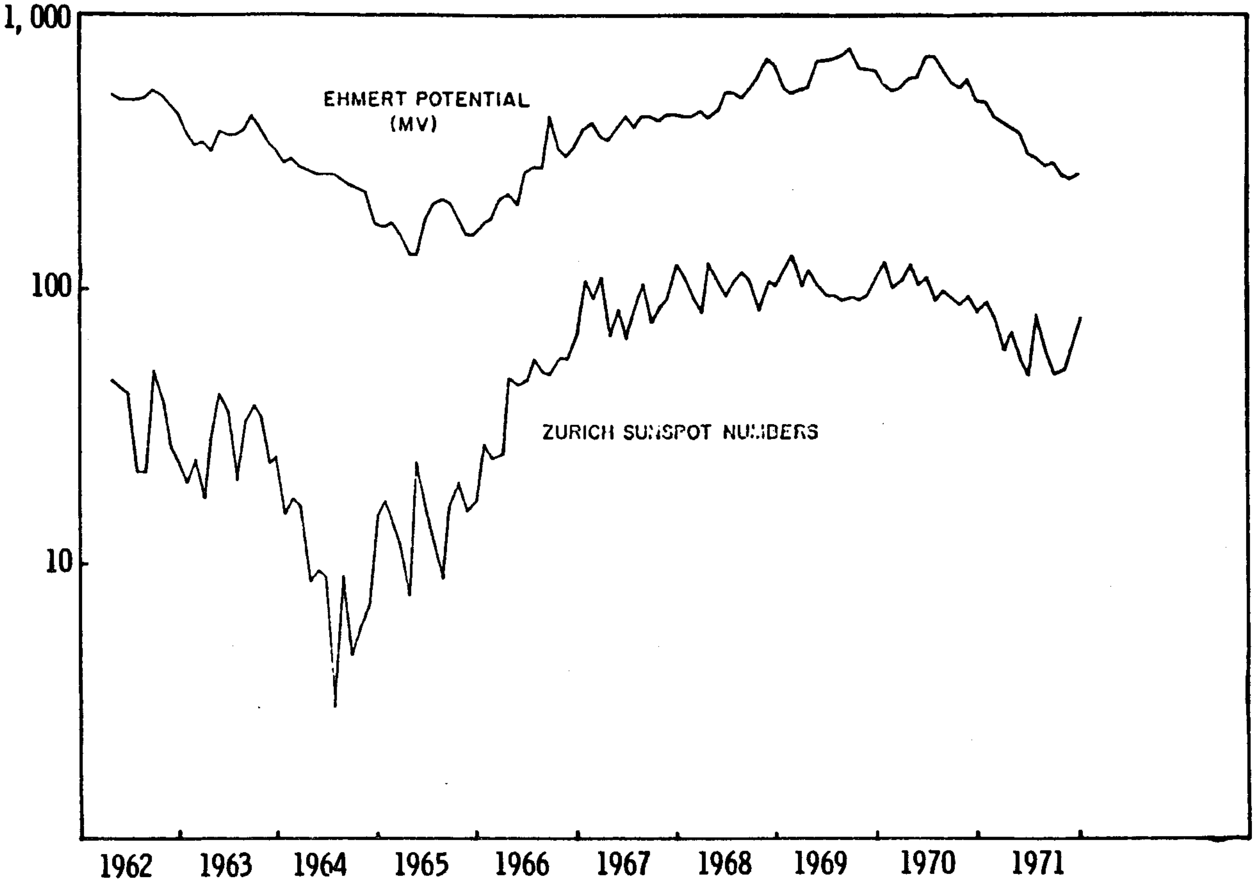

Figure 6

SOLAR ACTIVITY AND FLARE PROTON FLUENCE

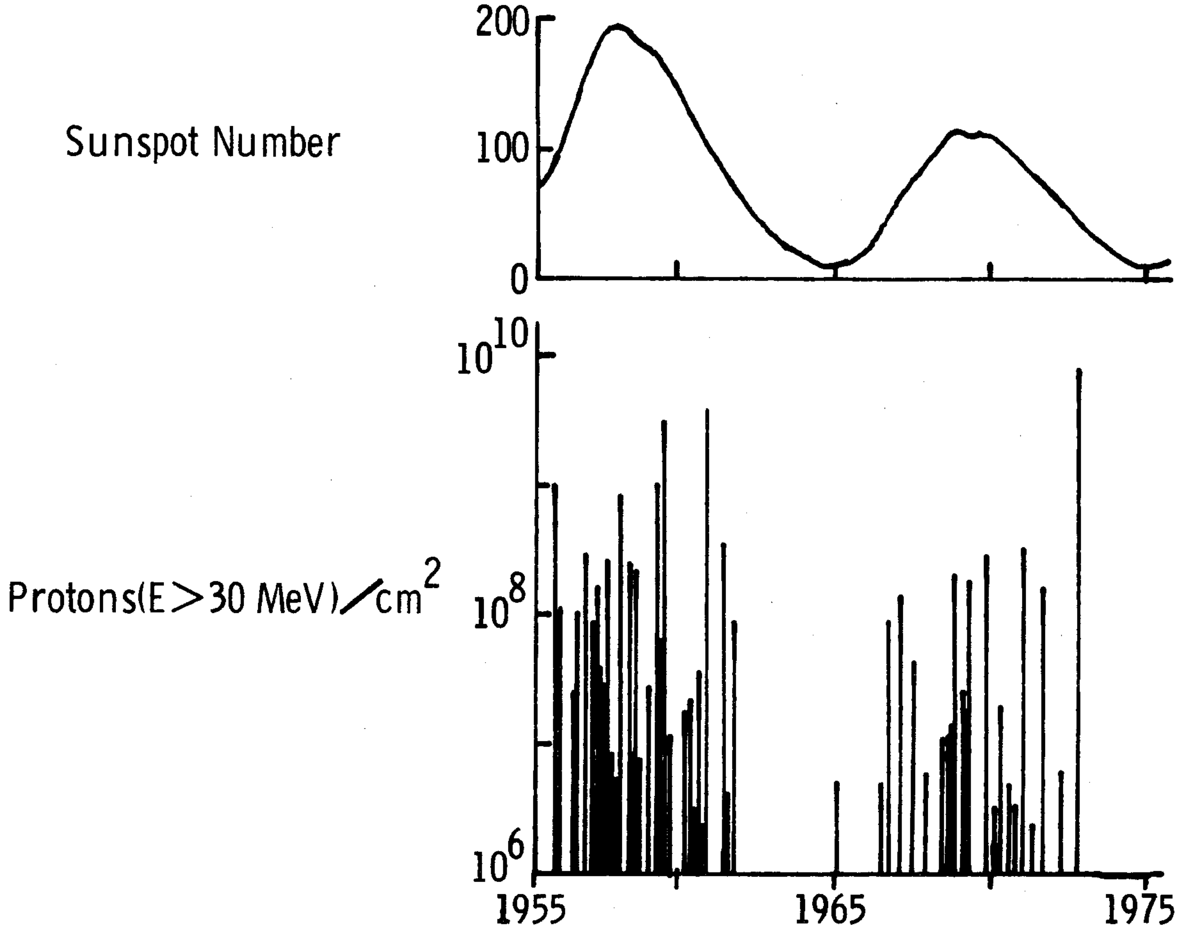

Figure 7

MAJOR SOLAR PARTICLE EVENTS OF THE LAST THREE SOLAR CYCLES

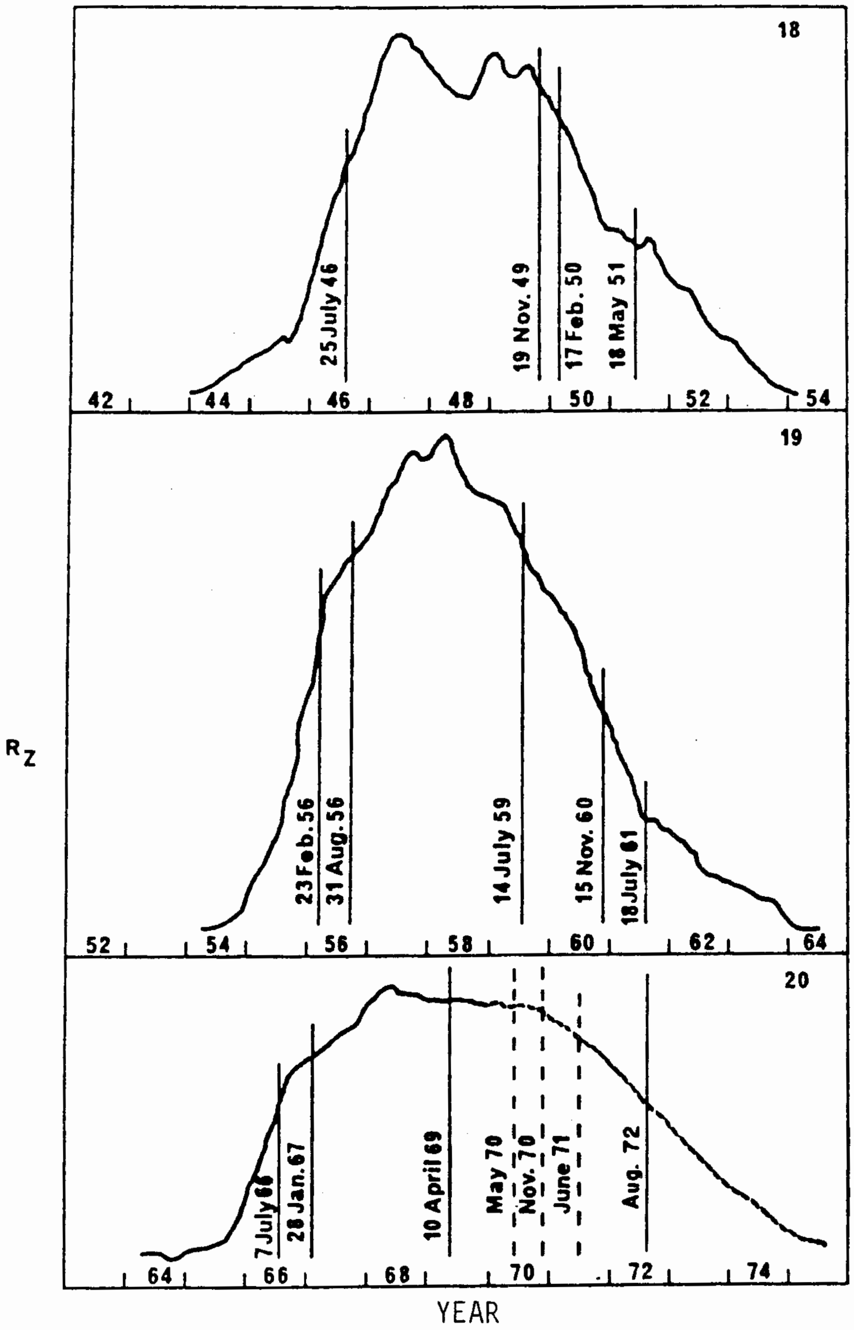

Figure 8

cycle. Major events are usually absent during solar maximum, and, of course, also during solar minimum. Data were taken from Blizard (1969) and King (1974).

There is a rough correlation between the solar activity and the particle fluences that are observed in any given year. Plotted in Figure 9 are proton yearly fluences as a function of the yearly sunspot number during cycle 19 for protons of energy greater than 1 MeV (upper curve), greater than 10 MeV (middle curve), and greater than 40 MeV (lower curve). There is some sort of general dependence of the fluence of particles associated with sunspot number, although there are significant deviations. These correlations are made for predictive purposes. If the sunspot numbers in the next cycle can be predicted, a correlation between sunspot number and particle fluence can be made. Then it is possible to make an estimate of what sorts of exposure might be expected in the coming solar cycle. Data were taken from Webber (1966) and Curtis et al. (1969).

A set of such predictions based on the correlations shown in Figure 9 is shown in Figure 10 for some predictive models on solar cycles. We plotted the calendar year as a function of the proton fluence and we show cycle 19 on which the correlations were based. The solid curves are the observed values going into cycle 20, and the predicted values are shown by the dashed curves. The predictions were fairly accurate up to August 1972; after that there are rather large deviations from the predictive curve. In fact, while we thought that cycle 20 was going to be a rather mild occurrence it turned out that the largest event, as far as space exposure is concerned, occurred

SOLAR COSMIC RAY YEARLY FLUENCE DURING CYCLE 19

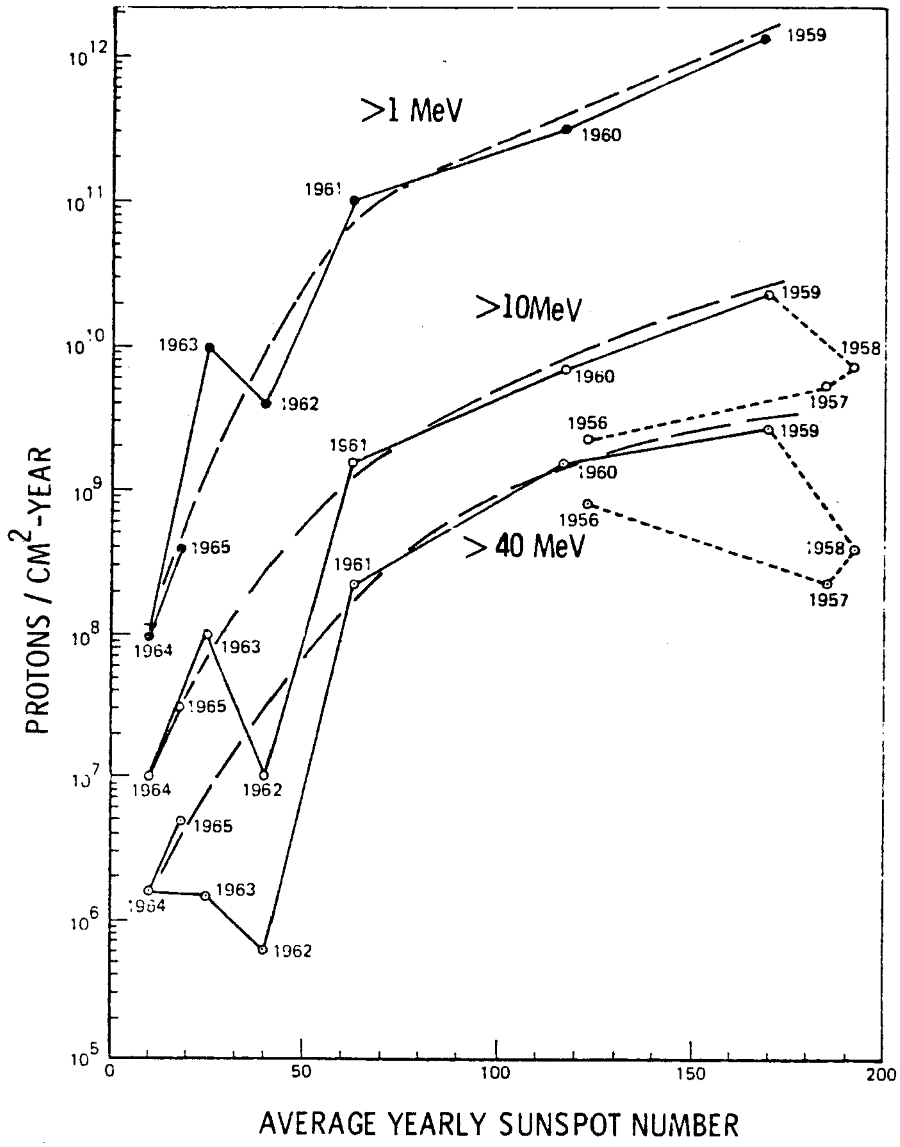

Figure 9

YEARLY PROTON FLUENCE AT GEOSTATIONARY ORBIT

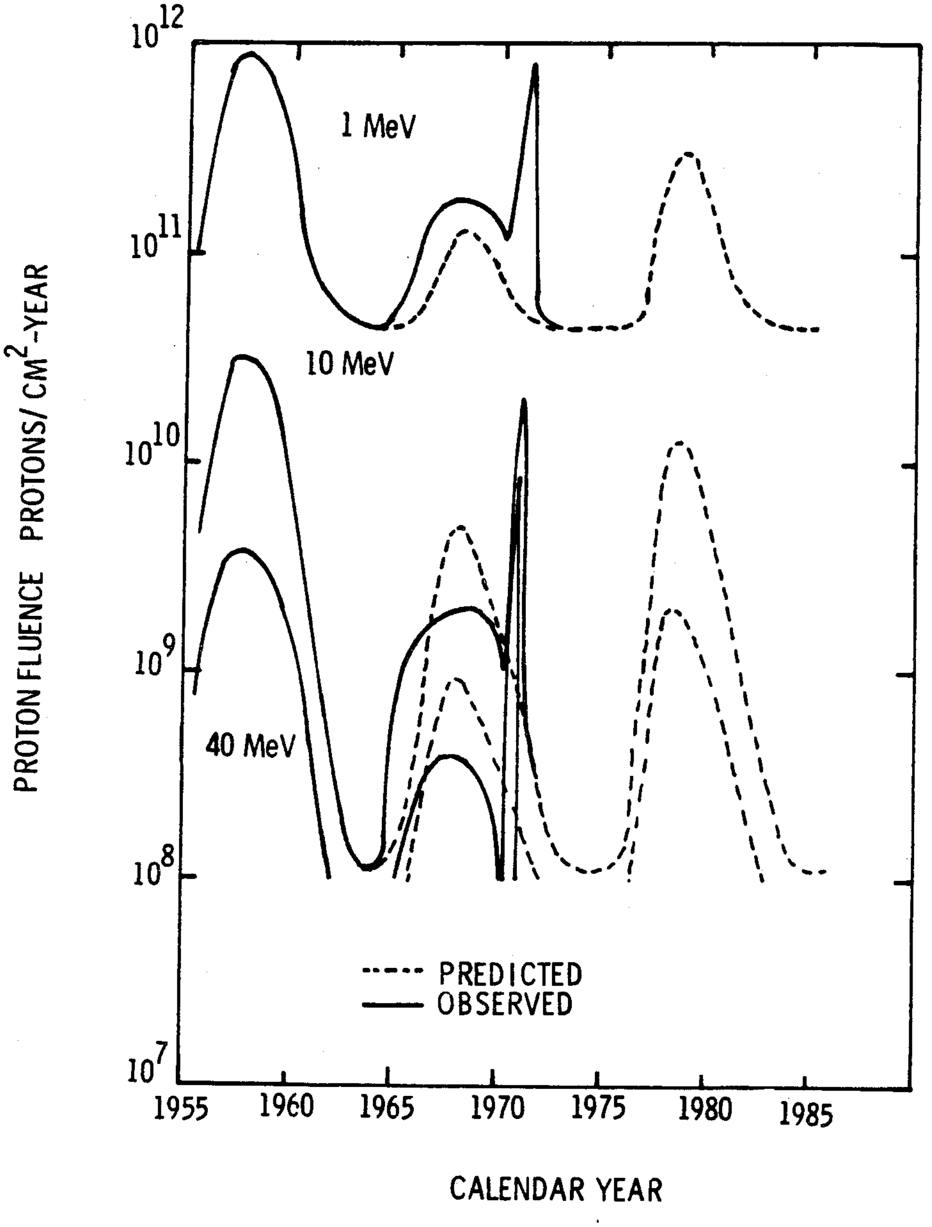

Figure 10

during this rather ordinary cycle--consequently changing our thinking about the importance of solar flares. We always thought solar flares were serious but we did not realize just how hazardous they were until August 1972. Data were taken from Curtis and Wilkinson (1971) and King (1974).

Figure 11 shows the data for energies above 10 MeV as a function of sunspot number from cycle 19 (Figure 10), with the observation made during cycle 20 added to it. We see that the August 1972 event gives most of the contribution during that particular year. Keeping the correlation curve of Figure 9 in mind and comparing the location of the 1962 event and 1972 event (or the 1962 year and the 1972 year), these correlations are accurate within about a factor of ten on the basis of the data we have now.

In particular, the event of November 1960 and the May-July event series of 1959 were previously thought to be the most serious events we had to design for. Now we find that the exposure from the August 1972 event is about three to four times those two earlier events. Whether or not we will have a future event that will exceed the dose of the August 1972 event is an open question.

The solar cosmic rays produced on the sun must still travel to earth. The transit time between the sun and earth is typically 20 minutes for relativistic particles, but sometimes it takes up to a few hours depending on the spectrum and the interplanetary magnetic field configuration (Figure 12). The spectral distribution at earth changes as a function of time because high energy particles tend to arrive before lower energies. The angular distribution of the particles

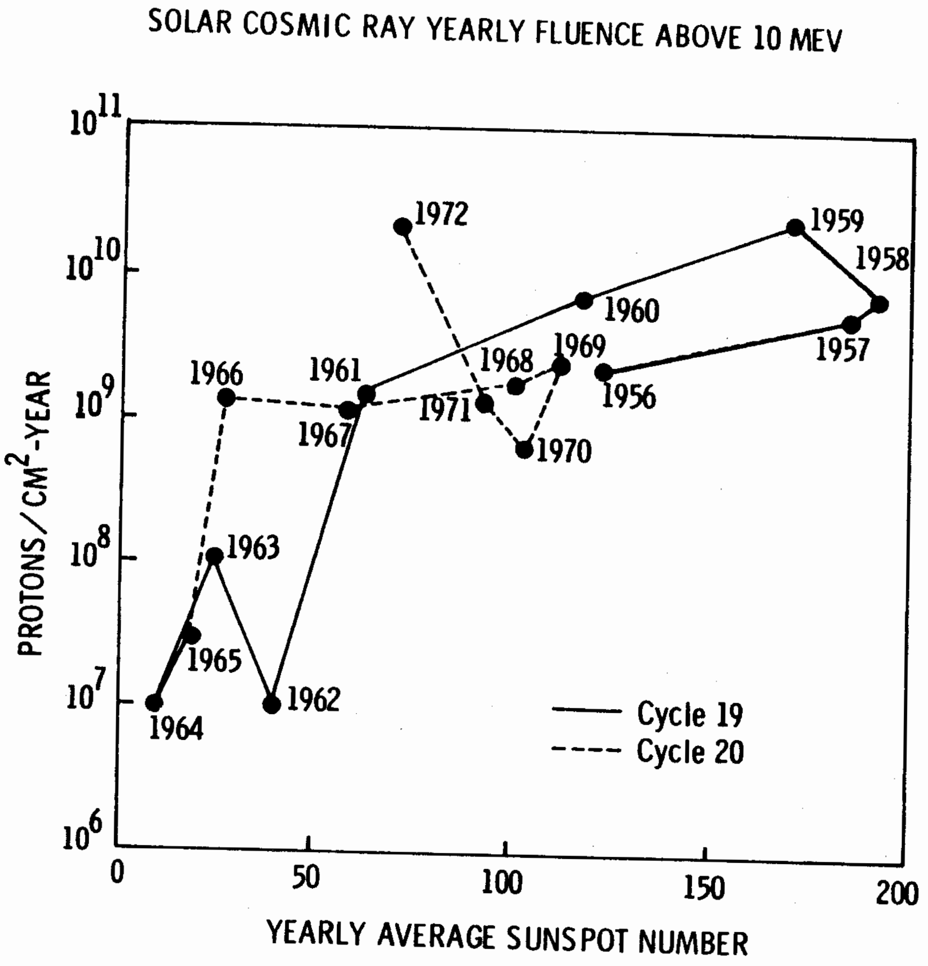
SOLAR COSMIC RAY YEARLY FLUENCE ABOVE 10 MEV
PROTONS/CM^2-YEAR
10^{11}
10^{10}
10^{9}
10^{8}
10^{7}
10^{6}
0
50
100
150
200
YEARLY AVERAGE SUNSPOT NUMBER
1972
1959
1958
1960
1969
1968
1966
1961
1971
1967
1970
1957
1956
1963
1965
1962
1964
Cycle 19
Cycle 20

Figure 11

SOLAR COSMIC RAY EARTH INTERACTION

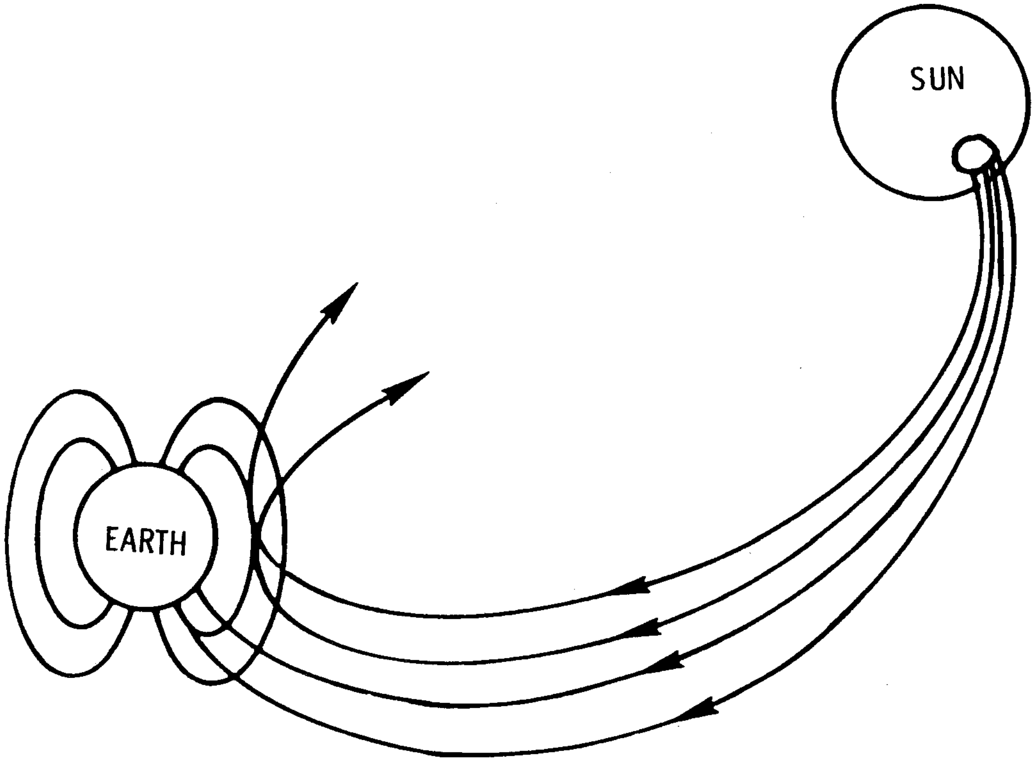

Figure 12

varies greatly from event to event. During some of the high energy events, the particles tend to be directional early in the event and approach isotropy later in the event as the low energy particles arrive. Similar to galactic cosmic rays, the solar protons tend to be eliminated from equatorial regions of the earth's magnetosphere. However, nearly all particles incident in polar regions are transmitted to low altitudes.

The proton transmission factor is the number of protons seen effectively by a spacecraft in a circular orbit. Figure 13 shows this transmission factor for 260 NMi circular orbits at two different inclinations. The proton energy is shown on the abscissa, and the curve is the number of protons that effectively penetrate the magnetic field to that orbit. The polar orbit, or course, spends one-third of its time in the polar cap region; transmission in those polar regions contributes very heavily to the effective transmission factor. At a 50^{o} inclination most of the time in this orbit is spent below the polar cap region, and so there are fairly large effective cutoffs of the proton energy up to 180 MeV, which greatly diminishes the transmission. When using curves like this it should be kept in mind that these solar flare events usually occur in series. It is unusual when a number of sunspots come together to form a plage that causes a solar flare and the emission of a few particles. What usually happens is that a turbulent region exists, and this turbulent region may give rise to many small flares over a period of days before the advent of the main solar event in which high energy particles are emitted. The main particle event may be preceded by a solar flare which emitted

PROTON GEOMAGNETIC TRANSMISSION FOR 260 N. MI. ORBITS

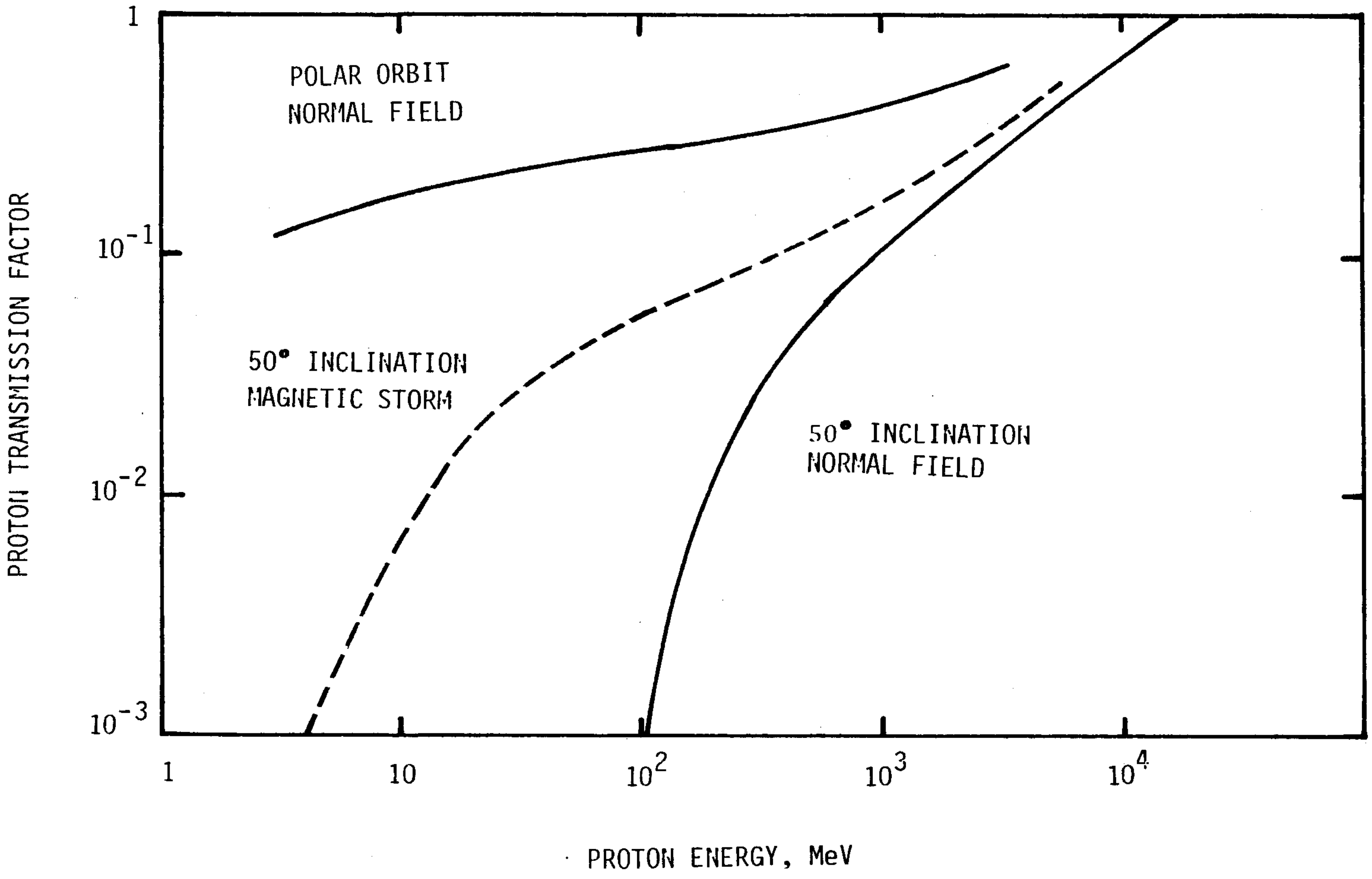

Figure 13

a very fast moving dense plasma. When this plasma interacts with the earth's magnetic field, the field becomes depressed and the cutoffs change drastically because the geomagnetic fields have been disturbed. During an intense magnetic disturbance, the orbit transmission factor for normal field conditions does not apply since the proton cutoff is drastically reduced. Proton cut-off models based on the Stoermer theory are discussed by Kuhn _et_ _al_. (1966) and calculations here were made by Curtis _et_ _al_. (1969).

The integral fluence spectra of three major proton events observed during cycles 19 and 20 are shown in Figure 14. It was previously thought that the November 1960 event was the most hazardous, and we were basing our designs on this limit. As the figure shows, the August 1972 event dominates at energies below 100 MeV, and it has changed our thinking about the limits for the most hazardous case. We originally considered the largest event observed in the cycle of greatest activity to be the worst case event; hence, November 1960. Now a much larger event has occurred in a rather inactive cycle which destroys our logic. Someday the August 1972 event may well be overshadowed by some future event. The data were taken from Foelsche (1963) and King (1974).

The dose equivalent in the center of the sphere of radius _r_ is shown in Figure 15. Compare the August 1972 depth-dose relation to that of the February 1956 event. Clearly in the region about 1 to 20 g/cm^2, which is the important region for spacecraft shielding, the August 1972 event is (in places) an order of magnitude more serious than the February 1956 event. The November 1960 event lies about halfway between these two curves. The data were taken from Wilson and Denn (1976).

PROTON FLUENCE OF THREE MAJOR SOLAR EVENTS

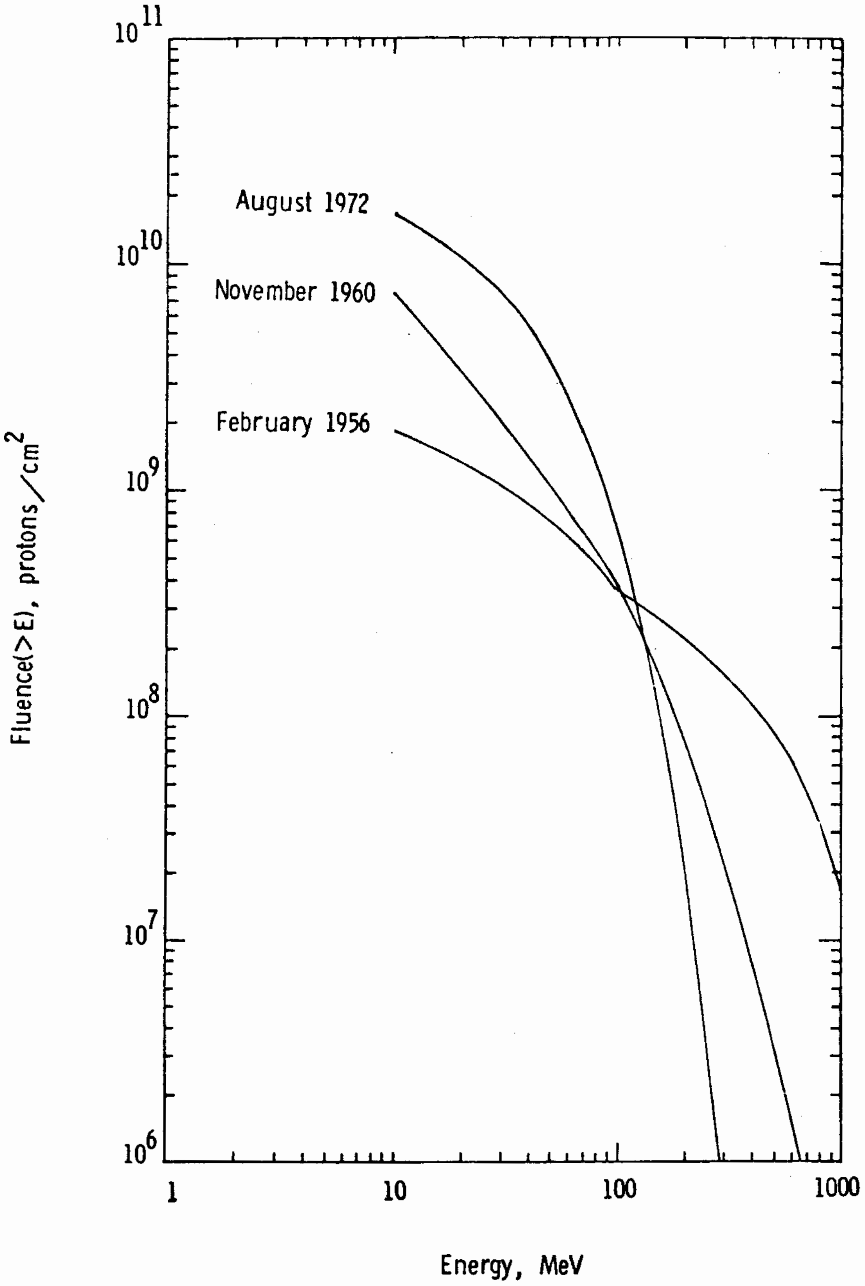

Figure 14

DOSE EQUIVALENT FROM TWO MAJOR SOLAR EVENTS

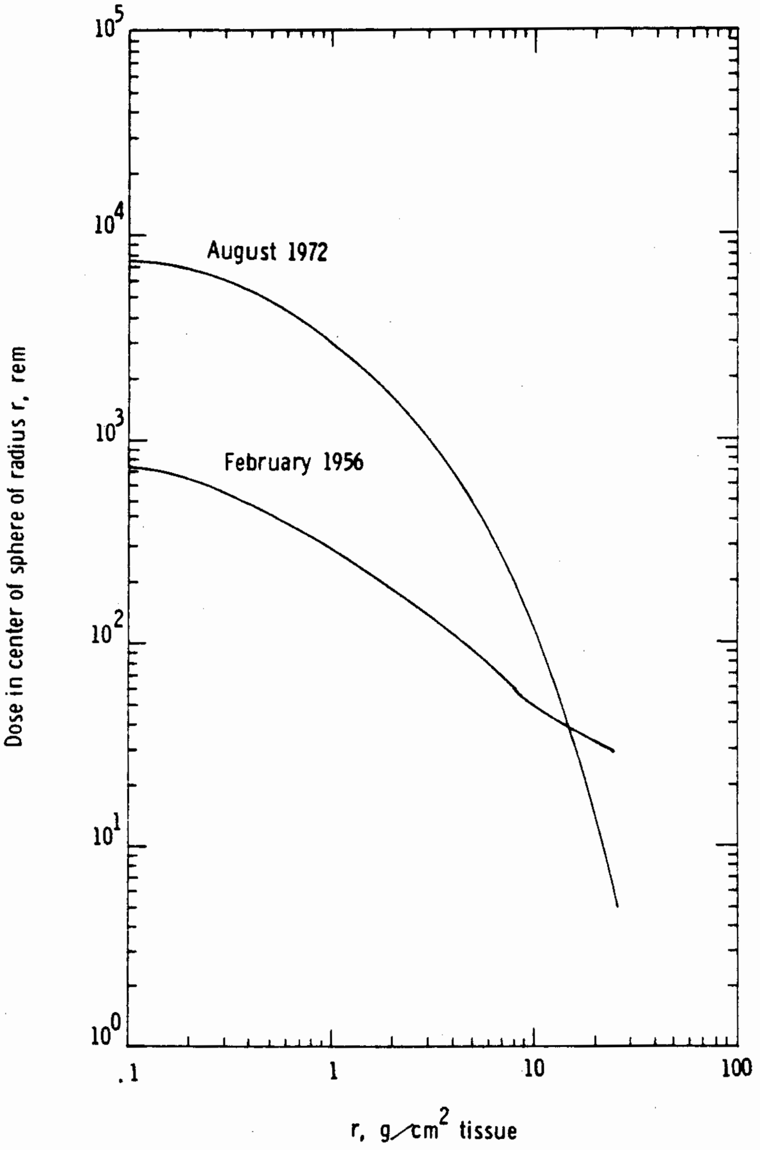

Figure 15

In Figure 16 the dose behind a shield of 1 g/cm^2 during the August 1972 event is compared with the exposure limits. We obtained dose limits by calculating the effective average quality factor for the August 4, 1972 event. This average quality factor is about 1.3, and it is the value used in deriving this graph. Of course the average quality factor is spectrum dependent; 1.3 can't be used for all the events, rather it depends very much on the energy content of the event. For this particular quality factor the exposure limits are reached for the lens of the eye first and the skin later. Note that the dose greatly exceeds the allowed limits behind 1 g/cm^2 of shielding which in the past has been a typical thickness for spacecraft shielding. These curves also take into account the body geometry. Data were taken from Wilson and Denn (1976).

The 30-day exposure limits and also the time required to reach these exposure limits during the August 1972 event are shown in Figure 17. This is the time after the onset of the particle emission; not the time after the optical flare is observed but rather the time after the particles are first seen arriving at earth's orbit. Generally, if a person is very lightly shielded he still has about two to four hours to seek shelter. This is adequate time to move to a more protective region. At 10 g/cm^2 of tissue equivalent material, the dose limits to the marrow and skin are never reached. The limiting factors are the lens of the eye and the testes, and these can be taken care of by using personal shielding. Therefore, a shelter of about 10 g/cm^2 of a material like polyethylene (plus personal shielding) would be adequate protection from the August 1972 event. Data were taken from Wilson and Denn (1976).

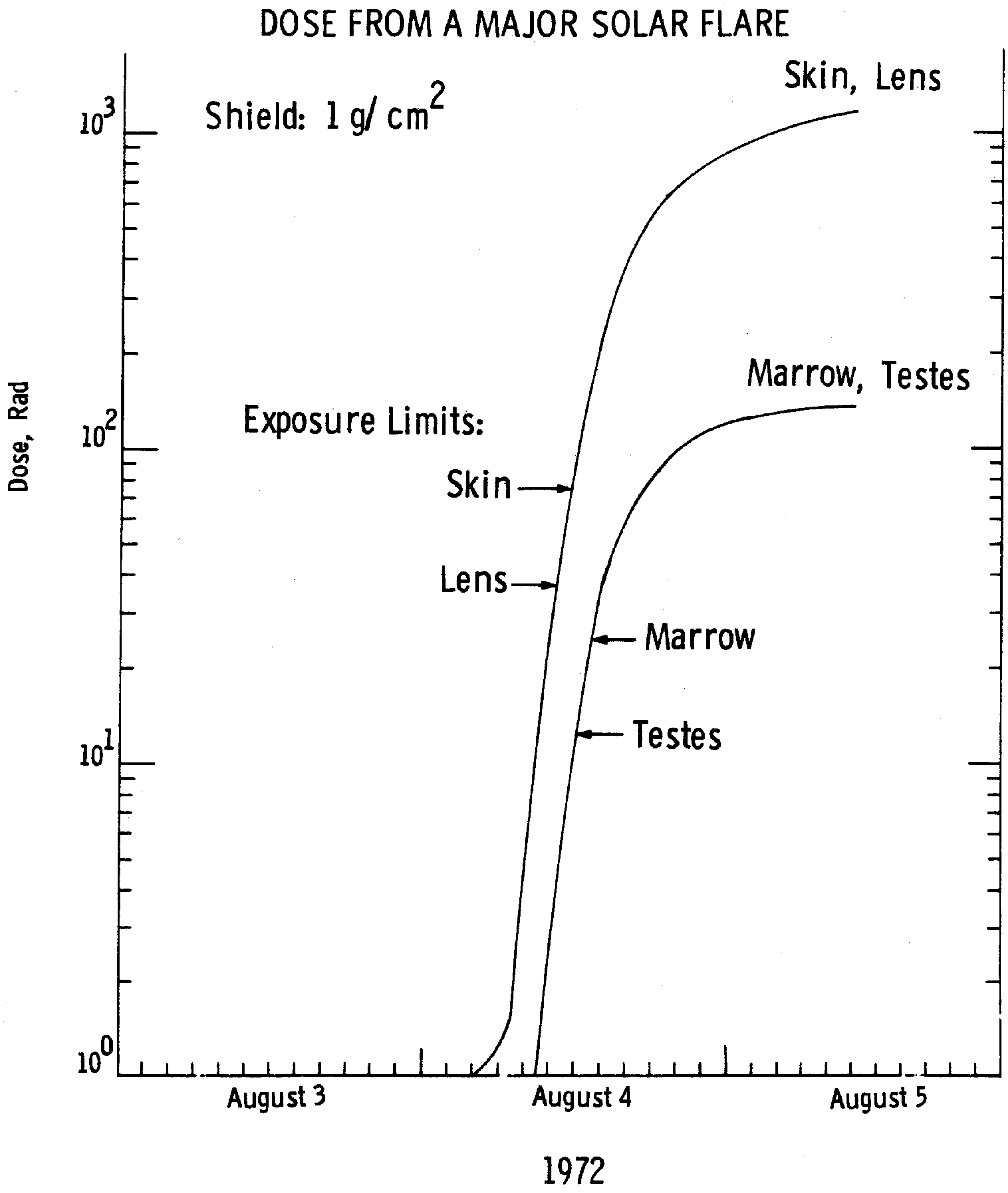
DOSE FROM A MAJOR SOLAR FLARE
Shield: 1 g/cm^2
Dose, Rad
10^3
10^2
10^1
10^0
Skin, Lens
Marrow, Testes
Exposure Limits:
Skin
Lens
Marrow
Testes
August 3
August 4
August 5
1972

Figure 16

THIRTY DAY EXPOSURE LIMITS

	Marrow	Skin	Lens	Testes
rem	25	75	37	13
rad*	19.2	57.7	28.5	10

*DE $\approx$ 1.3D where DE is the dose equivalent and D is the dose.

TIME REQUIRED TO REACH EXPOSURE LIMITS FOR AUGUST 4 EVENT

Shield, g/cm^2	Marrow, hr	Skin, hr	Lens, hr	Testes,* hr
0.2	6.0	3.0	1.9	4.4
.4	6.1	3.5	2.4	4.9
1	6.3	4.7	3.6	5.2
5	8.9	8.0	6.5	7.3
10	∞	∞	11.7	12.7

*Values are overestimated since the testes dose is taken to be the same as the marrow dose.

Figure 17

I would now like to change the discussion from solar and galactic cosmic rays and talk just a little bit about the trapped radiations. Stassinopoulos is going to talk about these radiations also, so I am going to try to omit the topics that he will discuss in more detail. The trapped radiation, illustrated in Figure 18, follows a helical path along the magnetic field lines between the mirror points. The location of the mirror points along the field line depends on the pitch angle at the magnetic equator and the energy of the particle. The greater the energy or higher-pitch angle, the deeper the mirror point lies in the magnetic field. If the particle energy and pitch angle are sufficiently large, the mirror point is so deep that the particle interacts with the atmosphere and is lost from the particle population. For the inner zone it appears at least for the protons that the particle source is primarily neutrons which are produced in atmosphere by solar and galactic cosmic rays. The outer zones appear to be something like a pipe line with strong sources and strong sinks. The particles flow rapidly through these regions, and on the average they maintain a fairly high population density although the residence time is short (see Singley and Vette, 1972).

The earth's magnetic field is not centered at the earth's geographic center. Also, the main dipole moment, along the principal axis of the magnetic field, is tilted with respect to the earth's rotational axis so that the geomagnetic field is not symmetrical with respect to geographic coordinates. Figure 19 shows the spatial variation of trapped electrons. The penetration of radiation to low altitudes at latitudes below 50° is due to the displacement of the center

GEOMAGNETIC EFFECTS ON COSMIC AND TRAPPED RADIATIONS

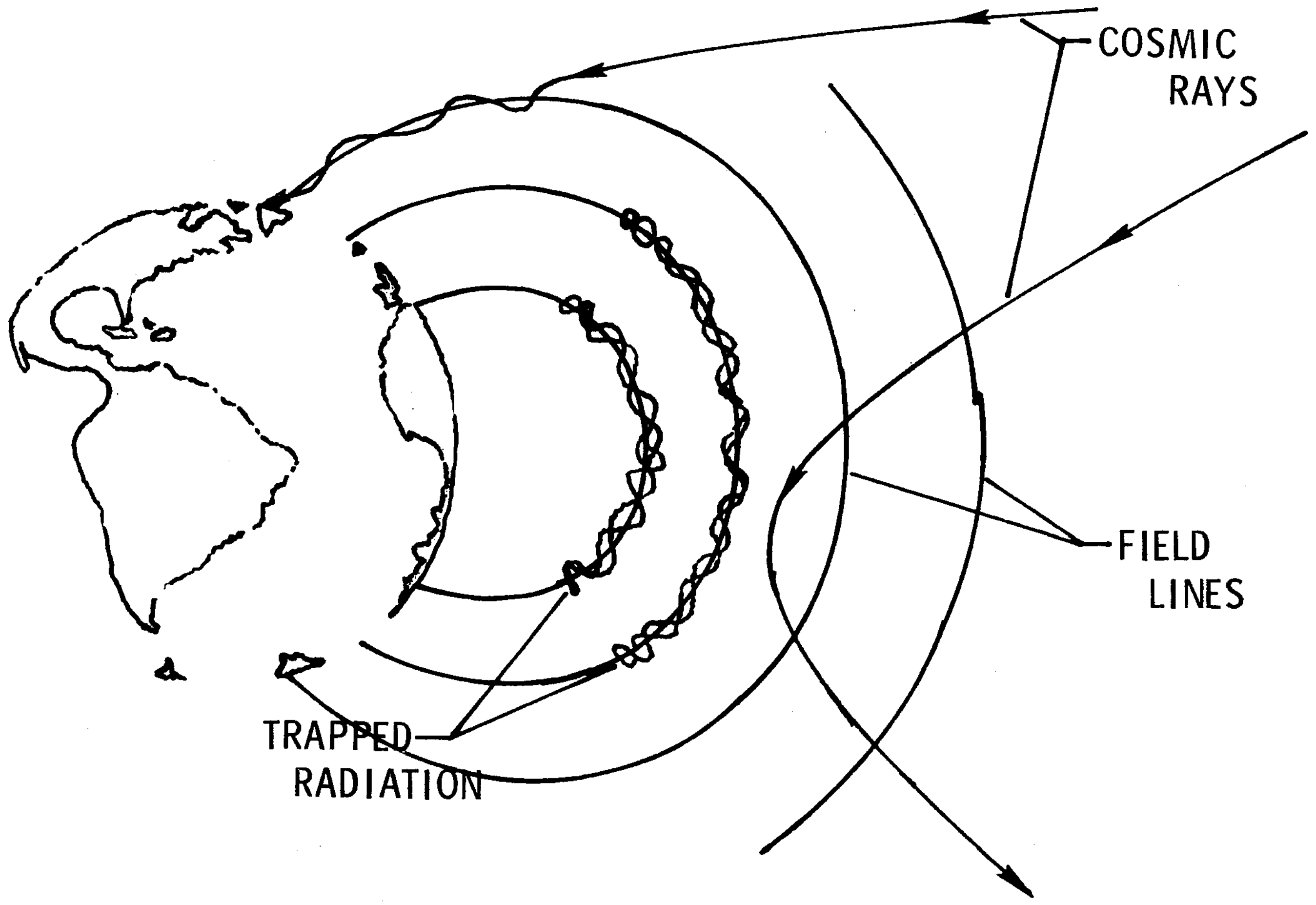

Figure 18

of the magnetic field with respect to the earth's center. These low altitudes occur over the south Atlantic. The effects of the tilt of the axis as a general north-south asymmetry can also be seen. There are two regions where the radiations occur; the first is primarily centered at 2,000 km which is the inner zone, and the second is the outer zone with a central region located at 20,000 km. Data were taken from Noll and McElroy (1975).

Because of this displacement and tilt of the magnetic field, these asymmetries show up as a function of orbital inclination angle for fixed altitude (Figure 20). Generally, a maximum exists in the exposure rate at about 30^0 inclination, which is the optimum launch inclination for Kennedy. There is a relatively radiation-free zone at low altitudes and low inclinations. At the high inclinations not only the inner zone radiation but also some of the outer zone radiation, which comes down to fairly low altitudes at the outer edge of the polar caps, can be seen. Data taken from Noll and McElroy (1975).

Figure 21 gives an idea of where the particles generally lie. The curves are dose rates for equatorial circular orbits as a function of orbital altitudes, so it is roughly a radial sweep of the radiation belts. This is old data from AP5 and AP6, but it still tends to convey the general shape of the radiation zones. For those particles that are biologically most important a peak can be seen at about 2,000 nautical miles. The doses that cause material problems, especially to thermal control coatings, peak much higher, at 10,000 nautical miles. Data taken from Cladis *et al*. (1971).

Figure 22 clearly shows the inner and outer zone for the trapped

SPATIAL VARIATION OF TRAPPED ELECTRONS

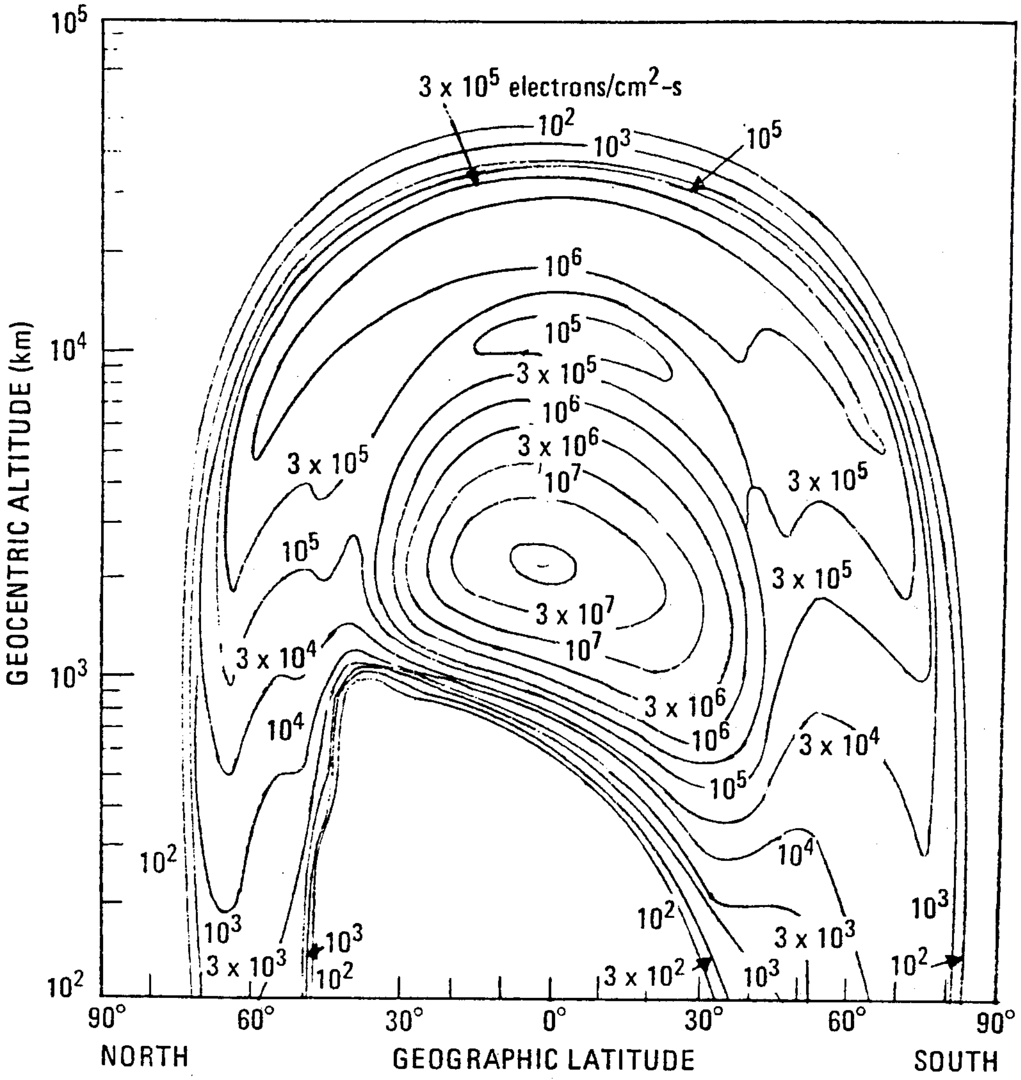

Figure 19

VARIATION OF TRAPPED RADIATION IN LOW EARTH ORBIT

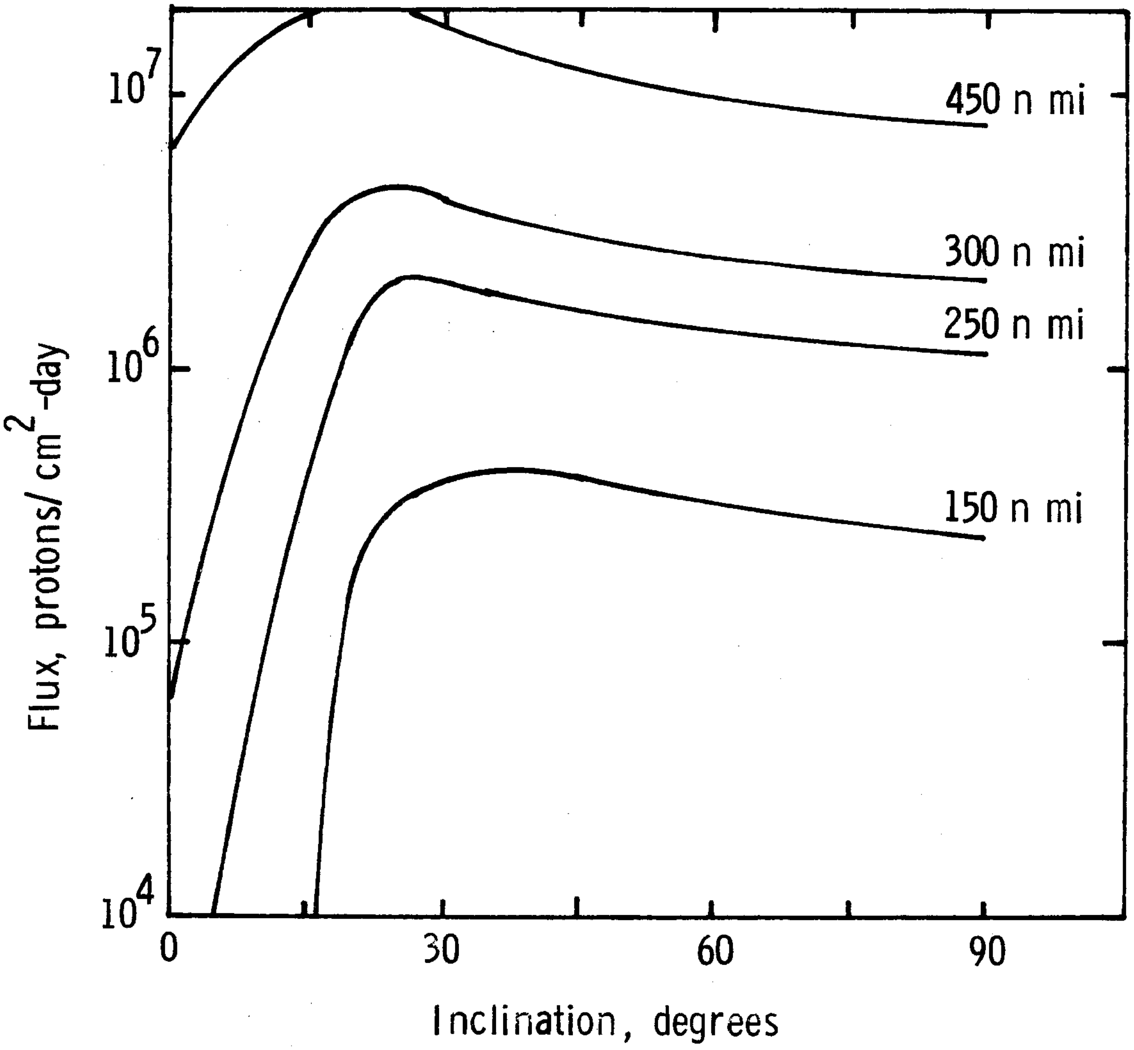

Figure 20

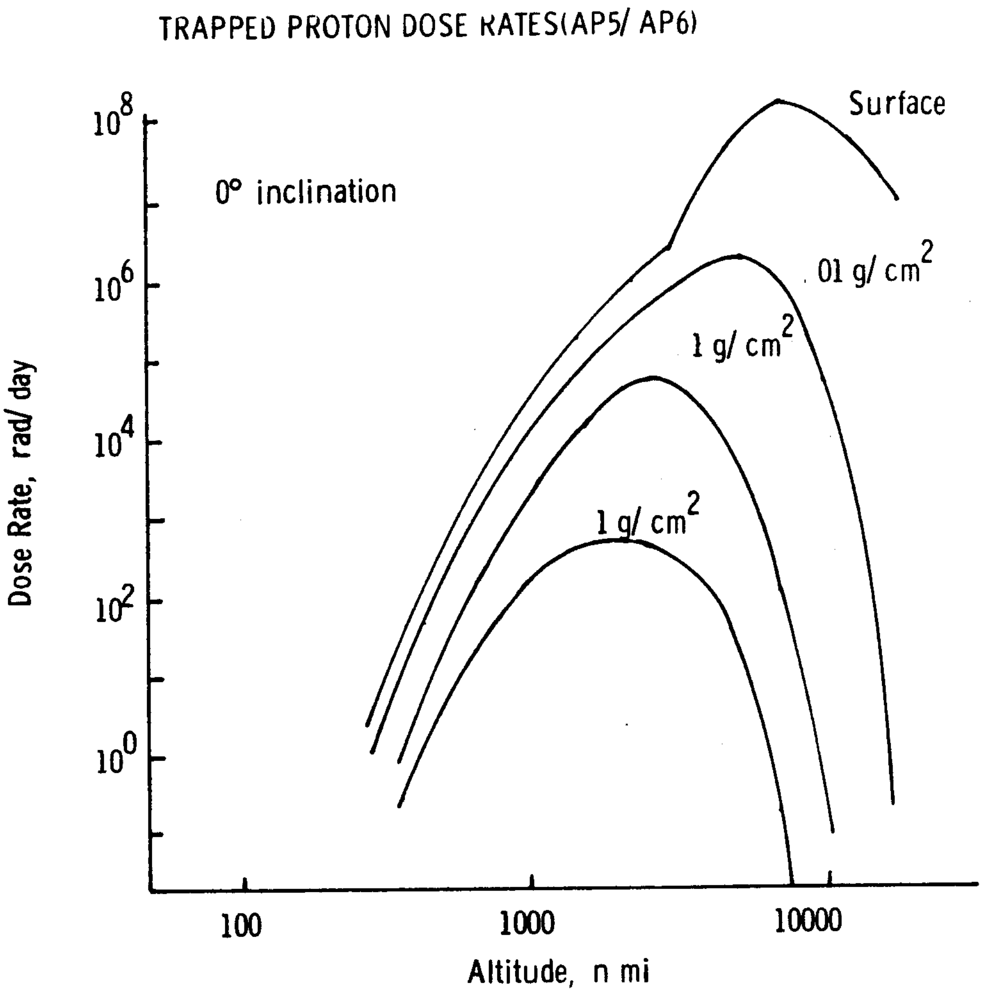
TRAPPED PROTON DOSE RATES(AP5/ AP6)
0° inclination
Surface
.01 g/ cm2
1 g/ cm2
1 g/ cm2
Dose Rate, rad/ day
10^8
10^6
10^4
10^2
10^0
100
1000
10000
Altitude, n mi

Figure 21

electrons. Again, these are old data (AE2), and it is extremely inaccurate in the geosynchronous region. However, as in the case of the protons, going from the low earth orbit which is down around a few hundred nautical miles to geosynchronous orbit at 20,000 nautical miles there are some very intense regions for the orbital transfer. These intense regions will pose some problems from the material point of view considering vehicle structures, thermal control coatings, etc. Data were taken from Cladis et al. (1971).

Figure 23 is a summary of the way things look from a biological point of view. This curve shows the time limit on operations imposed by trapped radiations behind about 2 g/cm^2 of aluminum. The curve represents the number of days in orbit per year it would take to reach the yearly exposure limits. These are not, when the dose rate limits are examined, the actual number of days a person could be exposed in one continuous visit, yet the curve gives an idea of the amount of time that one could spend in various regions. In particular, it is easy to see that in a little over a day in the heart of the zone, the exposure will already reach the yearly limit. The exposure throughout the central region is quite high. There is a decrease in the dose rate approaching very low altitude which is due to the fact that the losses in the inner zone are associated with the interactions of the earth's atmosphere. To limit exposure in this region one has the tendency to do operations at as low an altitude as possible. But the atmospheric interaction, which is the same thing that limits the dose rate, also increases the drag of the vehicle. If one thinks in terms of a large structure which has virtually no mass and an extreme

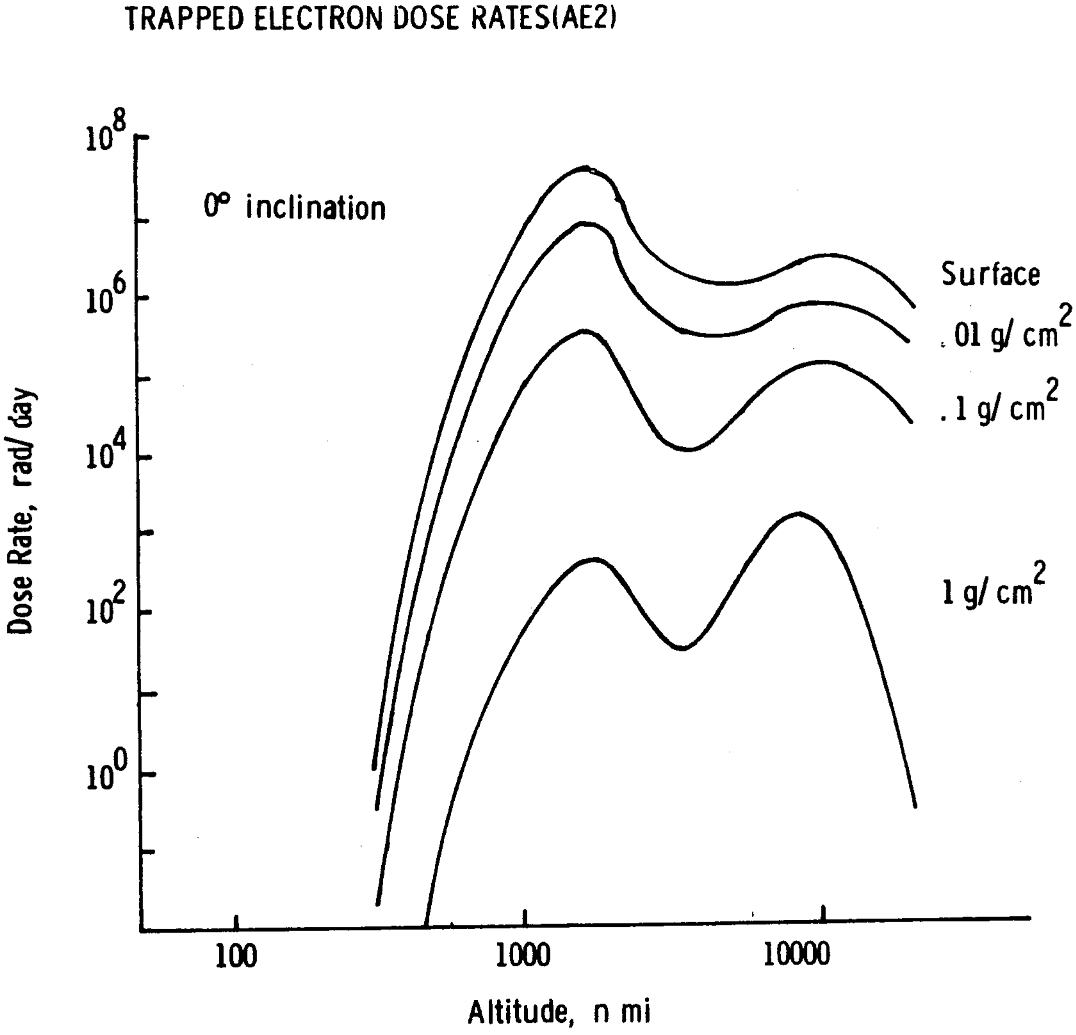
TRAPPED ELECTRON DOSE RATES(AE2)
0° inclination
Dose Rate, rad/day
10^8
10^6
10^4
10^2
10^0
100
1000
10000
Altitude, n mi
Surface
.01 g/cm^2
.1 g/cm^2
1 g/cm^2

Figure 22

LIMITS IMPOSED BY TRAPPED RADIATIONS ON SPACE OPERATIONS WITHIN A 2 g/cm^2 ALUMINUM SHIELD

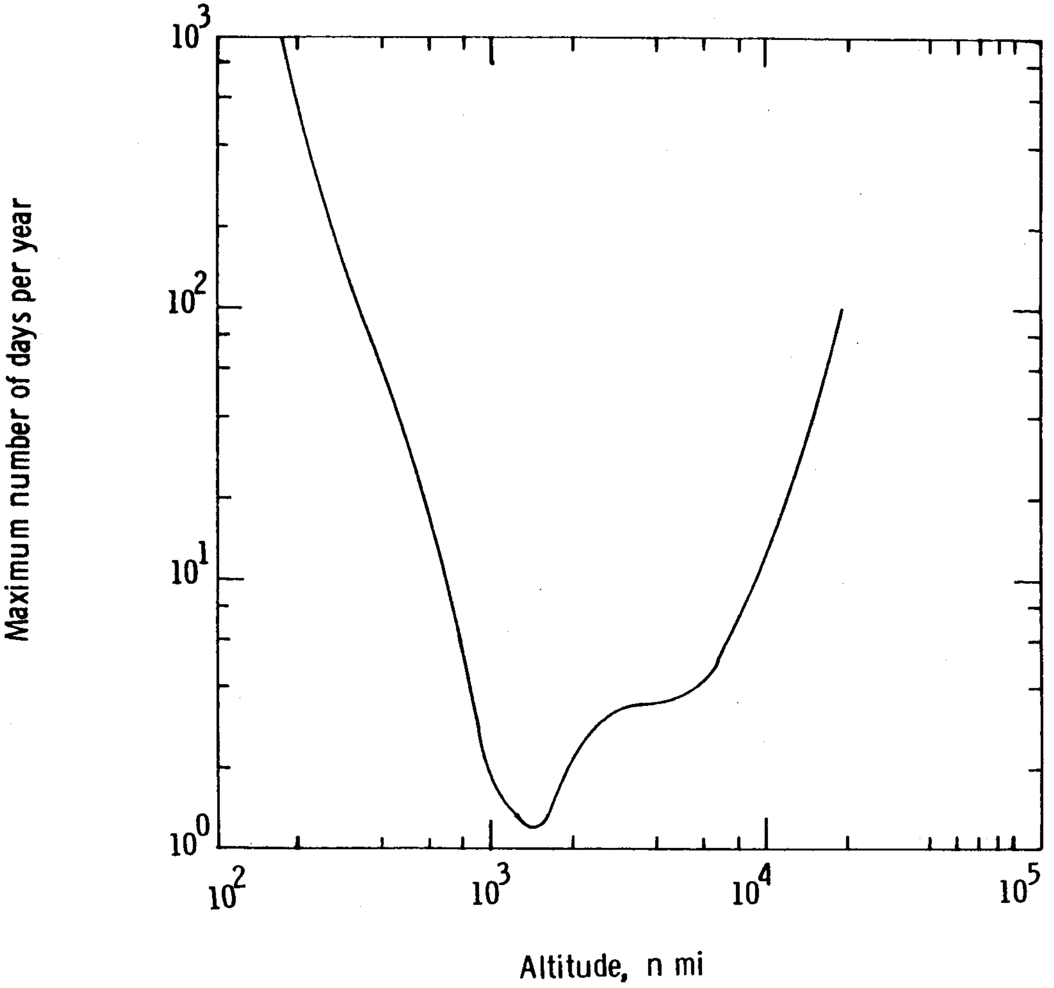

Figure 23

cross section, the drag forces are very large and the kinetic energy very small. Therefore, one must look closely at tradeoffs to be made between these two effects in this region when constructing large structures in low earth orbit. The data were taken from Burrell and Watts (1968) and Wilson and Denn (1977).

I will now consider the AE4 model representation of the outer zone omnidirectional flux (Figure 24), and discuss how the model actually relates to the physical data. In particular, there are times when the required information is not directly available through the model, and these will be discussed later. The omnidirectional flux $\underline{J}$ in the outer zone is a function of the particle energy, the geomagnetic coordinates, and longitude which is related to local time at any fixed universal time $\underline{t}$. The equation is written in terms of $\underline{N}$, which is the local time-averaged equatorial omnidirectional flux that varies as a function of universal time. The function Φ relates the omnidirectional flux to the local time or the longitude, and $\underline{G}$ relates to how the belts vary as the latitudes change along the given $\underline{L}$ shell of the geomagnetic field. The model assumes there is no coupling between latitudinal and longitudinal dependence. These two functions, Φ and $\underline{G}$, are normalized so that Φ averaged over all local time is unity and that $\underline{G} = 1$ on the geomagnetic equator. For further discussion see Singley and Vette (1972), and Wilson and Denn (1976, 1977a).

To relate the omnidirectional flux to the universal time dependence we made a graph (Figure 25) of electron fluxes at geosynchronous altitude greater than 1 MeV and greater than 1.9 MeV as a function of time. The longitudinal dependence of these data has been removed,

MODEL REPRESENTATION OF OUTER ZONE OMNIDIRECTIONAL FLUX

$$J(E, B, L, \varphi, t) = N(E, L, t)\ \Phi(E, L, \varphi, t)\ \ G(B, L)$$

E = electron energy

B, L = magnetic coordinates

φ = local time (longitude)

t = universal time

$N(E, L, t)$ = local time averaged equitorial flux

$\Phi(E, L, \varphi, t)$ = local time factor

$G(B, L)$ = relates to latitudinal variations

Figure 24

so this graph is roughly indicative of the averaged value over the longitude of the equatorial electron flux as a function of universal time. Plotted along the bottom of the graph is a measure of the planetary field index (K_p), which is an average of the log of magnetic intensity at a number of ground stations and is a global measure of the magnetic field. Perhaps the fluctuations in the magnetic field intensity are in some way related as there appear to be some correlations between them. The important point is that the electron flux will grow by two orders of magnitude or more in a couple of hours, followed by decay over several days. Also when the peak flux is reached the dose rate behind fairly light shielding, e.g., a 0.5 g/cm^2, is sufficiently high that the dose limits are met in about a half hour. When the electrons do fluctuate and go to high values they are extremely high values indeed. The few hours rise time and the time required to reach exposure limits will probably be long enough to move to a more shielded area when one of these large fluctuations begin. But there are still several unanswered questions: what about the false alarm rate? What effect do the disturbances have on crew performance? This is a very fruitful area of study and it should be explored. Data were taken from Paulikas and Blake (1971).

During these large scale fluctuations, it appears that electrons are inserted into the magnetic tail region. These inserted electrons undergo radial diffusion to a lower altitude over a period of days as shown by the December event of 1962 (Figure 26). The main loss of these inserted electrons is pitch angle diffusion and precipitation into the atmosphere in polar regions. Data from Frank and Van Allen (1966).

ELECTRON FLUCTUATIONS AT GEOSTATIONARY ALTITUDE

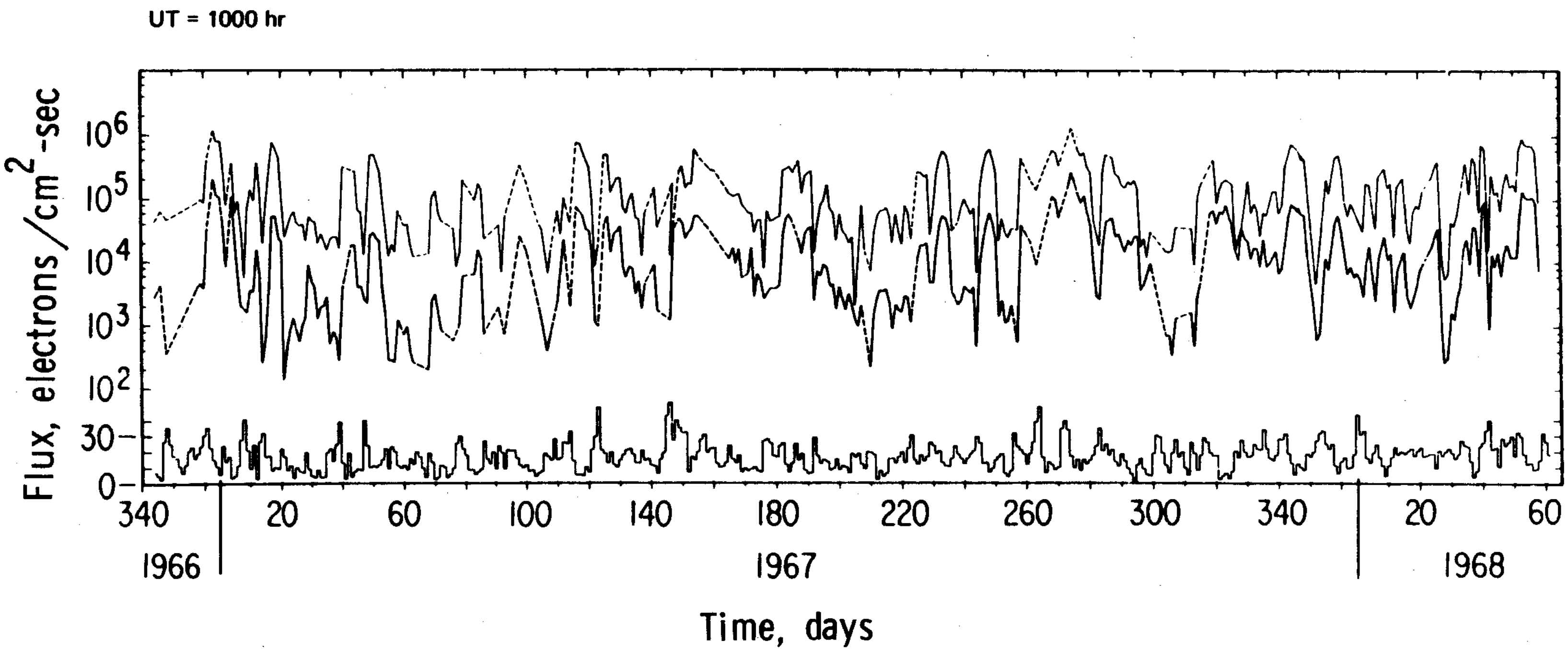

Figure 25

One rather strange thing about these electron fluctuations in universal time is that if they are randomly sampled and a probability distribution is drawn, they turn out to be normally distributed. Figure 27 is the accumulative probability as a function of electron fluence observed for different energies. The symbols are the data points; the curve is a previous model and should be ignored. The point is that these data fall nicely on a normal distribution which is to me remarkable. Data were taken from Paulikas and Blake (1971).

By missing the major part of these large time fluctuations, we have the potential of reducing the exposure quite a bit. What we show in Figure 28 at geostationary altitudes is the exposures on the least extreme days. That is, on the most extreme days we go to a heavy shelter, on the least extreme days we are out doing normal work activities. P is the fraction of days over which we average the dose. P = 1 means that we are out in the normal areas 100% and we never go to a heavier shielded area; P = 0.8 says we spend 20% of the time in heavily shielded areas and 80% of the time out working. Therefore, by eliminating 20% of the worst days one can reduce exposure by a factor of four or so. Depending on how much you want to limit yourself you can continue to drive the dose down by limiting the number of work days. On this figure there are basically two curves. These are the penetrating electrons themselves which continue to drop (dropping off very rapidly and limiting penetration to perhaps about 2 g/cm^2) and a very penetrating component caused by the bremsstrahlung. Whatever type of shield we eventually use for the habitat will be a composite; it seems practical to use a low Z material on the outside to keep

ELECTRON INJECTION DURING A MAGNETIC STORM FOLLOWED BY RADIAL DIFFUSION

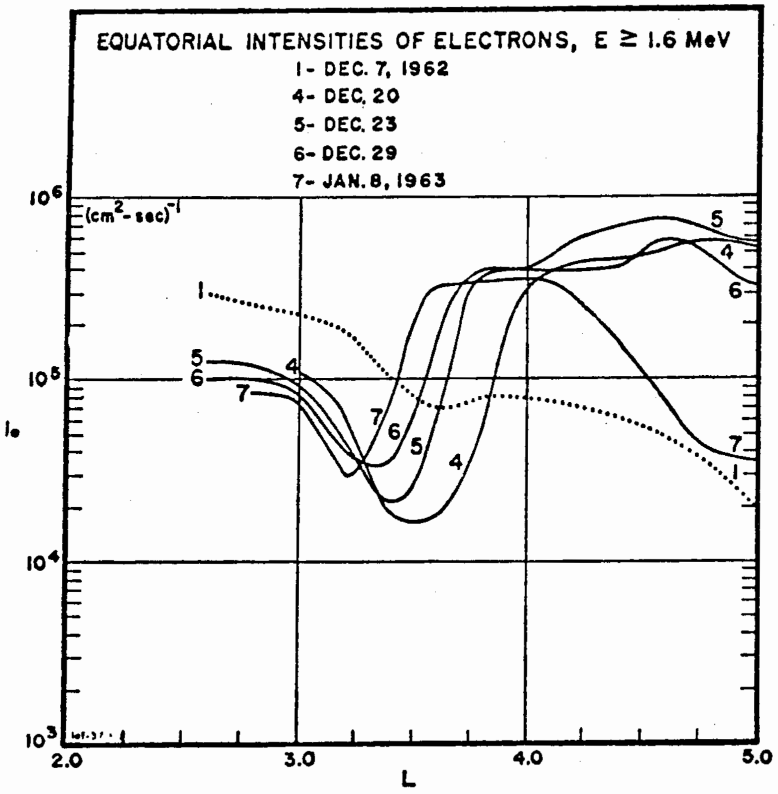

Figure 26

CUMULATIVE ELECTRON FLUX DISTRIBUTION AT GEOSYNCHRONOUS ALTITUDE

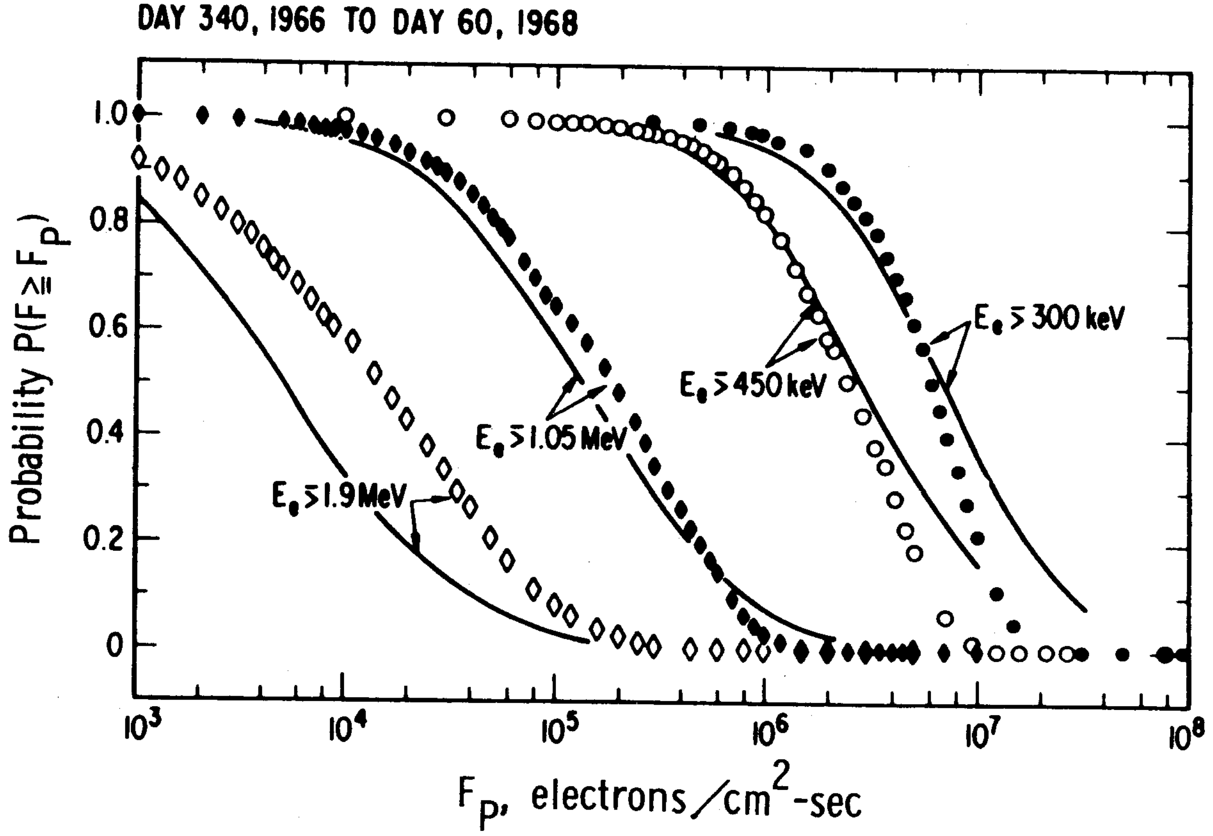

Figure 27

GEOSTATIONARY EXPOSURE FOR FRACTION OF LEAST EXTREME DAYS

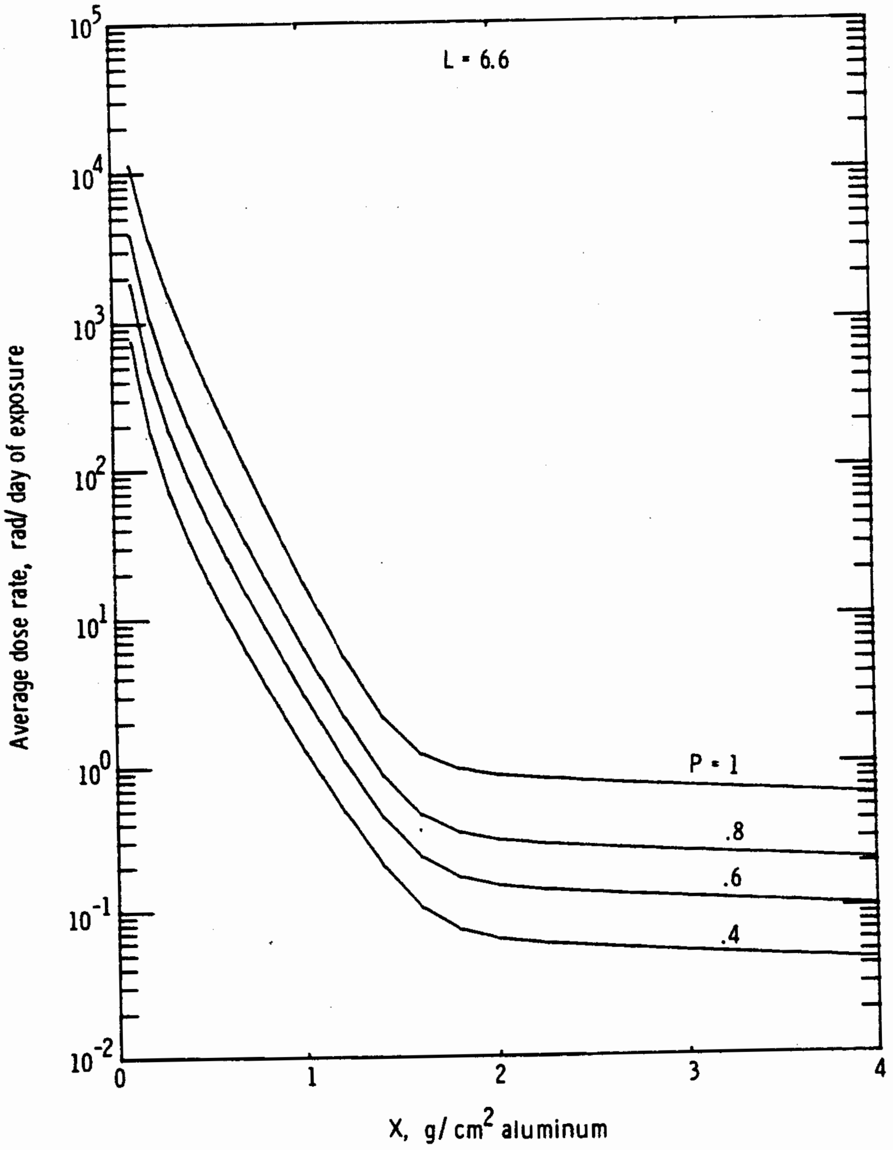

Figure 28

the bremsstrahlung low, and a high Z material on the inside to cutoff the bremsstrahlung. Data were taken from Wilson and Denn (1977a).

Figure 29 indicates the basic model parameters, which are equatorial flux on a given L shell as a function of universal time, the latitudinal variation G, and the local time dependence Φ. The model parameters are found as follows. The log of the equatorial flux is averaged over a time period, which generally has to be on the order of four months to get a sufficiently good average. This average equatorial flux still depends on the epoch in which the averaging is done. This is usually associated with solar activity, and we have two models, one at solar maximum and one at solar minimum. The standard deviation, which is related to the variation about the log mean, again depends on the solar epoch. The average flux is not just 10 raised to the mean log flux as an exponent, but it also gets a contribution from the standard deviation as well. The latitudinal dependence G is given by the ratio $(B/B_0)^m$ where B_0 is the value of the field intensity on the geomagnetic equator and m(L) is about 0.6. (There is a bit of uncertainty depending on what set of data is used.) The parameter m(L) generally depends on the latitudes the satellites were located when the data were collected. This point holds throughout the entire outer zone. The local time variation depends on the cosine of longitude; the coefficient of local time variation again depends on solar epoch and we show this in Figure 30. Further discussion can be found in Singley and Vette (1972), and Wilson and Denn (1977a).

In Figure 30, the coefficient of the local time variation appears to be correlated with the sunspot number, Z. We have specific data for

MODEL PARAMETERS

$$N(E, L, t) = 10^{\mu_T(E, L) + \delta(E, L, t)}$$

$$\mu_T(E, L) = \frac{1}{2\tau}\int_{-\tau}^{\tau} \log\left[N(E, L, T + \tau')\right] d\tau'$$

$$\sigma_T(E, L) = \left[\frac{1}{2\mathrm{T}}\int_{-\mathrm{T}}^{\mathrm{T}} \delta^2(E, L, T + \tau')\, d\tau'\right]^{1/2}$$

$$\overline{N}(E, L, T) = 10^{\mu_T(E, L) + \frac{1}{2}\sigma_T^2(E, L) \ln(10)}$$

$$G(B, L) = \left[B/B_0(L)\right]^{-m(L)}$$

$m(L) = .6 \qquad 4 \leq L \leq 8.5$

$$\Phi_T(E, L, \varphi) = \frac{1}{F\left[C_T(E, L)\right]} 10^{C_T(E, L) \cos\frac{\pi}{12}(\varphi - 11)}$$

Figure 29

different sunspot numbers compared with curves of a function that was fit to these data. Notice there is really only one outlying point and that is the Z = 17 data point. One surprising thing is that the local time dependence is greatest at solar minimum and least at solar maximum. The data were taken from Singley and Vette (1972) and Wilson and Denn (1977a).

Thicker walls can be used to reduce the exposure in the geosynchronous region. The other factor for reducing exposure is the time variation; a local time dependence can be used during solar minimum but not really during solar maximum because local time variations are very small there. The main thing one can do to reduce exposure is to move to an orbit that is slightly inclined; by going to the small inclinations the changing latitude at fixed radius reaches higher L shells (Figure 31). The geosynchronous region ($L = 6.6$) is very close to the outer edge of the belts. Therefore, by changing the inclinations slightly, if that is consistent with the mission requirements, the exposures can be reduced through increased L values. Of course, even in an inclined orbit the equatorial regions are crossed and this is a limitation. However, on the extremes of the orbit times operations can be performed with relatively less shielding necessary, and this may prove to be important. The higher L numbers, in essence, can be picked up by going up to the higher latitudes or inclined orbits. Data were taken from Wilson and Denn (1977a).

The latitudinal dependence is shown in Figure 32 as a function of the inclination in completing one orbit. Data were taken from Wilson and Denn (1977a).

COEFFICIENT OF AVERAGE LOCAL TIME VARIATION AT GEOSYNCHRONOUS ALTITUDE

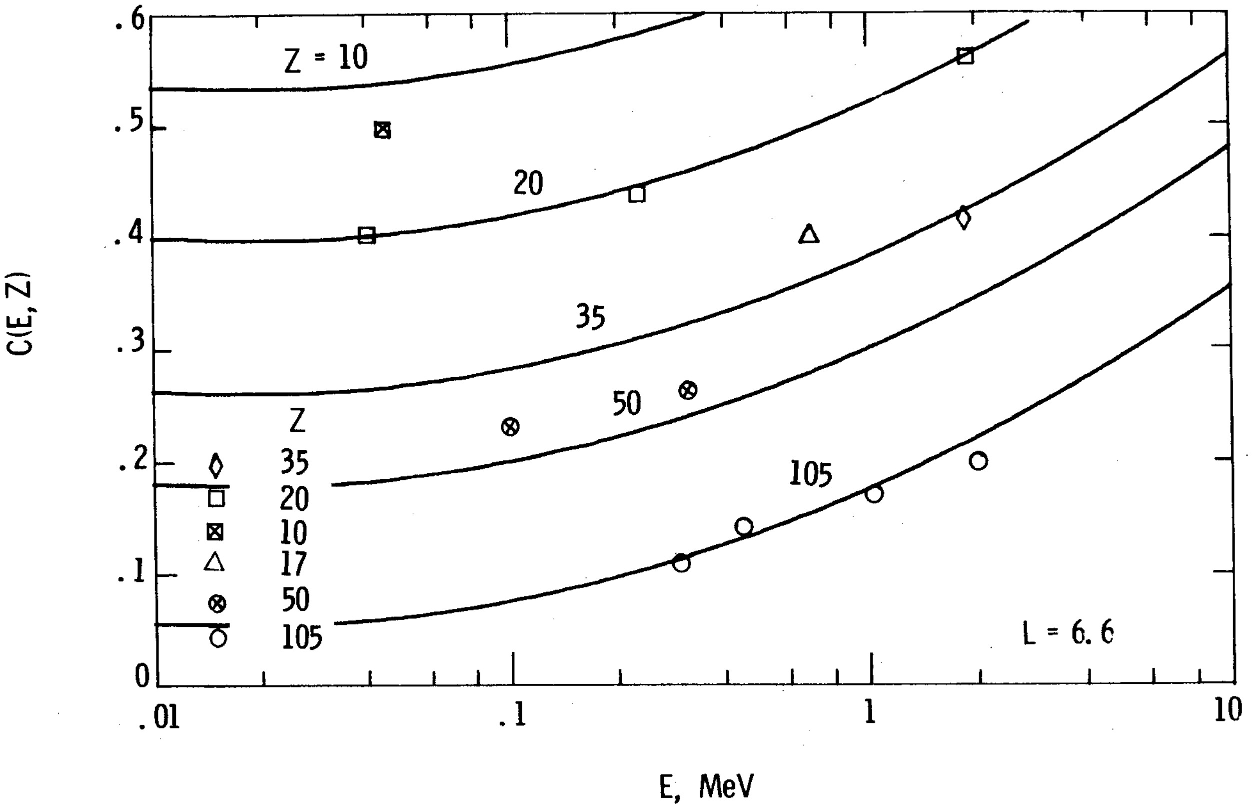

Figure 30

DOSE IN HIGH ALTITUDE EQUITORIAL ORBIT

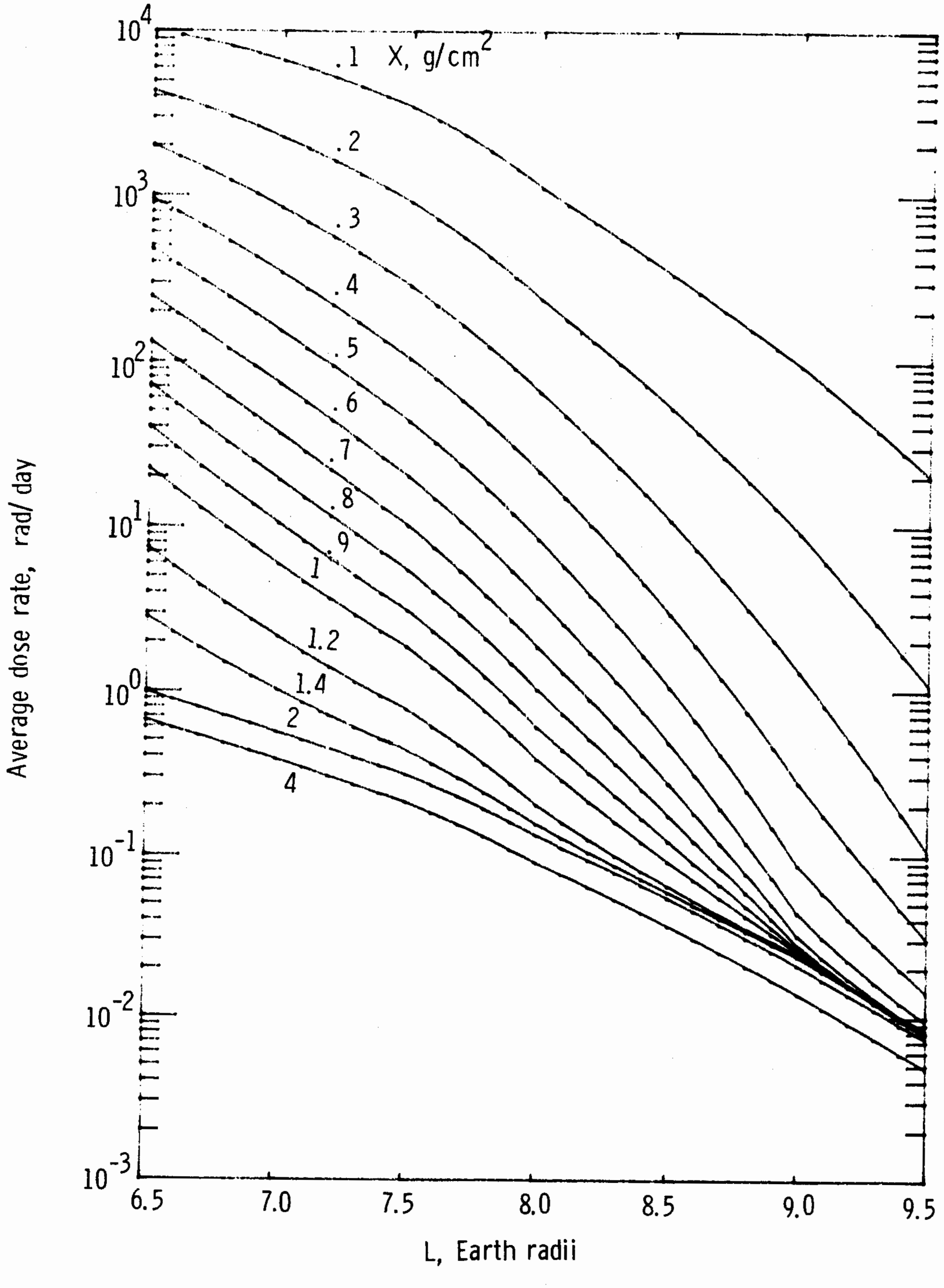

Figure 31

Figure 33 shows the dose rate in a 30° inclined orbit for a fixed geographic location. The dose rate at different shield values is given as a function of the orbital phase which is related to the latitude. This is a rather high inclined orbit, but it produces a radiation free period. Data were taken from Wilson and Denn (1977a).

The fraction of the quarterly exposure limit per quarter at geosynchronous orbit inclined at 10° at the particular geographic longitude of 290° is shown in Figure 34. Clearly, if we consider vehicles with 1 to 5 g/cm^2 shielding like we had in the past, the time spent onsite will be severely limited. Again, it points out that if the shield is designed properly to eliminate the bremsstrahlung for the habitat, shield requirements could be reduced to a few g/cm^2. It also illustrates the importance of using multilayered shields to attenuate the bremsstrahlung. The data were taken from Wilson and Denn (1977a).

I would now like to discuss some of the physical parameters related to shielding calculations. The dominant term in a shielding calculation is energy loss through ionization; that is, a collision between the incoming charged particle (whether it is a proton, electron, or heavy ion) and the orbital electrons of the shielding material (Figure 35). They interact through a coulomb scattering and the energy transferred to the orbital electron is labeled Q. The cross section has an inverse Q^2 dependence, and therefore the energy transfer is usually quite small.

When the electron is bound in an atomic orbital, there is a second option of producing excitation when specific energy transfers are made or further ionization where Q must be greater than the ionization

VARIATION OF GEOGRAPHIC COORDINATES FOR INCLINED GEOSYNCHRONOUS ORBITS

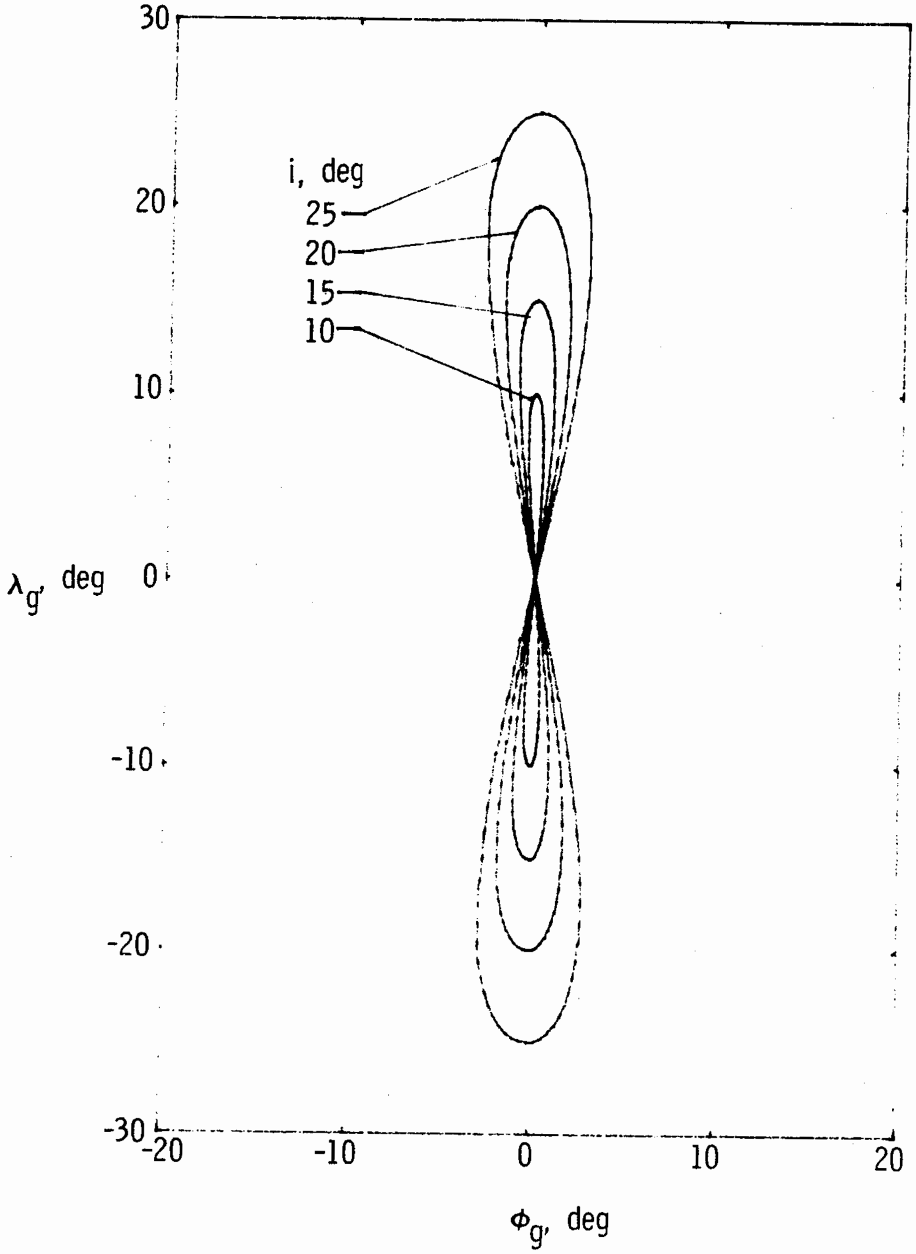

Figure 32

YEARLY AVERAGE DOSE RATE FOR 30 DEGREE INCLINED ORBITS

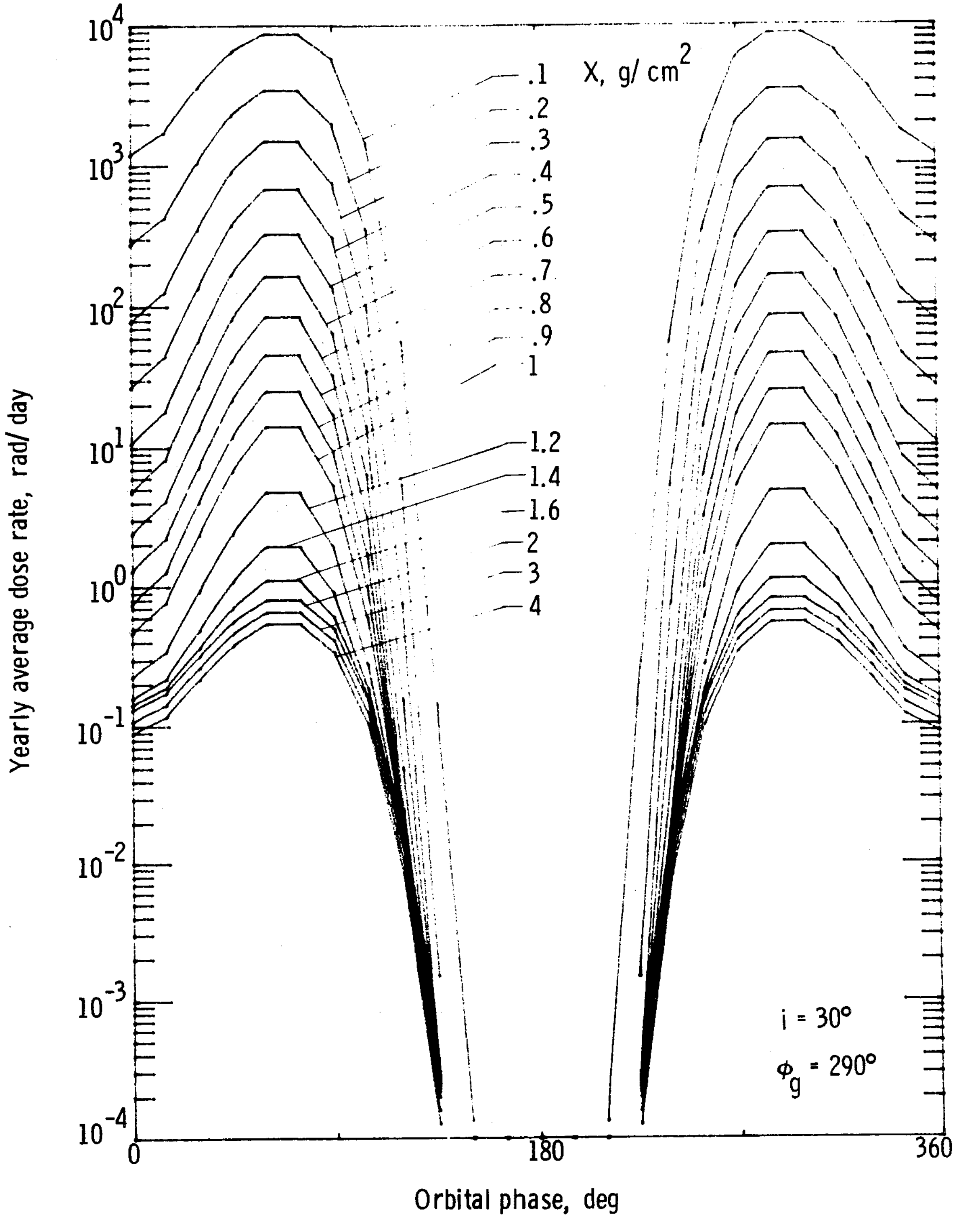

Figure 33

DOSE AT GEOSYNCHRONOUS ORBIT

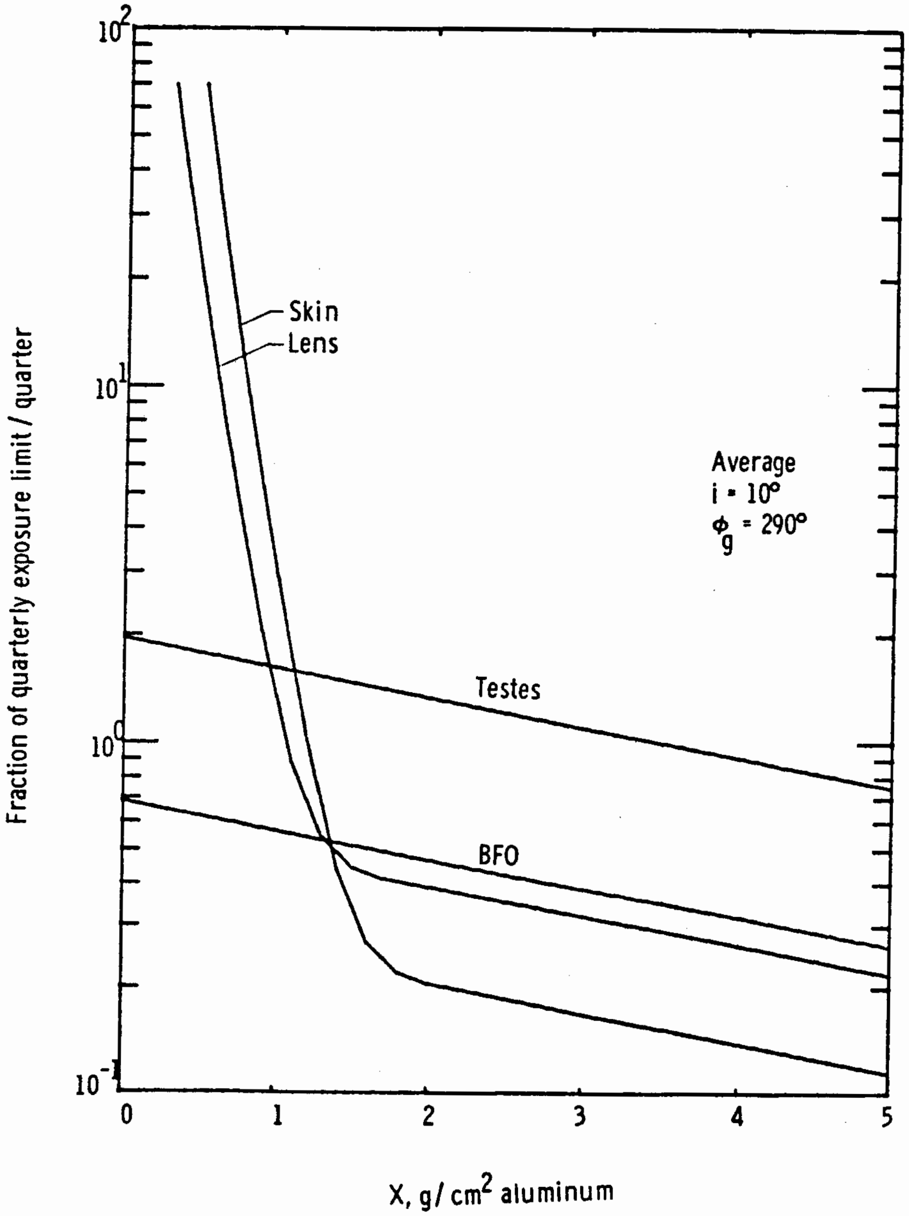

Figure 34

COULOMB SCATTERING

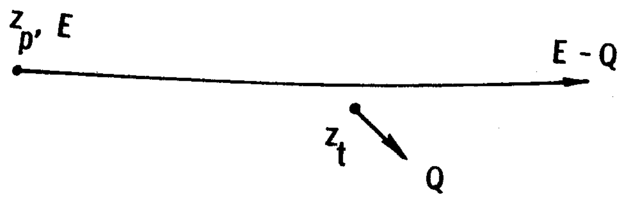

$$0 < Q < \frac{4\, m_p m_t}{(m_p + m_t)^2} E$$

$$\frac{d\sigma}{dQ} = \frac{2\pi z_p^2 z_t^2}{\mu V^2} \frac{1}{Q^2}$$

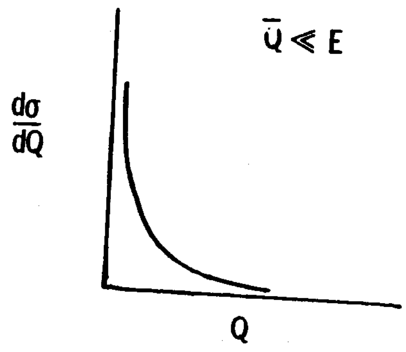

Figure 35

potential (Figure 36). The cross section is related to this energy transfer and goes like the inverse of $\underline{Q}^2$. Another process that is extremely important, especially for incident electrons, is coulomb interaction with the atomic nucleus which results in multiple scattering effects. Later we show that these multiple scattering effects are extremely important for electron shielding.

The cross sections for secondary electrons produced from impacts with atoms like those described above are shown in Figure 37. The graph contains some experimental data at 1 and 5 MeV proton impact and again the inverse $\underline{Q}^2$ dependence above about 20 eV for the secondary electron energy is evident. The corrections below 20 eV are due to binding effects. The electron is actually stuck to an atom, and these binding effects become important when the energy transfer is on the order of the binding energy. This type of data is important in giving the lateral spread of the energy from the track as the particle passes through a material. The data were taken from Manson *et al*. (1975).

There are a number of other degrees of freedom that one has to contend with when looking at molecular systems. Shown in Figure 38 is a collection of data for N_2 molecules, which we chose as a typical molecule mainly because we could find the most data for it. Vibrational excitation is important for electron energies below about 10 eV. Once the electronic excitation or ionization threshold is past, everything becomes heavily dominated by those two processes alone. In about half the cases ionization results in dissociation; and, according to the data that I have been able to collect, most of the molecules that have electronic excitation result in dissociation. There is,

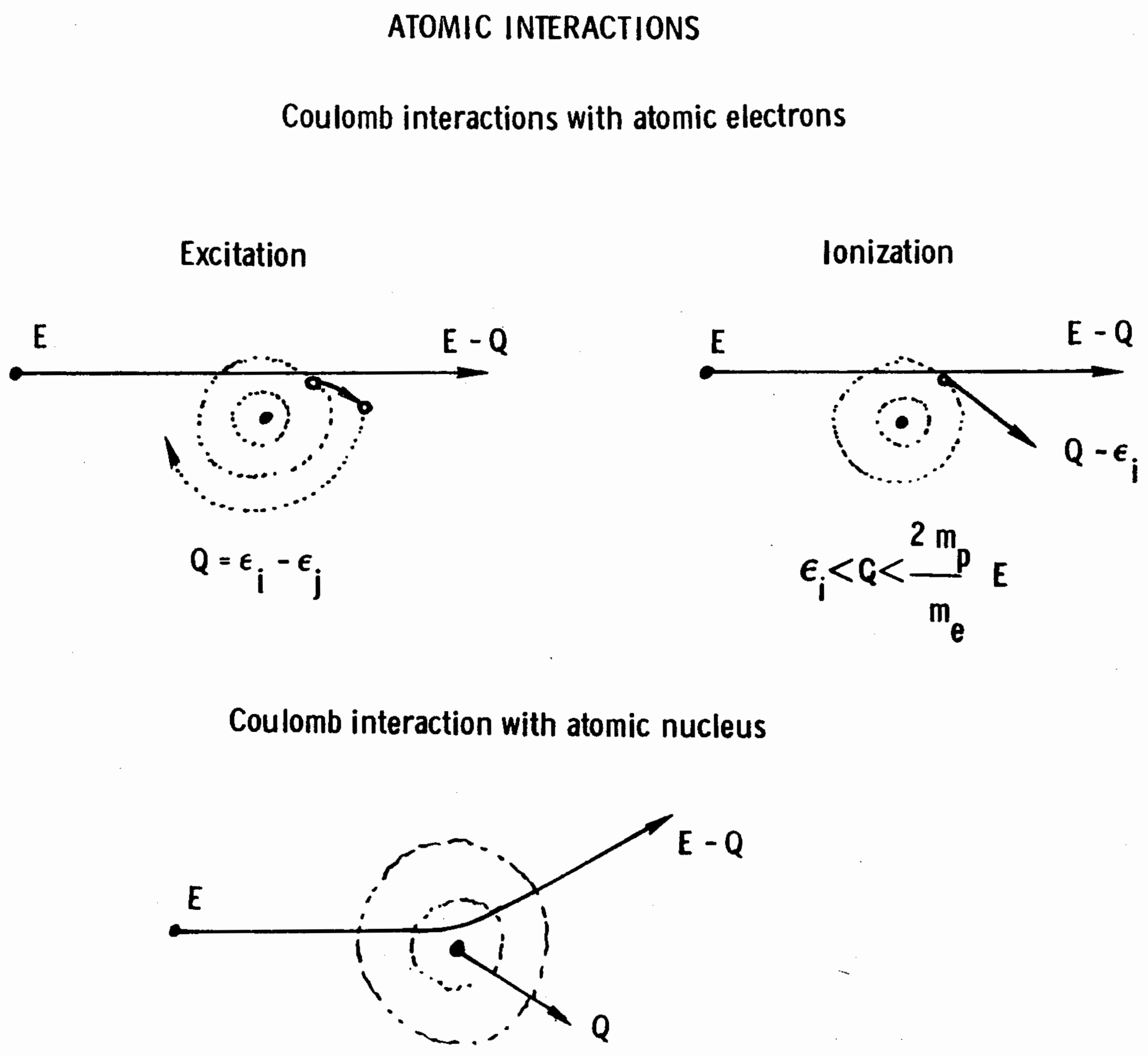
ATOMIC INTERACTIONS
Coulomb interactions with atomic electrons
Excitation
E
E - Q
$Q = \epsilon_i - \epsilon_j$
Ionization
E
E - Q
$Q - \epsilon_i$
$\epsilon_i < Q < \frac{2 m_p}{m_e} E$
Coulomb interaction with atomic nucleus
E
E - Q
Q

Figure 36

SECONDARY ELECTRON PRODUCTION FROM PROTON IMPACT

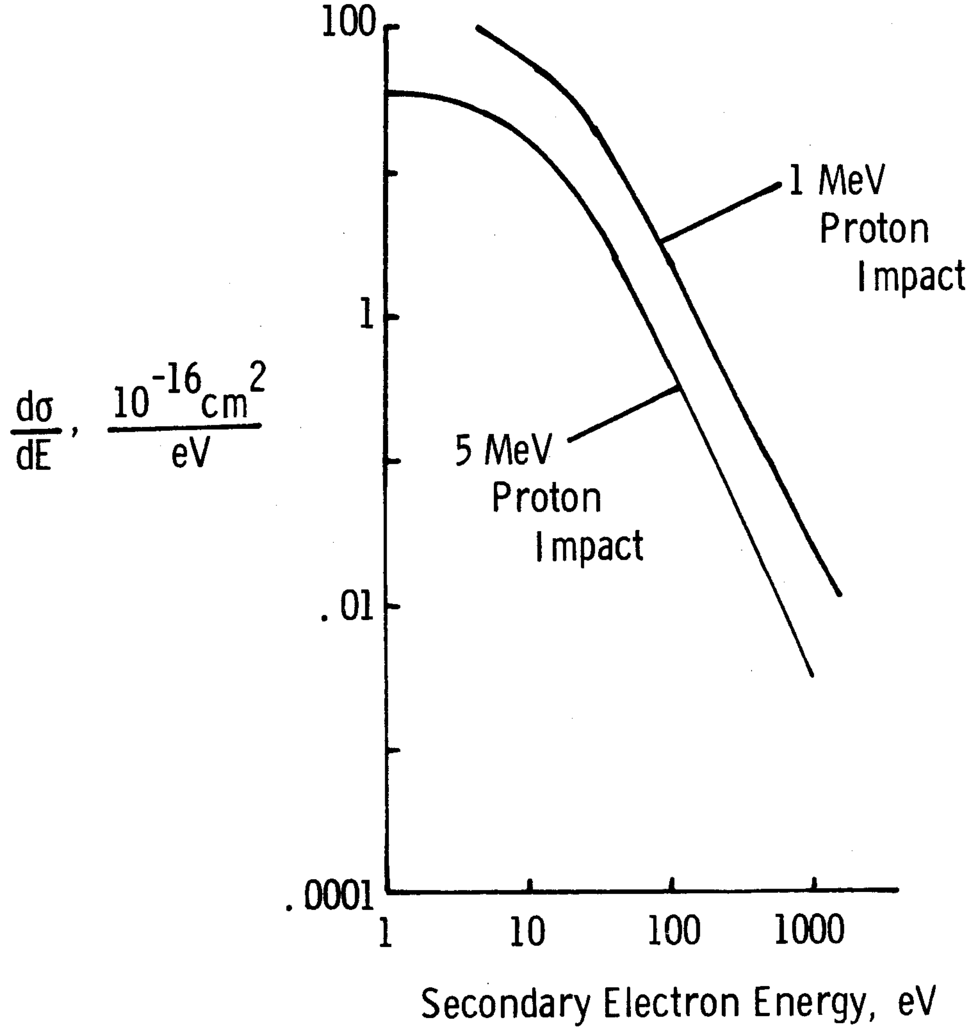

Figure 37

506-25-33

ELECTRON IMPACT WITH N_2 MOLECULES

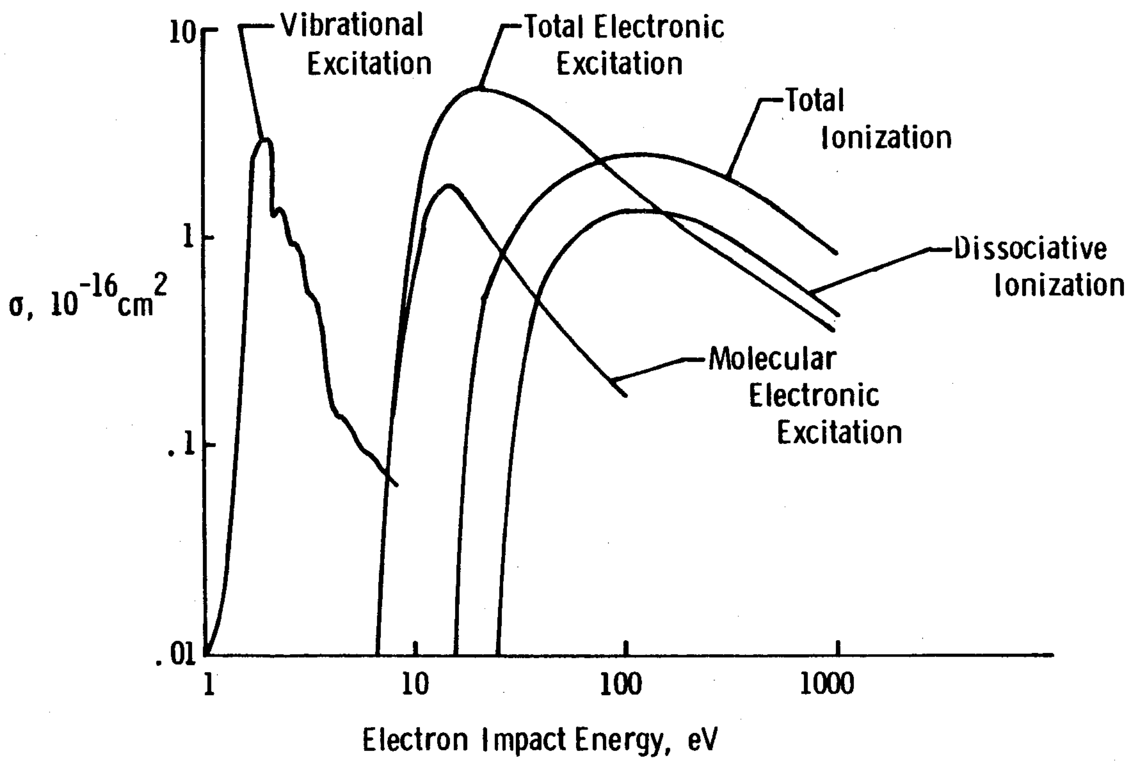

Figure 38

however, a considerable difference in the dissociation for the two processes, but that is probably due to the small number of molecular states observed in the experiments. This will probably change as future experiments are performed, and total dissociative cross section will probably show the same energy dependence as the others at high energy. The data are taken from Schulz (1976), Cartwright _et al_. (1977), Kollmann (1975), and Wright _et al_. (1976).

I would now like to talk a little bit about some work that is going on at Langley on proton stopping theory performed by members of my group. The Meador-Weaver proton stopping model explicitly treats charge transfer, the neutral hydrogen stripping and transport, and it accounts for the initial motion of the atomic electrons (Figure 39). In most calculations people generally use the impulse approximation where the atom is basically frozen while the incoming particles quickly sweep by. This new model accounts for the fact that this system really is not stationary especially at low incident energy. It also incorporates a continuous slowing down approximation in which they were able to calculate the error term. Their model proved to be quite accurate down to 1 eV where the error is about 1 part in 10^5 in the correction to the slowing down approximation. For the purposes of comparison, Figure 39 also includes another calculation by Hassan which treats charge transfer but ignores the neutral hydrogen transport, solving the problem by using discrete energy steps. The results from Hassan's calculation are shown in Figure 40 for comparison to the Meador-Weaver model.

The unusually high stopping power in the Hassan calculation is of course associated with the neglect of the neutral hydrogen once

MEADOR-WEAVER PROTON STOPPING THEORY

- Explicitly treats charge-transfer and neutral hydrogen stripping and transport
- Accounts for initial motion of atomic electrons
- Continuous slowing down approximation

HASSAN PROTON STOPPING THEORY

- Treats charge-transfer but ignores neutral hydrogen
- Solves using discrete energy steps

Figure 39

it has captured an electron. Figure 40 shows a comparison between the Langley calculations by Meador and Weaver and the experimental data; the Bethe slowing-down theory, which is catastrophic at low energy, has also been included. This type of calculation looks very encouraging. The other interesting feature of this calculation is that the secondary electron distributions will be treated in far more detail so that track structure may be better understood. Further discussion may be found in Meador and Weaver (1979).

Up to now we have talked about the proton slowing down in collisions with atomic electrons. In the case of electron irradiation, the multiple scattering from the nucleus is also important. To demonstrate this rather dramatically, Figure 41 graphs the electron energy deposition coefficient, both neglecting multiple scattering effects and with multiple scattering. The location of the peak due to multiple scattering depends on the atomic number of the shield as shown in Figure 42. The data were taken from Mar (1966) and Wilson and Denn (1976).

Figure 42 graphs the energy deposition coefficient behind three different shield materials as a function of fractional penetration depth for 0.5 MeV normally incident electrons. The differences observed for the three materials are the multiple scattering effects. Of course, one should bear in mind that increased multiple scattering also results in increased bremsstrahlung. Hence, there is always a tradeoff between decreased electron penetration and increased bremsstrahlung production in increasing multiple scattering effects. Data taken from Wilson and Denn (1977b).

STOPPING CROSS SECTION FOR PROTONS IN HELIUM

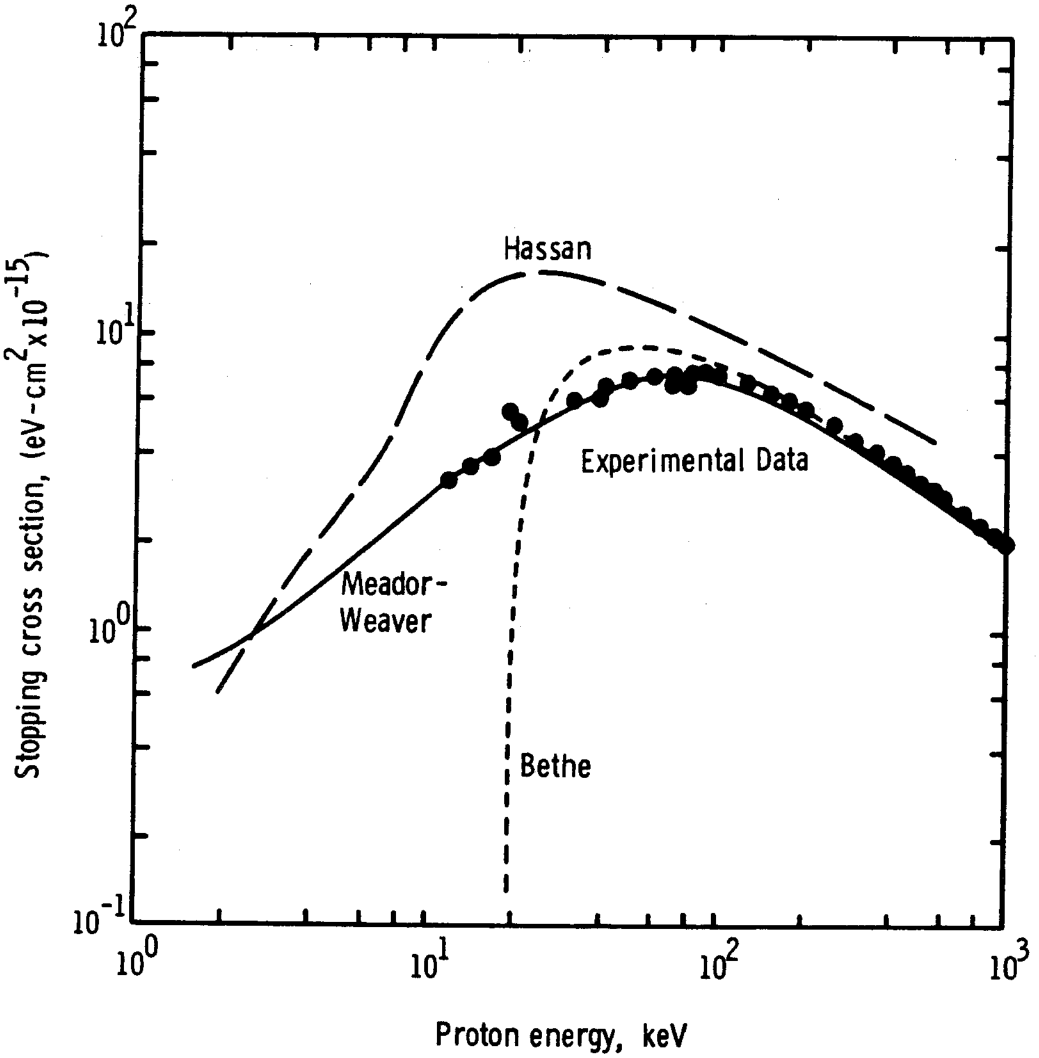

Figure 40

ELECTRON ENERGY DEPOSITION COEFFICIENT

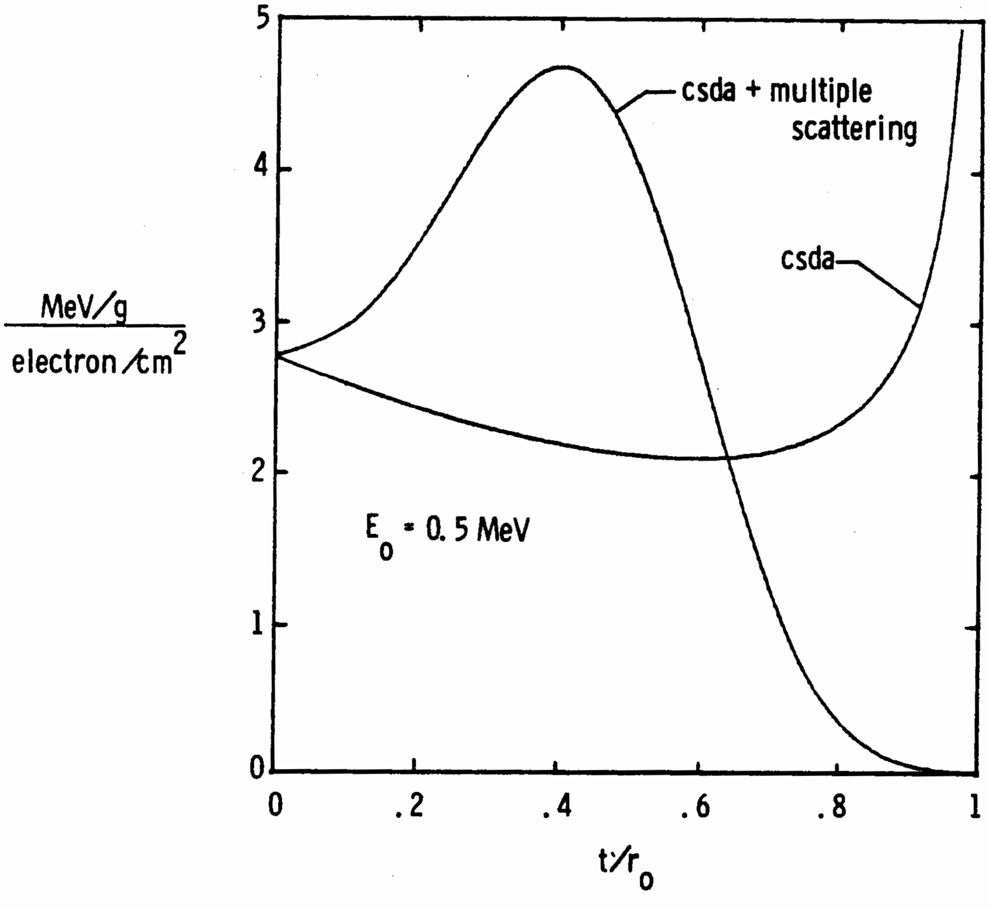

Figure 41

ENERGY DEPOSITION OF .5 MeV ELECTRONS BEHIND DIFFERENT SHIELDS

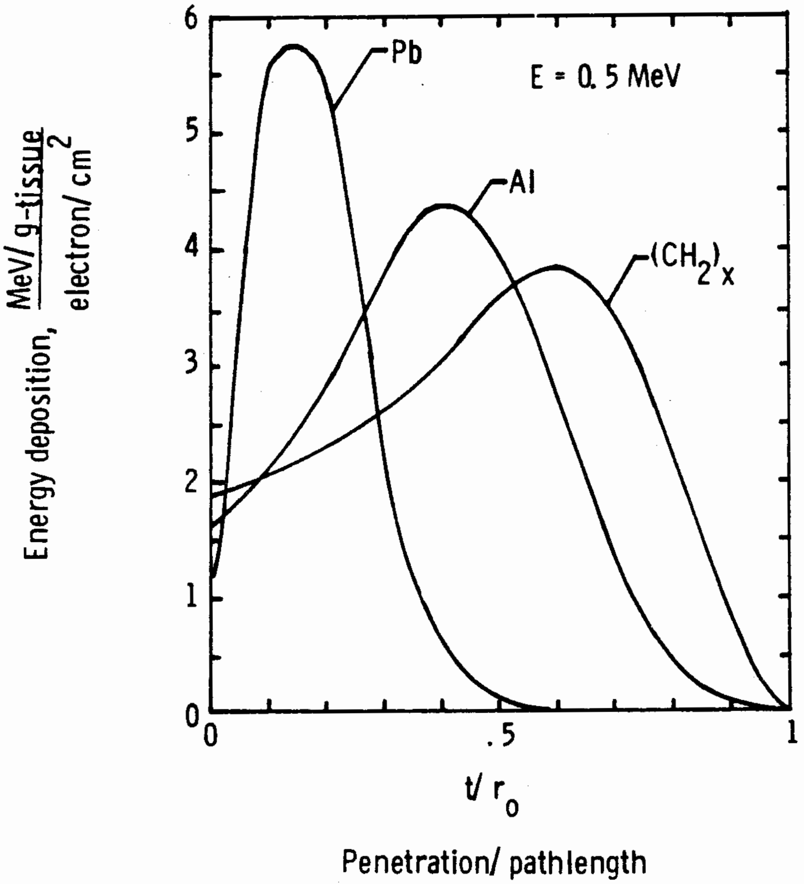

Figure 42

To show some of the effects of this multiple scattering in a practical shield situation, Figure 43 shows the dose in MeV per gram per unit fluence of electrons behind a composite shield with an aluminum outer skin. In this graph we give the shield thickness in terms of the shield mass, or the mass per unit area. If we use a pure aluminum shield the dose decreases exponentially with total shield mass. If either tantalum or lead is installed after about 100 mils of aluminum, we can reduce the dose considerably without increasing the shield weight. And this is just the difference between multiple scattering effects in the aluminum as compared to the tantalum and lead, although there is a slight change in the bremsstrahlung. It is primarily multiple scattering that is causing this. Data from Morel (1975).

There are several important factors to be considered for proton shielding. Figure 44 shows the absorbed dose as a function of depth for 592-MeV protons. The graph also shows some monte carlo calculations which include nuclear reaction effects. The dash-dot curve is the dose due to the surviving uncollided protons. The difference between the dose of uncollided protons and the upper curves are estimates of effects due to nuclear reactions. Therefore, for distances comparable to the dimensions of the human body, the secondary particles are extremely important for proton dose at this particular energy. At higher energy, nuclear effects are more important; at lower energy, these nuclear effects are not quite so important. These data are for the physical dose, and they were taken from Wilson and Khandelwal (1974, 1976), Goebel and Baarli (1965), Turner _et_ _al_. (1964), Alsmiller _et_ _al_. (1970).

Figure 45 graphs the dose equivalent build-up factor, derived

ELECTRON DOSE BEHIND A COMPOSITE SHIELD WITH AN ALUMINUM SKIN

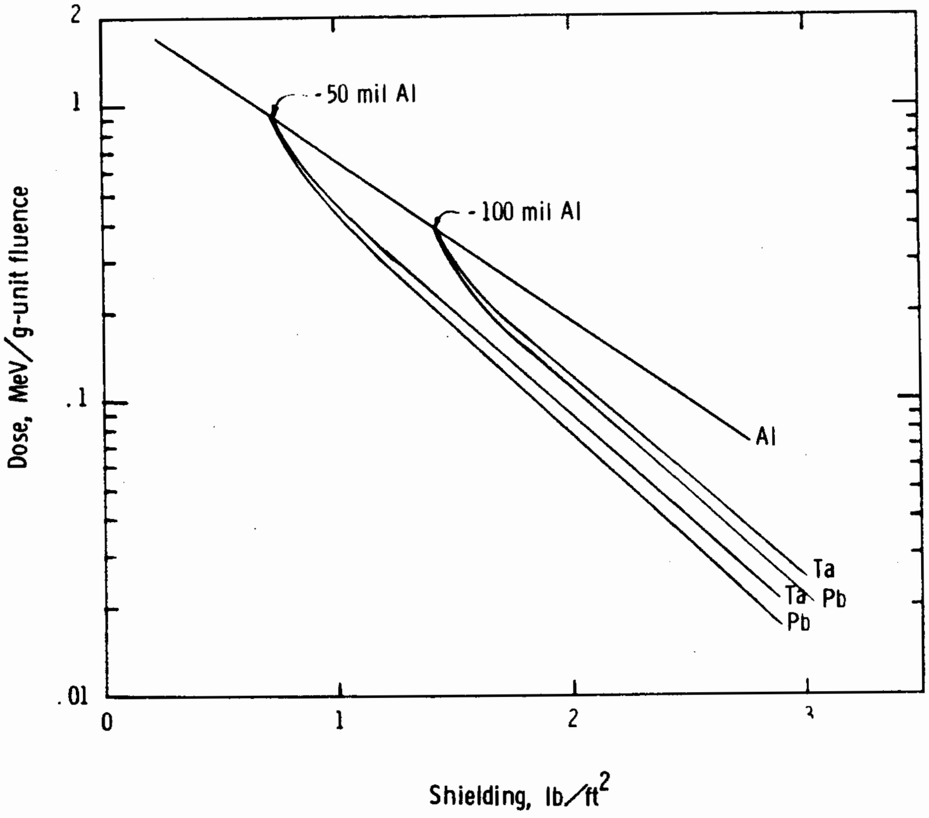

Figure 43

PROTON DEPTH-DOSE RELATION INCLUDING NUCLEAR EFFECTS

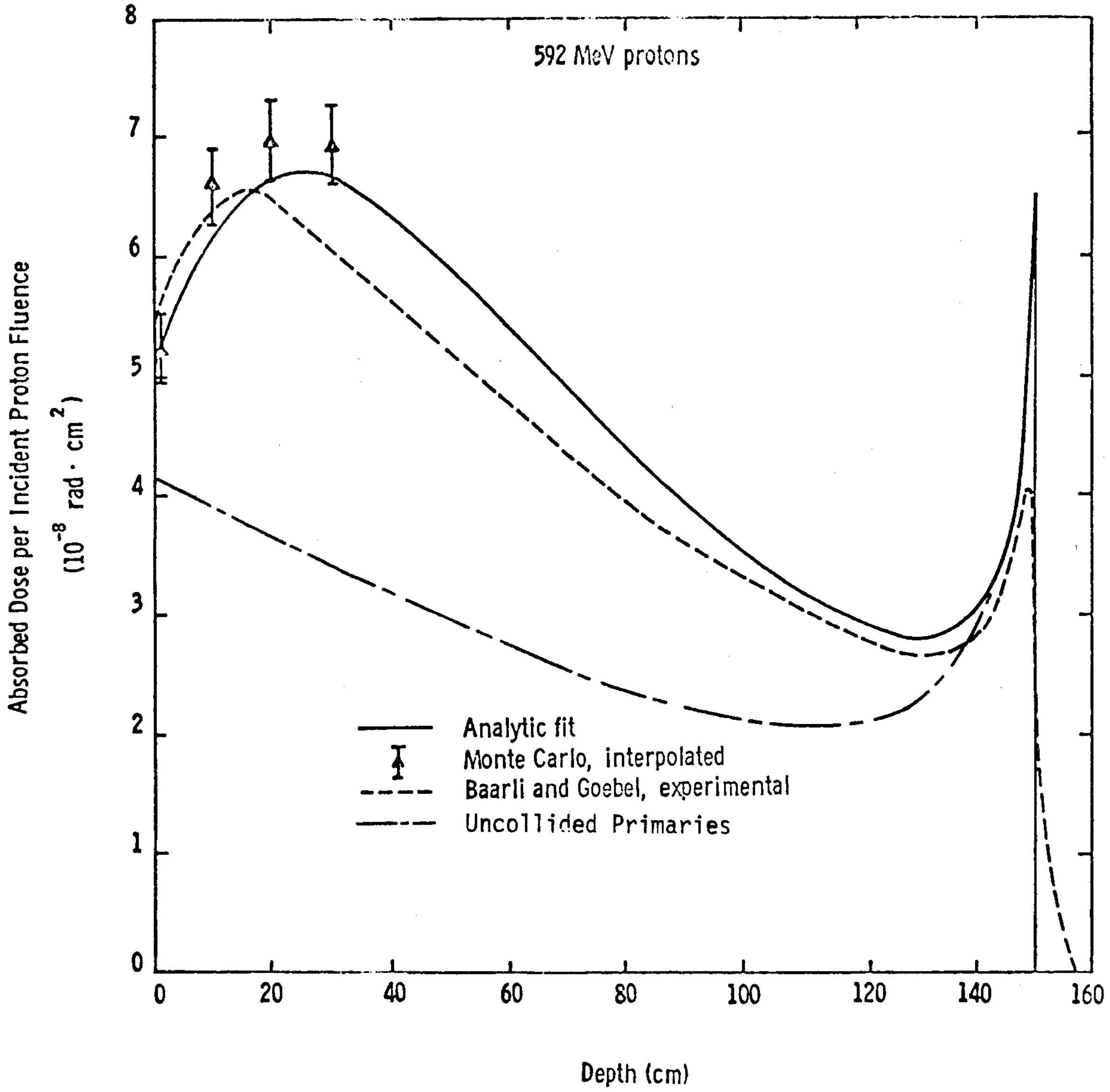

Figure 44

by fitting to Monte Carlo calculations for dose equivalent using the quality factors as assigned by the ICRP. $\underline{Z}$ is the depth in tissue at which the build-up factor is calculated. The rather long vertical dashes are the Monte Carlo calculations which tend to get more uncertain at higher energies. At lower energies, the build-up factor tends to decrease to somewhere near 1, but it can get quite large at higher energies. Data taken from Wilson and Khandelwal (1976).

The dose equivalent for a unit fluence of 600-MeV protons, or corresponding roughly to Figure 44 for absorbed dose, is shown in Figure 46. Drawn separately is the primary contribution to dose equivalent, and the total is also shown. Certainly on the order of body dimensions large errors are committed when nuclear reaction effects are not included. The data were derived from Wilson and Khandelwal (1976).

One of the things we have been doing is trying to replace the Monte Carlo calculations with a deterministic calculation, thus eliminating the statistical fluctuations. We developed a theory that we have named the perturbation theory. Figure 47 graphs the dose versus depth: the circles are the Monte Carlo results for secondary contribution to the dose from secondary protons, neutrons, and heavy nuclei. Also shown is the uncollided primary beam. The curves are our calculations and we feel very hopeful about doing this type of calculation, which is sort of an analytic-numerical approach. Data taken from Wilson and Lamkin (1975).

We have also been looking at the question of shielding against heavy ions. The transition matrix for the interaction of two heavy ions as they come together is denoted by the large circle in Figure

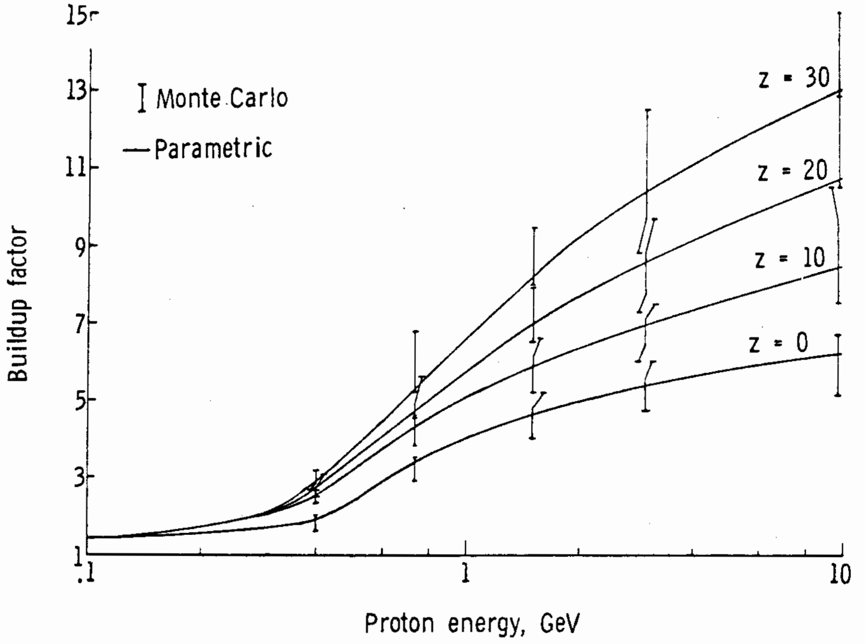

PROTON DOSE EQUIVALENT BUILDUP FACTORS FOR SEVERAL DEPTHS IN TISSUE

Figure 45

PROTON DEPTH-DOSE EQUIVALENT RELATION INCLUDING NUCLEAR EFFECTS

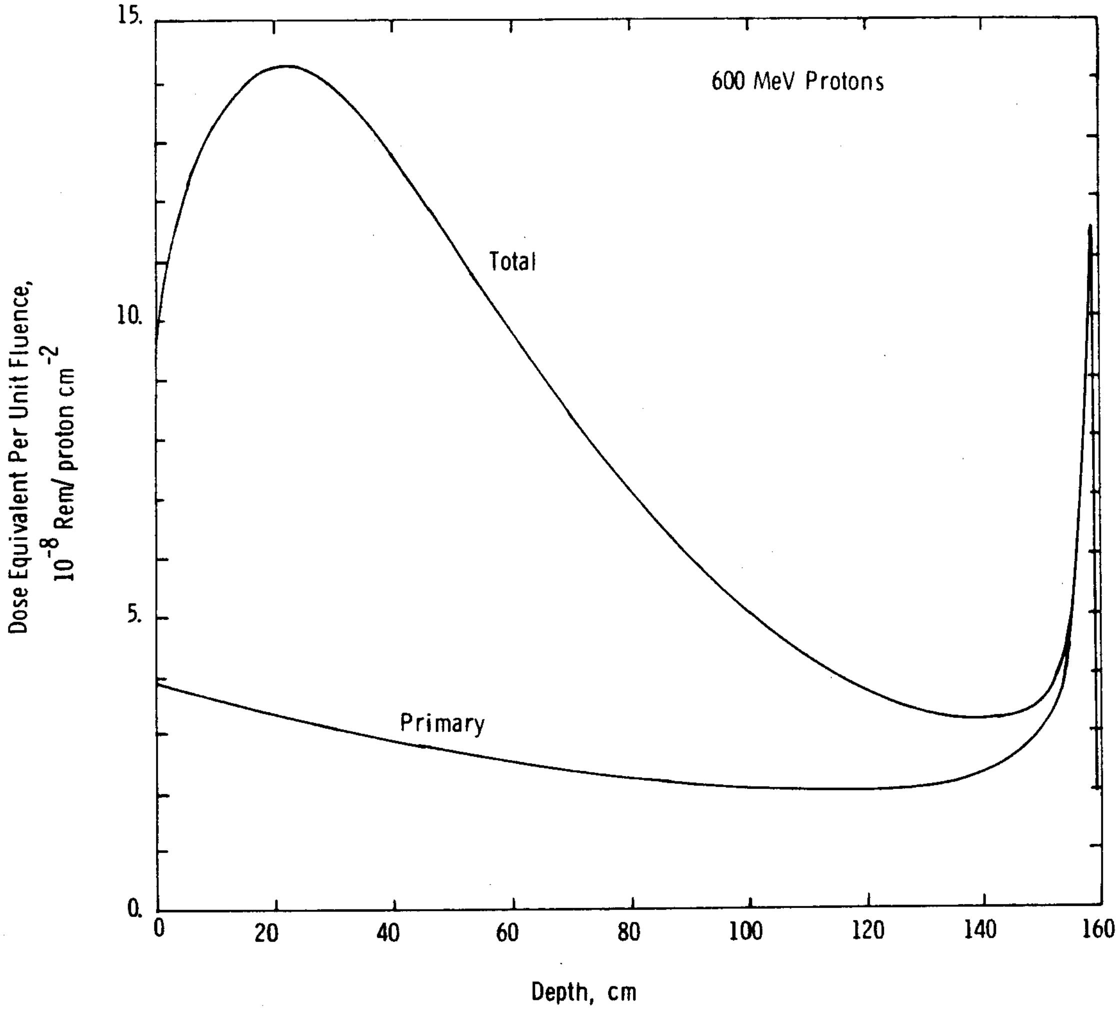

Figure 46

ONE GeV PROTONS ON TISSUE SHOWING PRIMARY AND SECONDARY CONTRIBUTIONS

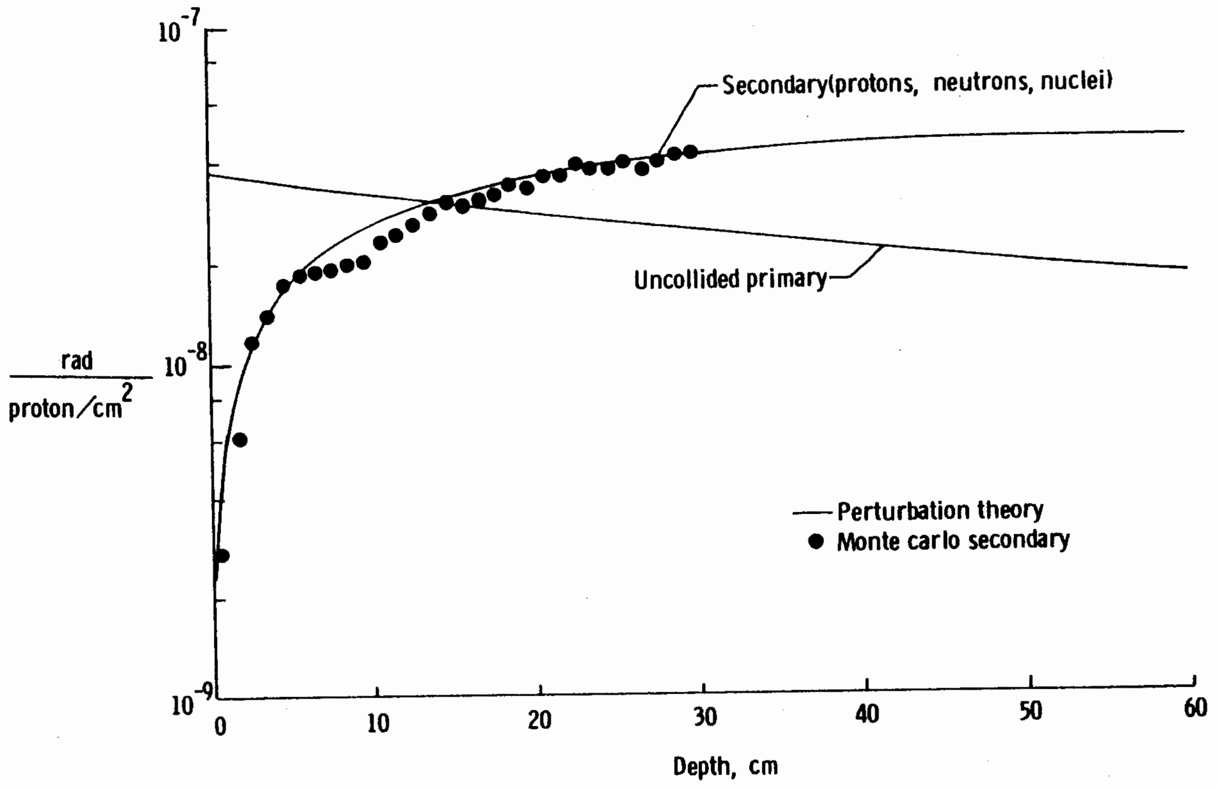

Figure 47

48. We have been making multiple scattering expansions where the round circles correspond roughly to nuclear wave functions, and the hexagons correspond to two nucleon scattering amplitudes. The first graph on the right is single scattering. Nuclear double scattering occurs in two different ways and higher order terms are indicated. For further discussion see Wilson (1974, 1975).

We took one of the nuclei to be a neutron, and this is compared with a compilation of neutron data in Figure 49. Generally, the calculations of total cross section are quite good; however, there is some question in the comparisons below 0.3 GeV which appears to be due to the use of the eikonal approximation. It remains to be shown that a partial wave expansion will improve the agreement. The data were taken from Wilson (1974, 1975), Schimmerling _et_ _al_. (1973) and Barashenkov _et_ _al_. (1969). The results for absorption cross section in comparison to experiments are shown in Figure 50.

Figure 51 is a comparison of neutron nucleus total cross sections at 1 GeV with the data measured by Schimmerling (1973). We used three different nuclear models: gaussian, Saxon-Woods (which is very good), and a uniform nuclear model. The parameters that went into these models were all taken from the same data set. The differences are due to the details of the shape of the nuclear density, which is different in each model. The data were taken from Wilson (1975). Figure 52 shows the corresponding absorption cross sections.

Figure 53 shows a comparison of triton-nucleus scattering. This is very old data at 100 MeV per nucleon for which agreement is not too bad. The data were taken from Wilson (1975) and Millburn _et_ _al_. (1954).

MULTIPLE SCATTERING EXPANSION OF NUCLEUS-NUCLEUS INTERACTION

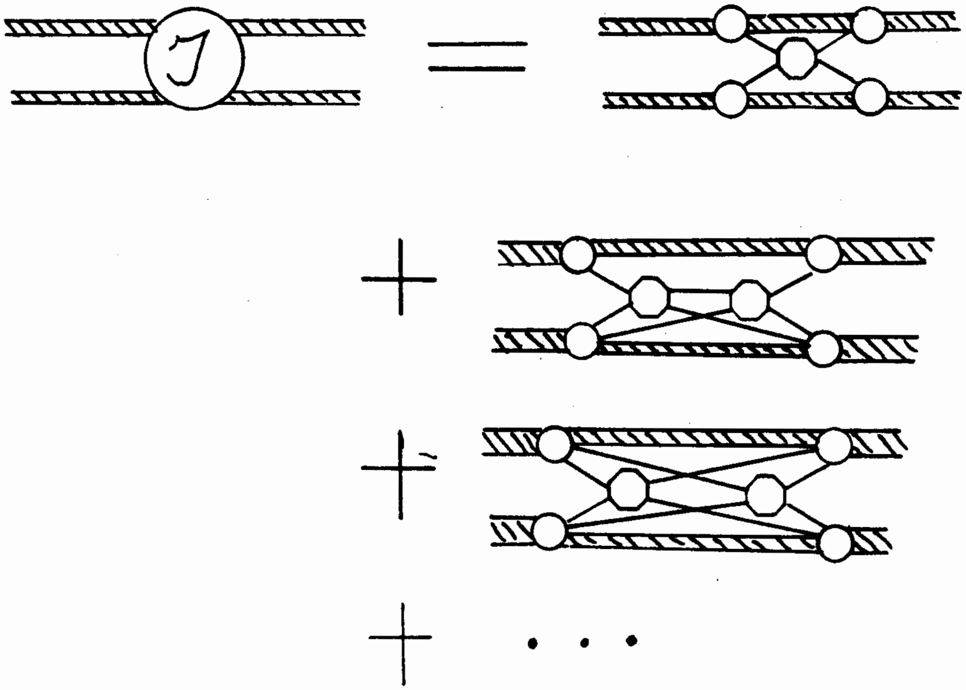

Figure 48

NEUTRON CARBON TOTAL CROSS SECTION

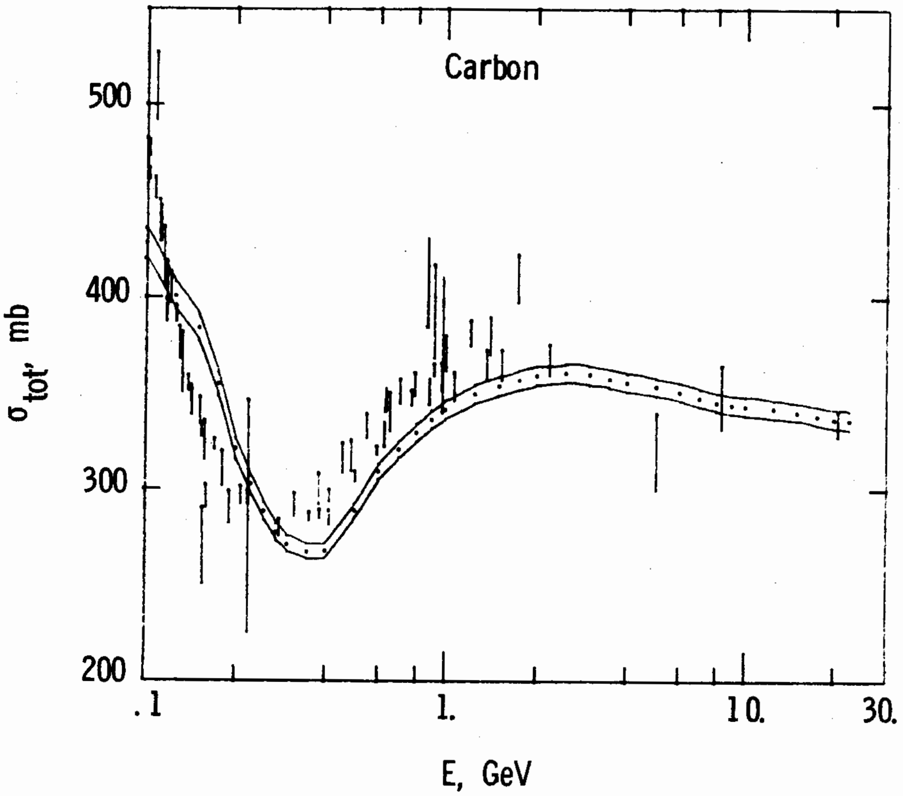

Figure 49

NEUTRON CARBON ABSORPTION CROSS SECTION

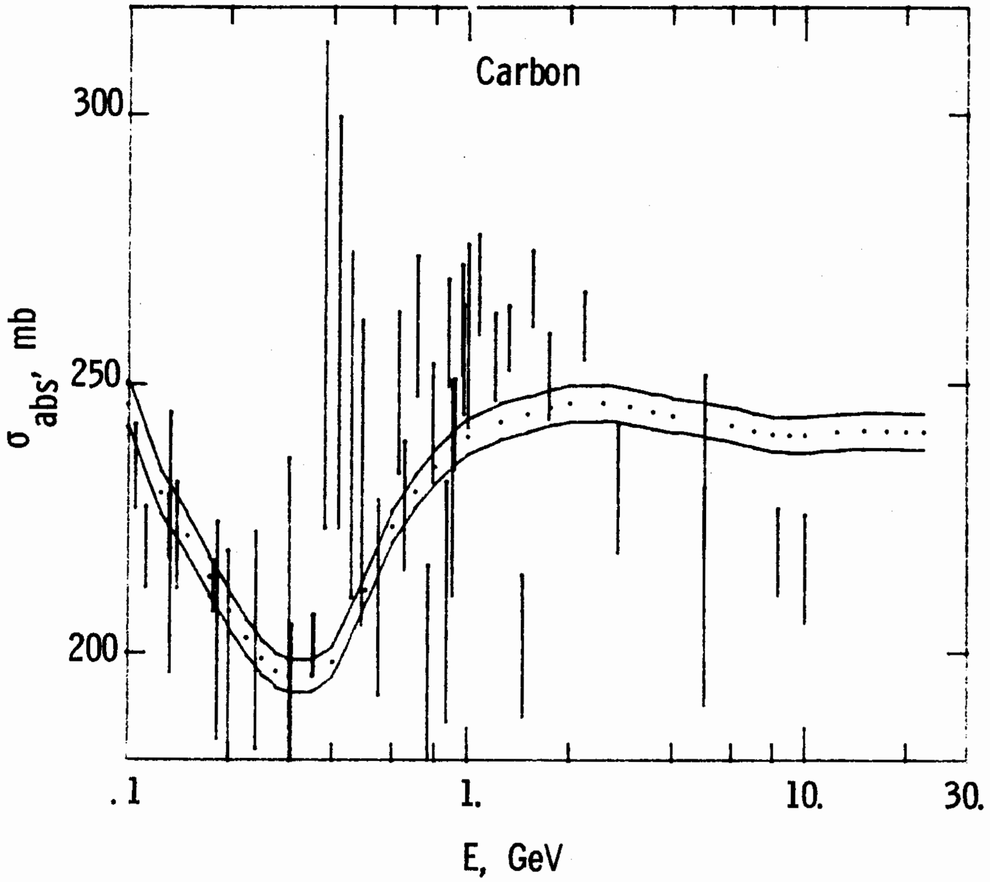

Figure 50

NEUTRON NUCLEUS TOTAL CROSS SECTION

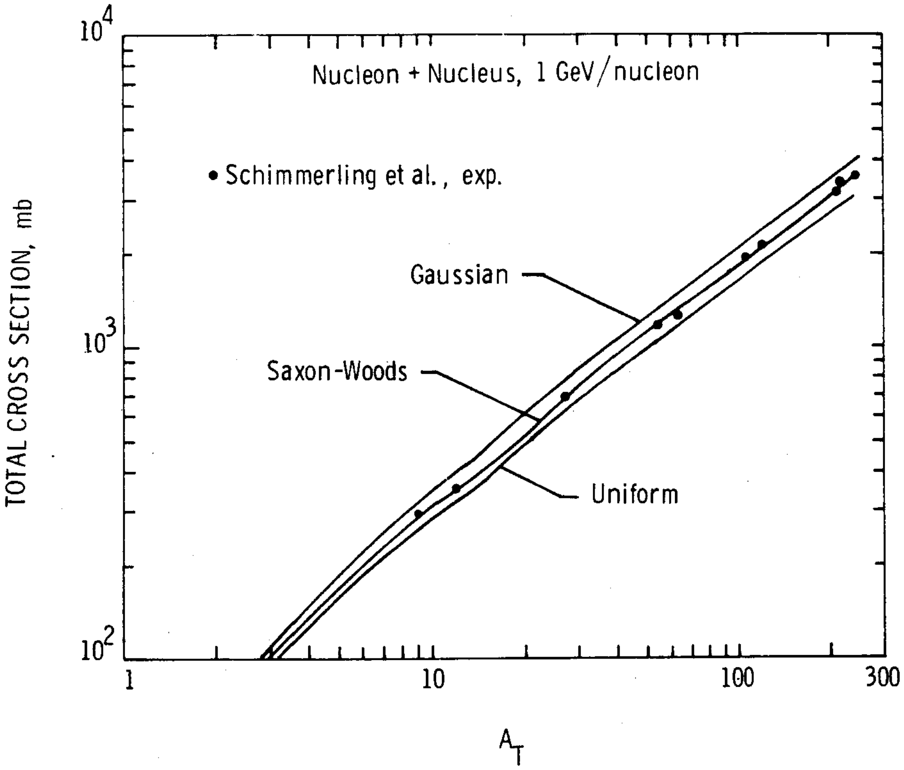

Figure 51

Figure 54 is a comparison of more recent data for oxygen-nucleus scattering, 2 GeV per nucleon, using the Saxon-Woods density and experiments reported by Lindstrom _et_ _al_. (1974) as obtained by the Heckman group. The data were taken from Wilson and Costner (1976).

To incorporate this type of information into an ion transport calculation, we have made what is in essence a very similar type of approximation to the perturbation series that we were talking about before. It is an expansion. Figure 55 plots some of the Bragg curves of several diferent ions that we calculated in a relatively simple implementation of the perturbation expansion. One of the most interesting features about these calculations was that if a few nucleons are stripped from a heavy ion, the range of that ion is very near what the initial ion was before the stripping reaction. Therefore, at high atomic numbers the Bragg curves of the secondary and the primary ion coalesce. Although we generally focus our attention on the uncertainties in the fragmentation parameters, there is some question of what role shielding is going to play in these cases. In particular, if there are any saturation effects in biological response involved, breaking these ions into more parts may be even more damaging than the initial ion. There are other questions to look at. Further details may be found in Wilson (1977_a_, 1977_b_).

NEUTRON NUCLEUS ABSORPTION CROSS SECTION

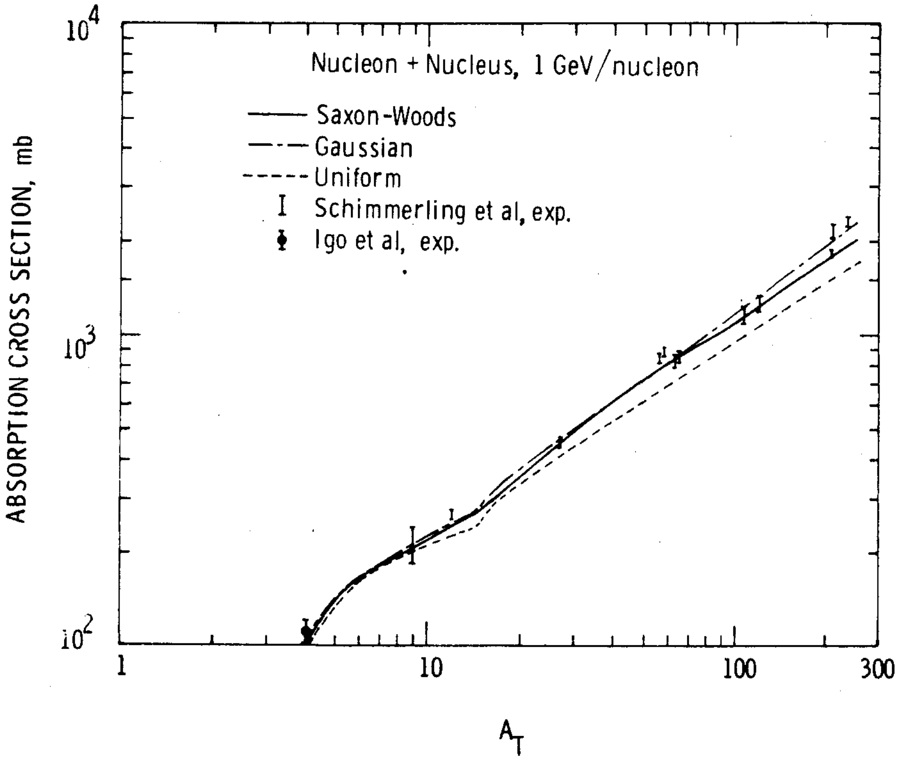

Figure 52

TRITON NUCLEUS ABSORPTION CROSS SECTION

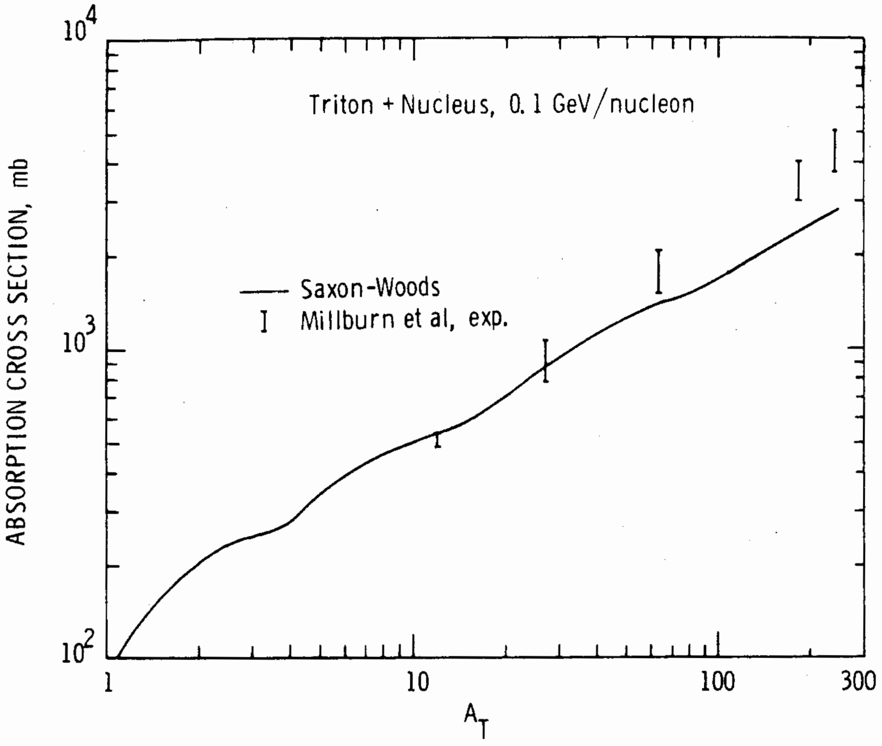

Figure 53

OXYGEN NUCLEUS ABSORPTION CROSS SECTION

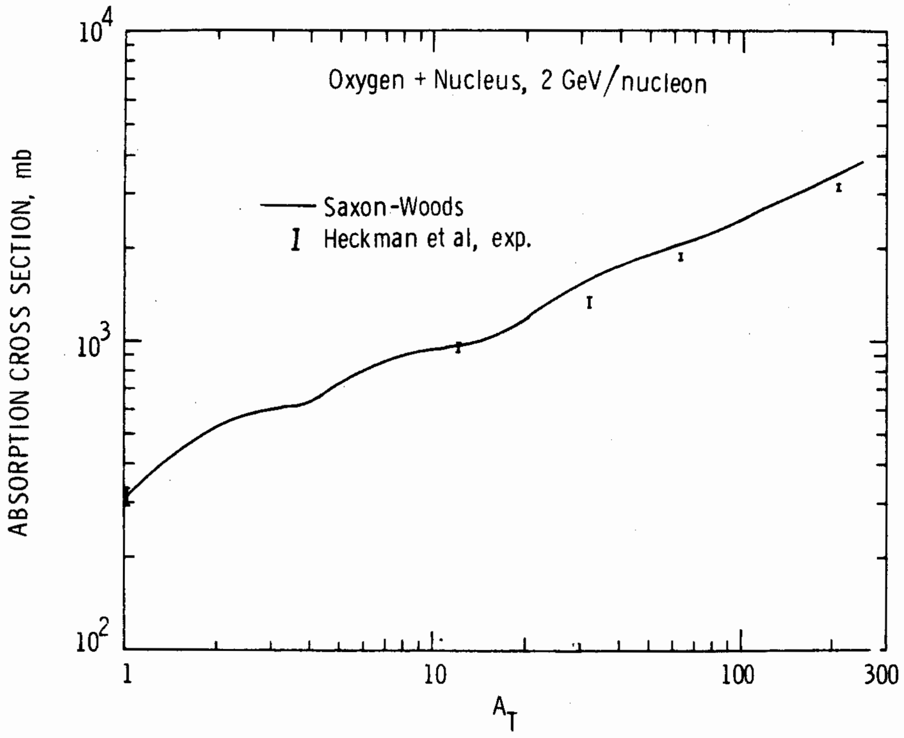

Figure 54

BRAGG CURVES FOR INDICATED ION TYPES

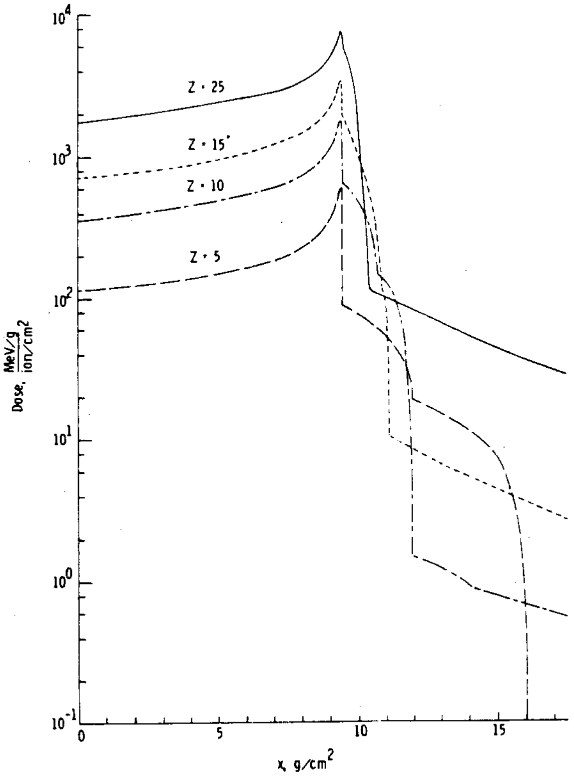

Figure 55

REFERENCES

Alsmiller, R.G., et al. 1970. The absorbed dose and dose equivalent induced by medium energy neutrons and protons. Nucl. Sci. Eng. 42, 367.

Barashenkov, V.S., Gudima, K.K., and Toneev, V.D. 1969. Cross sections for fast particles and atomic nuclei. Prog. Phys. 17, 683-723.

Burrell, M.O. and Watts, J.W. 1968. An analysis of energetic space radiation and dose rates. NASA TN D4404.

Blizard, J.B. 1969. Long range solar flare predictions. NASA CR-61316.

Cartwright, D.C., et al. 1977. Electron impact excitation of the electronic states of N_2. Phys. Rev. A16, 1041.

Cladis, J.B., Davidson, G.T., and Newkirk, L.L. 1971. The Trapped Radiation Handbook. DNA 2524H.

Curtis, S.B., et al. 1969. Study of radiation hazards to man on extended near earth missions. NASA CR-1469.

Curtis, S.B. and Wilkinson, M.C. 1971. Radiation hazards to man. Boeing Technical Report D180-12878-1.

Divine, N. 1975. Interplanetary charged particles. NASA SP-8118.

Foelsche, T. 1963. Specific solar flare events and associated radiation doses. Space Radiation Effects. ASTM Special Technical Publication No. 363.

Frank, L.A. and Van Allen, J.A. 1966. Correlation of outer radiation zone electrons with solar activity cycle. J. Geophys. Res. 71, 2697.

Goebel, K. and Baarli, J. 1965. Properties of high energy beams from a 600-MeV synchrocyclotron. Proceedings, XI International Congress of Radiology, Rome, Italy.

Johnson, F.S., ed. 1965. Satellite Environment Handbook. Palo Alto: Stanford University Press.

King, J.H. 1974. Solar proton fluences for 1977-1983 space missions. J. Spacecr. Rockets 11, 401.

Kollmann, K. 1975. Dissociative ionization of H_2, N_2, and CO by electron impact. Int. J. Mass Spectrom. Ion Phys. 17, 261.

Kuhn, E., Schwamb, F.E., and Payne, W.T. 1966. Solar flare hazard to earth-orbiting vehicles. Fairchild-Hiller Report FHR-1395-3.

Lindstrom, P.J., et al. 1974. Fragmentation of B = 16 hadrons at 2.1 GeV/n. Bull. Am. Phys. Soc. 19, 518.

Manson, S.T., Toburen, L.H., Madison, D.H., and Stolterfoht, N. 1975. Energy and angular distribution of electrons ejected from helium. Phys. Rev. A12, 60.

Mar, B.W. 1966. An electron shielding analysis for space vehicles. Nucl. Sci. Eng. 24, 193.

McDonald, F.B., ed. 1963. Solar Proton Manual. NASA TR R-169.

Meador, W.E. and Weaver, W.R. 1979. Improved solution to Boltzmann equations for transport of heavy ions in plasmas. Submitted to Phys.Fluids.

Millburn, G.P., et al. 1954. Nuclear radii from inelastic cross-sectional measurements. Phys. Rev. 95, 1268.

Morel, J.E. 1975. Doses to a thin silicon slab behind aluminum, aluminum-tantalum, and aluminum-lead shields for isotropic fission electrons. AFWL Technical Note DYT TN-75-1.

National Academy of Sciences. 1973. HZE-Particle Effects in Manned Spaceflight.

Noll, R.B. and McElroy, M.B. 1975. The earth's trapped radiation belts. NASA SP-8116.

O'Brien, K. 1972. The cosmic ray field at ground level. Second International Symposium on the Natural Radiation Environment, Houston, Texas, August 7-11, 1972.

Paulikas, G.A. and Blake, J.B. 1971. The particle environment at synchronous altitude. Long-Term Time Variations: Models of the Trapped Radiation Environment, vol. VII. NASA SP-3024.

Schimmerling, W.S., Devlin, T.J., Johnson, W.W., Vosburgh, K.G., and Mischke, R.E. 1973. Neutron-nucleus total and inelastic cross sections: 900 to 2600 MeV/n. Phys. Rev. C 7, 248-262.

Schulz, G.J. 1976. A review of vibrational excitation of molecules by electron impact at low energies. Principles of Laser Plasmas. New York: Wiley-Interscience.

Simpson, J.A. and Garcia-Munoz, M. 1970. Unpublished data measured aboard Imp 4.

Singley, G.W. and Vette, J.I. 1972. A model environment for outer zone electrons. NASA TM X-69989.

Sleeper, H.P. 1972. Planetary resonances, bi-stable oscillation modes, and solar activity cycles. NASA CR-2035.

Slutz, R.J., et al. 1971. Solar activity predictions. NASA CR-1939.

Turner, J.E., et al. 1964. Calculation of radiation dose for protons to 400 MeV. Health Phys. 10, 783.

Webber, W.R. 1966. An evaluation of solar-cosmic-ray events during solar minimum. Boeing Technical Report D2-84274-1.

Wilson, J.W. 1974. Heavy ion scattering, Glauber theory and optical model. Phys. Lett. 52B, 149.

Wilson, J.W. 1975. Composite particle reaction theory. Ph.D. Dissertation, College of William and Mary.

Wilson, J.W. 1977a. Analysis of the theory of high-energy ion transport. NASA TN D-8381.

Wilson, J.W. 1977b. Depth-dose relations for heavy ion beams. V. J. Sci. 28, 136.

Wilson, J.W. and Costner, C.M. 1976. Nucleon and heavy ion total and absorption cross section for selected nuclei. NASA TN D-8107.

Wilson, J.W. and Denn, F.M. 1976. Preliminary analysis of the implications of natural radiations on geostationary operations. NASA TN D-8290.

Wilson, J.W. and Denn, F.M. 1977a. Implications of outer-zone radiations on operations in the geostationary region utilizing the AE4 environmental model. NASA TN D-8416.

Wilson, J.W. and Denn, F.M. 1977b. Methods of shield analysis for protection against electrons in space. Nucl. Technol. 35, 178.

Wilson, J.W. and Khandelwal, G.S. 1974. Proton dose approximation in arbitrary convex geometry. Nucl. Technol. 23, 298.

Wilson, J.W. and Khandelwahl, G.S. 1976. Proton tissue dose build-up factors. Health Phys. 31, 115.

Wilson, J.W. and Lamkin, S.L. 1975. Perturbation theory for charged particle transport in one dimension. Nucl. Sci. Eng. 57, 292.

Wright, G.R., et al. 1976. Dipole excitation, ionization and fragmentation of N_2 and CO in the 10-60 eV region. J. Phys. B9, 675.

Wright, H.A., *et al*. 1971. Effects of lateral scattering on absorbed dose from 400-MeV neutrons and protons. Proceedings, International Conference Protection Against Accelerator and Space Radiations. Cern 71-16, vol. 2, p. 207.

INSTRUMENTATION FOR RADIATION MEASUREMENTS IN SPACE

John P. Wefel

Enrico Fermi Institute
The University of Chicago
Chicago, Illinois 60637

INTRODUCTION

Research in the "particles and fields" area has been a part of the U.S. space program almost since the first successful satellite launching in the 1950s. The particles and fields area encompasses measurements of charged particles from protons and electrons through UH (ultra-heavy, $Z > 28$) nuclei, covering low (eV/ion) to extremely high ($> 10^3$ GeV/nucleon) energies, for particles whose origins are as diverse as the galactic cosmic radiation, solar particles, and magnetospheric radiation. This intense interest in charged particle investigations is the result of several factors. First, energetic charged particles represent a window to our galaxy which complements the information provided by the photon spectrum. The charged particles interact strongly with interstellar matter and electromagnetic fields, thereby providing clues to the nature of the interstellar medium. Further, the elemental and isotopic composition of the galactic cosmic rays carries information on the nucleosynthesis and acceleration processes in the source regions. Thus, the investigation of these particles has been called charged particle astronomy.

Closer to home, the sun is a copious source of energetic charged particles emitted both during solar flare outbursts and continuously in the form of the solar wind. The solar magnetic fields carried outward by the streaming solar wind inflate a large cavity in the local interstellar medium, the heliosphere which controls the access of galactic particles to the solar system, and interact directly with planetary magnetic fields to produce magnetospheres. The study of the composition and energy spectra of solar particle radiations provides information on the elemental or isotopic ratios in the region of the sun from which the particles emerge, and offers clues to the specialized conditions responsible for accelerating these nuclei.

Planetary magnetospheres contain large fluxes of low energy particles trapped within the magnetic field lines. The origin of this trapped radiation is generally thought to involve the solar wind and/or solar flares, but in recent years it has been found that the magnetospheres of the planets, especially Jupiter, can themselves act as accelerators of electrons (Pyle and Simpson, 1977). In addition, evidence now exists for the acceleration of particles in situ in the interplanetary medium via the action of shock waves associated with solar wind streams (Barnes and Simpson, 1976).

The vast diversity of the phenomena to be studied has required a large variety of instruments and involved measurements both in space and with high altitude research balloons. Many major discoveries have been made in "particles and fields" research, and they owe their existence as much to technological break-throughs in detector systems as to improvements in satellites and launch vehicles.

Space instrumentation has traditionally been that of small, low-power detector systems carried on small satellites with low data bit rates. This has been necessitated by the weight, power, and budgetary limitations of satellite technology. In addition, a space experiment differs from the usual laboratory investigations in that, once launched, the instrumentation is unavailable for modifications. This situation leads to design criteria that differ markedly from laboratory instrumentation, in particular, redundancy and reliability are stressed, and only specially screened radiation resistant parts can be used in construction. Furthermore, experiments are designed for simplicity in logic and operation in order to minimize failure modes and to allow commandable reconfiguration of the experiment.

This philosophy of space instrumentation is on the verge of a radical change with the coming of the shuttle era. Man can be put back into the experimental loop when he is on board a shuttle or in space platforms such as the SPS. Instruments will be controllable in real-time, and even limited repair or refurbishment, on-orbit, can be considered. The effects of this new era on instrument design will probably be a deemphasis of redundancy and reliability as design criteria, and a move towards larger more complex experiments. Whatever the changes, however, the shuttle era promises to be an exciting time for studying charged particle radiations in space.

It is not the purpose of this paper to describe the scientific discoveries made in charged particle astronomy over the past two decades, but rather to discuss some of the space instrumentation that has been employed. This introduction has been provided to give the reader an appreciation of the diversity of the astrophysical problems in which charged particle detectors have played a role.

The SPS mission is not designed as a means for studying the radiation environment, but must focus on the question of the interaction of ionizing radiation with both men and materials in orbit. In the current configuration, the SPS mission will involve both low altitude and geostationary orbital operations, and it will be exposed to the three major sources of charged particles discussed above: the galactic cosmic radiation, solar flare particles, and geomagnetically trapped radiation. Because the SPS is a manned station, its operation must include radiation monitoring both internal and external to the satellite. Inside the SPS, secondary radiations (neutrons, gammas, x-rays, or heavy ions), generated by interaction of primary particles in the spacecraft walls, present a different set of radiation problems. However, the monitoring of these fluxes can be performed in a "shirt-sleeves" environment by trained personnel using many of the techniques employed in terrestrial laboratories. It is the radiation external to the SPS that presents a problem similar to that encountered in particles and fields research, and most of the remainder of this paper is devoted to discussing the techniques applicable to external monitoring.

The next section discusses the composition and energy spectrum of the charged particle radiation and gives a brief overview of the experimental techniques used in different energy regions. This is followed by a more detailed description of the operation of a solid-state detector telescope system showing some of the evolution of these instruments over the past decade. Finally, a summary of the present state of space instrumentation is given along with some comments on the problems particular to the SPS mission.

EXPERIMENTAL TECHNIQUES: A BRIEF OVERVIEW

Charged particle radiation in space is characterized by its composition, energy spectrum, intensity, and anisotropy. Each event is completely specified by measuring the parameters of charge, mass, kinetic energy, and arrival direction. Intensity is determined by collecting events over selected time intervals or by recording counting rates from one or more detectors. A large variety of techniques have been employed to investigate one or several of the above parameters, and these techniques divide naturally into groups based upon the particle and the energy range studied.

Figure 1 shows the energy spectra of galactic cosmic ray protons, helium, boron, and carbon measured on the IMP 7 spacecraft in 1973 (Garcia-Munoz et al., 1975c). Above approximately 1 GeV/nucleon, the spectra are power laws falling with total energy as $E^{-\gamma}$, with a spectral index, γ, of ~ 2.6. Below 1 GeV/nucleon the particles are modulated in the heliosphere. The solid curves give the unmodulated spectra in local interstellar space which are compared to the spectra observed at earth, shown by the experimental points. The continuation of this spectrum to lower energies is shown on Figure 2 with data for carbon and oxygen, and the helium spectrum is shown for comparison (from the summary by Garcia-Munoz, 1973). Note that the spectrum turns up at very low energies giving a composite energy spectrum such as that illustrated in Figure 3 for protons (Zamow, 1975). In the region below ~10 MeV/nucleon it is difficult to differentiate between galactic and solar particles except during times of very low solar activity. This is because the spectrum of solar particles is quite

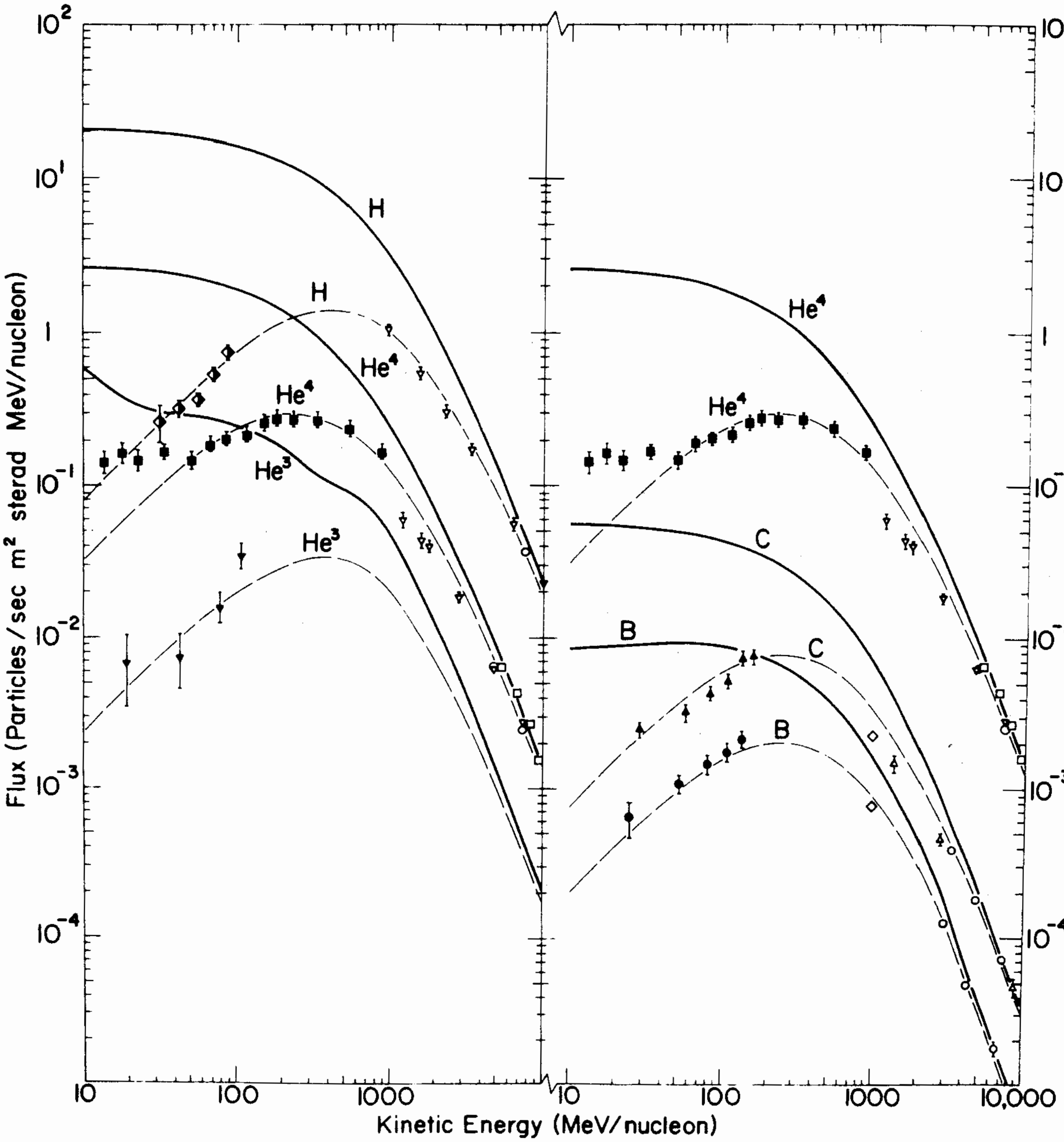

Figure 1: Differential energy spectra of galactic cosmic ray hydrogen, helium, boron, and carbon. Solid curves show unmodulated spectra in local interstellar space and dashed curves show modulated spectra at 1 A.U.

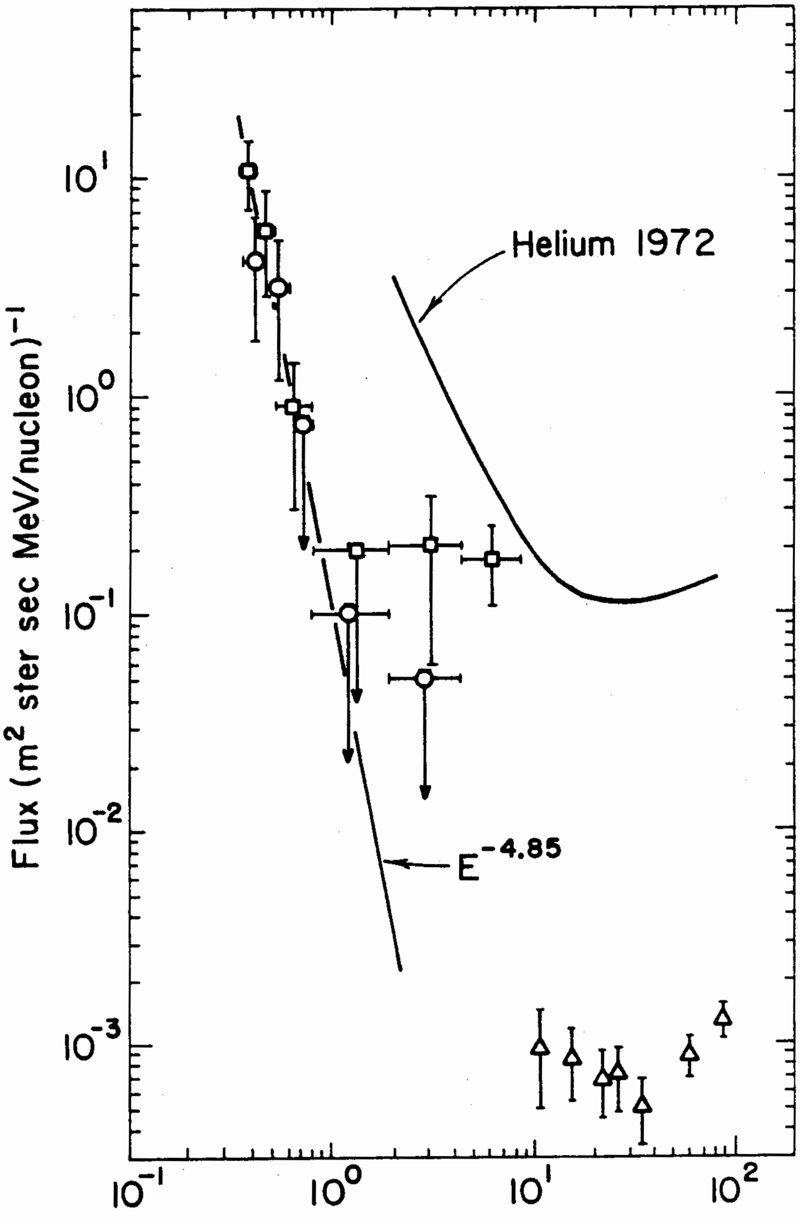

Figure 2: Differential energy spectra of low energy carbon (O) and oxygen (□,△) nuclei. The 1972 helium spectrum is sketched for comparison.

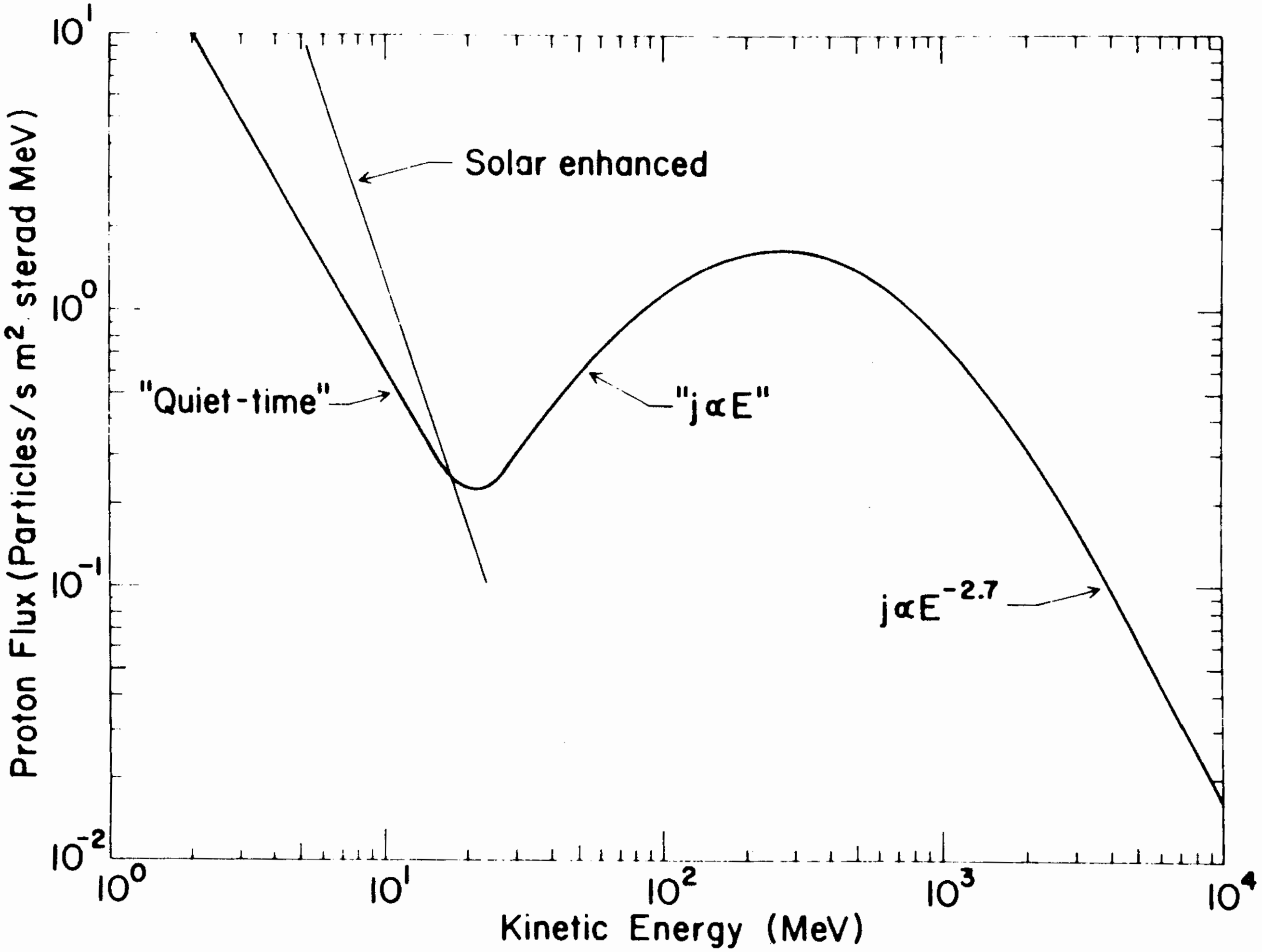

Figure 3: Schematic representation of the galactic cosmic ray proton spectrum indicating the region of enhancement by solar particles.

steep as illustrated by Figure 4 for the solar flares of 14 October 1969 and 30 July 1970 (Anglin, 1975). These proton spectra decrease with energy approximately as E^{-3}, but the spectral index for solar flare nuclei is variable from values as steep as -4.5 or 5 to as flat a spectrum as $E^{-1.5}$ at very low energies. Trapped particles in the radiation belts exhibit even steeper energy spectra than solar flare particles.

Figures 3 and 4 illustate some of the problems involved in charged particle measurements. Detectors designed for the intermediate energy nuclei, 10^2 to 10^3 MeV/n, may be swamped by the higher fluxes at a few MeV and are of insufficient size to record a significant sample of events at extremely high energies. In addition, the techniques used to measure the particles change drastically with energy. At very low energies nuclear particles can penetrate only a small amount of matter which severely retricts the choice of detectors. Thin window gas proportional chambers combined with solid-state detectors have given excellent results at energies around 1 MeV/nucleon (Hovestadt et al., 1973) and at still lower energies electrostatic analyzer systems (Fan et al., 1975) have been flown. Etched plastic track detectors have been employed successfully to measure heavy ions ($Z \gtrsim 8$) at energies above ~10 MeV/n (Chan and Price, 1975), but the need to recover these detectors for processing in the laboratory has limited the opportunities for space exposures. At energies above ~20 MeV/nucleon solid-state detectors and scintillators have been used with remarkable success by several groups (see, for example, Garcia-Munoz et al., 1973; McDonald et al., 1974; Mewaldt et al., 1975).

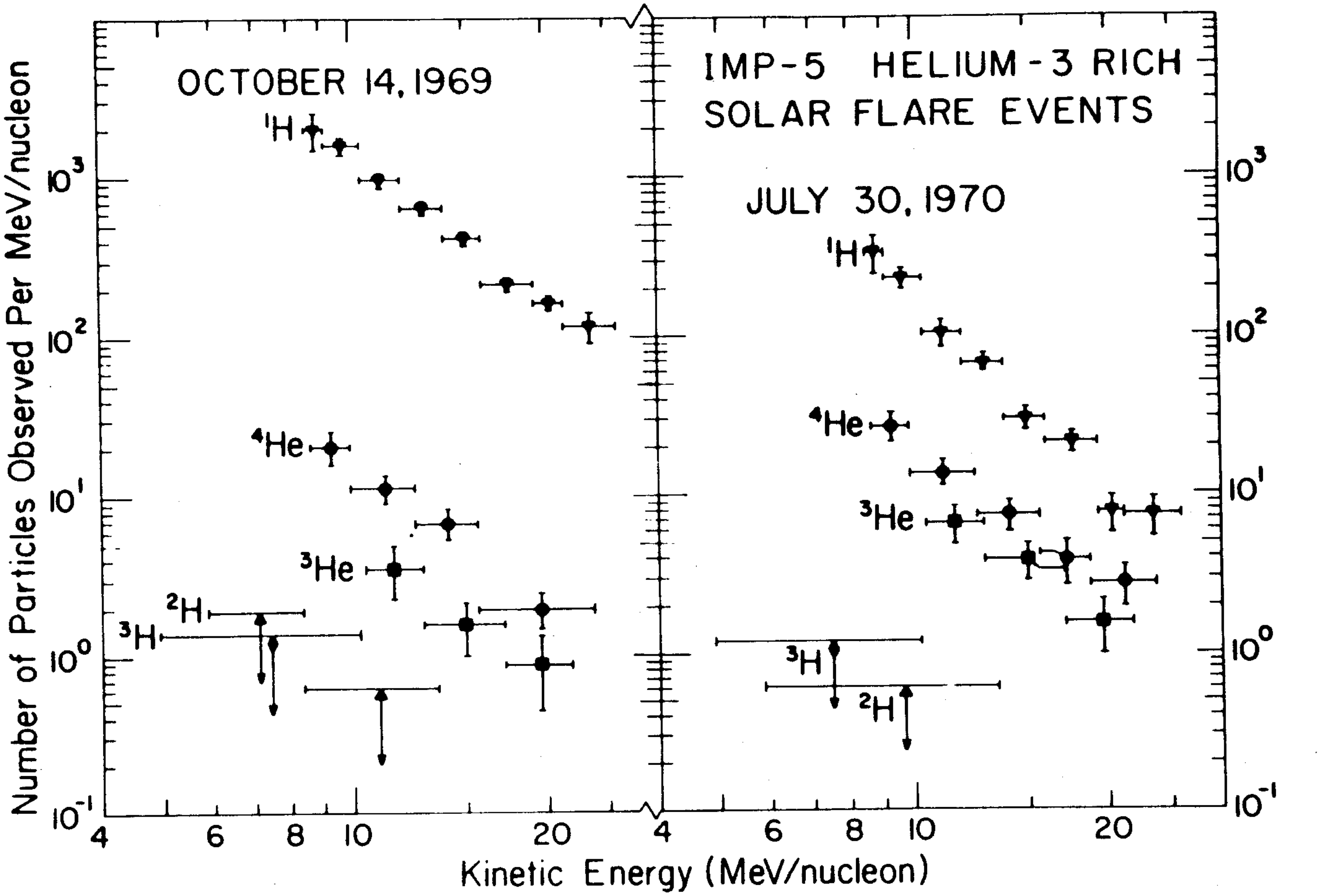

Figure 4: Differential energy spectra of hydrogen and helium from solar flares of October 14, 1969 and July 30, 1970.

At still higher energies, above ~ 0.5 GeV/nucleon, Cherenkov detectors must be used (Julliot _et_ _al_., 1975; Mason, 1972), and beyond several GeV/nucleon experiments have, so far, been performed mainly with balloon instruments of large size and weight. At these high energies, superconducting magnetic spectrometers (Smith _et_ _al_., 1973; Badhwar _et_ _al_., 1977) high pressure gas Cherenkov counters (Caldwell, 1977), ionization spectrometers (Balasubrahmanyan and Ormes, 1973), multiple Cherenkov counter arrays (Lund _et_ _al_., 1975), and transition radiation detectors (Cherry _et_ _al_., 1974) have been developed and proposed for space flight on shuttle missions.

The type of particle under investigation can also affect the choice of experimental technique. Figure 5 shows the charge composition of the galactic cosmic rays at low energies compared to solar system abundances. Hydrogen and helium are the most abundant species in the radiation and the odd-Z elements are significantly scarcer than their even-Z neighbors. The charge separation $\Delta Z/Z$ decreases with increasing charge, thereby requiring greater precision in experiments designed to study the high-Z elements. Only small instruments are needed to study protons and alpha particles, but considerably larger experiments are needed to collect statistically significant samples of many of the odd-Z nuclei.

Figure 6 shows a plot of the enhancement factors, relative to oxygen:

$$Q = R(Z)/R_{sun}(Z), \text{ where } R(Z) = N(Z)/N(^{16}O)$$

observed for particles emitted in several solar flares (Dietrich and Simpson, 1978). Note that the heavier nuclei such as iron may be

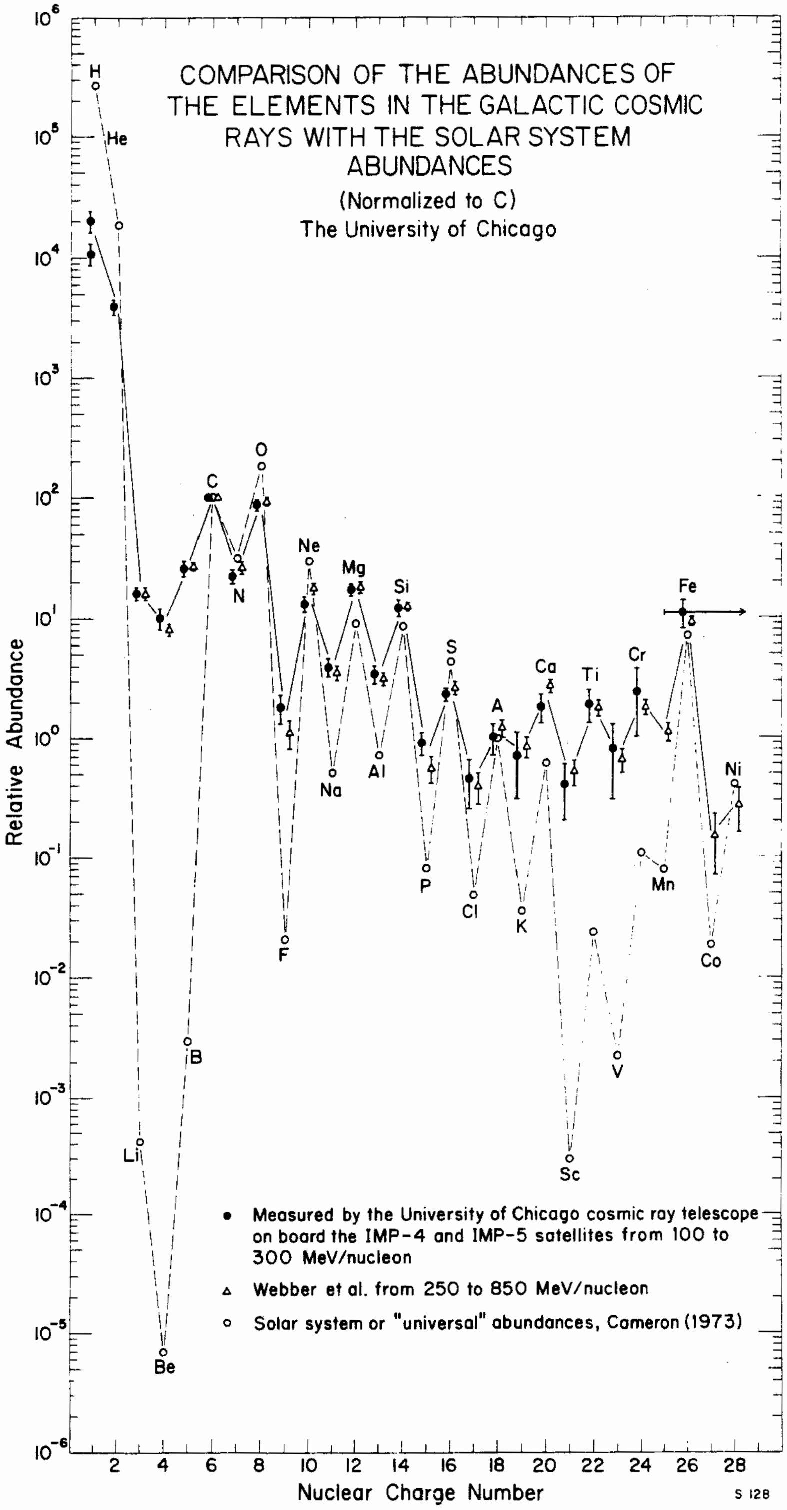

Figure 5: The measured abundances of the elements, relative to carbon, in the galactic cosmic radiation compared to the solar system abundance compilation of Cameron (1973).

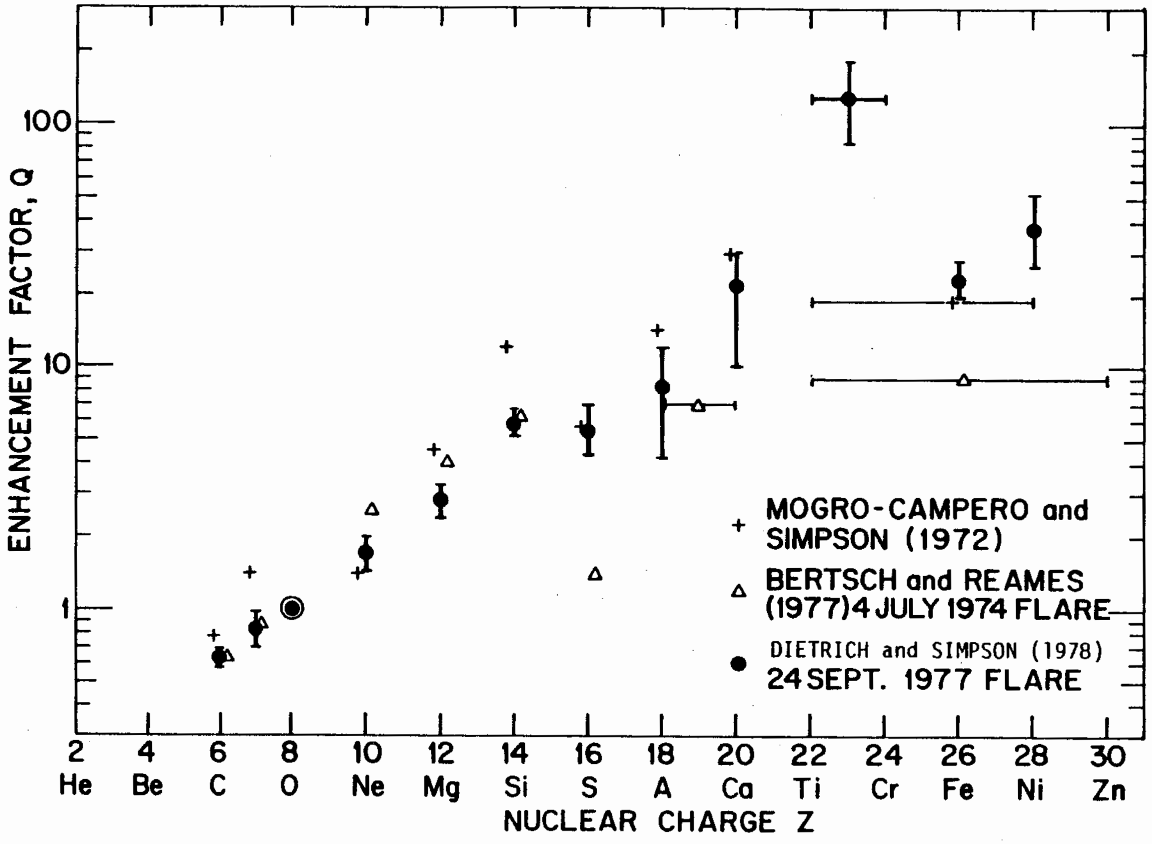

Figure 6: The enhancement factors for heavy nuclei, relative to oxygen, observed among solar flare particles as a function of the particle charge.

enhanced by almost two orders of magnitude over the normal solar abundances, indicating some type of preferential acceleration in the flare region. Protons, helium, and sometimes electrons are still the dominant particles emitted by solar flares, but the heavy elements can become quite important. Figure 7 shows the time profile of the particle emission in a typical solar flare event (Hamilton, 1977) as observed by IMP 8 and by Pioneer 11. The intensity shows a rapid rise to maximum, but a much longer decay phase. The entire particle production lasts for, at most, a week and can be much shorter in many flares. Thus solar flare particles can be studied, completely, only by satellite experiments that are in orbit for long periods of time and that are equipped to record the high event rates which may be encountered.

A final component of the galactic cosmic radiation and solar flare particles is the UH nuclei. Figure 8 shows measured abundances of UH particles in the galactic cosmic rays compared to solar system material for $Z < 60$ elements (Wefel et al., 1977). The most prominent feature of Figure 8 is the decrease in relative abundance by three to four orders of magnitude between iron and the $Z > 32$ elements. Beyond $Z = 60$ the abundances fall by another factor of ~ 4 before reaching Pb, but some trans-Pb events have been observed (Fowler, 1973). The UH nuclei have not been studied from unmanned satellites because of the enormous collecting areas required, but two UH experiments, consisting of ionization chambers or gas scintillators and Cherenkov counters, are being readied for launch on the HEAO-C and UK-6 satellites.

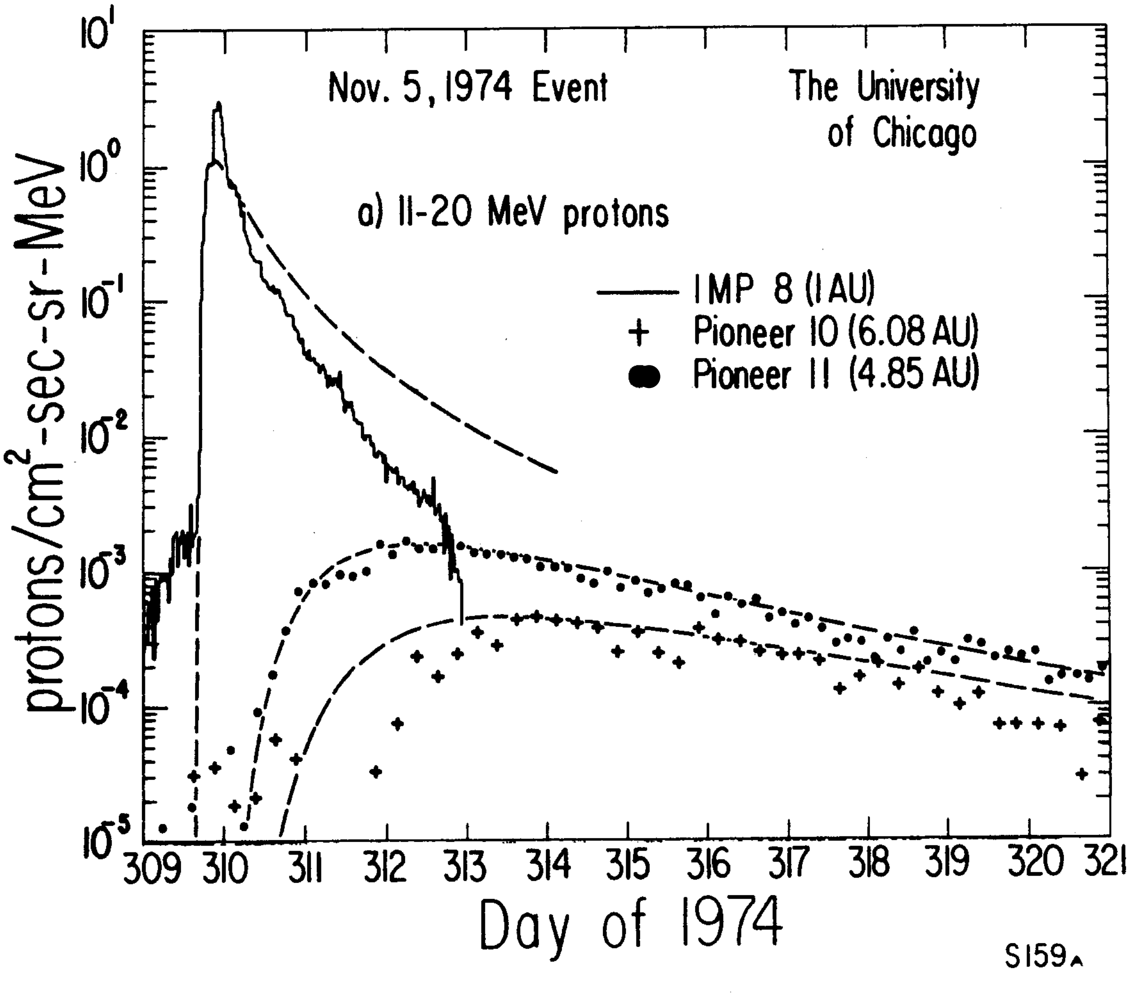

Figure 7: The time evolution of the proton intensity for the November 5, 1974 solar flare as observed by three spacecraft at different locations in the heliosphere. The dashed curves show calculated fits to the data.

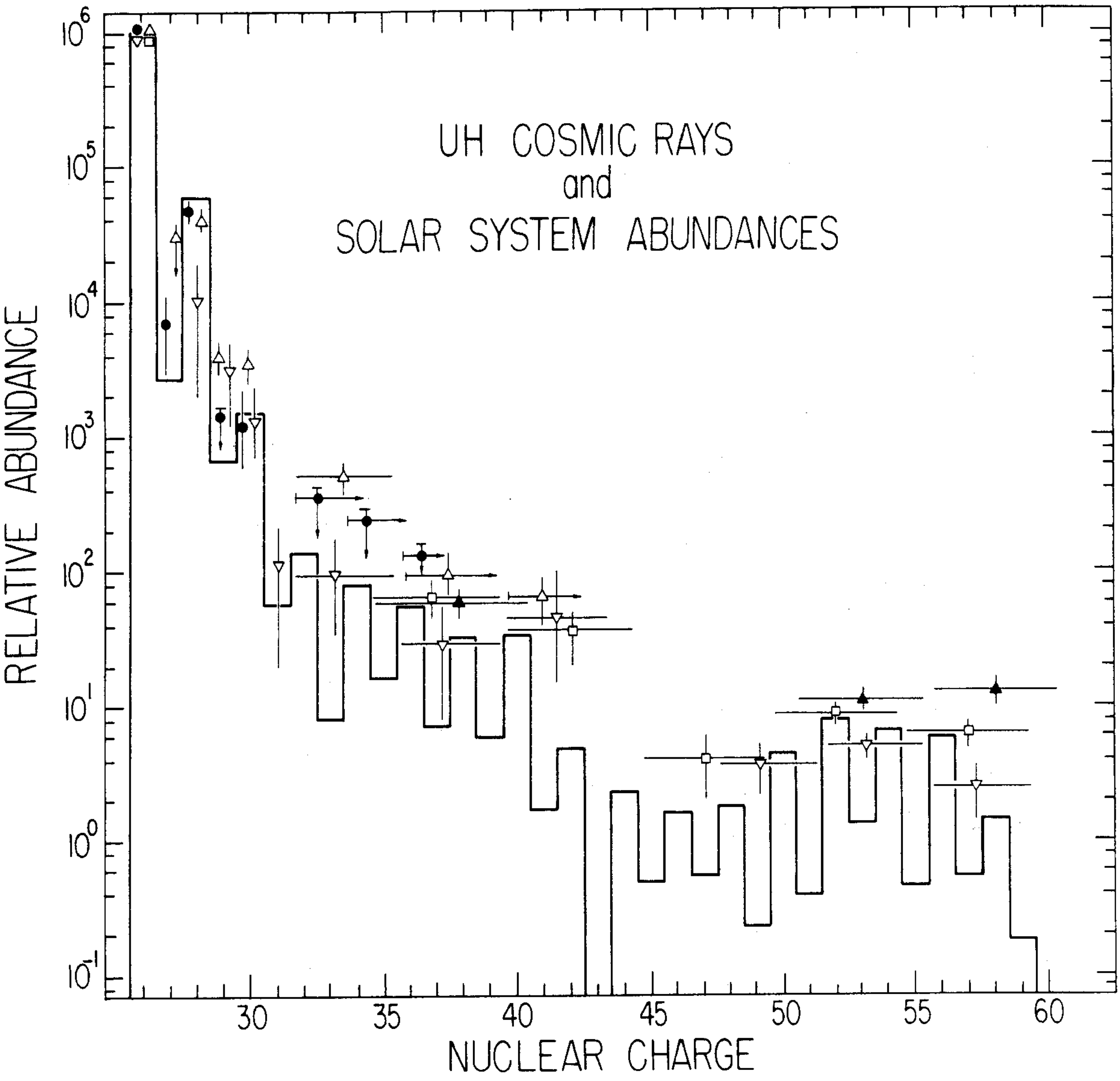

Figure 8: The measured abundances, relative to iron, of the ultra-heavy galactic cosmic rays compared to the solar system abundance compilation of Cameron (1973) shown as the solid histogram.

Mass measurements--the study of isotopic composition--is another area of considerable interest. Current space instrumentation is capable of isotopic separation for protons through the C, N, O nuclei, under favorable circumstances, and the detailed investigation of cosmic ray isotopes will be pursued with the next generation of instruments, some of which were launched recently on the ISEE-C satellite.

The investigation of electron fluxes is a somewhat more complex problem experimentally, but electrons are an important component of the cosmic rays and are produced copiously in solar flare processes and in planetary magnetospheres. Figure 9 shows the electron counting rates observed by the Pioneer 11 spacecraft on its mission to Jupiter. Solar flare events (sf) are indicated. An increase of several orders of magnitude in electron flux is measured by the time of encounter and Jovian electrons are observable over long distances in interplanetary space (Chenette et al., 1977).

Compared to protons of the same kinetic energy, electrons are highly relativistic and interact electromagnetically with matter to produce cascades. In addition, electrons are scattered easily in detectors or in the walls of the spacecraft. At low energies, care must be taken to ensure electron and proton separation in the measuring system (see, for example, Lin et al., 1972). At higher energies, Cherenkov detectors and shower counters are used to differentiate between the protons and electrons (L'Heureux et al., 1972).

The theory of operation of these diverse detectors all depend upon the interaction of charged particles with matter or electromagnetic fields (for a general discussion of this area, see Gloeckler, 1970).

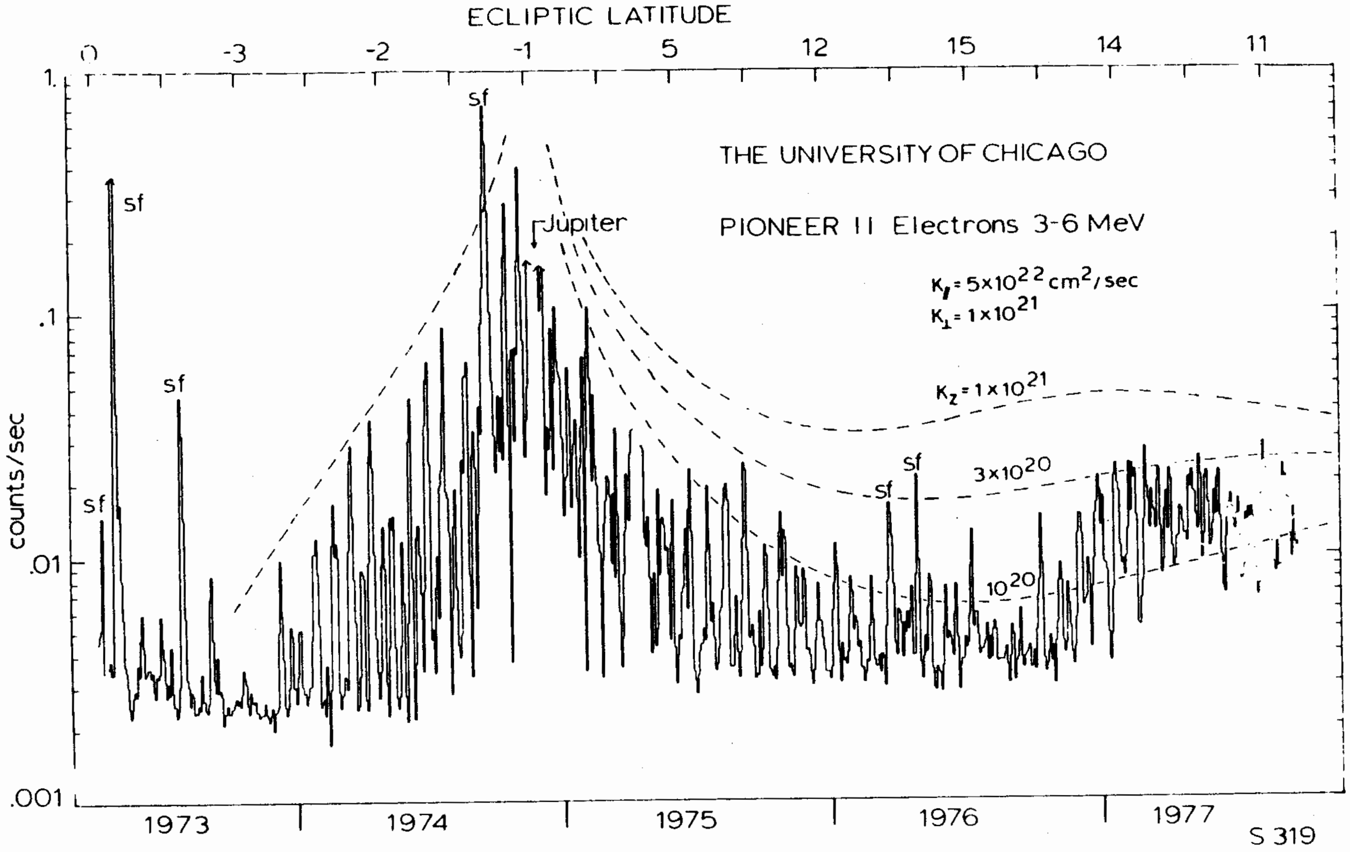

Figure 9: The time history of the intensity of 3 to 6 MeV electrons observed by the Pioneer 11 spacecraft over the last five years. The notation "sf" indicates a solar flare, and the dashed curves represent model fits to the data.

Electric or magnetic fields are employed to bend the particles in electrostatic analyzers and magnetic spectrometers and thereby gain information on the charge (mass) and velocity of the event. The operation of solid-state detectors, ionization chambers, proportional counters, and scintillators is based upon the ionization energy loss of the particle in the detector material. Briefly, the charged particle interacts with the electrons in the matter causing atomic excitations, ionizations and possibly displacements of the atoms. The secondary electrons (delta-rays) excited by the particle travel in the material producing secondary ionization and distributing the energy around the path of the incident particle. The net effect is to transfer energy from the incident ion to the detector material thereby causing the particle to slow down and, if enough matter is present, come to rest. The energy transferred to the detector material appears as the "signal." In the case of silicon detectors, the energy produces free electrons and "holes" in the silicon crystal, and these are driven to the surface electrodes by the applied electric field and collected as a current pulse. This process is illustrated schematically in Figure 10. In ionization chambers and proportional counters the energy deposited by the particle produces electrons and positive ions which are collected by an applied electric field. Scintillation detectors produce a light pulse as the output signal. In this case the energy deposited by the particle causes excitation of the atoms of the material which then de-excite by the emission of photons. Visualizing detectors such as plastic track detectors or nuclear emulsions operate on similar principles. In the first case the energy deposited produces sufficient radiation damage along the particle trajectory

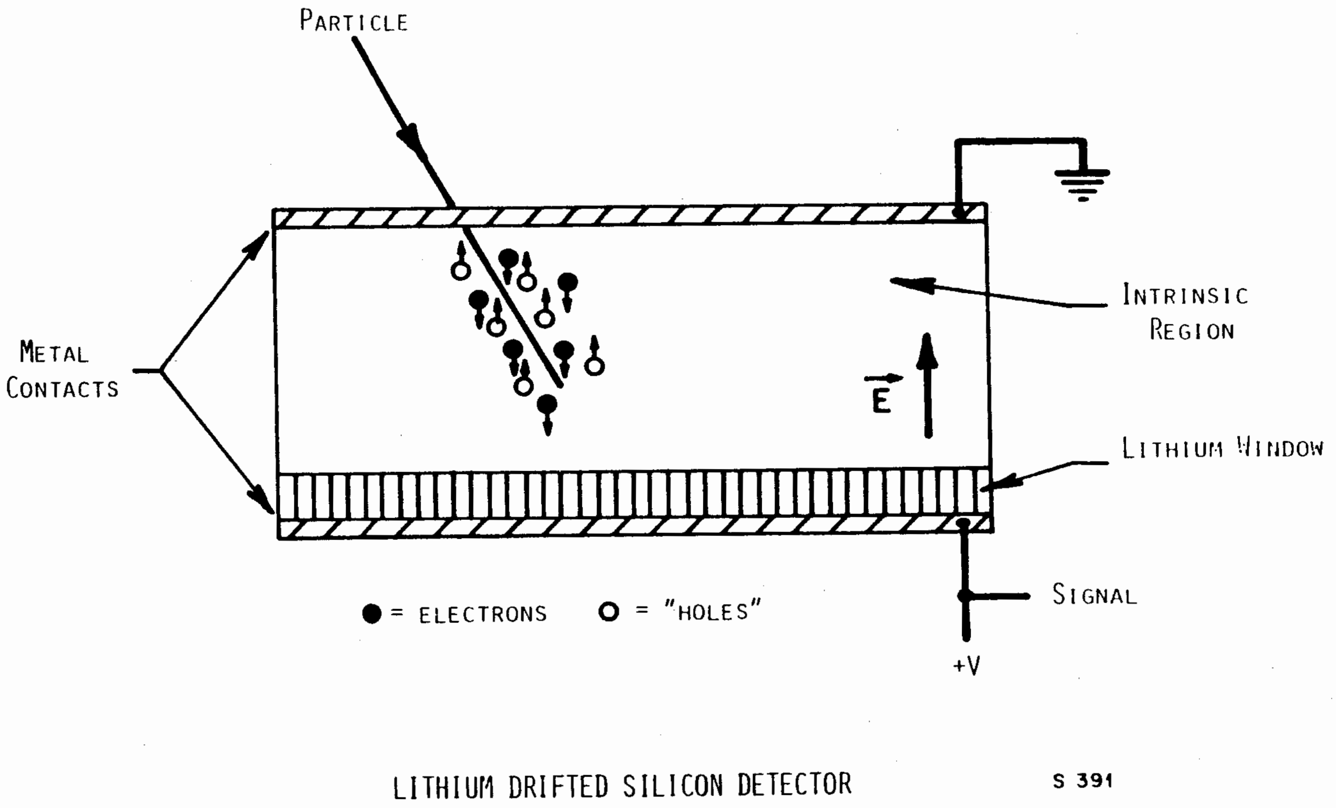

Figure 10: Schematic representation of the operation of a lithium-drifted silicon detector.

to produce an enhanced chemical etching rate. In nuclear emulsions the delta-rays sensitize grains of silver bromide which are then developed by photographic techniques.

Cherenkov counters and transition radiation detectors operate on a different type of particle-matter interaction. Photons are emitted by a dielectric medium whenever it is traversed by a charged particle with velocity exceeding the phase velocity of light in the dielectric. This phenomenon was discovered by P.A. Cherenkov in 1937 and now bears his name. Cherenkov radiation exhibits a threshold character which is extremely useful in many applications. Transition radiation refers to photons (usually at x-ray energies) emitted by a charged particle traversing a boundary between two materials of different indices of refraction. The light yield per boundary is extremely small, but if sufficient transitions are made (for example, in a stack of many thin layers of plastic) a detectable photon pulse is produced. An important feature of transition radiation is that the yield varies with the particle Lorentz factor (E/Mc^2), thereby providing a means to measure the energy for extremely high energy particles.

Selecting a detector to be used for a specific experiment is only the beginning, because the output signal must next be processed electronically. Figure 11 shows schematically the electronic modules required to transform the detector output signal into a digital number that can be employed for further data analysis. Note that several stages of amplification and signal shaping are required before the output pulse is "frozen" by the peak detector and translated by the analog-to-digital converter. For scintillation detectors an additional

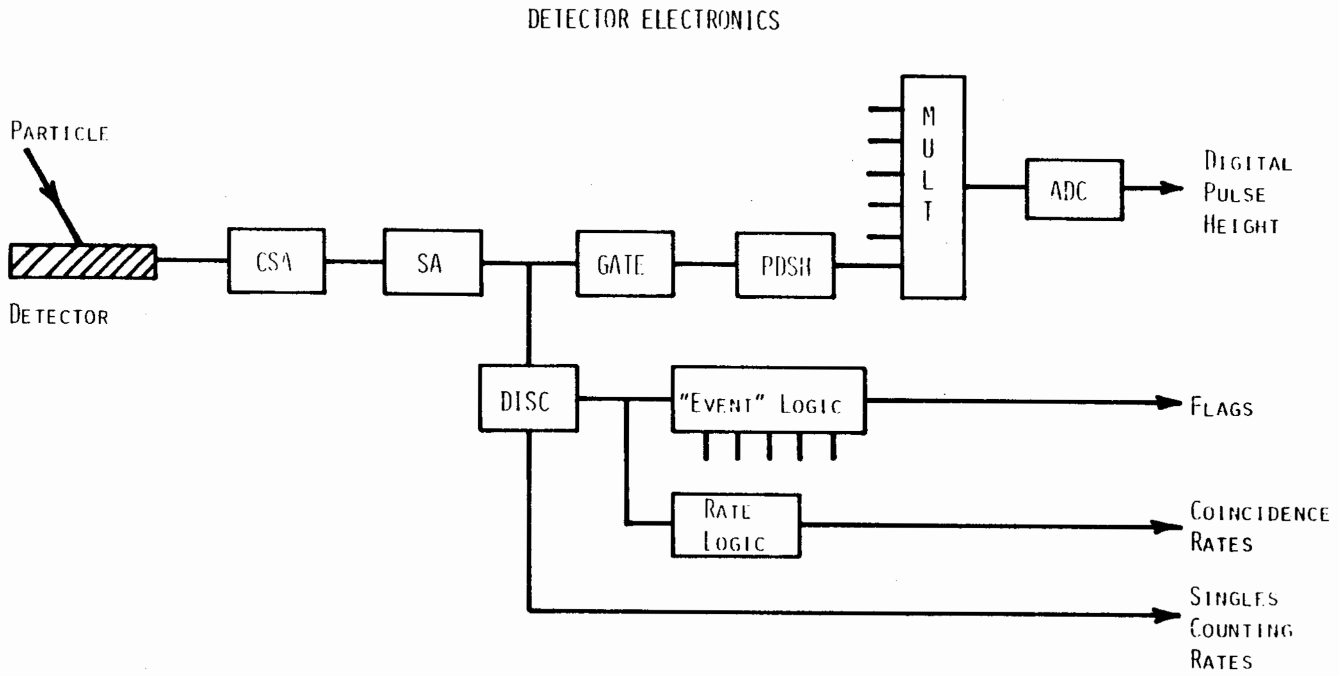

CSA = CHARGE SENSITIVE PRE-AMPLIFIER
SA = SHAPING AMPLIFIER
PDSH = PEAK DETECT SAMPLE AND HOLD
DISC = DISCRIMINATOR
MULT = MULTIPLEXER
ADC = ANALOG TO DIGITAL CONVERTER

S 392

Figure 11: A block diagram of the electronic circuitry required to process a signal from a charged particle detector.

piece of hardware such as a photomultiplier tube or photodiode is required to convert the light pulse from the detector into a current pulse that can then be amplified, etc. For a space experiment each of these electronic components must be carefully fabricated and tested to ensure survivability in the space environment and, moreover, these electronic modules must retain their calibration in space over long periods of time (typically years). It must be emphasized here that the electronic circuitry attached to a detector is equally as important to the success of a specific experiment as is the detector itself. The precision with which measurements can be made--and the validity of the scientific results derived from those measurements--is a combination of the detector resolution and the accuracy of the electronic readout circuitry. Many of the recent advances in space instrumentation have as their basis improvements in electronics technology.

All of the detection techniques mentioned above produce signals that depend upon more than a single property of the incident particle, usually a function of the charge, mass and energy. Thus, none of the detectors, used alone, can provide complete information on the observed particles. This leads to the use of multiple detectors of the same or different types combined into telescope systems whose purpose is to measure sufficient parameters to characterize the event. The use of telescopes, of course, complicates the needed electronic circuitry and the data reduction, but it provides the analytical power necessary to study space radiations in detail. Telescope systems vary from simple experiments to very complex instruments, and their description is probably best accomplished by some examples.

TELESCOPE SYSTEMS: EVOLUTION AND OPERATION

Figure 12 shows the Climax neutron monitor counting rate for the present and the last two solar cycles with the space missions that carried University of Chicago experiments superimposed (Simpson, 1978). Note that only 1.5 solar cycles have been studied in detail from satellites, and the present cycle is significantly different from the previous one. The University of Chicago has had telescope systems, composed of silicon detectors, scintillators, and Cherenkov counters, in both near-earth space and in the outer solar system, and these experiments will be used as examples to explain the evolution and operation of telescope systems.

The simplest configuration is a single detector enclosed by passive shielding as illustrated in Figure 13. The passive shielding determines the telescope aperture and is of sufficient thickness to stop most low energy particles. A calculation of the energy deposited by different particles in a single detector is plotted in Figure 14 as a function of the incident kinetic energy. The expected signal rises to a maximum just before the particle penetrates the detector, and thereafter decreases. If electronic discriminator thresholds are set at t_1, t_2, and t_3, the counting rates for events exceeding the thresholds provides an approximate flux measurement. The t_3 rate measures $Z > 2$ nuclei over different energy ranges depending upon the species. Particles with $Z > 1$ trigger the t_2 rate and protons are recorded as t_1 events over the energy range 0.5 to 8 MeV. If it is known, from other information, that protons are the dominant species in the radiation field, then the t_1 rate gives the proton flux with only a small correction required

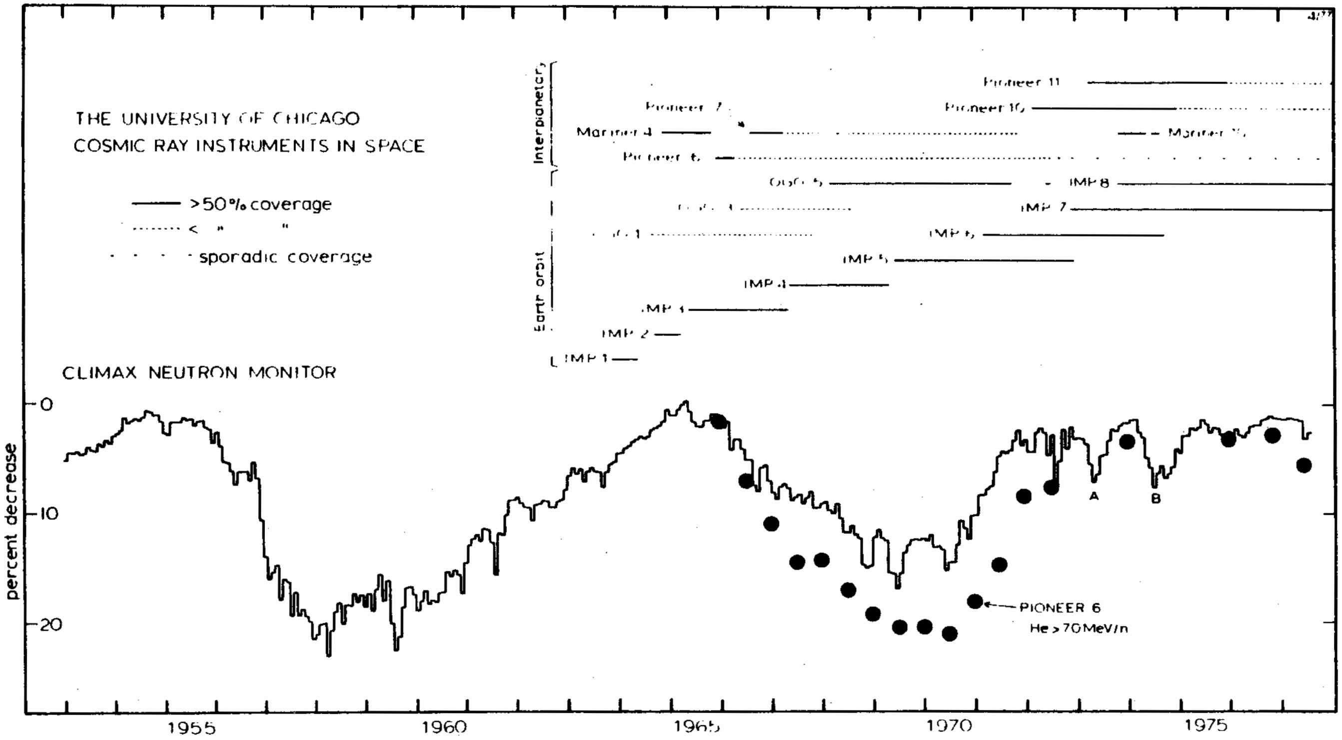

S 271A

Figure 12: The Climax neutron monitor counting rate for the period 1953 to 1977 with space missions containing University of Chicago telescope systems superimposed for comparison.

University of Chicago
Low Energy Proton and Alpha Detector (LEPA)

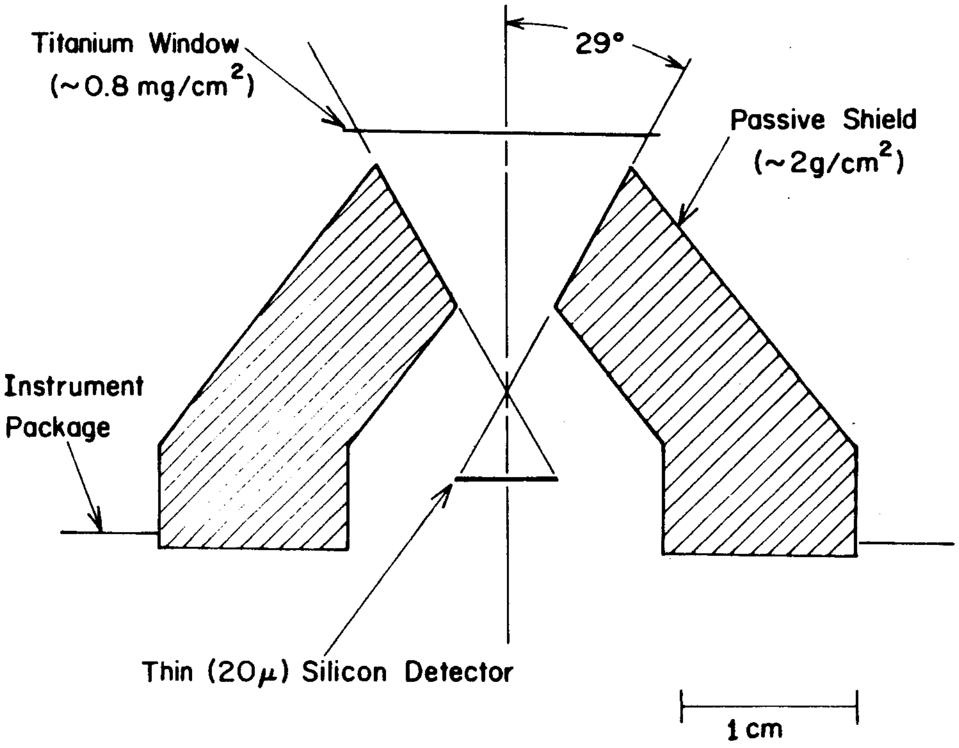

Figure 13: Schematic diagram of a passively shielded single detector telescope system.

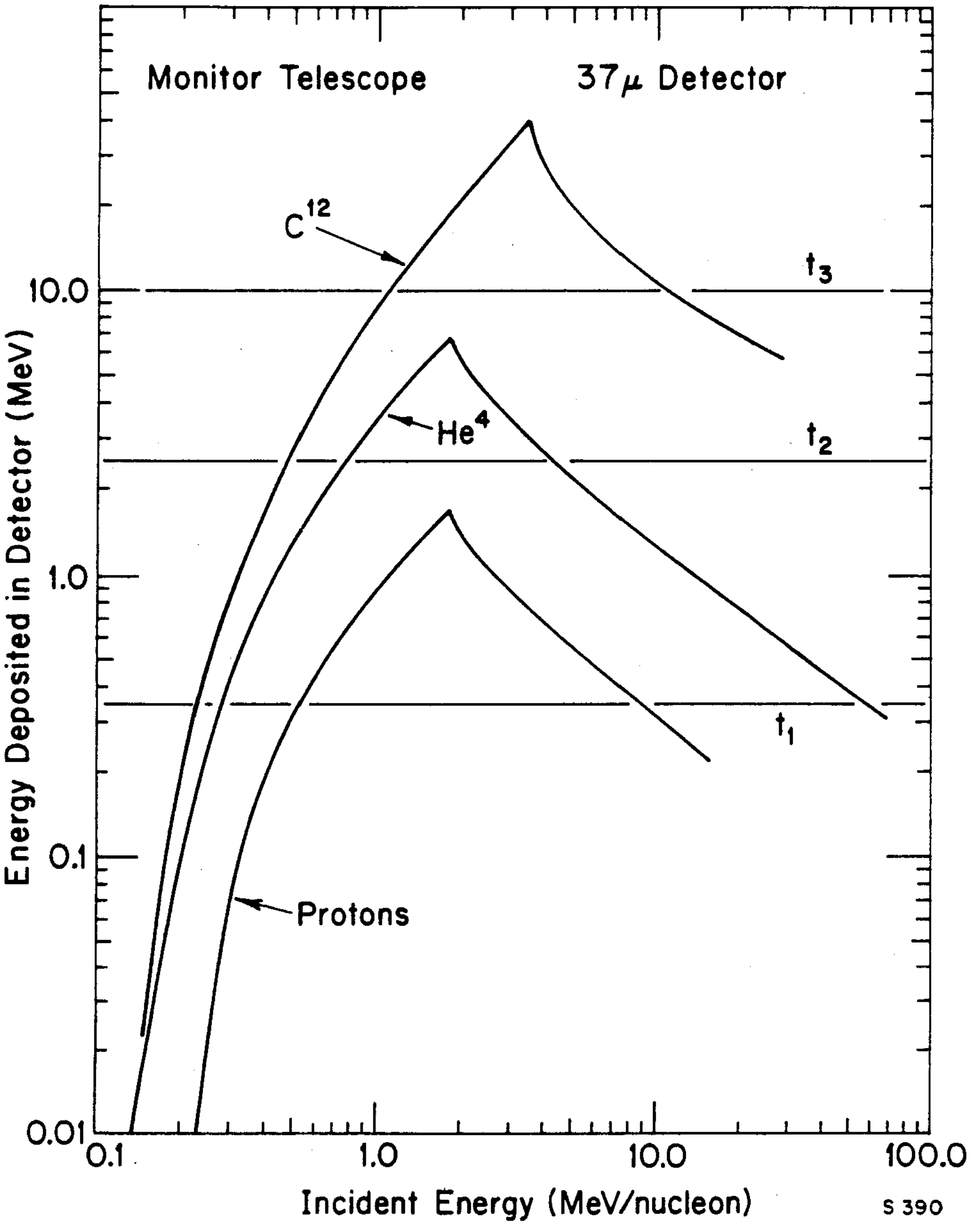

Figure 14: The energy deposited in a single detector of 37 microns thickness by protons, alphas, and carbon particles as a function of the incident kinetic energy of the particle. Discriminator thresholds t_1, t_2, t_3 at 350 keV, 2.5 MeV, and 10 MeV, respectively, are indicated.

for helium and heavier nuclei. In an unknown radiation environment, it can often be difficult to unfold the counting rate information to give particle intensities.

The next level of complication involves using a second detector in the telescope as shown for the low energy telescope (LET) in Figure 15. The added detector L_a acts as an anti-coincidence guard detector. Counting rates are formed by setting threshold discriminator levels on detectors L_1 and L_f. Many different rates can be formed by requiring particles to be above a threshold or bracketed by two thresholds in L_1 and, simultaneously above or below selected thresholds in L_f, thus turning the telescope into a type of single channel analyzer in counting rates. LETs have been used successfully on several missions for solar flare and magnetospheric studies.

In order to obtain more information on the charged particles, it is necessary to perform pulse height analysis (PHA) on one or more detectors in the telescope. The electronics needed for PHA work were sketched in Figure 11. If the particles are of sufficiently low energy to stop in the telescope, the dE/dx versus residual energy technique can be used for identification. This procedure is shown schematically in Figure 16. PHA is performed on both the detector in which the particle comes to rest and the detector preceding it. In a plot of the signal from the dE/dx detector versus the signal from the stopping detector, particles of different charge fall along separate curves in the matrix. This type of telescope is illustrated in Figure 17, which shows the IMP III instrument and the results from six months of data collection. In this design, detectors D1 and D3 are analyzed,

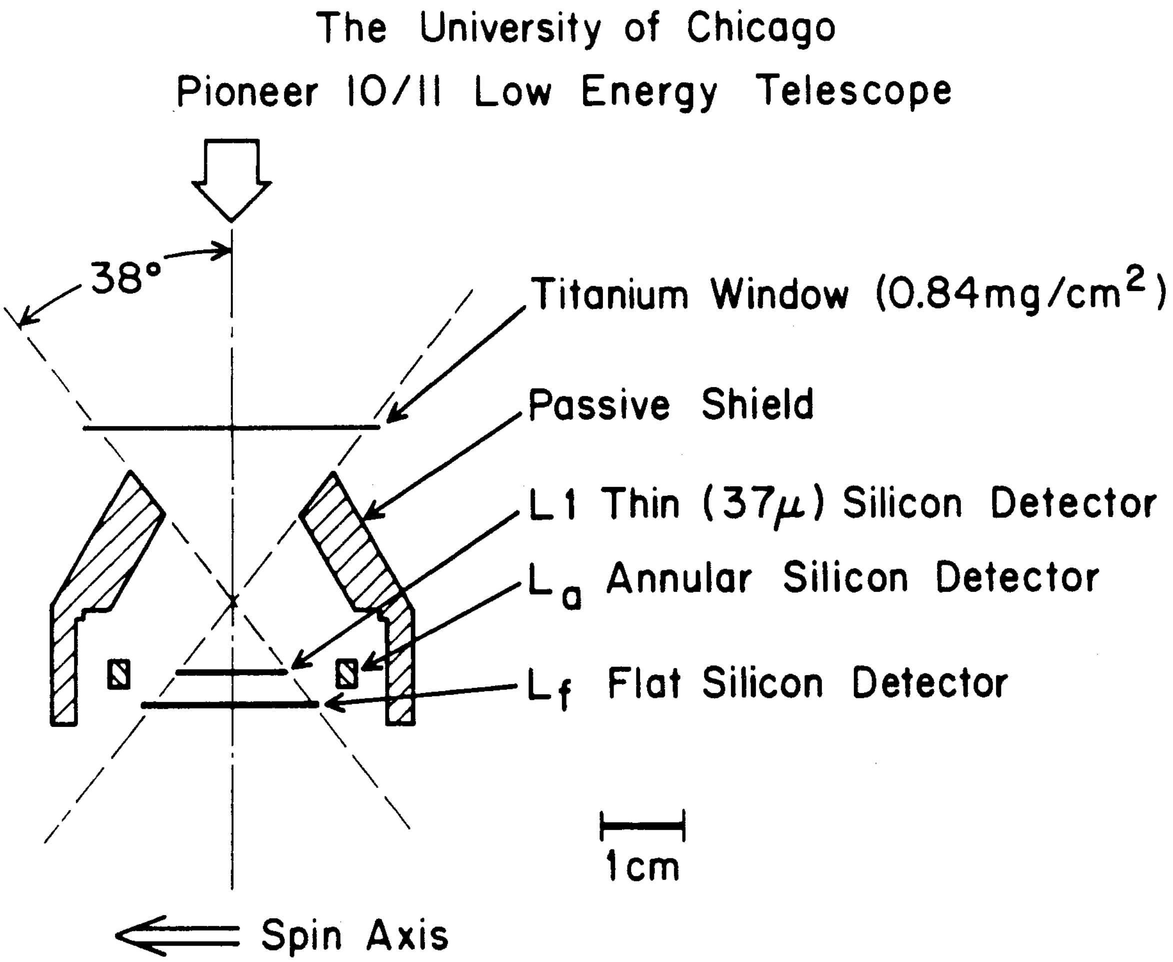

Figure 15: Schematic diagram of the low energy telescope employed in the Pioneer 10/11 experiments.

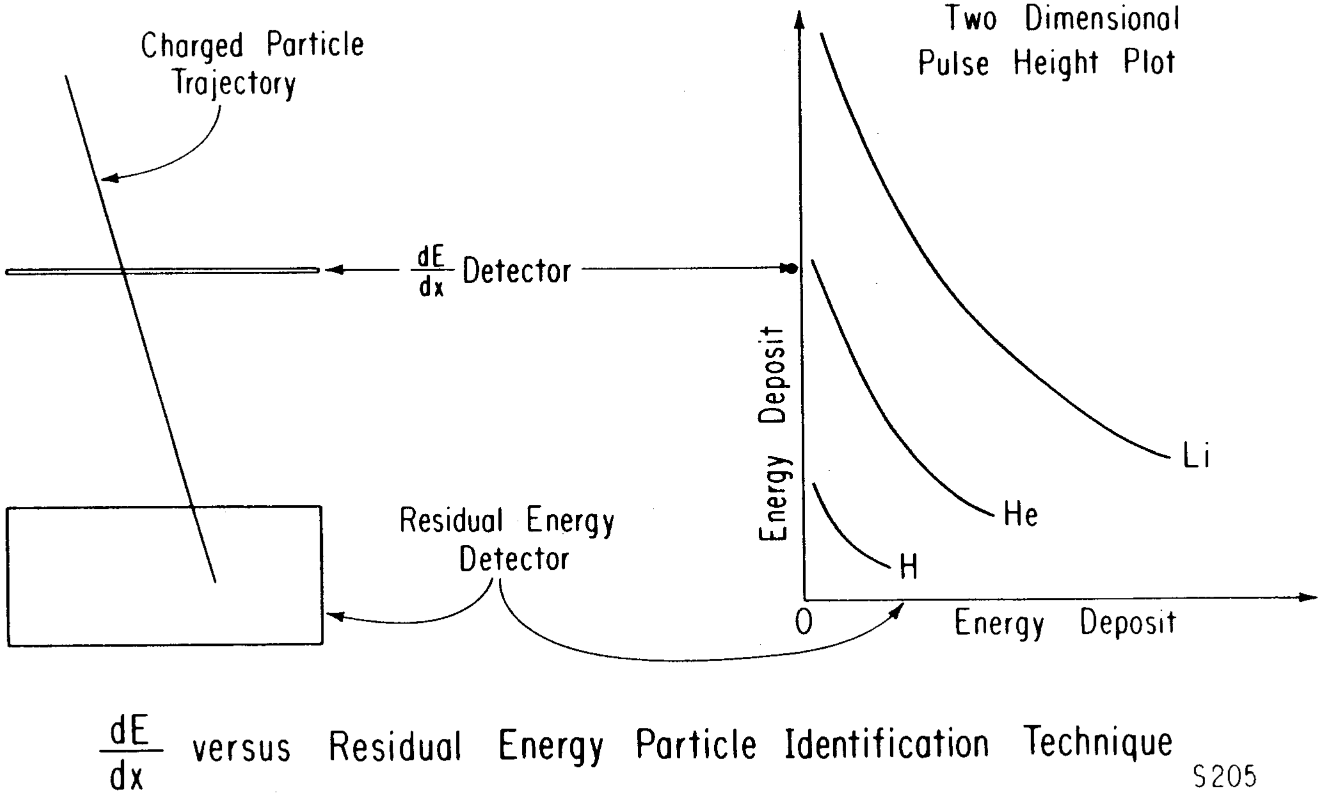

Figure 16: A schematic representation of particle identification by the dE/dx versus residual energy technique.

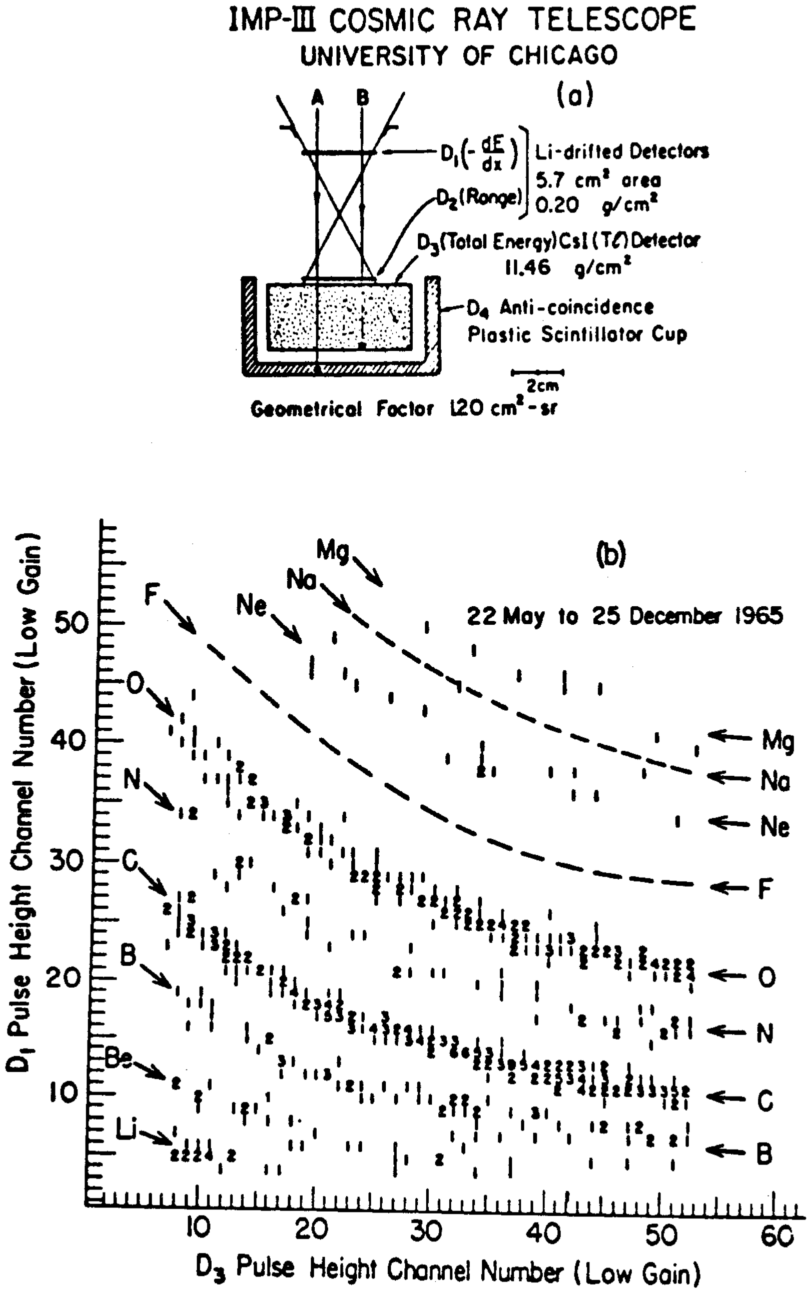

Figure 17: Part (a): diagram of the IMP III charged particle telescope.
Part (b): the dE/dx versus residual energy matrix obtained by IMP III in about 6 months of data collection.

D2 restricts the acceptance cone, and D4 is used in anti-coincidence to restrict analysis to particles that stop in the CsI (Tl) detector. The pulse height matrix reveals good charge resolution with little "background" for elements through oxygen, but the statistics for heavier nuclei are meager. The IMP III experiment was quite successful, providing some of the early results on the elemental composition of heavy nuclei.

Pulse height matrices such as Figure 17 can also be used to obtain clean data on particle intensities and energy spectra. To obtain the flux of carbon nuclei, for example, one merely counts the events within the carbon track, and divides by the time and the instrument geometrical factor. The position of a given event along the carbon track is directly related to the particle's incident energy. Thus, after calibrating the track position in terms of energy, the track may be subdivided and used to determine the particle energy spectrum. This technique is superior to the use of detector counting rates because it is relatively free of contamination by particles of different charge. Further, the entire procedure can be computerized, and intensities calculated for different time bases.

Figure 18 shows the IMP 4 and IMP 5 telescopes which were flown in the late 1960s and early 1970s (Garcia-Munoz et al., 1973). The entire detector stack is enclosed in an anti-coincidence scintillator and three of the detectors are pulse height analyzed and recorded. Three parameter analysis permits efficient rejection of background events and increased confidence in the charge measurements. The residual energy detector is a large CsI (Tl) scintillator viewed by photodiodes, which is divided into two separate pieces in the IMP 5 design. In

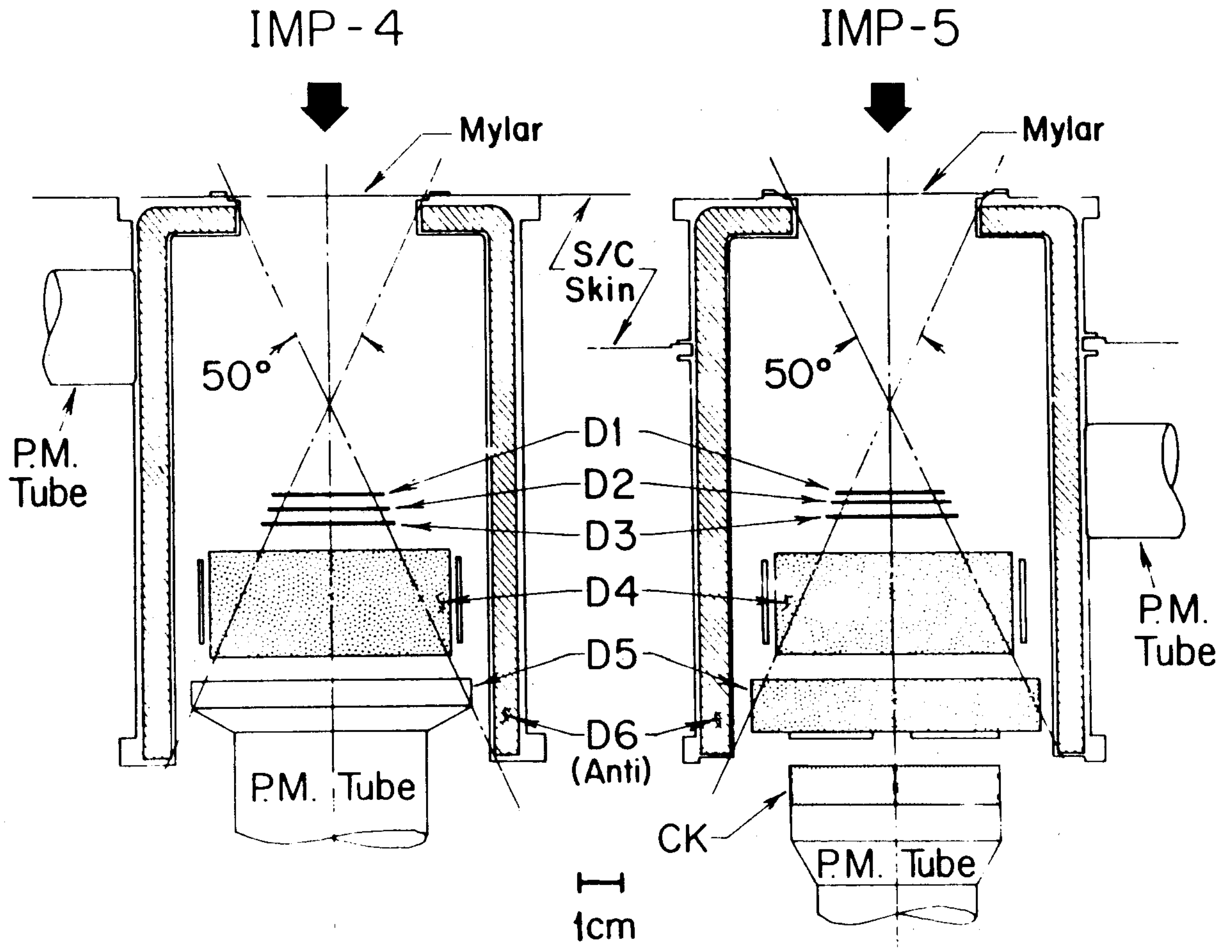

Figure 18: Diagram of the University of Chicago charged particle telescopes on-board the IMP 4 and IMP 5 spacecraft.

addition, IMP 5 incorporated a sapphire Cherenkov counter to extend the energy range over which measurements were made. Along with improvements in detector technology and telescope design, the IMP 4/5 instruments incorporated advances in electronic circuitry that permitted a wide dynamic range and excellent stability for long periods of time. Further, these instruments employed a priority system which guaranteed that virtually all $Z > 2$ particles were recorded at the expense of protons and alphas. Counting rates from various sets of detectors allow the efficiency of event selection by the priority system to be determined.

The IMP 4 experiment was able to study the magnetosphere as illustrated in Figure 19, which shows the increases in the low energy proton/electron counting rate at the time of radiation belt passes. The major objectives of the IMP 4/5 experiments were the study of the charge (and mass) composition of solar flare particles and galactic cosmic rays. Figure 20 shows the D1 vs. D2 matrix obtained for the July 30, 1970 flare (Anglin, 1975). Note that the resolution of this system is sufficient to separate the isotopes of hydrogen and helium, although few deuterium and tritium events were produced by this flare. The charge spectrum obtained by these instruments was shown in Figure 5, and all of the elements except the iron peak are completely resolved.

The basic limitation to resolution in the IMP 4/5 technology was the spread in particle pathlengths within the 50^0 opening cone of the telescopes. This pathlength variation leads to a broadening of the tracks in the matrix, and thereby limits the isotope resolution capability. Figure 21 shows the results of a Monte Carlo study of this pathlength distribution. For a flat detector, the deviation

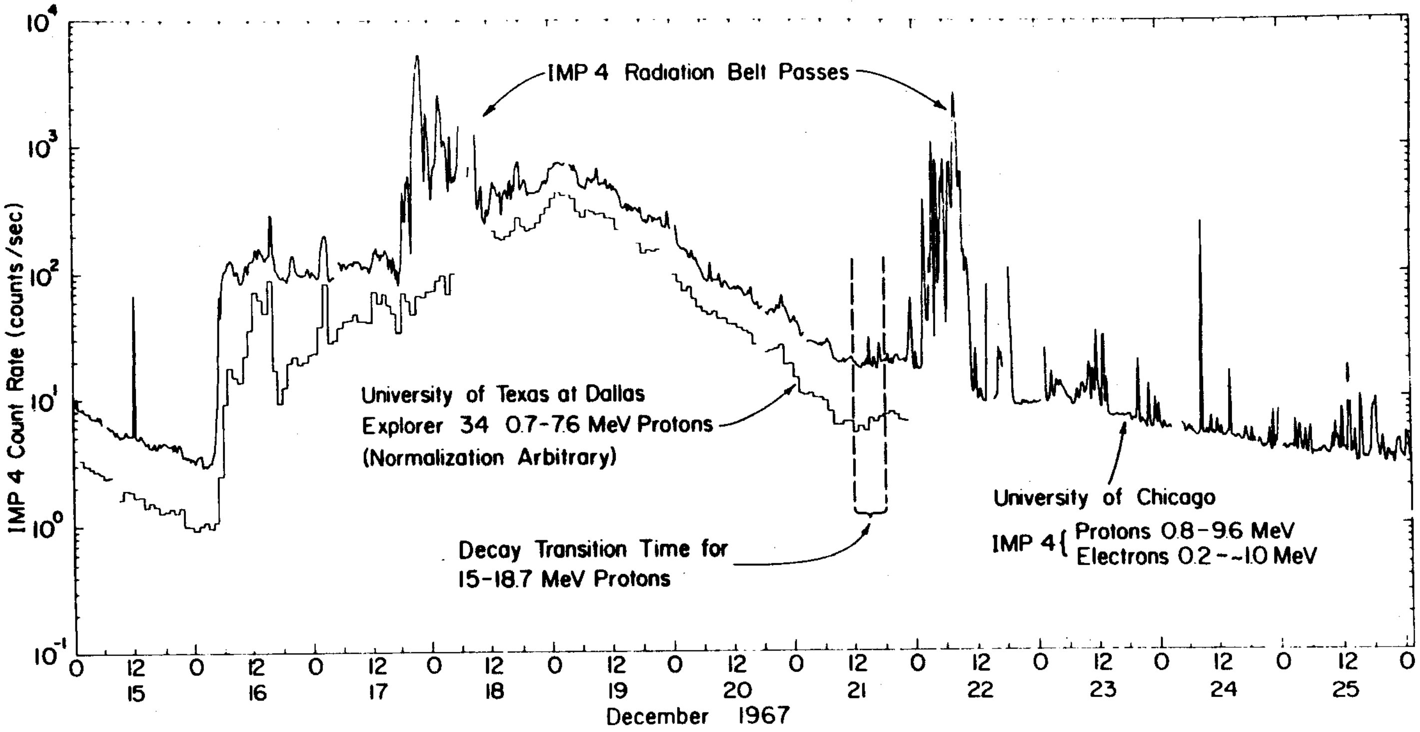

Figure 19: Time profile of the low energy proton/electron counting rate observed by the IMP 4 experiment compared to a similar rate measured by Explorer-34. Passes through the radiation belts are indicated.

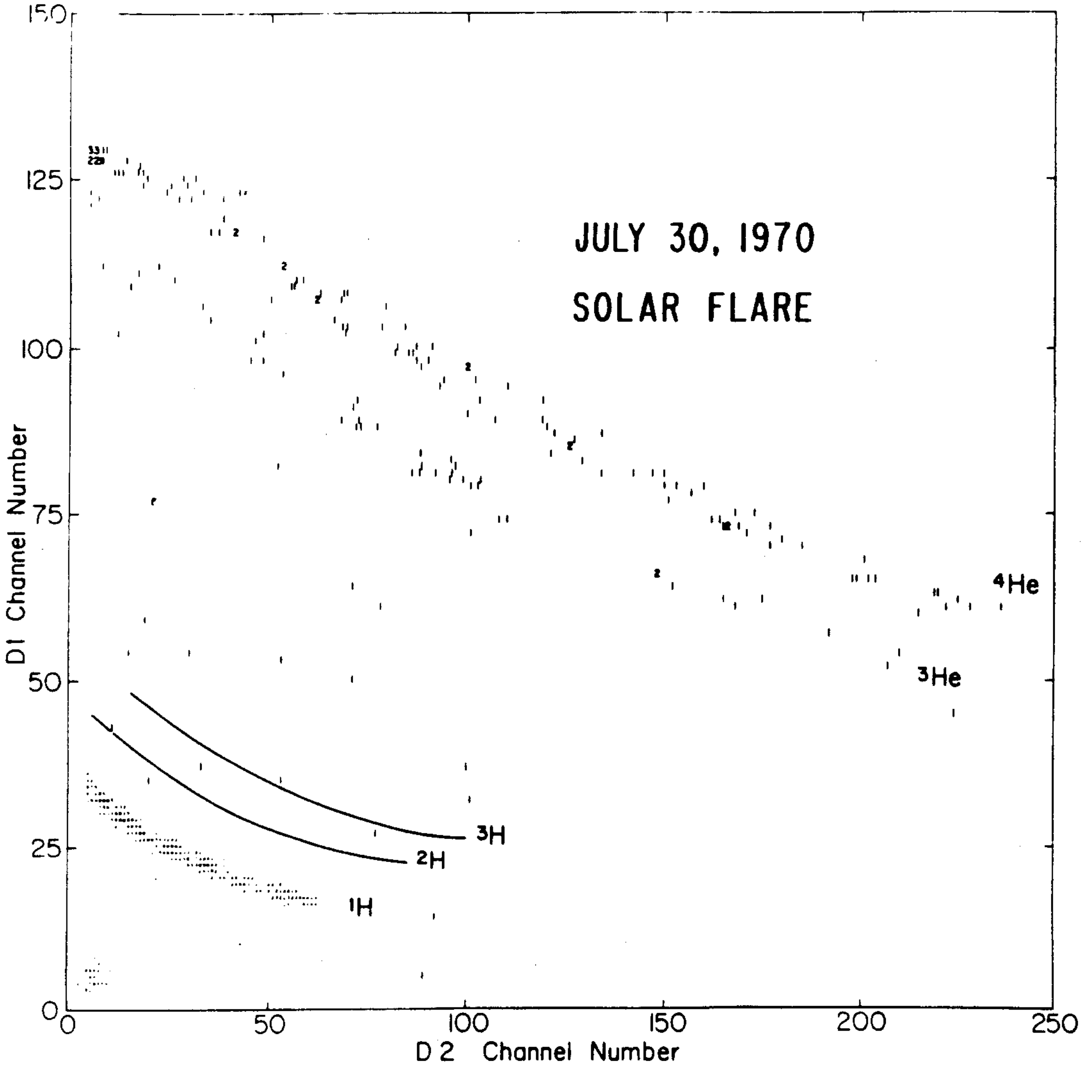

Figure 20: The D1 versus D2 pulse-height matrix for hydrogen and helium measured by the IMP 5 experiment for the July 30, 1970 solar flare, showing the separation of the isotopes of helium.

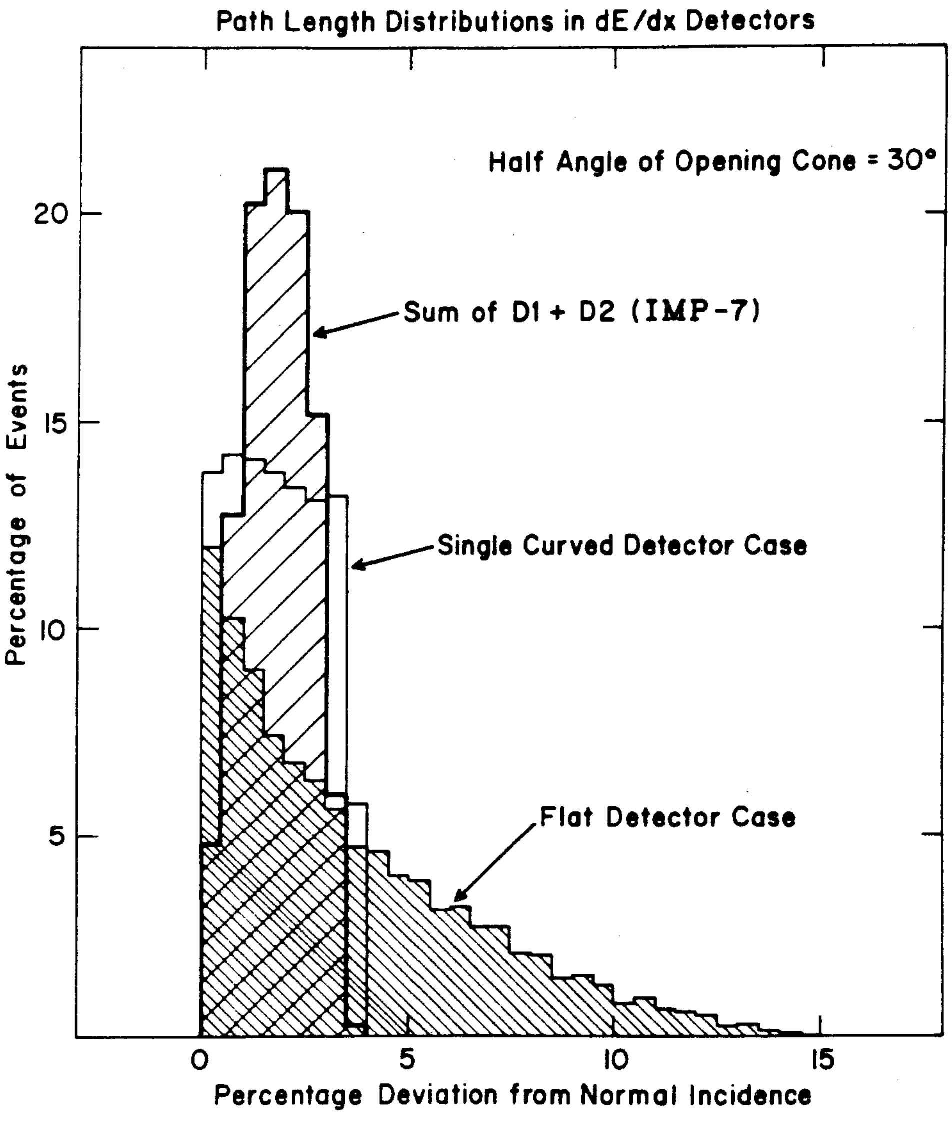

Figure 21: The results of a Monte Carlo calculation comparing the pathlength distribution obtained for flat and curved detectors exposed to an isotropic particle flux.

extends to about 15%. However, if the detectors are formed as sections of a sphere, the deviation is reduced to under 5% for a single detector and to about 4% if two curved detectors are used simultaneously. Thus, the development of a technology for constructing curved silicon detectors was the next step in improving charged particle detection techniques, and this was accomplished in the late 1960s (Perkins et al., 1969).

Curved silicon detectors were used in the cosmic ray telescopes on board the IMP 6 earth orbiting mission. The insert in Figure 22 shows the telescope and the remainder of the figure presents an example of the instrumental resolution for the isotopes of hydrogen, where the deuterium and tritium peaks are seen to be clearly resolved from the tail of the proton distribution (Anglin et al., 1973). The IMP 6 spacecraft also carried an "on-board computer" (OBC) which could control the data acquisition and telemetry. In certain program modes, for example, the OBC would discriminate against proton events and only allow $Z \geq 2$ particles to be recorded. Furthermore, the computer could be programmed from the ground in order to be able to respond to any change in instrumental characteristics or mission objectives.

An almost identical telescope was carried on the Pioneer 10 and 11 missions to the outer solar system. Figure 23 is an engineering sketch of the telescope configuration, and Figure 24 shows the instruments mounted on the Pioneer spacecraft. The experimental package was extremely small and light-weight, characteristic of all experiments on spacecraft to the outer solar system. Nevertheless, the Pioneer missions have been extremely productive in the study of Jupiter and its environs, for investigations of solar modulation and solar particle propagation,

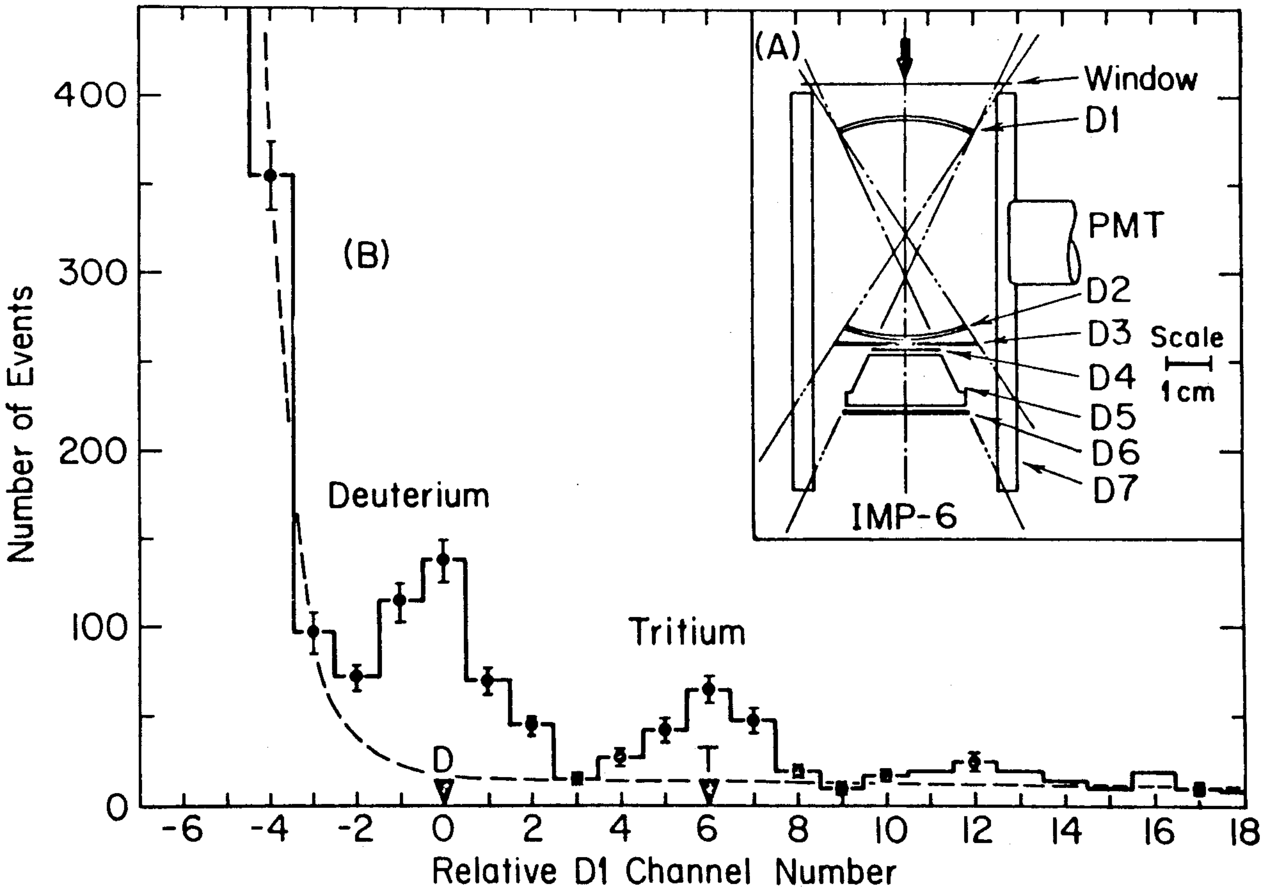

Figure 22: Part (a): diagram of the IMP 6 particle telescope employing curved silicon detectors.
Part (b): results of the IMP 6 analysis of the isotopes of hydrogen showing separation of the deuterium and tritium peaks from the tail of the proton distribution.

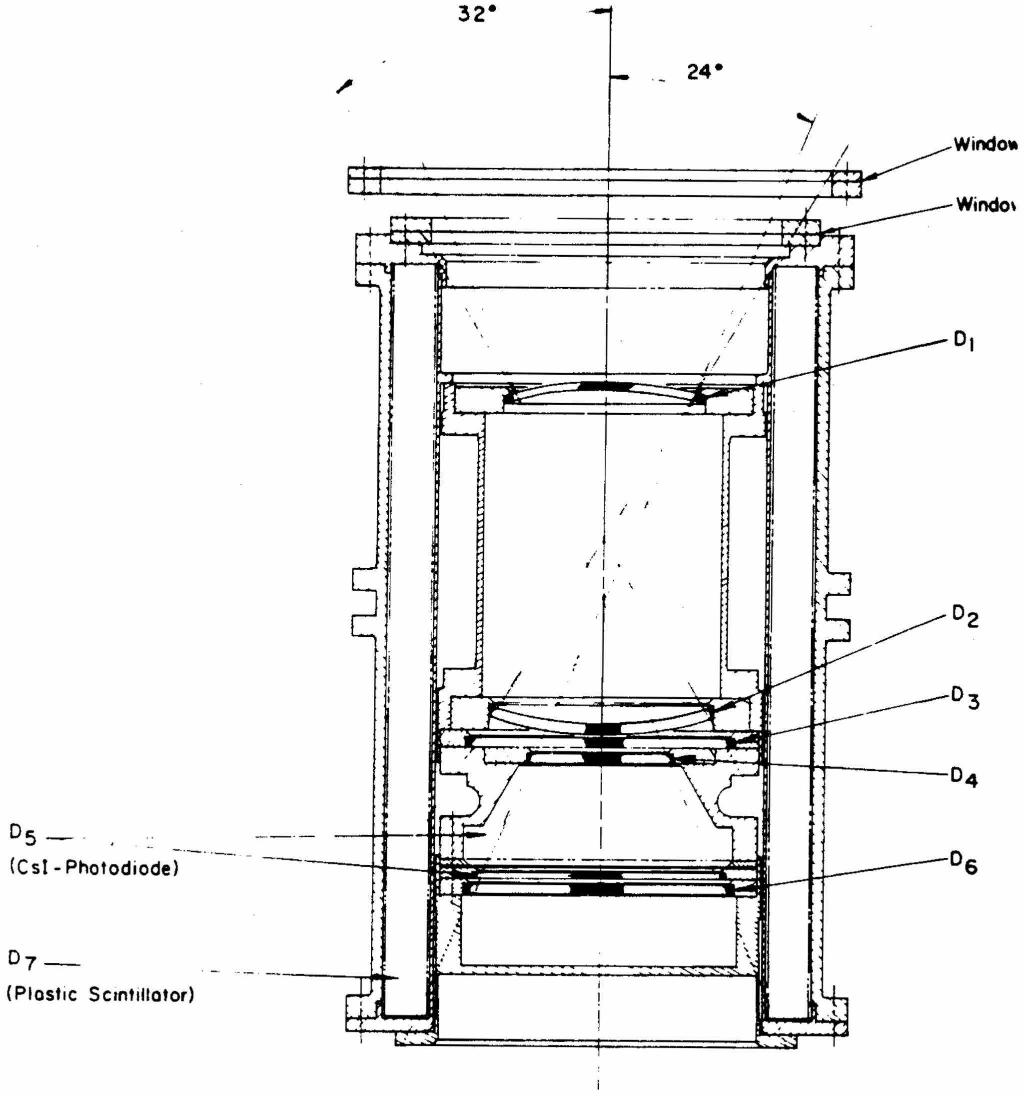

Pioneer F/G Main System Telescope
The University of Chicago

Figure 23: Mechanical assembly drawing for the University of Chicago Pioneer 10/11 (F/G) charged particle telescope.

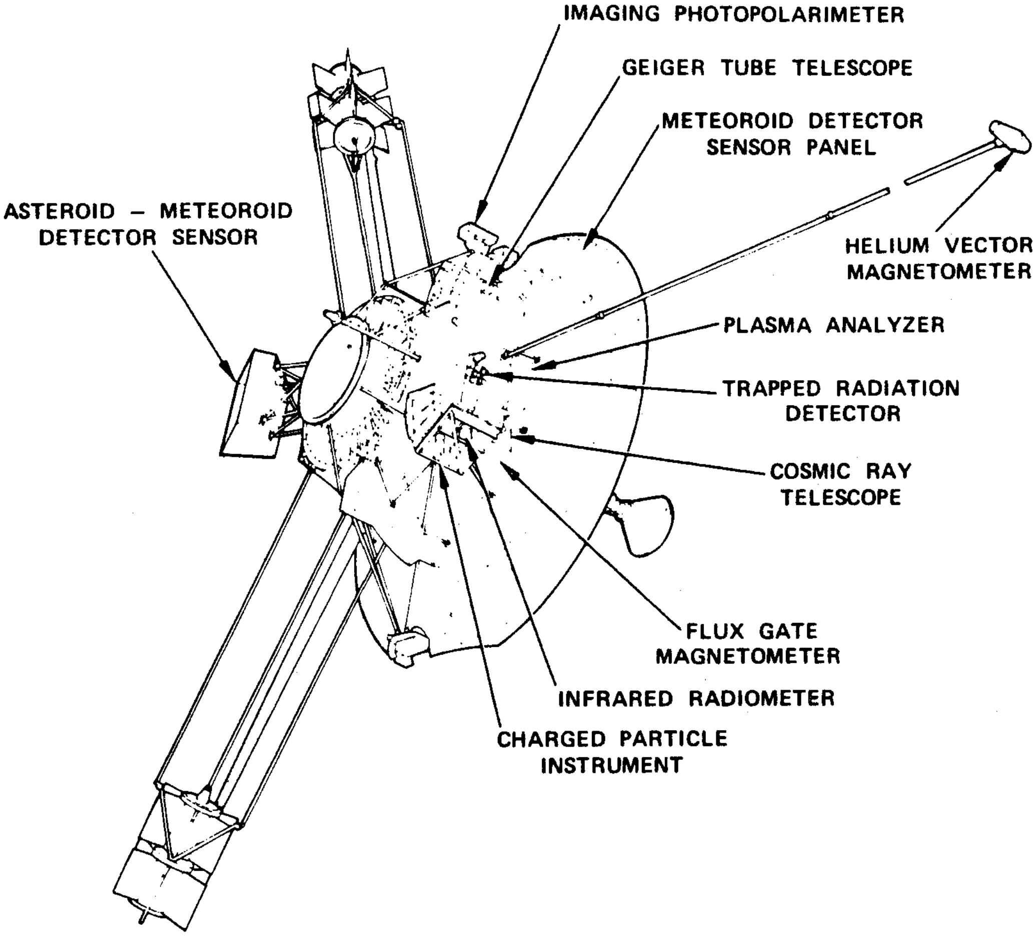

Figure 24: Diagram of the Pioneer 10/11 spacecraft indicating the location and size of the charged particle instruments.

and for the study of interplanetary processes (see the summary in Science 188, 445, 1975).

Charged particle telescope systems were further improved by the development of larger area curved silicon detectors which were employed on the IMP 7 and IMP 8 missions, launched respectively in 1972 and 1973, which are still providing high quality data. The IMP 7/8 telescope design is shown in Figure 25 and consists of two curved detectors preceding a CsI (Tl) residual energy scintillator, D4, viewed by photodiodes. In addition, a sapphire Cherenkov counter is used to provide anti-coincidence protection for D4 and to extend the energy range over which measurements are made. Furthermore, significant improvements in electronic logic were incorporated into the design such that each particle is characterized by an ID flag determined by a complex logic involving discriminators associated with each detector. The logic also assigns a priority to each particle and determines which three of the four detectors indicated by an asterisk on the figure will be pulse height analyzed and recorded. These IMP systems have performed quite well and yielded a wealth of data which is currently being analyzed.

An example of the data returned by the IMP 7/8 instruments is shown in Figure 26 where the left hand portion is the raw data matrix and the right side shows, for comparison, the location of various isotopes. The "knees" in the curves represent an amplifier gain switching point. The amplifiers each have three separate gain regions in order to achieve sufficient dynamic range to study all elements between hydrogen and nickel. With some imagination, separate tracks can be observed for the Be, B, and N isotopes, and over a limited range the

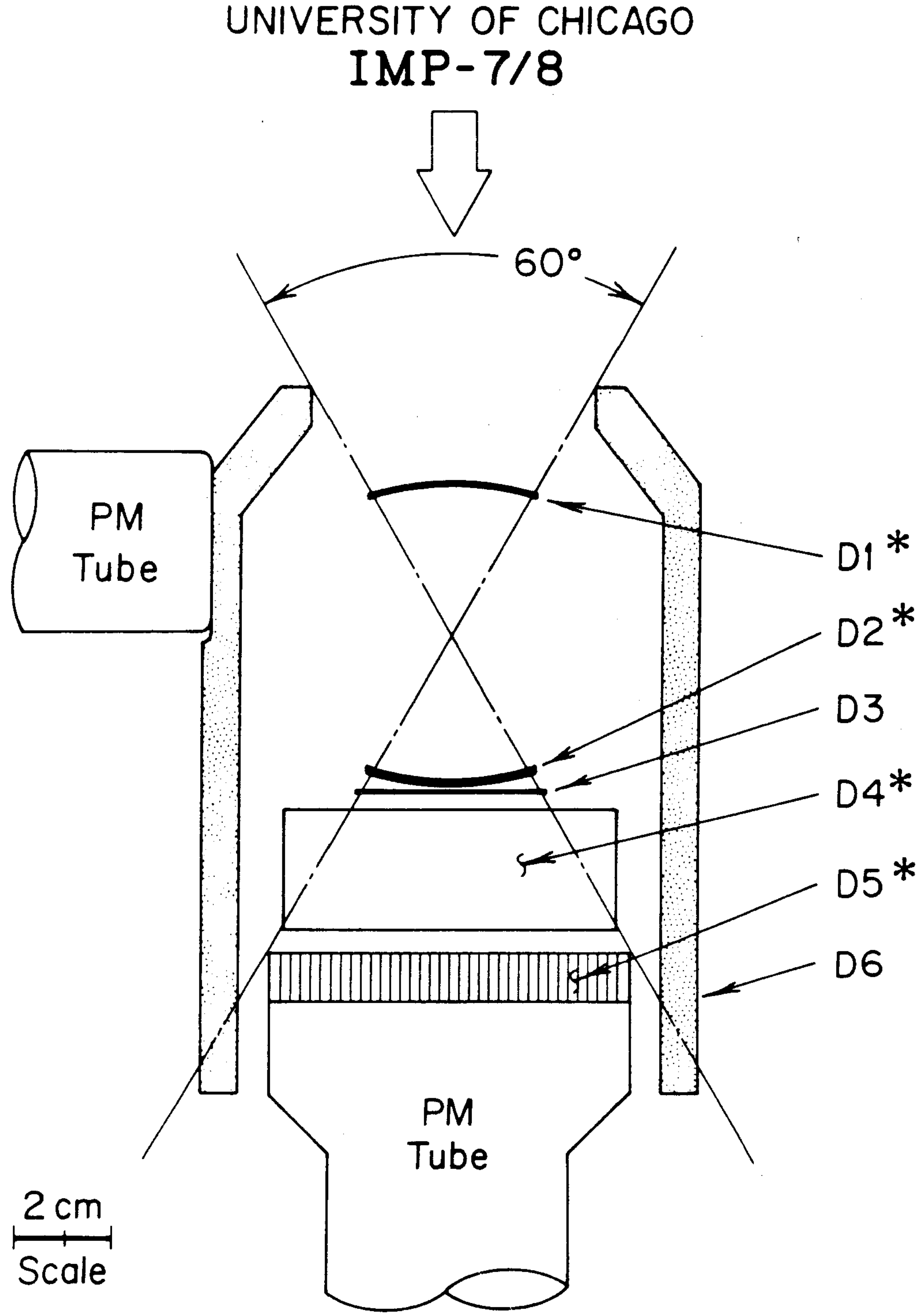

Figure 25: Diagram of the IMP 7/8 telescope system from the University of Chicago. The asterisks indicate detectors which are pulse-height analyzed.

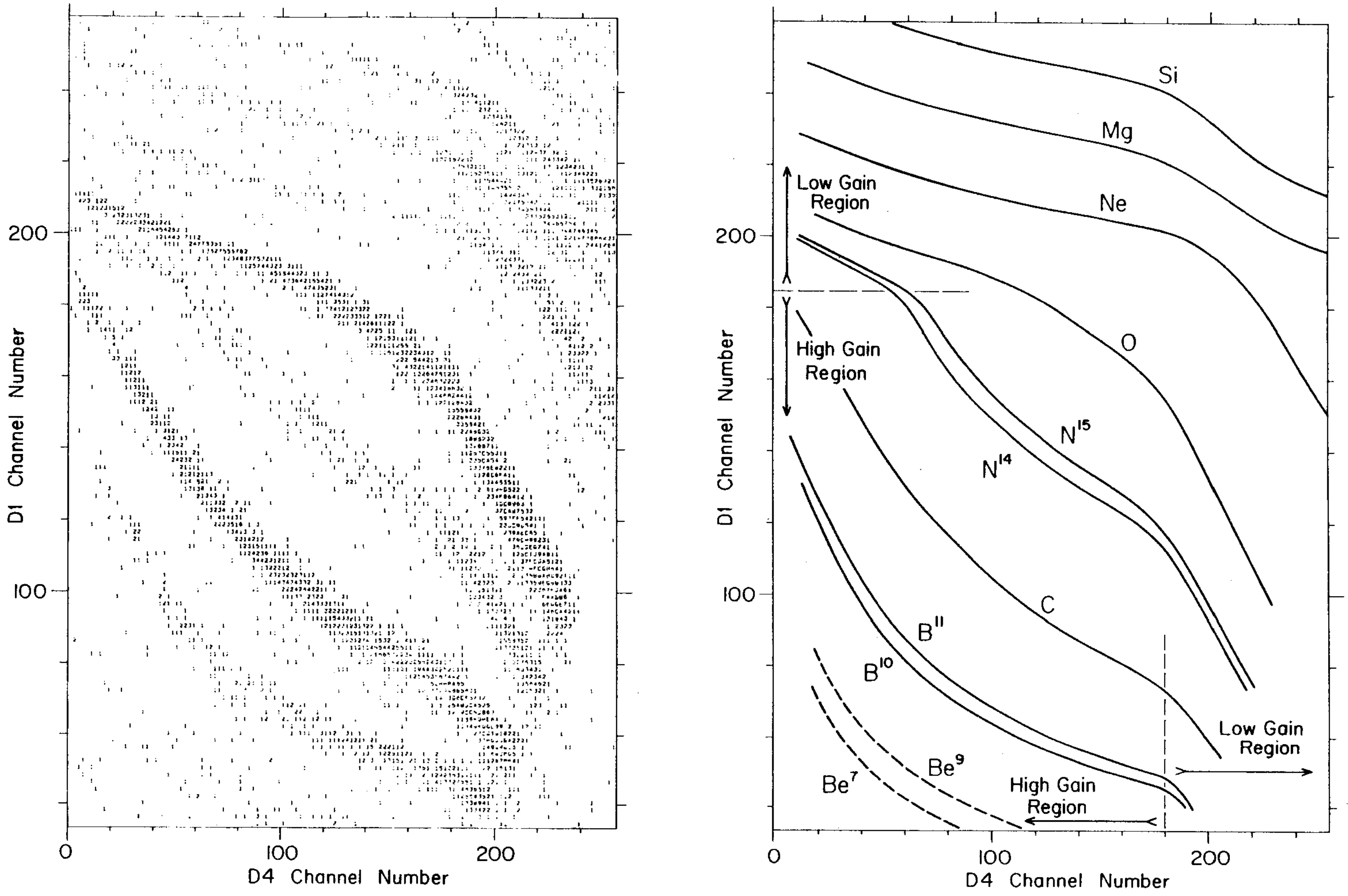

Figure 26: Raw data returned by the IMP 7 experiment (left) compared to the expected positions of the tracks for various isotopes and elements.

isotopic composition of neon can also be measured (Garcia-Munoz _et al._, 1978). With the IMP 7/8 system, the isotopic composition of the light elements, Li, Be, B, has been studied (Garcia-Munoz _et al._, 1975_b_) and in particular, the important radioactive isotope Be^{10} has been isolated to yield a measurement of the cosmic ray "age" as illustrated in Figure 27 (Garcia-Munoz _et al._, 1977_a_). This investigation was aided by calibrations of an identical, back-up telescope at the LBL Bevatron using separated beams of the Be isotopes, as shown on the lower portion of Figure 27. This calibration demonstrated that the instrument possesses the resolution necessary to separate Be^9 and Be^{10} and adds confidence to the measurement of an extremely small concentration of Be^{10} in the flight data--yielding a "long" cosmic ray lifetime in the galaxy.

The large dynamic range of the IMP 7/8 instruments has provided high quality data ranging from the hydrogen and helium isotopes, as illustrated on Figure 28 for the 1974 solar quiet period (Garcia-Munoz _et al._, 1975_a_), to individual charge resolution for the iron peak elements (Garcia-Munoz _et al._, 1977_b_). In addition, the Cherenkov counter analysis has made it possible to measure the differential energy spectra of many of the heavy elements. Some of these spectra, covering the range from tens of the MeV/nucleon to about 1 GeV/nucleon, are shown in Figure 29 for the time period 1974 to 1976 (Garcia-Munoz _et al._, 1977_c_). In summary, the IMP 7/8 experiments have been and continue to be one of the most successful and scientifically productive satellite experiments of the past decade.

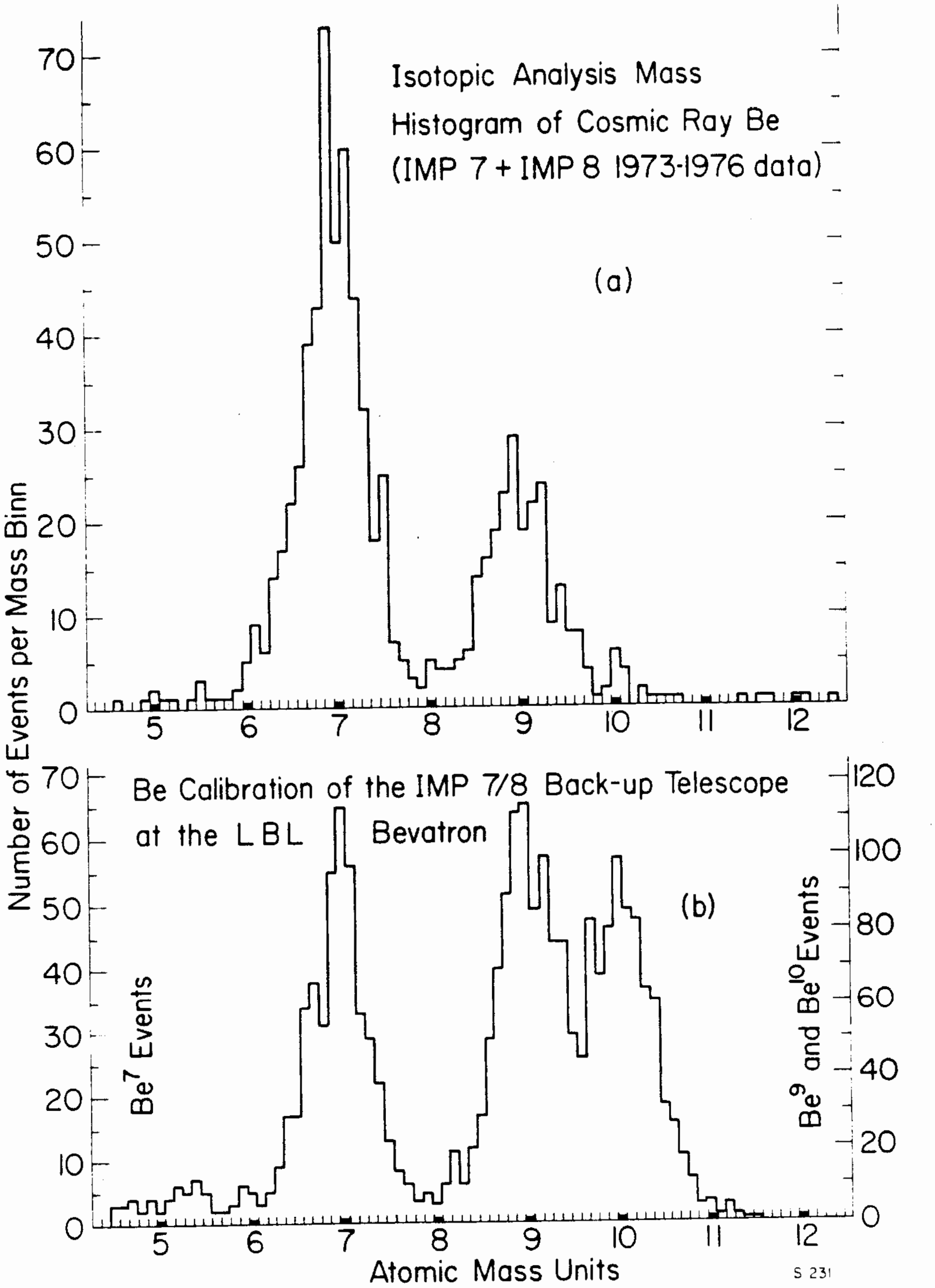

Figure 27: Part (a): isotopic distributions for Be cosmic rays recorded by the IMP 7/8 experiments.
Part (b): isotopic distributions for Be heavy ions from the LBL Bevatron recorded in the IMP back-up telescope.

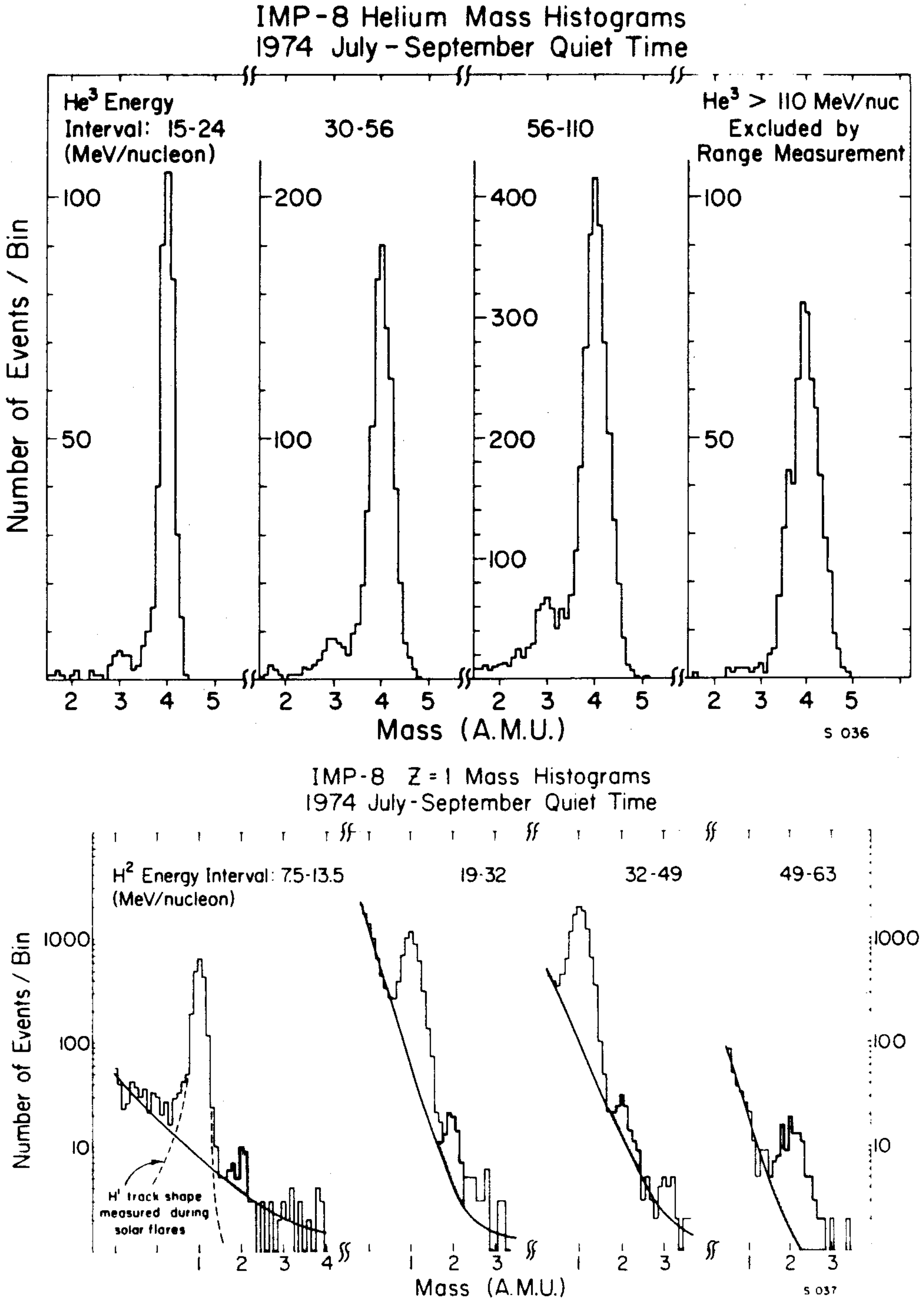

Figure 28: Mass histograms for hydrogen and helium in various energy intervals measured by the IMP 8 experiment for solar quiet periods.

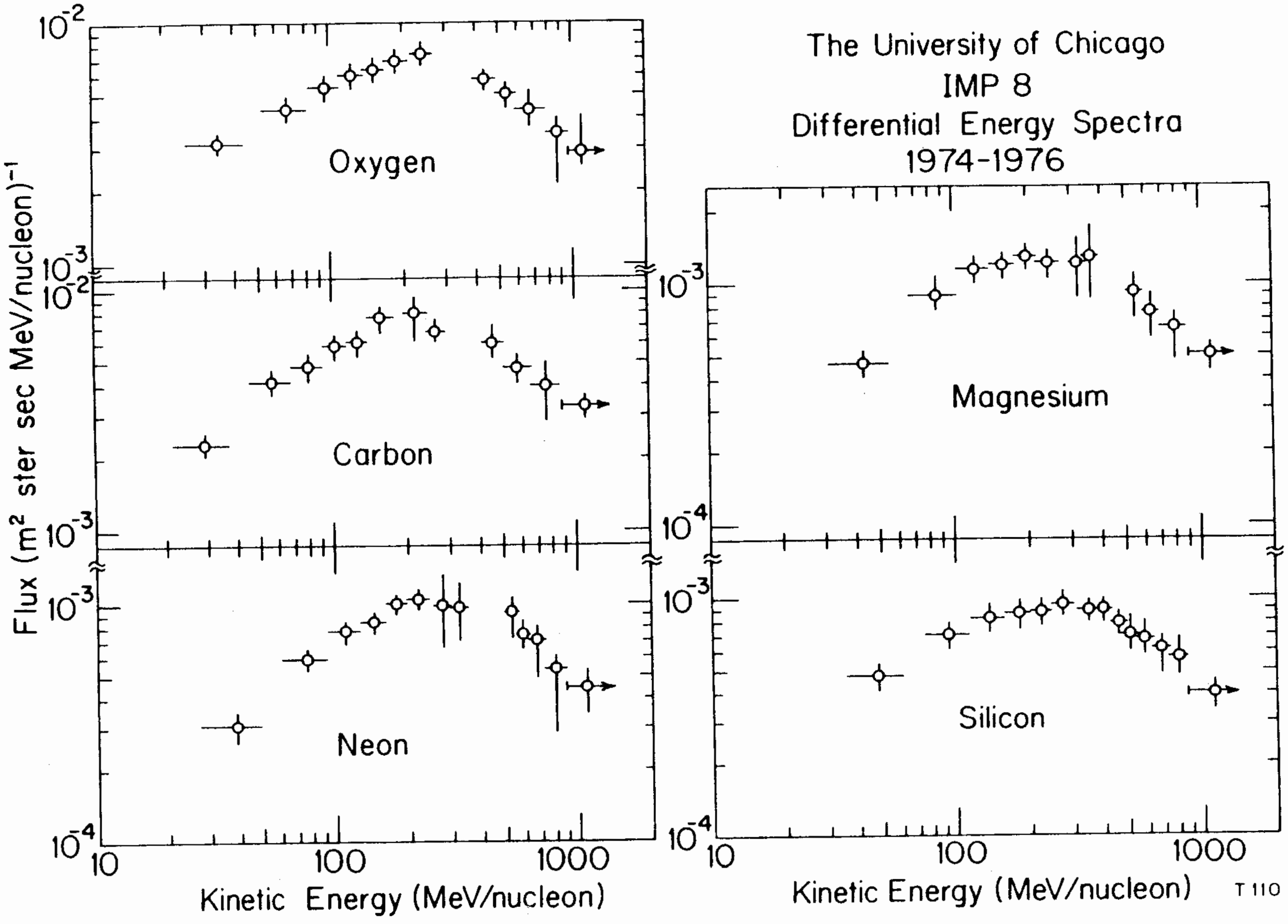

Figure 29: Differential energy spectra of heavy particles measured by the IMP 8 telescope over the period 1974 to 1976.

Nevertheless, the IMP instruments have their limitations. Mass resolution above silicon is virtually impossible due to the residual pathlength variations, even in curved detectors, together with small shifts in the detector electronics. The IMP experiments are also telemetry limited in terms of the number of measurements that can be made on a single event, and the small size of the telescopes requires long collection times to obtain statistically significant samples of many of the less abundant species. The IMP 7/8 technology is incapable of solving one of the major questions in cosmic ray research--the isotopic composition of iron nuclei--and further advances in detector and electronic technology are needed.

The new concept that has evolved for charged particle telescopes is the use of position-sensitive detectors (PSD). In this scheme, the trajectory of the particle through the telescope is measured directly which results in a minimum of pathlength uncertainty and provides the exact position of the incident particle on the face of each detector. This latter point permits any nonuniformities in the detectors to be compensated during the data analysis. There are many techniques for determining the position of incidence of a charged particle, which have been developed and used principally in accelerator experiments (strip scintillators, etched plastics and nuclear emulsions, wire proportional or ionization chambers, spark chambers, drift chambers), but not all of these are easily adaptable for use in space.

Figure 30 shows a sketch of a silicon position sensing detector that has been developed at the University of Chicago (Lamport *et al.*, 1976). The electrical contact on one surface of the silicon wafer

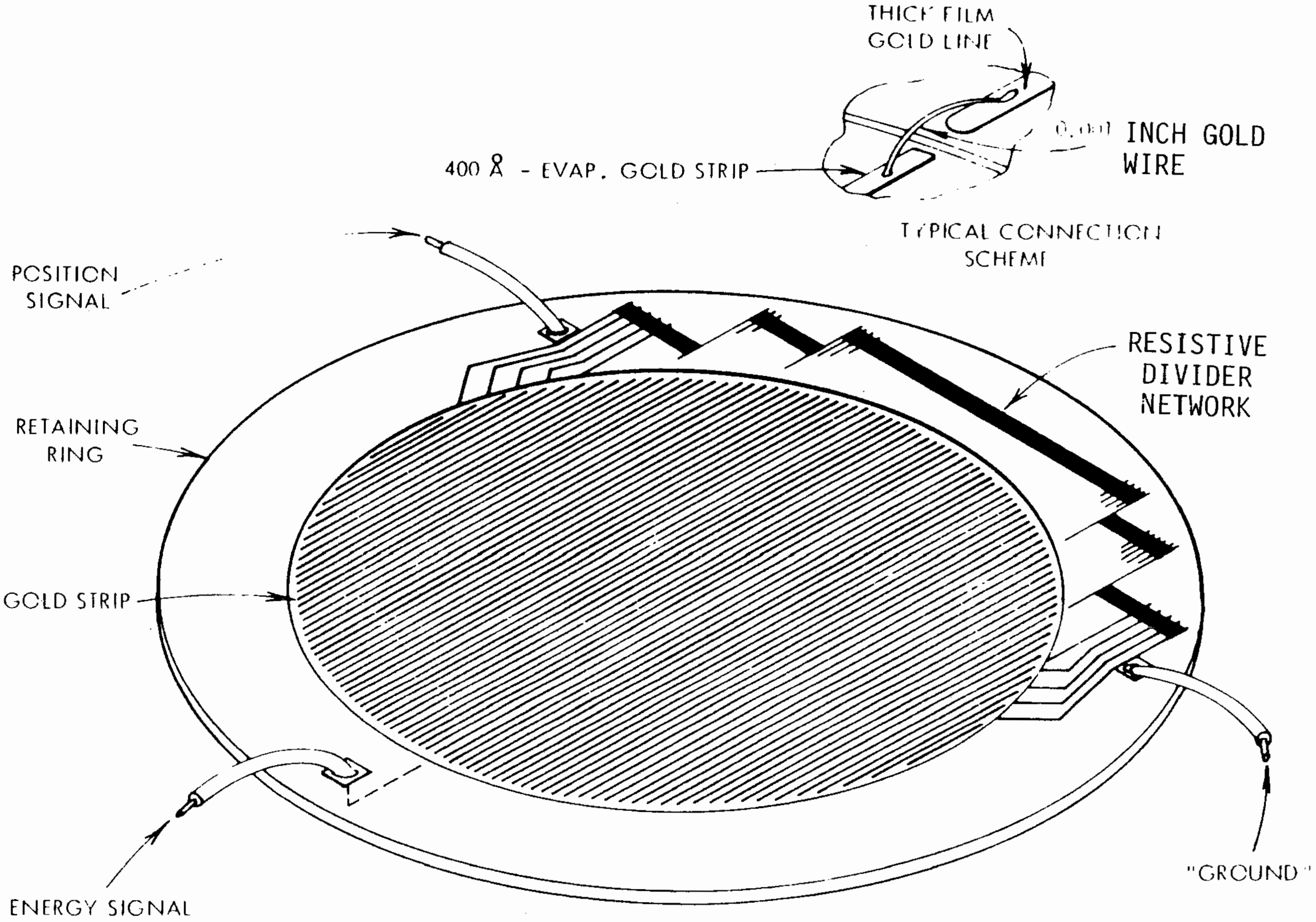

Figure 30: Schematic representation of a one-dimensional position sensitive silicon detector. Note the resistive divider network for read-out.

is divided into many separate gold strips. The two strips nearest the trajectory of the charged particle collect the signal which is then read out through a resistive divider network. The opposite side of the detector is a single contact which provides a signal proportional to the total charge liberated in the detector. Thus, the ratio of the "position" signal through the resistive divider to the total charge collected gives the position of incidence of the particle, in one dimension, on the face of the detector. Two of these PSDs oriented at right angles to one another provide a measurement of both the X and Y coordinate of the point of incidence on the detector surface. One of the attractive features of this technique is its simplicity in that only two signals are recorded from each detector, and only two sets of amplifiers and other electronic circuitry are needed. In addition, the detectors are fully qualified for space flight.

A high energy telescope incorporating these PSDs is shown in Figure 31. Note that two separate planes of PSDs, each consisting of three separate detectors for redundancy, are included, and this system measures the angle of incidence of a charged particle with a precision of $\lesssim 1^{\circ}$. The PSDs are followed by a stack of thick (0.5 cm) lithium drifted silicon detectors which represent a new generation of detectors. Each of the detectors D1-D6 and K1-K8 are pulse-height analyzed with 12 bit ADCs, and this information along with all discriminator flag bits and detector counting rates is recorded, giving over 300 bits of information per particle. This bit rate represents a giant step over systems such as the IMP 7/8 experiments, but this type of detail is needed for measurements at the subpercent level

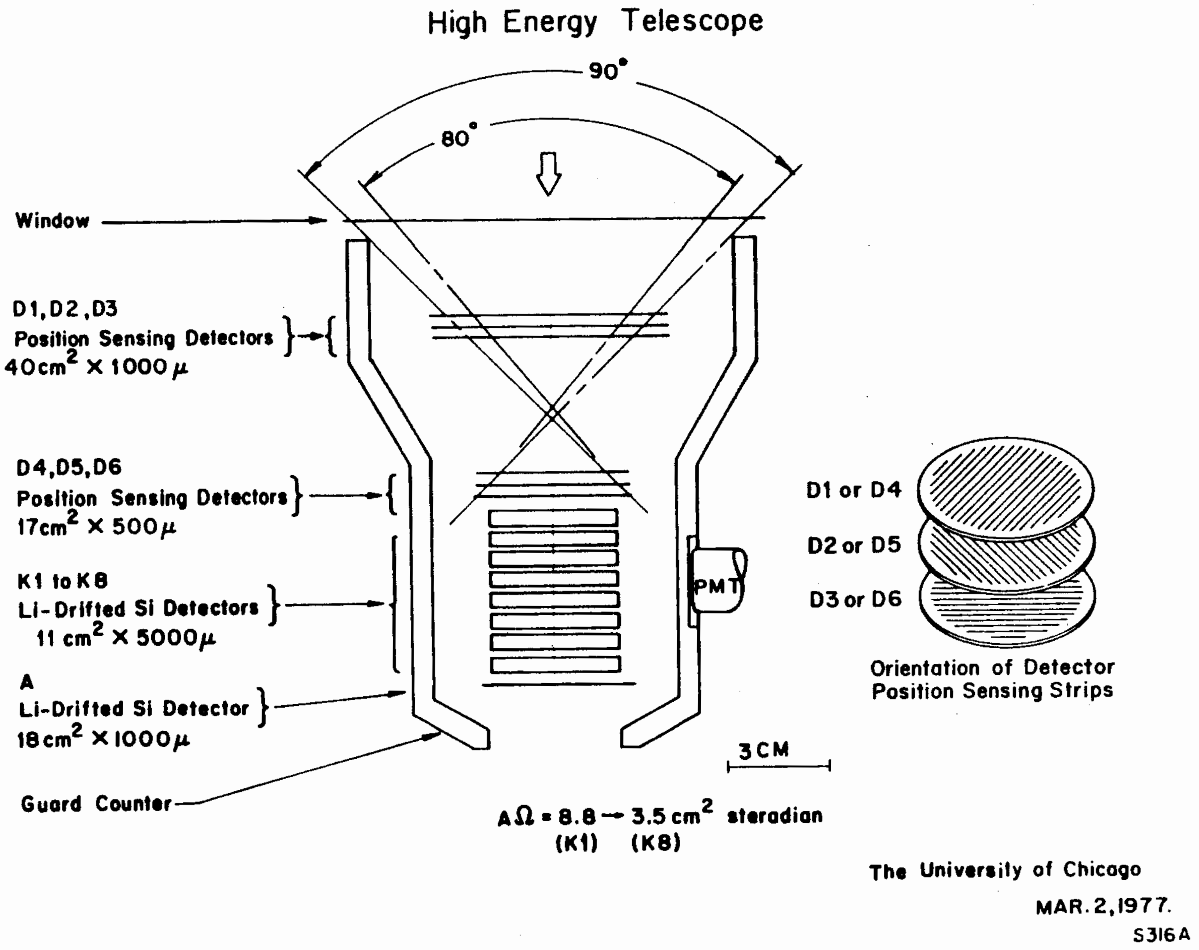

Figure 31: Diagram of the University of Chicago high energy telescope employing six one-dimensional PSDs.

of accuracy required for separation of the iron isotopes.

The development of a telescope system such as that shown in Figure 31 would have been almost impossible without the availability of high energy, heavy ion (HZE) beams at the Bevalac. The HZE beams have permitted telescopes to be designed, tested, modified, and retested to ensure, before launch, that all components function as designed and that the total system resolution is sufficient for a successful experiment. During this process, several unexpected effects in both the detectors and the electronics have been discovered and corrected. Without the calibrations at the Bevalac, these effects would have been discovered after launch when corrective action is impossible. Figure 32 shows a summary of the mass resolution achieved by the high energy telescope of Figure 31, compared to a theoretical prediction of the expected resolution. Points are shown for nitrogen, magnesium, argon, and iron beams. Figure 33 shows the mass histogram obtained with the Fe^{56} beam in the first two of the thick detectors in the stack. Data are presented for only a single angle, but the trajectory measuring system of the telescope is employed to determine the incidence angle used in the analysis. Figure 34 shows a plot of the mass resolution observed in the same detector pair for various angles of incidence of the Fe^{56} ions. The resolution is approximately constant for both positive and negative angles indicating that the PSD performance is not the limiting factor in the resolution. The measured isotopic resolution, in this preliminary data, is sufficient to study the relative abundances of the iron isotopes in the galactic cosmic radiation.

Detector systems similar to this high energy telescope have been

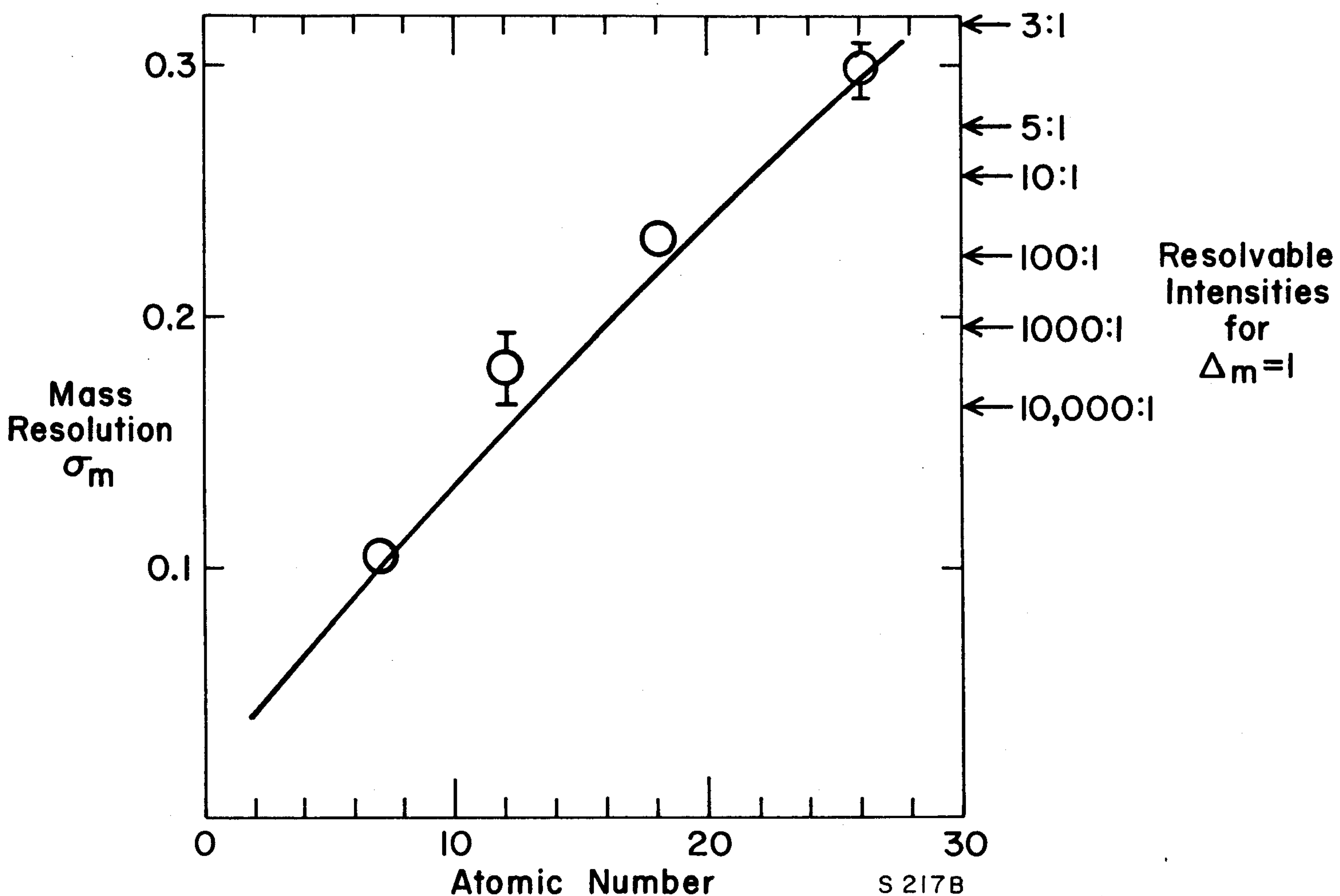

NOV. 1977.

Figure 32: Preliminary mass resolution measured for heavy ion beams of nitrogen, magnesium, argon, and iron in the University of Chicago high energy telescope.

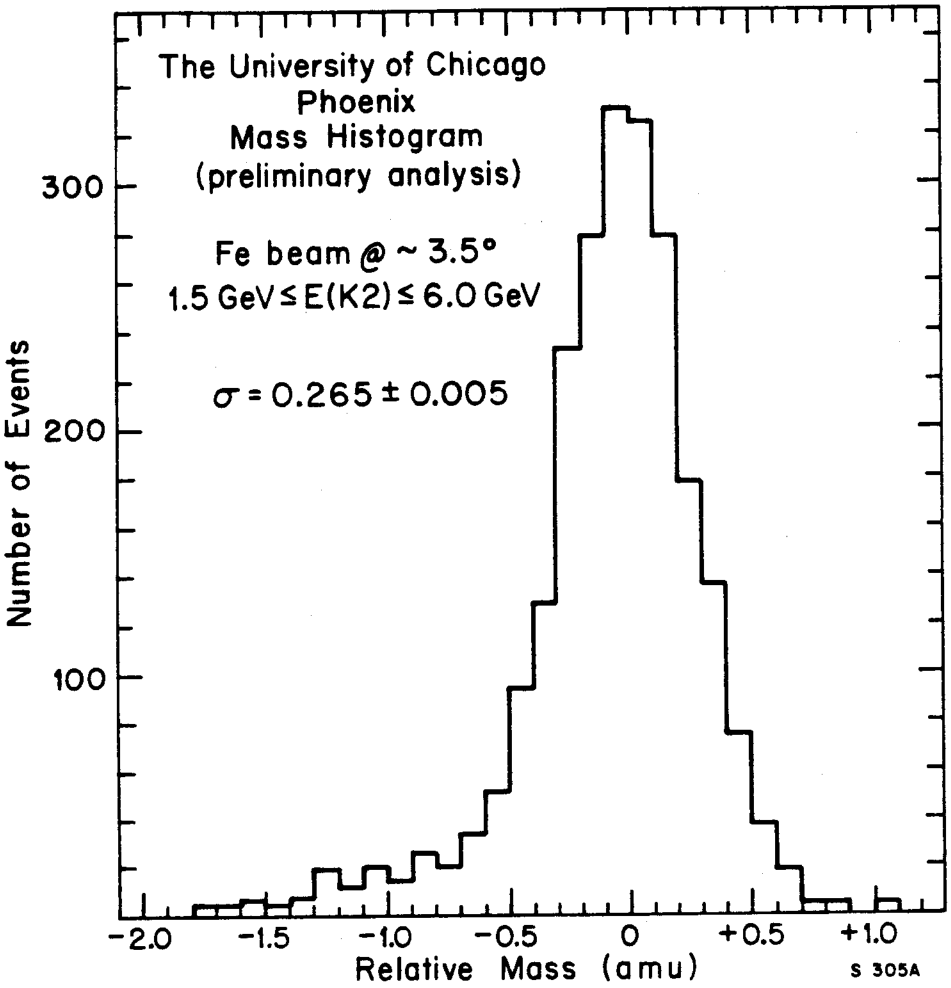

Figure 33: Fe^{56} mass histogram from an analysis of events stopping in detector K2 of the high energy telescope.

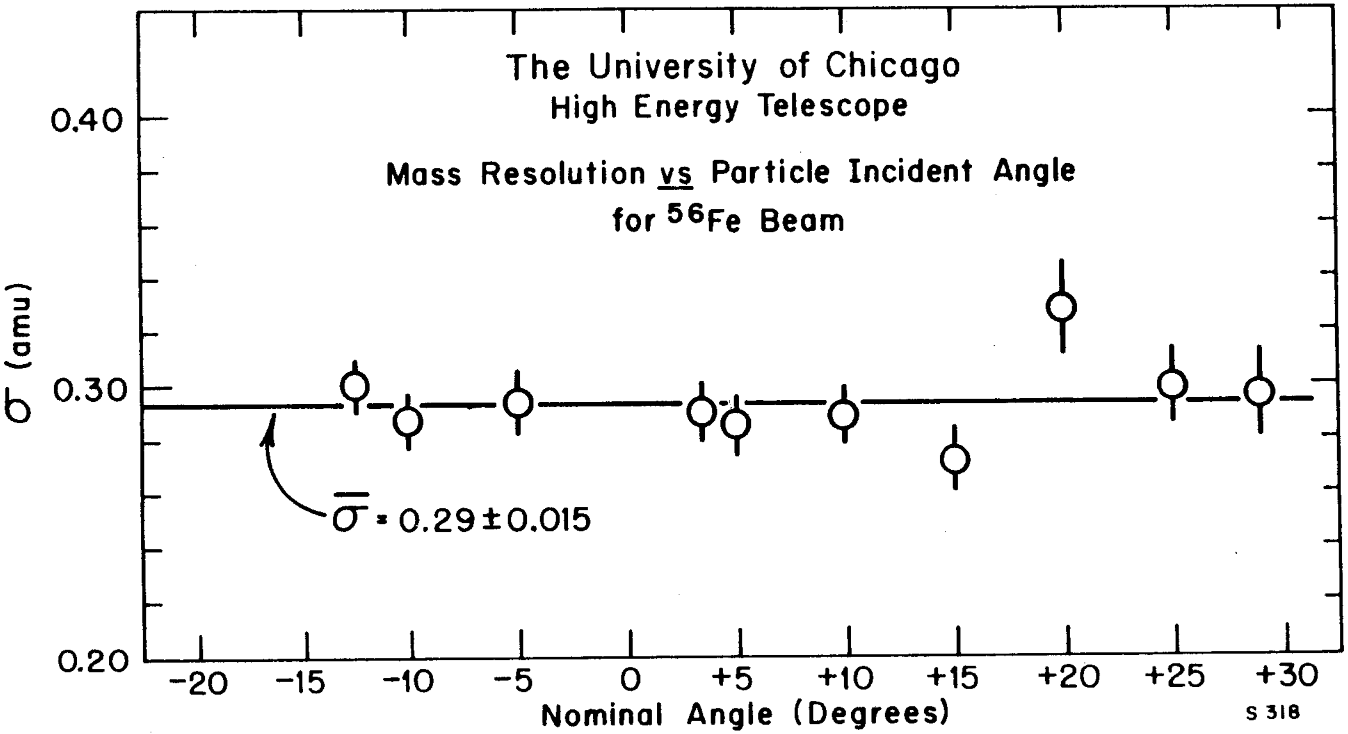

Figure 34: The high energy telescope mass resolution as a function of the angle between the telescope axis and Fe^{56} beam direction. All events stopping in detector K2 are included in the analysis.

developed by LBL and Cal Tech. The LBL technique uses drift chambers for position determination, followed by a stack of ten thick silicon detectors. The Cal Tech experiment, at somewhat lower energies, employs strip silicon detectors in which each strip is connected to its own amplifier/discriminator system. Two planes of these matrix detectors are followed by silicon detectors of graded thicknesses to record the dE/dx and residual energy. Both of these systems have been calibrated with HZE beams and display excellent resolution. The LBL and Cal Tech experiments were successfully launched, recently, on the ISEE-C satellite, and they will be returning data over the next several years.

A major limitation to the telescope system of Figure 31 is its high energy threshold. This is due to the requirement that particles penetrate to detector K1, a range of ~ 4.5 mm of silicon, for isotopic analysis. Solar flare particles are concentrated at lower energies, making this telescope inappropriate for solar flare studies. Thus, in order to retain the concept of trajectory measurements, it is necessary to develop a PSD containing significantly less material.

A PSD development effort has been underway for the last several years at the University of Chicago. From this, the low energy telescope system shown in Figure 35 has evolved. The PSDs are 50 micron wafers of silicon containing a set of strips to measure the X position on the top surface and another set of strips, rotated 90^o, on the bottom surface to record the Y position. Each set of strips is read out through a resistive divider network. Two of these detectors, arranged as shown, provide excellent trajectory information with only 0.1 mm of material in the particle's path, which permits measurements down

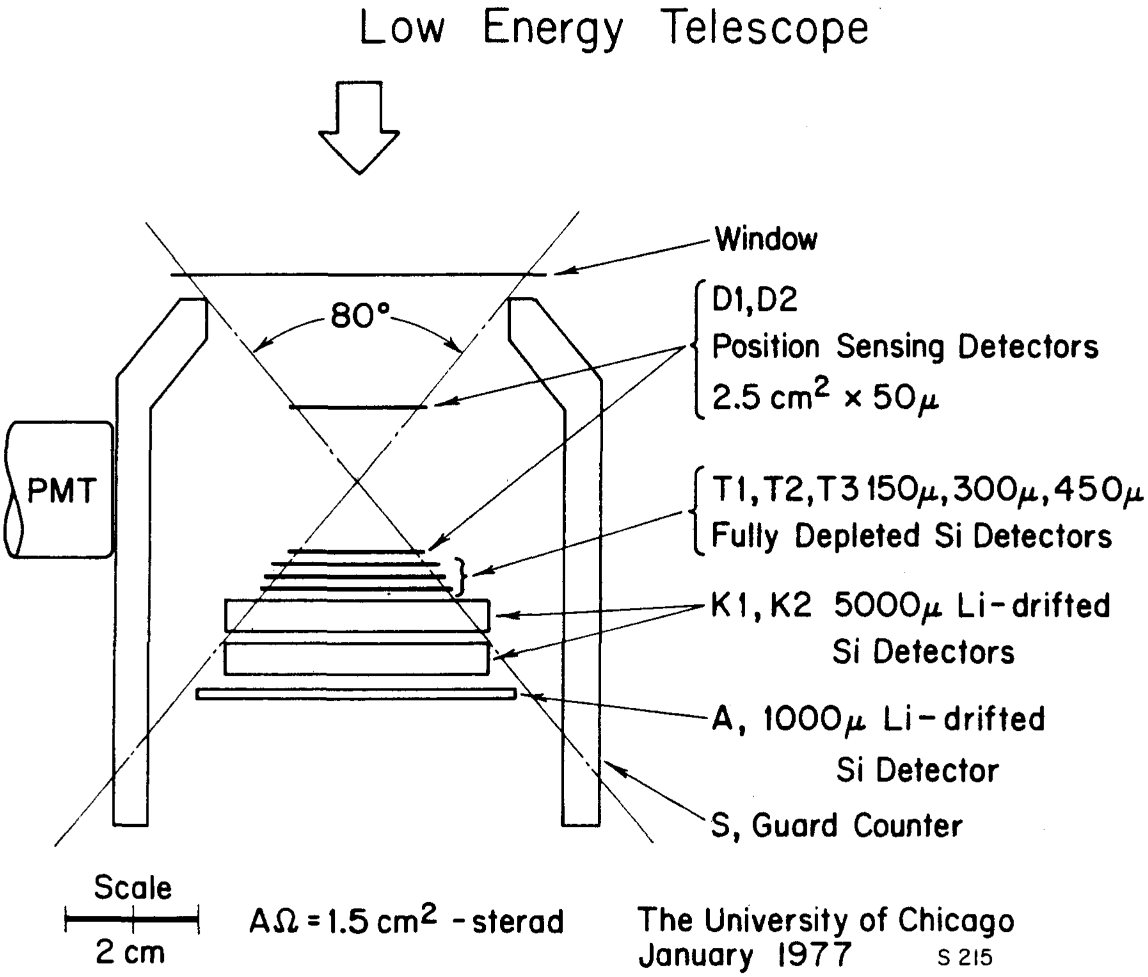

Figure 35: Diagram of the University of Chicago low energy telescope employing two-dimensional PSDs.

to MeV energies. Following the PSDs are a set of three totally depleted silicon detectors of graded thickness, and two 5-mm thick lithium-drifted silicon detectors. This stack provides multiple dE/dx measurements for stopping particles over a total energy interval which overlaps the energy range of the high energy telescope shown in Figure 31. The low energy telescope system has been calibrated at the Bevalac and exhibits resolution comparable to that obtained with the high energy instrument. The high and low energy telescopes, along with a monitor telescope similar to that shown in Figure 13, are combined into a single instrument package, whose electronic block diagram is shown in Figure 36, for launch into a polar orbit in the near future. This instrument array will study galactic cosmic rays, solar flare particles, and low energy radiation penetrating or trapped in the magnetosphere.

The high and low energy telescope systems represent the current state of the art in charged particle telescope systems, and future advances will depend upon the performance of these systems in space. The high and low energy telescopes, along with the experiments of other groups, will begin the painstaking task of mapping, with high resolution, the characteristics of the charged particle radiation in space. However, this is only part of the job that must be done. Figure 37 shows a schematic representation of the heliosphere with the region that has been and will be explored by these experiments indicated. Note that most of the heliosphere remains unexplored, and it is to be expected that the charged particle populations studied to date in the ecliptic plane will not be the same elsewhere in the heliosphere. In particular, it is possible that in the north and

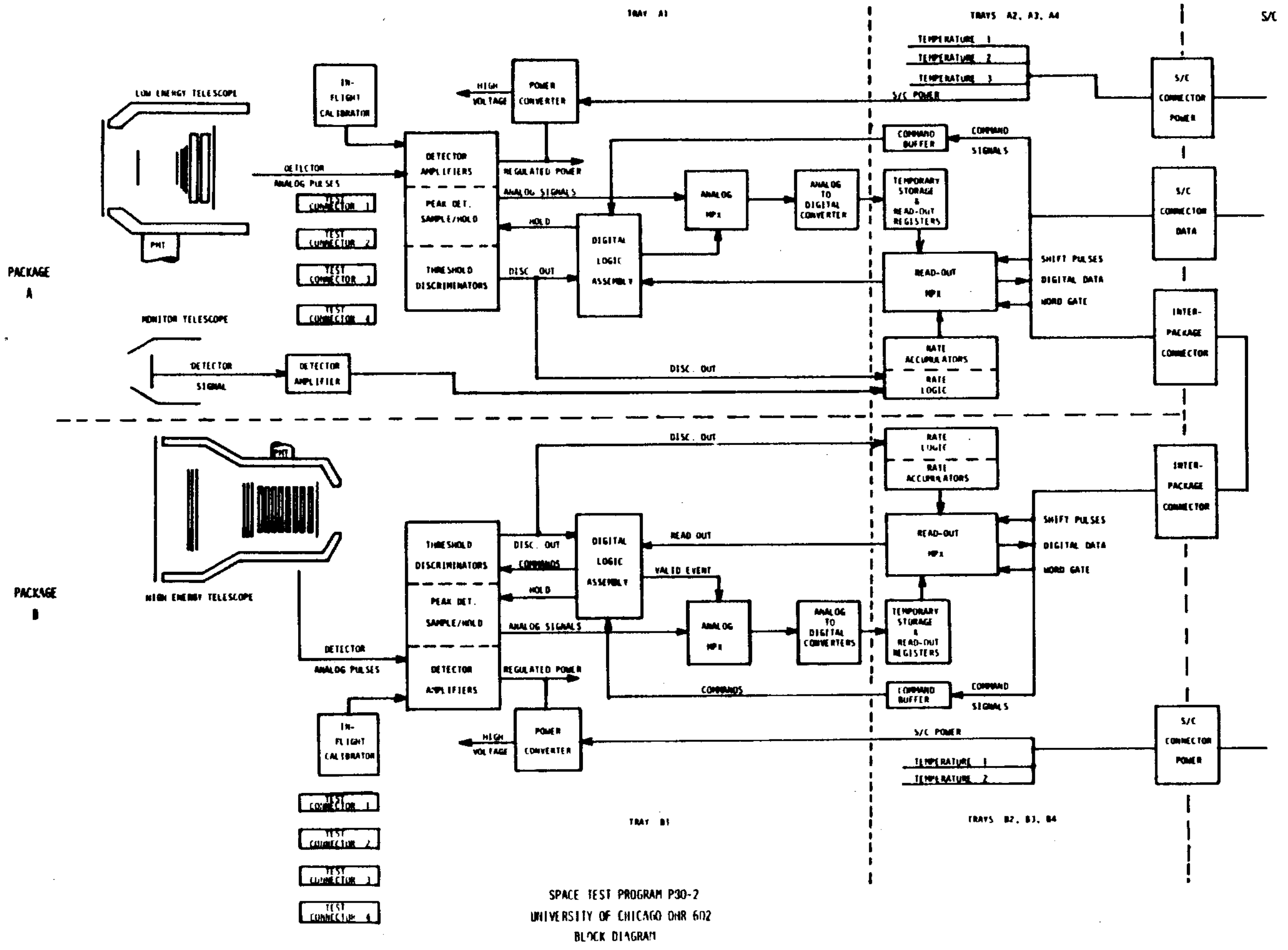

Figure 36: Electronic block diagram for the combined instrument package including a high energy telescope, a low energy telescope, and a monitor telescope.

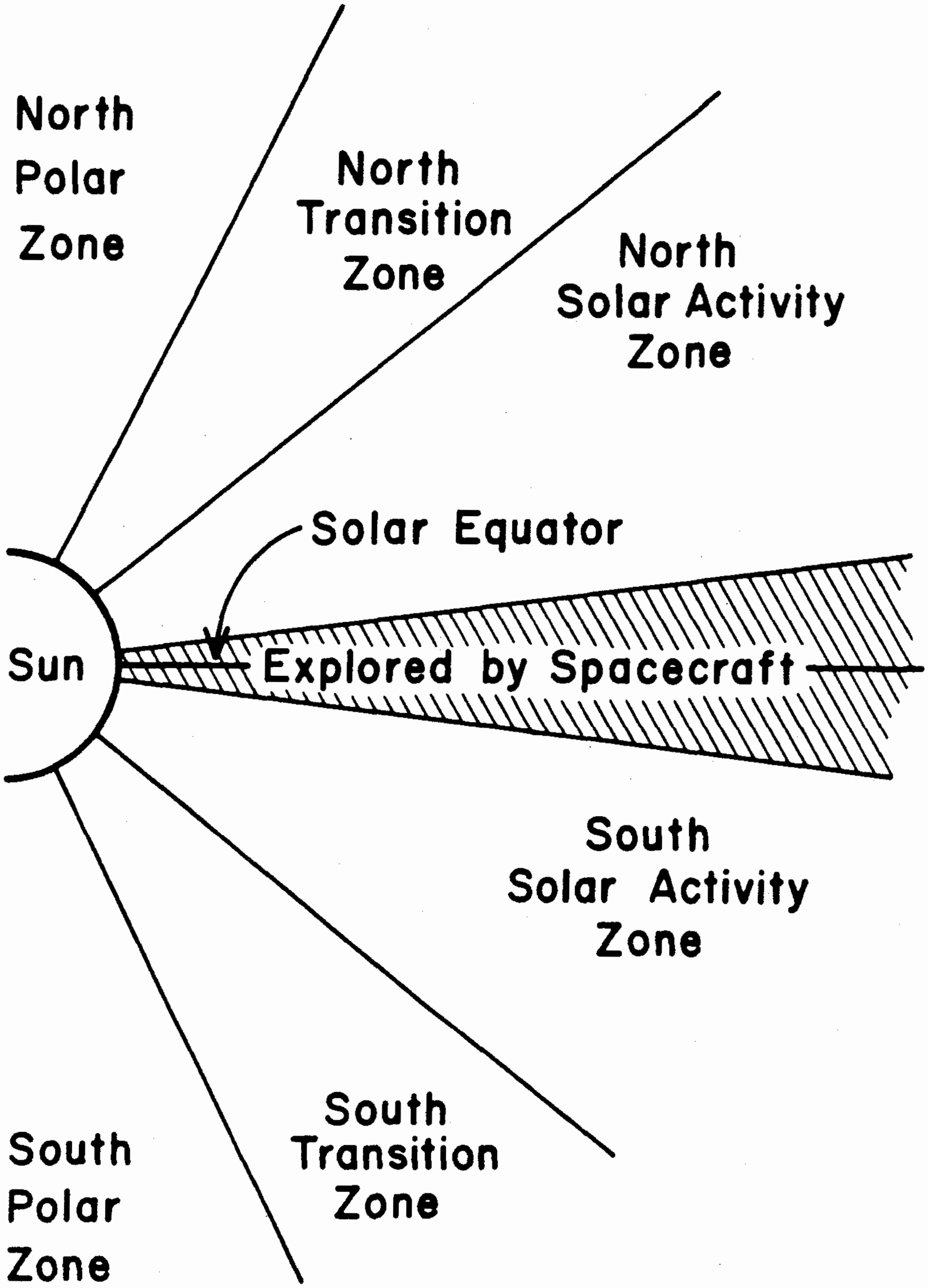

Idealized Meridional Diagram of Solar Regions Connecting with the Interplanetary Medium

Figure 37: Schematic view of the heliosphere indicating the various solar regions. The region of the ecliptic plane is shaded.

south polar zones, galactic cosmic rays may have relatively free access to the heliosphere. A first look at the high latitude portions of the solar cavity will be obtained in the mid-1980s by NASA's Solar Polar Mission which will carry, among other instruments, a version of the high energy telescope of Figure 31. Comparison of the measurements obtained over the poles with studies in the ecliptic plane will undoubtedly produce a new picture of charged particle radiation in the heliosphere.

SUMMARY

It has been my intent in this paper not to focus deeply on any particular problem, but to provide an overview of experimental techniques and the evolution of telescope systems. The reader should now be familiar with what is possible in the measurement of charged particles in space. (References are provided for anyone interested in pursuing a specific area.) The evolution of instrumentation for charged particle measurements has been rapid over the last decade, and similar development may be expected in the coming years. For the SPS, this implies that techniques superior to those now in use may be available before the start of construction. However, it appears that present technology is sufficient to monitor the charged particle radiation outside the SPS module.

The important question to be answered is, "What components of the radiation should be monitored?" The answer to this question depends, in detail, on the importance of the different components in producing radiation damage to people or materials. In addition, the answer defines the design parameters for the charged particle instrumentation. It seems necessary, as a minimum, to monitor the intensity of low energy protons and electrons in order to provide real-time data for solar flare hazard assessment. In addition, it is probably desirable to study the HZE component over a wide energy interval. Since the radiation damage effects of HZE particles are not completely understood, the study of the intensity and composition of HZE particles may provide invaluable information for radiation damage assessment. HZE particles are highly ionizing which gives them an importance far exceeding their actual numbers. This is illustrated by Figure 38 which shows a histogram of the relative abundances of the galactic cosmic rays weighted by the square of the particle's charge. This presentation emphasizes the ionizing ability of the radiation, and it is clear that the C, N, O nuclei and the iron peak elements begin to rival protons in importance.

The philosophy underlying radiation measurements on the SPS mission must be determined soon. Since the SPS may be one of the first long-term, manned ventures in space, radiation effects should remain at the forefront of planning. Complete charged particle instrumentation, perhaps orbiting in a satellite in the vicinity of the SPS module, would provide a complete data base on the radiation environment. This involves a quantity of information which is too large to be assimilated in real-time, but the recorded data will allow reconstruction of the radiation environment for later study or analysis in terms of specific radiation damage problems. Thus, it is highly recommended that the external radiation monitoring on the SPS mission include an entire complement of charged particle experiments to investigate, in detail, the complete radiation environment of the SPS satellites.

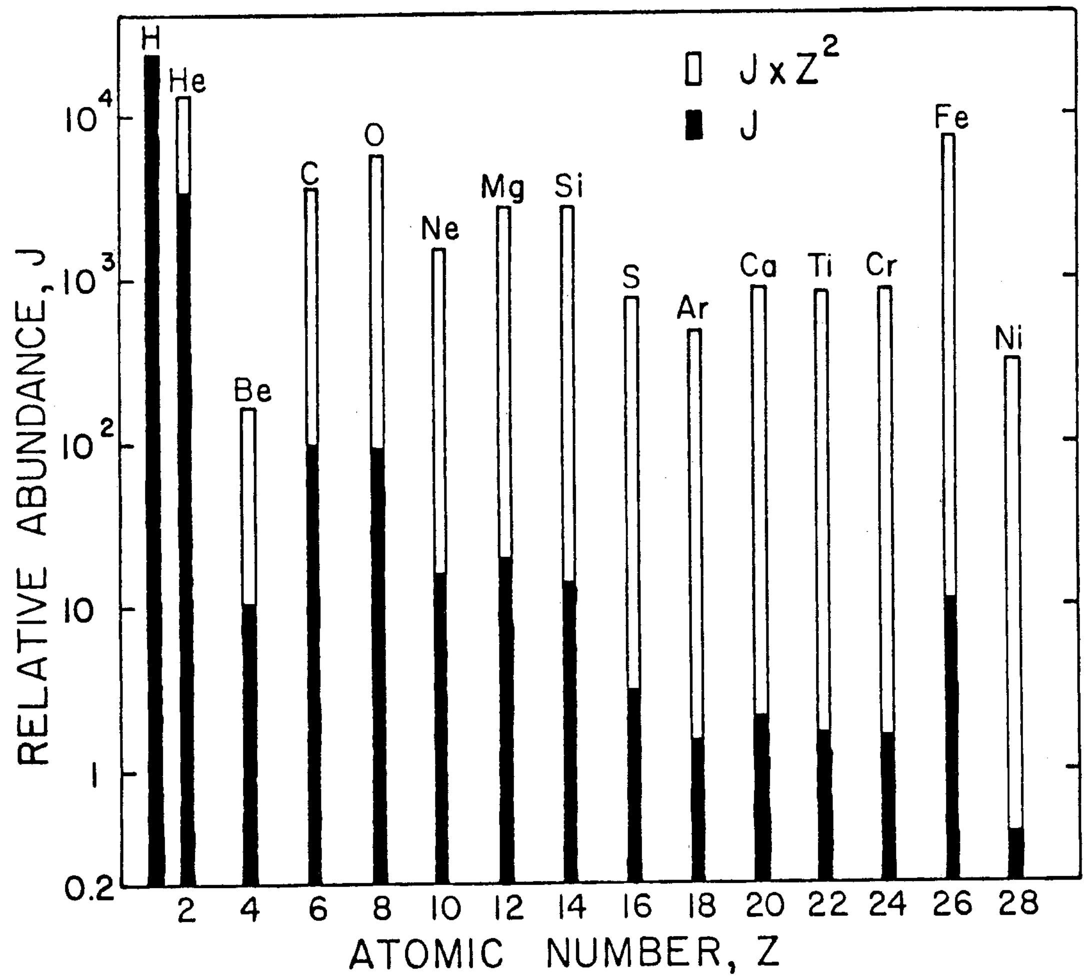

Figure 38: Histogram showing the relative abundances of the even numbered galactic cosmic ray nuclei (solid bars) compared to these abundances weighted by the square of the particle's charge to give a measure of the "ionizing power" of each element (open bars).

ACKNOWLEDGMENTS

The author would like to thank A.J. Tuzzolino for a critical review of the manuscript. Thanks are due to the staff of the Laboratory for Astrophysics and Space Research for the design and construction of the University of Chicago experiments described in this paper, and to the National Aeronautics and Space Administration for support over many years. The preparation of this manuscript was supported by NASA grant NGL 14-001-006 and contract NAS 5-11067.

REFERENCES

Anglin, J.D. 1975. Astrophys.J. 198, 733.

Anglin, J.D., Dietrich, W.F., and Simpson, J.A. 1973. Astrophys.J. 186, L41.

Badhwar, G.D., Daniel, R.R. Cleghorn, T., Golden, R.L., Lacy, J.L., Stephens, S.A., and Zipse, J.E. 1977. Proc. 15th Int. Cosmic Ray Conf., Plovdiv, 1, 204.

Balasubrahmanyan, V.K. and Ormes, J.F. 1973. Astrophys.J.Lett. 186, 109.

Barnes, C.W. and Simpson, J.A. 1976. Astrophys.J.Lett. 210, L91.

Caldwell, J.H. 1977. Astrophys.J. 218, 269.

Cameron, A.G.W. 1973. Space Sci. Rev. 15, 121.

Chan, J.H. and Price, P.B. 1975. Phys. Rev. Lett. 35, 539.

Chenette, D.L., Conlon, T.F., Pyle, K.R., and Simpson, J.A. 1977. Astrophys.J.Lett. 215, L95.

Cherry, J.L., Hartmann, G., Müller, D., and Prince, T.A. 1974. Phys. Rev. D 10, 3594.

Dietrich, W.F. and Simpson, J.A. 1978. Astrophys.J.Lett., in press.

Fan, C.Y., Gloeckler, G., and Hovestadt, D. 1975. Phys. Rev. Lett. 34, 495.

Fowler, P.H. 1973. Proc. 13th Int. Cosmic Ray Conf., Denver, 5, 3627.

Garcia-Munoz, M. 1973. Proc. 13th Int. Cosmic Ray Conf., Denver 5, 3513.

Garcia-Munoz, M., Mason, G.M., and Simpson, J.A. 1973. Astrophys.J. 184, 967.

Garcia-Munoz, M., Mason, G.M., and Simpson, J.A. 1975a. Proc. 14th Int. Cosmic Ray Conf., Munich, 1, 319.

Garcia-Munoz, M., Mason, G.M., and Simpson, J.A. 1975b. Astrophys.J. Lett. 201, L145.

Garcia-Munoz, M., Mason, G.M., and Simpson, J.A. 1975c. Astrophys.J. 202, 265.

Garcia-Munoz, M., Mason, G.M., and Simpson, J.A. 1977a. Astrophys.J. 217, 59.

Garcia-Munoz, M., Mason, G.M., and Simpson, J.A. 1977b. Proc. 15th Int. Cosmic Ray Conf., Plovdiv, 1, 264.

Garcia-Munoz, M., Mason, G.M., Simpson, J.A., and Wefel, J.P. 1977c. Proc. 15th Int. Cosmic Ray Conf., Plovdiv, 1, 230.

Garcia-Munoz, M., Simpson, J.A., and Wefel, J.P. 1978. Symposium on Cosmic Ray Astrophysics, Durham, New Hampshire, Sept. 28, 1978 (unpublished).

Gloeckler, G. 1970. Introduction to Experimental Techniques of High-Energy Astrophysics, edited by H. Ogelman and J.R. Wayland. NASA SP-243.

Hamilton, D.C. 1977. J.Geophys. Res. 82, 2157.

Hovestadt, D., Vollmer, O., GLoeckler, G., and Fan, C.Y. 1973. Phys. Rev. Lett. 31, 650.

Julliot, C., Koch, L., and Petrou, N. 1975. Proc. 14th Int. Cosmic Ray Conf., Munich, 12, 4118.

L'Heureux, J., Fan, C.Y., and Meyer, P. 1972. Astrophys.J. 171, 363.

Lamport, J.E., Mason, G.M., Perkins, M.A., and Tuzzolino, A.J. 1976. N.I.M. 134, 71.

Lin, R.P., Anderson, K.A., and Cline, T.L. 1972. Phys. Rev. Lett. 29, 1035.

Lund, N., Rasumssen, I.L., Peters, B., and Westergaard, N.J. 1975. Proc. 14th Int. Cosmic Ray Conf., Munich, 1, 257.

Mason, G.M. 1972. Astrophys.J. 171, 139.

McDonald, F.B., Teegarden, B.J., Trainor, J.H., and Weber, W.R. 1974. Astrophys.J. 187, L105.

Mewaldt, R.A., Stone, E.C., Vidor, S.B., and Vogt, R.E. 1975. Proc. 14th Int. Cosmic Ray Conf., Munich, 2, 798.

Perkins, M.A., Kristoff, J.J., Mason, G.M., and Sullivan, J.D. 1969. N.I.M. 68, 149.

Pyle, K.R. and Simpson, J.A. 1977. Astrophys.J.Lett. 215, L89.

Simpson, J.A. 1978. Private Communication.

Smith, L.H., Buffington, A., Smoot, G.F., Alvarez, L.W., and Wahlig, M.A. 1973. Astrophys.J. 180, 987.

Wefel, J.P., Schramm, D.N. and Blake, J.B. 1977. Astrophys. Space. Sci. 49, 47.

Zamow, R. 1975. Astrophys.J. 197, 767.

A PRELIMINARY STUDY OF THE CHARGED PARTICLE RADIATION FOR THE SATELLITE POWER SYSTEM

E. G. Stassinopoulos

NASA Goddard Space Flight Center
Greenbelt, Maryland 20771

INTRODUCTION

A preliminary radiation study was performed for the SPS project in order to determine the energetic charged particle environment for the three major phases of an SPS mission: the low earth orbit (LEO), the transfer ellipse (TE), and the synchronous geostationary trajectory (GEO).

For that purpose, extensive calculations were performed and a large data base was generated, processed, and analyzed. The results of this effort may be used as guidelines in other studies investigating the effects of radiation on materials and humans.

The external (surface incident) charged particle intensities, predicted for the SPS in each mission phase, were determined by orbital flux integration from the latest environment models.

Magnetic field definitions for the three trajectories were obtained from a current field model.

Spatial and temporal variations or conditions were considered and accounted for, wherever possible.

Limited shielding and dose evaluations were performed for a simple geometry.

The study, although comprehensive, is designated as "preliminary" because it was based on very tentative nominal flight path configurations. At a later time, as planning advances and mission parameters become better defined, it may be necessary to re-evaluate the SPS radiation predictions with new (firmer) orbital elements and information.

ORBIT SPECIFICATION

The analysis was performed for three nominal trajectories corresponding to the three phases of the SPS mission: a circular low earth orbit (LEO), a synchronous geostationary orbit (GEO), and singular outward parabolic transfer ellipse (TE) starting in the vicinity of LEO and terminating near a GEO. Specifically, each flight path was defined as follows:

LEO: inclination $i = 30^o$, altitude $h = 500$ km

GEO: inclination $i = 0^o$, altitude $h = 35790$ km, parking longitudes $\phi_p = 70^oW$ and $\phi_p = 160^oW$

TE: initial position: longitude $\phi = 172^oW$, geocentric latitude $\lambda = 13^oN$, altitude $h = 191$ km
final position: longitude $\phi = 73^oW$, geocentric latitude $\lambda = 12^oS$, altitude $h = 35621$ km.

TRAJECTORY GENERATION

A flight path ephemeris was generated for each trajectory (Stassinopoulous <u>et al</u>., 1973) for the indicated conditions:

LEO: for a 24-hour duration defined at two-minute intervals

GEO: for a 24-hour duration defined at three-minute intervals

TE: for a 5.25-hour duration defined at one-minute intervals

The length of simulated orbit time and the integration step size were especially selected in each case to provide sufficient point density to ensure an adequate sampling of the ambient radiation environment when flying the trajectories through the models.

The trajectories were subsequently converted from geodetic polar to magnetic B-L coordinates with Hassit and McIlwain's INVAR program (1967) and the field routine ALLMAG (Stassinopoulos and Mead, 1972), utilizing the BARRACLOUGH 1975 field model (Barraclough *et al.*, 1975). The spherical harmonic expansion coefficients of the field were extrapolated to tentative mission epochs with linear time terms representing secular variations of the field. (*Note*: The BARRACLOUGH 1975 model has replaced the older POGO 8/69 in the ALLMAG routine.)

CHARGED PARTICLE DOMAINS IN THE MAGNETOSPHERE

A brief discussion on this topic was given in a previous paper (Stassinopoulos, 1979). Of interest here is the distinction of electron populations into inner zone and outer zone constituents, and the limited range of energetic proton trapping.

The levels of radiation experienced by a satellite in a given orbit depends on the amount of visitation time in the volume of space occupied by each particle species, and on the extent to which the trajectory penetrates into the peak intensity regions of the different domains.

FLIGHT PATH EXPOSURE TO TRAPPING DOMAINS

The investigated flight-path configurations display distinctly different exposure characteristics.

LEO: The trajectory lies entirely within (a) the inner zone region of the electron environment, which is more benign and softer than that of the outer zone, and (b) the energetic proton domain. Also, LEO enters regions of space dominated by atmospheric cut-off conditions (loss of trapped particles due to interaction with atmospheric constituents) for about 22% of its time; that is, certain trajectory segments have a combination of B and L values that place them outside the atmospheric cut-off limits of the models.

GEO: A detailed description of synchronous geostationary trajectories was given elsewhere (Stassinopoulos, 1979). This class of orbits is quite unique. They lie outside the energetic proton trapping region, in the outer-zone electron domain, and they are 100% exposed to cosmic rays of galactic or solar origin (no geomagnetic shielding). Also, these orbits, having a range of L values from about 6.60 to about 7.02 earth radii, remain well above the peak intensity region of the outer-zone electrons, which occurs at about L = 4 earth radii. Since the flux variations over the possible GEO L-range ($6.60 \leq L \leq 7.02$) are significant, a GEO at each range end point was considered in the analysis, providing respectively worst and best case conditions.

TE: The particular TE selected for this study is supposed to represent a "typical" straight ascent trajectory for this type of mission as to force, shape, direction, start- and end-point location, velocity, epoch, etc. It yields certain specific radiation intensities that are unique to this TE. Any changes in flight path would affect this predicted vehicle-encountered flux values, conceivably by as much as several orders of magnitude. As it is, the TE passes through the inner and outer zone electron domains, the energetic proton region, and spends about 60% of its time in regions of space accessible to cosmic rays.

TRAPPED PARTICLE ENVIRONMENT

The fluxes in this study were obtained from current standard NASA models of the environment, as issued by the National Space Science Data Center (NSSDC) at Goddard Space Flight Center:

AE5:	inner zone electrons for solar minimum conditions (Teague and Vette, 1972)
AE6:	inner zone electrons for solar maximum conditions (Teague *et al*., 1976)
AE17-HI:	outer zone electrons (no solar cycle dependence) (Hills *et al*., 1979)
AP8-MAC: AP8-MIC	trapped protons for solar maximum (MAC) and solar minimum (MIC) conditions (Sawyer and Vette, 1976)

All models describe average static environments at a fixed epoch.

The new AP8 replaces all previously issued trapped proton models, each of which was valid over specific energy ranges. The AP8 now covers the entire energy spectrum. It also reflects solar cycle variations: the AP8-MIN describes an average solar minimum and the AP8-MAX an average solar maximum environment.

The AEI7 is a new interim model that has recently replaced the older outer zone AE4. For energies above 1.5 MeV, this interim model contains upper (AEI7-HI) and lower (AEI7-LO) limit values to account for the discrepancy between existing data sets. There is recent evidence that these discrepancies may be due to stochastic differences in yearly averaged flux levels. If this proves to be true, then these two limits bound the predictive uncertainty that will always exist at these high energies.

Further comments on the AEI7 and on modeling procedures in general are contained in another paper (Stassinopoulos, 1979).

ORBITAL FLUX INTEGRATIONS

Orbital flux integrations (OFI) for all mission phases were performed with advanced complex software systems (Stassinopoulos and Gregory, 1978; Stassinopoulos *et al*., 1977). The results were statistically processed and analyzed. Some OFI data were subsequently used in the dose and shielding evaluation.

FLUX DATA: TYPE, QUALITY, AND VARIATIONS

The computed trapped particle fluxes represent omnidirectional, integral intensities that one would expect to obtain as average values over periods in excess of six months. Over most regions of magnetospheric trapping space ($L \gtrsim 2$ earth radii), short term excursions can vary from these values by factors of 10^2 to 10^3, depending on the particle energies and type and intensity of event. The impact of these variations from the model-predictions on the three SPS phases may be summarized as follows.

LEO. Even a short-duration LEO mission is not affected by such fluctuations because of the low-inclination/low-altitude orbit (L value always less than 1.8 earth radii).

GEO. Activity areas with short-range concerns should be aware of the possibility for the occurrence of these fluctuations and take them into account; considerations for long-range effects need not concern themselves with these excursions.

TE. If the mission duration, to be finally determined for this phase, is as short as the one used in this work (5.25 hours), then the satellite could experience those excursions over most of its flight path.

Other variations affecting the trapped particle populations are: (a) the local time dependence, and (b) the solar cycle dependence. Both are briefly discussed relative to GEO by Stassinopoulos (1979). However, the impact of these variations on the LEO and TE environments is different. LEO does not experience any local time variations, while TE will be affected over the segment of its trajectory that has L-values above 5 earth radii.

In contrast, regarding these two orbits, the exact opposite is true for solar cycle variations; LEO does experience these long-term changes, while TE does not when L > 5 earth radii.

It is necessary to emphasize that the calculations, although based on the best data available for past epochs, can only serve as approximations for the future.

It should also be noted that the following basic uncertainty factors (u.f.) are attached to the flux values of the corresponding models.

AE5:	u.f. = 2
AE6:	u.f. = 5 : average value for this model (u.f. is a function of energy E and magnetic parameter L).
AP8:	u.f. = 2 : same value for solar maximum and for solar minimum version.
AEI7-HI:	in this particular case the electron results may be considered an upper limit (worst case) since this version of the AEI7 predicts the highest flux levels in accordance with Vampola's OV1-19 data and the ATS-6 data of Paulikas and Blake. If any uncertainties were to be attached to these data, it should be a fractional (reducing) factor of maybe 0.5, to bring the flux levels down and more in line with the other satellite measurements that indicate lower values.

No uncertainty factors were applied to the data contained in this report.

GEOMAGNETIC SHIELDING AND SOLAR FLARE PROTONS

A detailed description of this topic is given elsewhere (Stassinopoulos, 1979), particularly in reference to GEO. Therefore, only some comments relative to LEO and TE are presented here.

LEO. This trajectory is at all times 100% geomagnetically shielded from cosmic rays of galactic or solar origin in the investigated energy range from $E > 10$ MeV to $E < 200$ MeV.

TE. The flight path may be divided into two segments:

A. $L < 5$: shielded (1.90 hours)

B. $L > 5$: unshielded (3.35 hours)

Where $L = 5$ defines an average approximate cut-off shell of dipolar magnetic field lines for the indicated energy range. Because of the very short exposure duration (3.35 hours), TE need not be concerned with energetic solar proton fluxes (whether produced by ordinary event activity or by anomalously large event activity); accumulations for this part of the mission would be insignificant.

DOSE AND SHIELDING EVALUATION

Doses were calculated from the total orbit-integrated, surface incident, omnidirectional, functionally differentiated particle fluences by existing shielding codes (Watts and Burrell, 1971).

"Electron," "bremsstrahlung," "proton," and "total" aluminum doses were obtained by a plain straightforward approach: from a simple two-dimensional, infinite-slab geometry (2π steradian omnidirectional incidence) with a cosine law for the incident spectra.

More sophisticated procedures (solid angle sectoring or three-dimensional geometry) may be followed, if necessary, at a later evaluation.

STUDY RESULTS: DISCUSSION AND CONCLUSIONS

The results of this analysis are presented in tabular and graphical form, separately for each mission phase:

LEO. The orbit integrated, omnidirectional, integral daily electron and proton fluxes are given in Table 1 for both solar minimum and maximum conditions. The respective spectra are plotted in Figure 1 for the electrons and in Figure 2 for the protons. Noteworthy are the soft inner zone electron spectra, especially in regards to the steep falloff to zero flux in the energy range above 4 MeV. The apparent cutoff at these energies was established from experimental measurements after the higher energy artificials from the "Starfish" nuclear explosion had decayed down to natural background levels (Teague and Stassinopoulos, 1972).

With regard to the protons, the data display relatively hard spectra above 20 MeV.

A most interesting and potentially useful item is "flux-free" time where flux-free is defined as less than one particle per square centimeter for electrons with $E > 0.5$ MeV and protons with $E > 5$ MeV. The LEO orbit is about 86% of its total lifetime flux-free. This holds for both species of particles. In terms of continuous, uninterrupted, flux-free time intervals, the trajectory has about six consecutive revolutions per day in that category, for a maximum duration of about 10 hours.

Figures 3 and 4 show the dose contributions and the total aluminum dose for solar minimum and solar maximum conditions, respectively. When making a comparison of these dose-depth curves, it is necessary

ORBITAL RADIATION STUDY

(SOURCE: E. G. STASSINOPOULOS, NASA — GSFC, 1978)

LOW EARTH ORBIT RADIATION ENVIRONMENT: LEO

(CIRCULAR ORBIT, INCLINATION 30°, ALTITUDE = 500 km)

DAILY TRAPPED PARTICLE FLUXES

(AVERAGE ORBIT INTEGRATED, OMNIDIRECTIONAL, INTEGRAL, DAILY INTENSITIES)

ELECTRONS*			PROTONS*		
E (>MeV)	SOLAR MIN	SOLAR MAX	E (>MeV)	SOLAR MIN	SOLAR MAX
.1	4.587E 09	1.036E 10	5.0	9.344E 06	5.140E 06
.5	1.532E 08	2.253E 08	10.0	8.584E 06	4.712E 06
1.0	2.760E 07	2.761E 07	20.0	7.568E 06	4.204E 06
1.5	1.041E 07	1.041E 07	30.0	6.902E 06	3.862E 06
2.0	4.613E 06	4.613E 06	40.0	6.038E 06	3.557E 06
2.5	2.119E 06	2.119E 06	50.0	5.771E 06	3.279E 06
3.0	3.595E 05	3.595E 05	60.0	5.224E 06	3.005E 06
3.5	4.046E 04	4.046E 04	70.0	4.734E 06	2.758E 06
4.0	1.744E 03	1.745E 03	80.0	4.296E 06	2.533E 06
4.5	–	–	90.0	3.901E 06	2.329E 06
5.0	–	–	100.0	3.546E 06	2.143E 06
5.5	–	–	150.0	2.108E 06	1.320E 06
6.0	–	–	200.0	1.272E 06	8.261E 05
6.5	–	–	300.0	4.668E 05	3.040E 05
7.0	–	–	400.0	1.747E 05	1.139E 05
			500.0	6.632E 04	4.281E 04

* UNCERTAINTY FACTORS WERE NOT APPLIED TO THE DATA

EPOCH: 1979
MODELS: FIELD-BARRACLOUGH/75
ELECTRONS = IZ AE6 (SOLAR MAX)
= IZ AE5 (SOLAR MIN)
TRAPPED PROTONS = AP8 - MAC (SOLAR MAX)
= AP8 - MIC (SOLAR MIN)
MISSION DURATION: τ = 1 DAY

Table 1

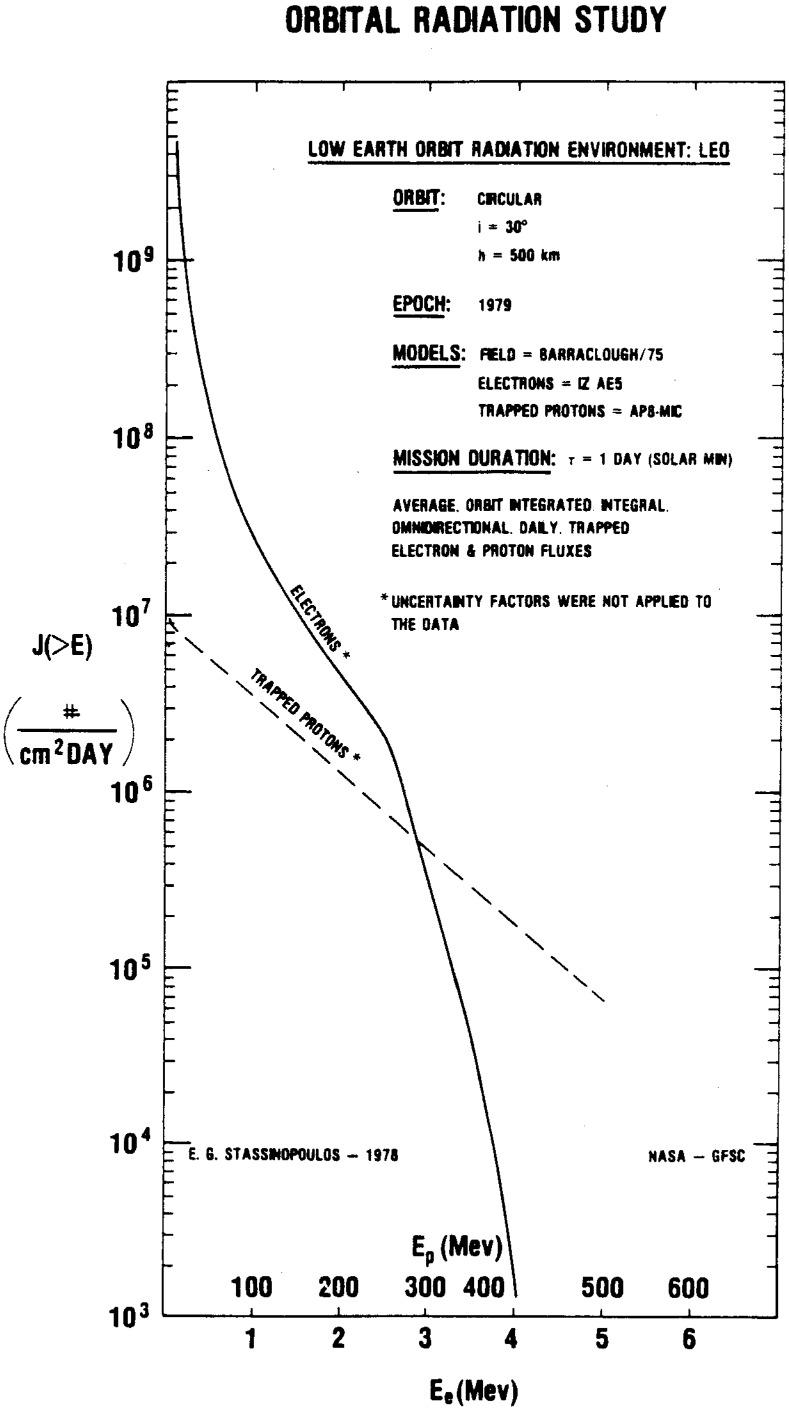

Figure 1. LEO: Electron and proton spectral profiles of orbit-integrated daily fluxes for solar minimum.

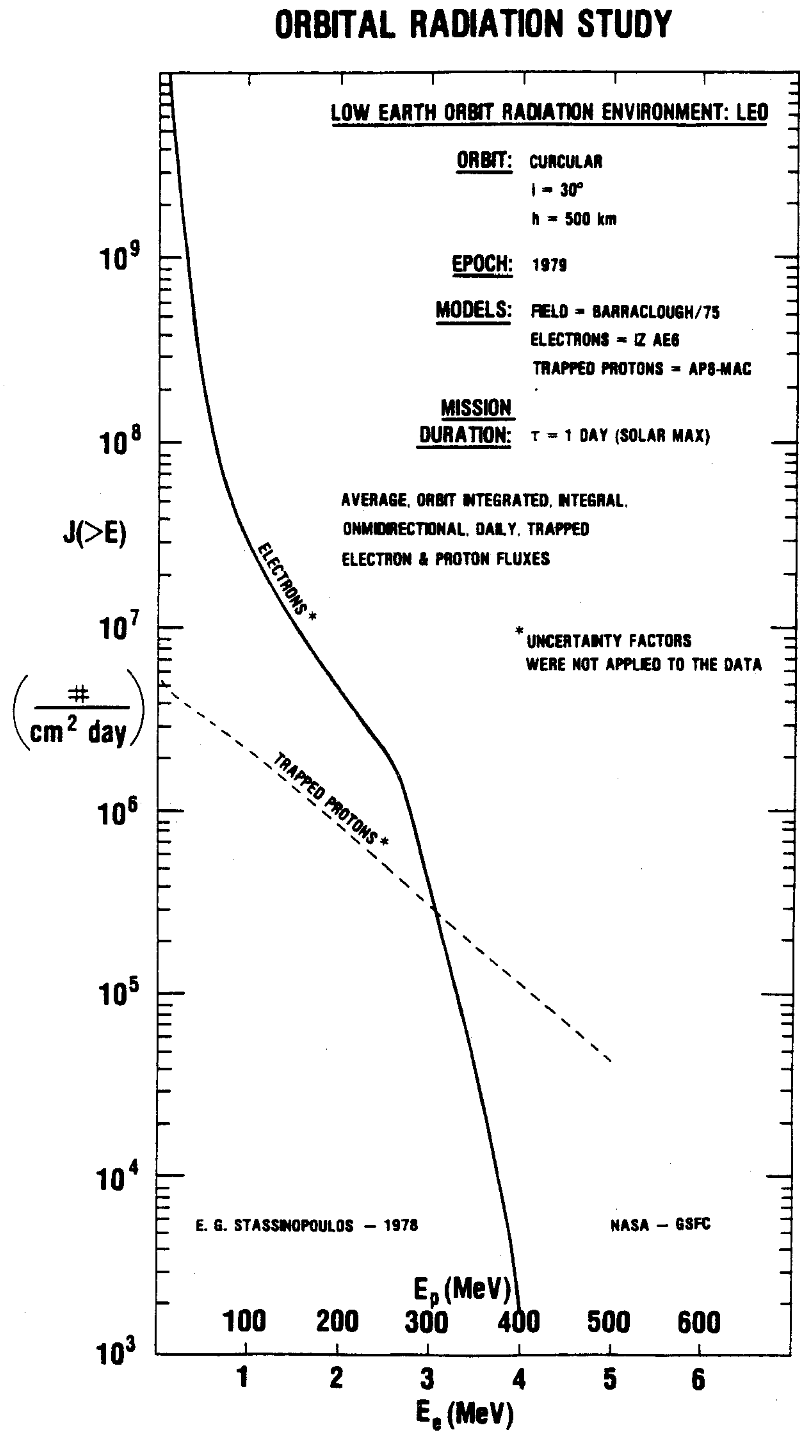

Figure 2. LEO: Electron and proton spectral profiles of orbit-integrated daily fluxes for solar maximum.

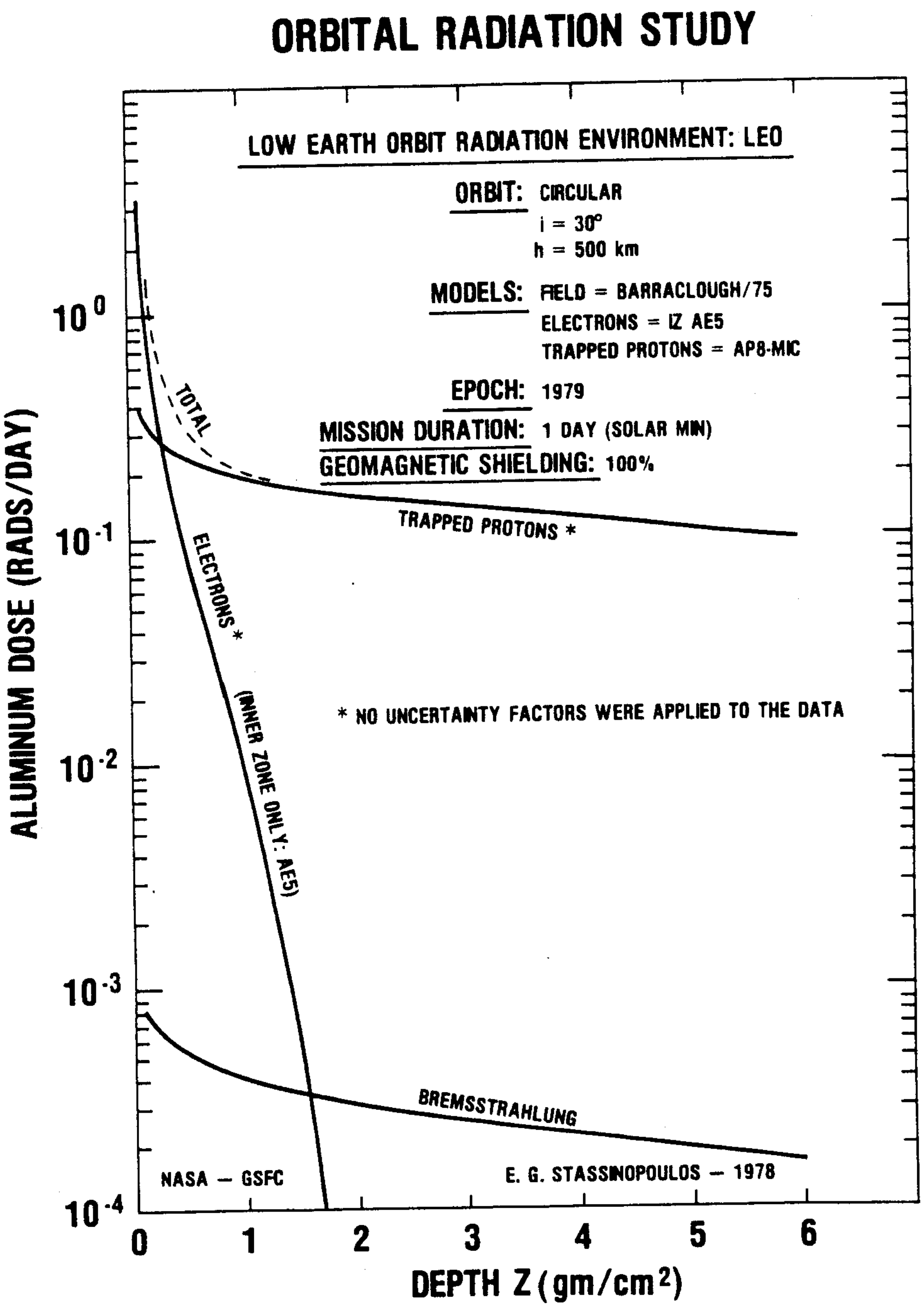

Figure 3. LEO: Dose-depth curves for solar minimum.

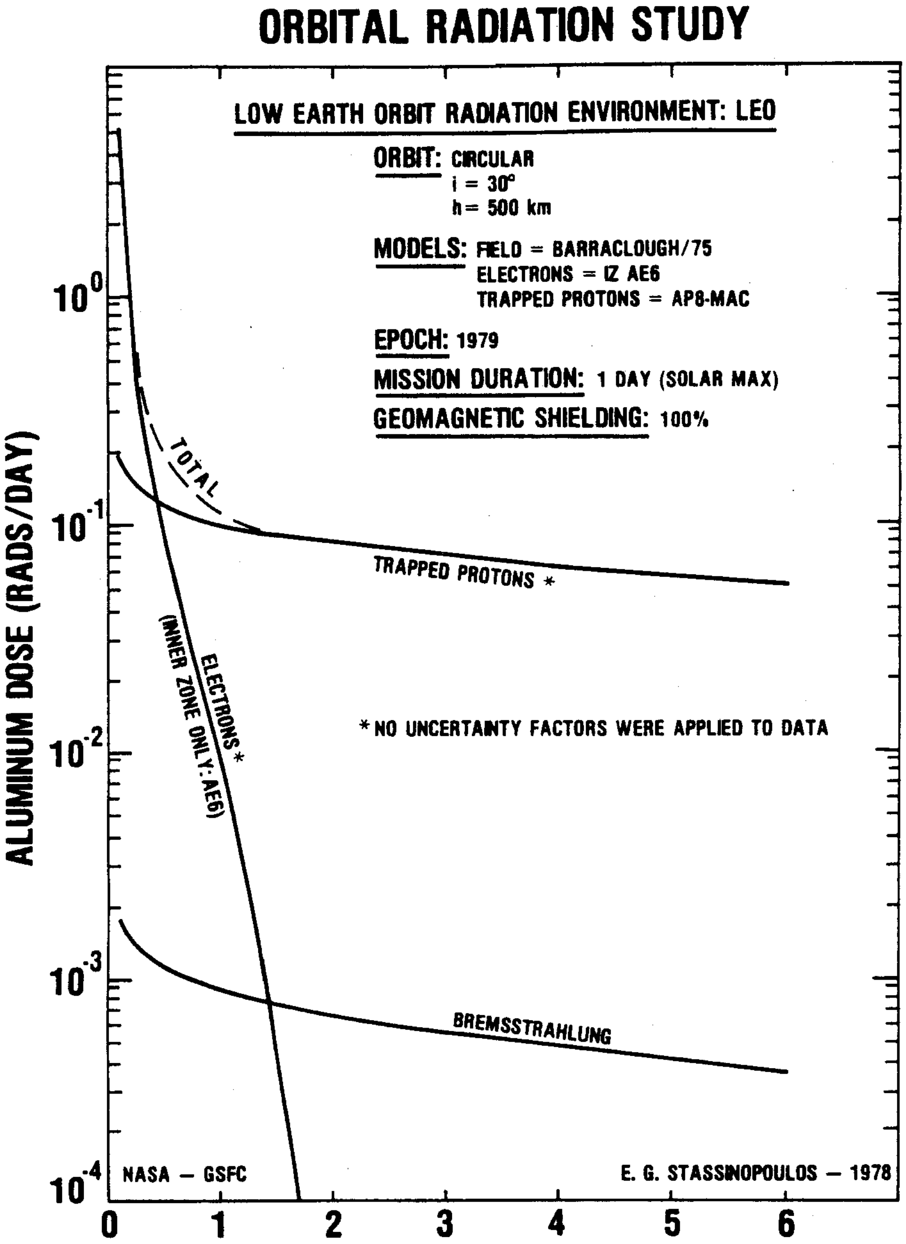

Figure 4. LEO: Dose-depth curves for solar maximum.

to remember that electron intensities are higher during solar maximum, and hence so is the dose from bremsstrahlung, while proton intensities are higher during solar minimum.

Due to the presence of the large trapped-proton component, the relative contribution from bremsstrahlung remains insignificantly low at all shield thicknesses.

GEO. These data are presented in Tables 6-9 and Figures 7-11. They are discussed by Stassinopoulos (1979)

TE. Table 4 gives the total accumulated electron and proton fluence, evaluated for solar maximum conditions, while Figure 5 plots the respective spectral profiles.

The corresponding dose values are given in Table 5 and are plotted in Figure 6. Here, the bremsstrahlung contribution completely dominates at shields heavier than 3 g/cm^2.

Some general comments are presented in the subsequent paragraphs.

Predictably, each phase of the mission encounters substantially different radiation exposures as to particle mixes, flux levels, and spectral distributions. Consequently, each phase experiences a dose rate varying not only in magnitude, but also in composition. This difference may be important when the effects of radiation on specific tasks or activities with given constraints and limitations have to be evaluated.

Such an evaluation was not performed in the present effort. It was not in the scope of this study to determine the impact of the particular radiation estimates on specific mission objectives.

ORBITAL RADIATION STUDY

(SOURCE: E. G. STASSINOPOULOS, NASA—GSFC, 1978)

LOW EARTH ORBIT RADIATION ENVIRONMENT: LEO

(CIRCULAR ORBIT, INCLINATION 30°, ALTITUDE = 500 km)

DAILY DOSES: SOLAR MIN.						
SHIELD THICKNESS (ALUMINUM)			ELECTRONS (INNER ZONE)	BREMSSTRAHLUNG	TRAPPED PROTONS	TOTAL DOSE
z (gm/cm^2)	t (mm)	t (mils)	(rads_{Al})	(rads_{Al})	(rads_{Al})	(rads_{Al})
.1	0.37	15	2.935E 00	8.200E-04	3.844E-01	3.318E 00
.2	0.74	29	6.905E-01	6.681E-04	3.110E-01	1.011E 00
.3	1.11	44	2.929E-01	5.913E-04	2.732E-01	5.666E-01
.4	1.48	58	1.561E-01	5.406E-04	2.498E-01	4.064E-01
.5	1.85	73	9.293E-02	5.033E-04	2.331E-01	3.264E-01
.6	2.22	87	5.827E-02	4.738E-04	2.209E-01	2.797E-01
.7	2.59	102	3.738E-02	4.497E-04	2.114E-01	2.492E-01
.8	2.96	117	2.399E-02	4.296E-04	2.032E-01	2.257E-01
.9	3.33	131	1.514E-02	4.121E-04	1.962E-01	2.118E-01
1.0	3.70	146	9.294E-03	3.967E-04	1.903E-01	2.022E-01
1.25	4.63	182	2.278E-03	3.651E-04	1.786E-01	1.812E-01
1.50	5.56	219	4.323E-04	3.403E-04	1.695E-01	1.703E-01
1.75	6.48	255	6.858E-05	3.197E-04	1.620E-01	1.624E-01
2.0	7.41	292	9.453E-06	3.023E-04	1.557E-01	1.559E-01
2.5	9.26	365	1.210E-07	2.737E-04	1.457E-01	1.460E-01
3.0	11.11	437	6.878E-09	2.507E-04	1.377E-01	1.380E-01
3.5	12.96	510	4.358E-10	2.314E-04	1.291E-01	1.293E-01
4.0	14.81	583	2.929E-11	2.147E-04	1.202E-01	1.204E-01
4.5	16.67	656	2.030E-12	2.000E-04	1.126E-01	1.128E-01
5.0	18.52	729	1.413E-13	1.869E-04	1.065E-01	1.067E-01
5.5	20.37	802	9.620E-15	1.750E-04	1.018E-01	1.020E-01
6.0	22.22	875	6.260E-16	1.641E-04	9.779E-02	9.798E-02

Table 2

ORBITAL RADIATION STUDY

(SOURCE: E. G. STASSINOPOULOS, NASA—GSFC, 1978)

LOW EARTH ORBIT RADIATION ENVIRONMENT: LEO

(CIRCULAR ORBIT, INCLINATION 30°, ALTITUDE = 500 km)

DAILY DOSE: SOLAR MAX.						
SHIELD THICKNESS (ALUMINUM)			ELECTRONS (INNER ZONE)	BREMSSTRAHLUNG	TRAPPED PROTONS	TOTAL DOSE
z (gm/cm^2)	t (mm)	t (mils)	(rads$_{Al}$)	(rads$_{Al}$)	(rads$_{Al}$)	(rads$_{Al}$)
.1	0.37	15	5.528E 00	1.892E-03	2.038E-01	5.735E 00
.2	0.74	29	8.539E-01	1.543E-03	1.630E-01	1.018E 00
.3	1.11	44	3.128E-01	1.367E-03	1.432E-01	4.574E-01
.4	1.48	58	1.588E-01	1.249E-03	1.313E-01	2.913E-01
.5	1.85	73	9.328E-02	1.163E-03	1.230E-01	2.174E-01
.6	2.22	87	5.833E-02	1.095E-03	1.169E-01	1.763E-01
.7	2.59	102	3.737E-02	1.040E-03	1.122E-01	1.506E-01
.8	2.96	117	2.400E-02	9.932E-04	1.084E-01	1.330E-01
.9	3.33	131	1.516E-02	9.530E-04	1.044E-01	1.206E-01
1.0	3.70	146	9.292E-03	9.174E-04	1.014E-01	1.115E-01
1.25	4.63	182	2.278E-03	8.450E-04	9.514E-02	9.831E-02
1.5	5.56	219	4.324E-04	7.870E-04	9.041E-02	9.162E-02
1.75	6.48	255	6.859E-05	7.399E-04	8.654E-02	8.735E-02
2.0	7.41	292	9.452E-06	6.991E-04	8.318E-02	8.393E-02
2.5	9.26	365	1.643E-07	6.331E-04	7.799E-02	7.862E-02
3.0	11.11	437	7.010E-09	5.801E-04	7.392E-02	7.449E-02
3.5	12.96	510	4.359E-10	5.351E-04	6.958E-02	7.010E-02
4.0	14.81	583	2.927E-11	4.966E-04	6.519E-02	6.571E-02
4.5	16.67	656	2.029E-12	4.625E-04	6.152E-02	6.198E-02
5.0	18.52	729	1.413E-13	4.320E-04	5.857E-02	5.897E-02
5.5	20.37	802	9.620E-14	4.044E-04	5.632E-02	5.671E-02
6.0	22.22	875	6.260E-16	3.793E-04	5.437E-02	5.476E-02

Table 3

ORBITAL RADIATION STUDY

(SOURCE: E. G. STASSINOPOULOS, NASA – GSFC, 1978)

ORBIT: TRANSFER ELLIPSE

INITIAL POSITION: $\Phi = -172°$, $\lambda = 13°$, $h = 191$ km
FINAL POSITION: $\Phi = -73°$, $\lambda = -12°$, $h = 35621$ km

TRAPPED PARTICLE FLUENCES FOR $\tau = 5.25$ HR.

(TOTAL, FLIGHT-PATH INTEGRATED, OMNIDIRECTIONAL, INTEGRAL FLUENCES)

E (>MeV)	ELECTRONS* INNER ZONE (e/cm^2)	OUTER ZONE (e/cm^2)	TOTAL (e/cm^2)	E (>MeV)	PROTONS* (p/cm^2)
.10	3.264E 09	3.987E 11	4.020E 11	5.	7.910E 06
.50	4.555E 07	8.756E 10	8.762E 10	10.	9.164E 05
1.00	1.513E 06	3.020E 10	3.020E 10	20.	1.714E 05
1.25	8.019E 05	1.912E 10	1.912E 10	30.	7.557E 04
1.50	4.303E 05	1.235E 10	1.235E 10	40.	4.635E 04
1.75	2.326E 05	8.139E 09	8.139E 09	50.	2.974E 04
2.00	1.263E 05	5.462E 09	5.463E 09	60.	2.135E 04
2.25	6.568E 04	3.979E 09	3.979E 09	70.	1.541E 04
2.50	3.430E 04	2.926E 09	2.926E 09	80	1.237E 04
2.75	1.508E 04	2.168E 09	2.168E 09	90.	8.271E 03
3.00	6.568E 03	1.616E 09	1.616E 09	100.	6.101E 03
3.25	3.009E 03	1.311E 09	1.311E 09	125.	3.003E 03
3.50	1.395E 03	1.066E 09	1.066E 09	150.	1.503E 03
4.00	3.498E 02	7.060E 08	7.060E 08	175.	7.929E 02
4.50	–	3.414E 08	3.414E 08	200.	3.629E 02
5.00	–	1.655E 08	1.655E 08	250.	–
5.50	–	4.917E 07	4.917E 07	300.	–
6.00	-	1.464E 07	1.464E 07	350.	–
6.50	-	1.411E 06	1.411E 06	400.	–
7.00	–	–	–	500.	–

*UNCERTAINTY FACTORS WERE NOT APPLIED TO THE DATA

EPOCH: 1979
MODELS: FIELD = BARRACLOUGH/75
ELECTRONS = IZ AE6
OZ AEI7-HI
TRAPPED PROTONS = AP8 - MAC

MISSION DURATION: TRANSFER FLIGHT
TIME τ = 5.25 HOURS

Table 4

ORBITAL RADIATION STUDY

(SOURCE: E. G. STASSINOPOULOS, NASA — GSFC, 1978)

ORBIT: TRANSFER ELLIPSE

INITIAL POSITION: $\Phi = -172°, \lambda = 13°, h = 191$ km

FINAL POSITION: $\Phi = -73°, \lambda = -12°, h = 35621$ km

ALUMINUM DOSE FOR $\tau = 5.25$ HOURS						
SHIELD THICKNESS (ALUMINUM)			ELECTRONS	BREMSSTRAHLUNG	TRAPPED PROTONS	TOTAL DOSE
z (gm/cm^2)	t (mm)	t (mils)	($rads_{Al}$)	($rads_{Al}$)	($rads_{Al}$)	($rads_{Al}$)
.10	0.37	15	1.293E 03	3.985E-01	5.536E-01	1.294E 03
.20	0.74	29	5.610E 02	2.903E-01	1.339E-01	5.614E 02
.30	1.11	44	2.980E 02	2.513E-01	6.473E-02	2.983E 02
.40	1.48	58	1.728E 02	2.275E-01	3.725E-02	1.731E 02
.50	1.85	73	1.075E 02	2.106E-01	2.381E-02	1.077E 02
.60	2.22	87	7.030E 01	1.975E-01	1.690E-02	7.051E 01
.70	2.59	102	4.773E 01	1.870E-01	1.281E-02	4.793E 01
.80	2.96	117	3.350E 01	1.782E-01	1.001E-02	3.369E 01
.90	3.33	131	2.419E 01	1.706E-01	8.085E-03	2.437E 01
1.00	3.70	146	1.791E 01	1.640E-01	6.700E-03	1.808E 01
1.25	4.63	182	9.110E 00	1.506E-01	4.633E-03	9.265E 00
1.50	5.56	219	4.901E 00	1.401E-01	3.514E-03	5.045E 00
1.75	6.48	255	2.608E 00	1.315E-01	2.826E-03	2.742E 00
2.00	7.41	292	1.307E 00	1.242E-01	2.339E-03	1.434E 00
2.50	9.26	365	2.535E-01	1.125E-01	1.701E-03	3.677E-01
3.00	11.11	437	3.502E-02	1.032E-01	1.317E-03	1.395E-01
3.50	12.96	510	3.770E-03	9.547E-02	1.052E-03	1.003E-01
4.00	14.81	583	3.685E-04	8.894E-02	8.606E-04	9.017E-02
4.50	16.67	656	3.578E-05	8.324E-02	7.282E-04	8.400E-02
5.00	18.52	729	3.450E-06	7.815E-02	6.257E-04	7.878E-02
5.50	20.37	802	3.233E-07	7.366E-02	5.485E-04	7.421E-02
6.00	22.22	875	2.885E-08	6.952E-02	4.851E-04	7.001E-02

Table 5

ORBITAL RADIATION STUDY

(SOURCE: E. G. STASSINOPOULOS, NASA – GSFC, 1978)

ORBIT: SYNCHRONOUS–GEOSTATIONARY

(INCLINATION = 0°, ALTITUDE = 35790 km, PARKING LONGITUDE = 160°W & 70°W)

TRAPPED ELECTRON FLUXES

(AVERAGE, ORBIT INTEGRATED, OMNIDIRECTIONAL, INTEGRAL, DAILY INTENSITIES)

E (>MeV)	WORST CASE: $\phi_p = 160^\circ W$ (e/cm^2 DAY)	BEST CASE: $\phi_p = 70^\circ W$ (e/cm^2 DAY)
.1	1.878E 12	1.446E 12
.5	2.789E 11	1.769E 11
1.0	5.861E 10	3.018E 10
1.5	1.375E 10	6.243E 09
2.0	3.224E 09	1.292E 09
2.5	8.832E 08	2.800E 08
3.0	2.419E 08	6.069E 07
3.5	1.313E 08	2.716E 07
4.0	7.122E 07	1.215E 07
4.5	3.153E 07	4.443E 06
5.0	1.396E 07	1.624E 06
5.5	3.862E 06	3.749E 05
6.0	1.069E 06	6.070E 04
6.5	–	–
7.0	–	–

NOTE: THESE FLUXES REPRESENT LOCAL-TIME (LT) AVERAGED VALUES

ELECTRON MODEL: OZ AEI7-HI: THE AEI7 IS AN INTERIM MODEL THAT HAS REPLACED THE OLDER AE4 MODEL. FOR ENERGIES ABOVE 1.5 MeV THIS INTERIM MODEL CONTAINS UPPER AND LOWER LIMIT VALUES TO ACCOUNT FOR THE DISCREPANCY BETWEEN EXISTING DATA SETS. THE AEI7-HI FAVORS VAMPOLA'S FIT TO THE OV1-19 DATA WHILE THE AEI7-LO IS MORE REPRESENTATIVE OF ALL DATA SETS PRESENTLY AVAILABLE TO NSSDC.

Table 6

ORBITAL RADIATION STUDY

(SOURCE: E. G. STASSINOPOULOS, NASA — GSFC, 1978)

ORBIT: SYNCHRONOUS—GEOSTATIONARY

(PARKING LONGITUDE: ANY)

ENERGETIC SOLAR FLARE PROTONS

(UNATTENUATED, INTERPLANETARY, OMNIDIRECTIONAL, INTEGRAL PROTON FLUENCES)

E (>MeV)	OR* FLUENCES (p/cm^2)$^+$	AL** FLUENCES (p/cm^2)$^{++}$	TOTAL (p/cm^2)
10	4.842E 08	1.680E 10	1.728E 10
20	4.134E 08	1.152E 10	1.193E 10
30	3.530E 08	7.900E 09	8.253E 09
40	3.014E 08	5.417E 09	5.718E 09
50	2.574E 08	3.714E 09	3.971E 09
60	2.197E 08	2.547E 09	2.767E 09
70	1.876E 08	1.746E 09	1.934E 09
80	1.602E 08	1.197E 09	1.357E 09
90	1.368E 08	8.210E 08	9.578E 08
100	1.168E 08	5.629E 08	6.797E 08
	ENCOUNTERED IN 90-DAY PERIOD WHEN <u>NO</u> AL EVENT OCCURS		ENCOUNTERED IN 90-DAY PERIOD WHEN <u>ONE</u> AL EVENT OCCURS

EPOCH: 1979
MODELS: FIELD = BARRACLOUGH/75
SOLAR FLARE PROTONS = SOLPRO

*OR = ORDINARY EVENT
**AL = ANOMALOUSLY LARGE EVENT
\+ TOTAL FLUENCES FOR τ = 90 DAYS
\+\+ TOTAL FLUENCES FOR 1 AL EVENT

Table 7

ORBITAL RADIATION STUDY

(SOURCE: E. G. STASSINOPOULOS, NASA—GSFC, 1978)

ORBIT: SYNCHRONOUS—GEOSTATIONARY

(CIRCULAR, INCLINATION 0°, ALTITUDE = 35790 km, PARKING LONGITUDES = 160°W & 70°W)

SHIELD THICKNESS (ALUMINUM)			DAILY DOSE					
			PARKING LONGITUDE: 70°W			PARKING LONGITUDE: 160°W		
			ELECTRONS (OUTER ZONE)	BREMSSTRAHLUNG	TOTAL	ELECTRONS (OUTER ZONE)	BREMSSTRAHLUNG	TOTAL
Z (gm/cm^2)	t (mm)	t (mils)	($rads_{Al}$)	($rads_{Al}$)	($rads_{Al}$)	($rads_{Al}$)	($rads_{Al}$)	($rads_{Al}$)
.1	0.37	15	2.805E 03	6.060E-01	2.804E 03	4.356E 03	9.756E-01	4.359E 03
.2	0.74	29	8.307E 02	4.797E-01	8.312E 02	1.429E 03	7.625E-01	1.430E 03
.3	1.11	44	3.134E 02	4.216E-01	3.137E 02	5.879E 02	6.682E-01	5.885E 02
.4	1.48	58	1.308E 02	3.841E-01	1.312E 02	2.631E 02	6.079E-01	2.637E 02
.5	1.85	73	5.951E 01	3.567E-01	5.986E 01	1.267E 02	5.644E-01	1.272E 02
.6	2.22	87	2.841E 01	3.356E-01	2.874E 01	6.384E 01	5.304E-01	6.436E 01
.7	2.59	102	1.399E 01	3.181E-01	1.430E 01	3.326E 01	5.027E-01	3.375E 01
.8	2.96	117	7.047E 00	3.036E-01	7.351E 00	1.786E 01	4.795E-01	1.834E 01
.9	3.33	131	3.630E 00	2.910E-01	3.921E 00	9.890E 00	4.595E-01	1.035E 01
1.0	3.70	146	1.918E 00	2.800E-01	2.198E 00	5.663E 00	4.422E-01	6.107E 00
1.25	4.63	182	4.496E-01	2.574E-01	7.068E-01	1.664E 00	4.063E-01	2.071E 00
1.5	5.56	219	1.383E-01	2.396E-01	3.778E-01	6.351E-01	3.781E-01	1.013E 00
1.75	6.48	255	5.186E-02	2.250E-01	2.770E-01	2.825E-01	3.551E-01	6.375E-01
2.0	7.41	292	2.030E-02	2.127E-01	2.330E-01	1.274E-01	3.356E-01	4.630E-01
2.5	9.26	365	2.733E-03	1.926E-01	1.953E-01	2.254E-02	3.038E-01	3.263E-01
3.0	11.11	437	3.071E-04	1.765E-01	1.768E-01	3.504E-03	2.786E-01	2.822E-01
3.5	12.96	510	3.400E-05	1.632E-01	1.632E-01	5.595E-04	2.576E-01	2.582E-01
4.0	14.81	583	3.926E-06	1.517E-01	1.517E-01	9.271E-05	2.397E-01	2.398E-01
4.5	16.67	656	4.600E-07	1.417E-01	1.417E-01	1.542E-05	2.239E-01	2.239E-01
5.0	18.52	729	5.337E-08	1.328E-01	1.328E-01	2.517E-06	2.099E-01	2.100E-01
5.5	20.37	802	5.995E-09	1.247E-01	1.247E-01	3.959E-07	1.974E-01	1.974E-01
6.0	22.22	875	6.414E-10	1.174E-01	1.174E-01	5.948E-08	1.859E-01	1.859E-01

Table 8

ORBITAL RADIATION STUDY

(SOURCE: E. G. STASSINOPOULOS, NASA–GSFC, 1978)

ORBIT: SYNCHRONOUS–GEOSTATIONARY

(CIRCULAR, INCLINATION 0°, ALTITUDE = 35790 km, PARKING LONGITUDES = 160°W & 70°W)

			DOSE FOR 90 DAYS					
SHIELD THICKNESS (ALUMINUM)			PARKING LONGITUDE: 70°W			PARKING LONGITUDE: 160°W		
			ELECTRONS (OUTER ZONE)	BREMSSTRAHLUNG	TOTAL	ELECTRONS (OUTER ZONE)	BREMSSTRAHLUNG	TOTAL
z (gm/cm^2)	t (mm)	t (mils)	(rads$_{Al}$)	(rads$_{Al}$)	(rads$_{Al}$)	(rads$_{Al}$)	(rads$_{Al}$)	(rads$_{Al}$)
.1	0.37	15	2.525E 05	5.454E 01	2.525E 06	3.921E 05	8.781E 01	3.923E 05
.2	0.74	29	7.476E 04	4.318E 01	7.481E 04	1.286E 05	6.862E 01	1.287E 05
.3	1.11	44	2.821E 04	3.795E 01	2.823E 04	5.292E 04	6.014E 01	5.296E 04
.4	1.48	58	1.177E 04	3.457E 01	1.181E 04	2.368E 04	5.472E 01	2.373E 04
.5	1.85	73	5.356E 03	3.210E 01	5.388E 03	1.140E 04	5.079E 01	1.145E 04
.6	2.22	87	2.557E 03	3.021E 01	2.587E 03	5.745E 03	4.774E 01	5.792E 03
.7	2.59	102	1.259E 03	2.863E 01	1.287E 03	2.993E 03	4.525E 01	3.038E 03
.8	2.96	117	6.342E 02	2.732E 01	6.616E 02	1.607E 03	4.315E 01	1.651E 03
.9	3.33	131	3.267E 02	2.619E 01	3.528E 02	8.901E 02	4.135E 01	9.316E 02
1.0	3.70	146	1.726E 02	2.520E 01	1.978E 02	5.097E 02	3.980E 01	5.496E 02
1.25	4.63	182	4.046E 01	2.316E 01	6.362E 01	1.497E 02	3.657E 01	1.864E 02
1.50	5.56	219	1.244E 01	2.157E 01	3.400E 01	5.716E 01	3.403E 01	9.121E 01
1.75	6.48	255	4.668E 00	2.025E 01	2.493E 01	2.542E 01	3.196E 01	5.738E 01
2.0	7.41	292	1.827E 00	1.914E 01	2.097E 01	1.147E 01	3.021E 01	4.167E 01
2.5	9.26	365	2.459E-01	1.733E 01	1.758E 01	2.029E 00	2.735E 01	2.937E 01
3.0	11.11	437	2.764E-02	1.589E 01	1.592E 01	3.154E-01	2.508E 01	2.540E 01
3.5	12.96	510	3.060E-03	1.469E 01	1.469E 01	5.035E-02	2.319E 01	2.324E 01
4.0	14.81	583	3.533E-04	1.366E 01	1.366E 01	8.344E-03	2.157E 01	2.158E 01
4.5	16.67	656	4.140E-05	1.275E 01	1.275E 01	1.388E-03	2.016E 01	2.016E 01
5.0	18.52	729	4.803E-06	1.195E 01	1.195E 01	2.265E-04	1.890E 01	1.890E 01
5.5	20.37	802	5.395E-07	1.122E 01	1.122E 01	3.563E-05	1.776E 01	1.776E 01
6.0	22.22	875	5.772E-08	1.056E 01	1.056E 01	5.353E-06	1.673E 01	1.673E 01

Table 9

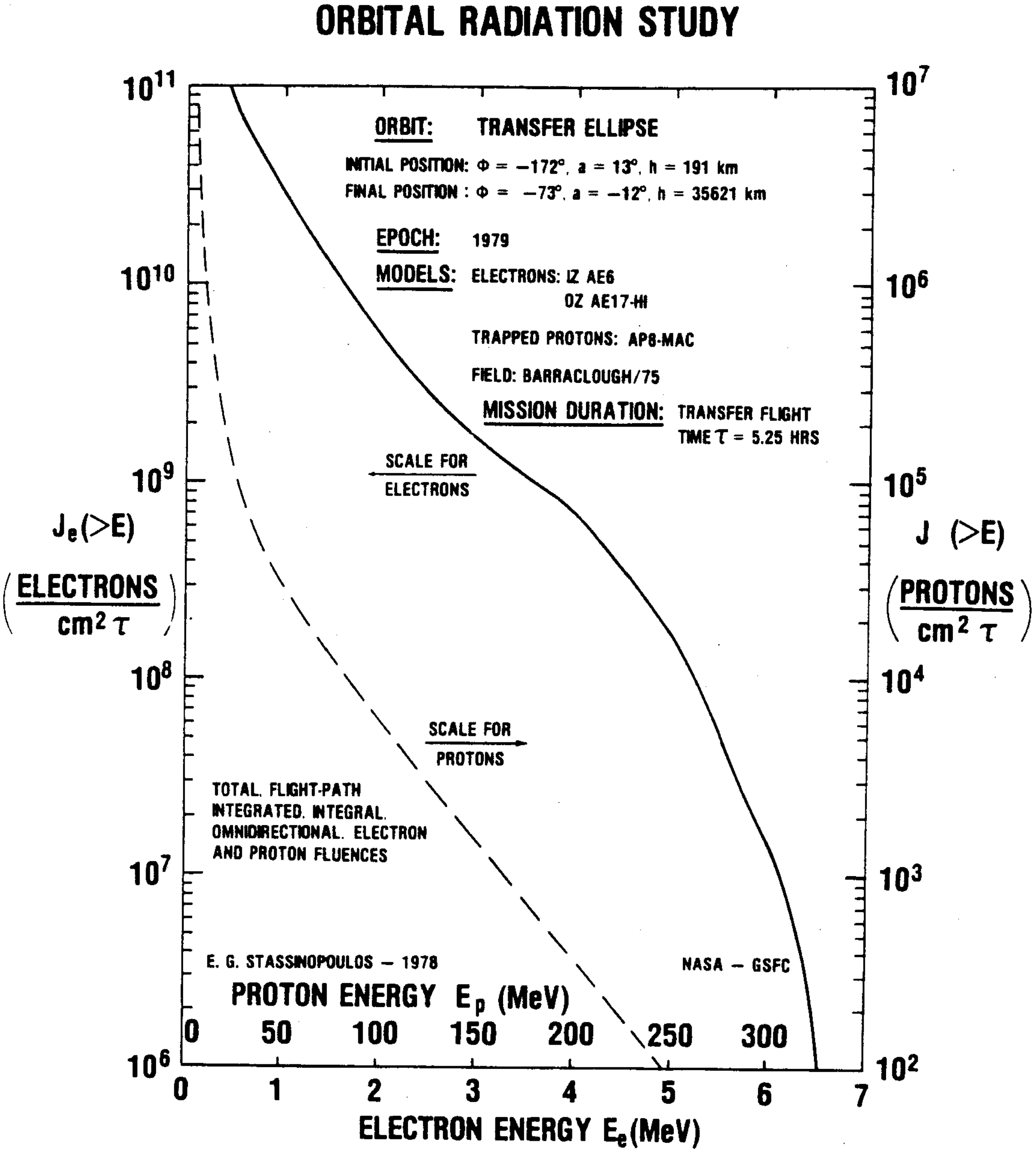

Figure 5. TE: Electron and proton spectral profiles of total accumulated fluences for solar maximum.

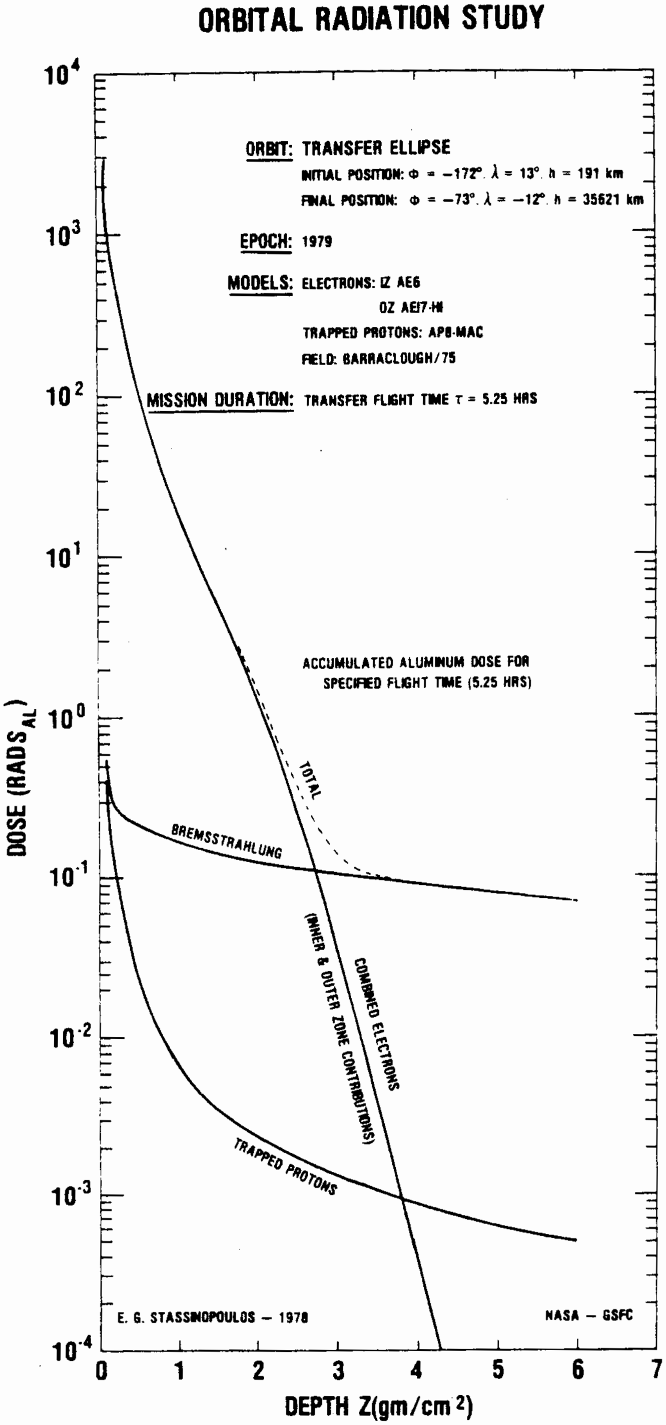

Figure 6. TE: Dose-depth curves for solar maximum.

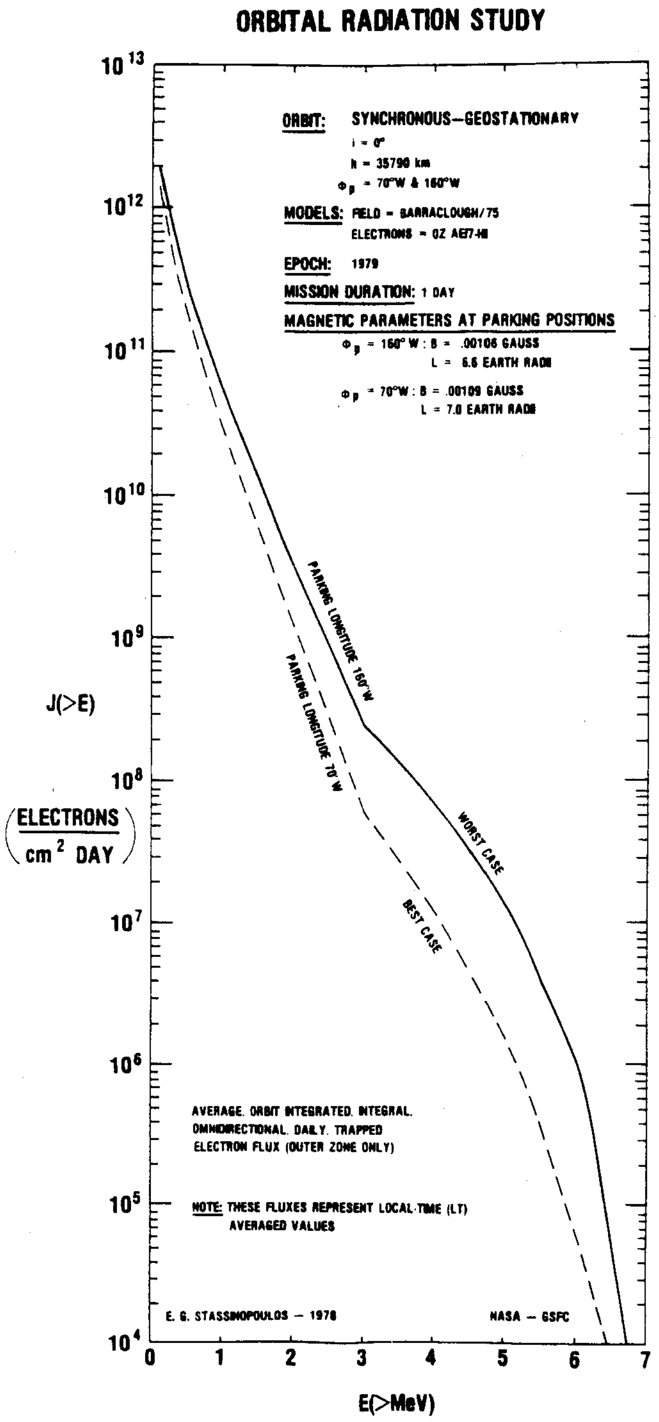

Figure 7. GEO: Electron spectral profiles for best and worst case longitudinal parking positions.

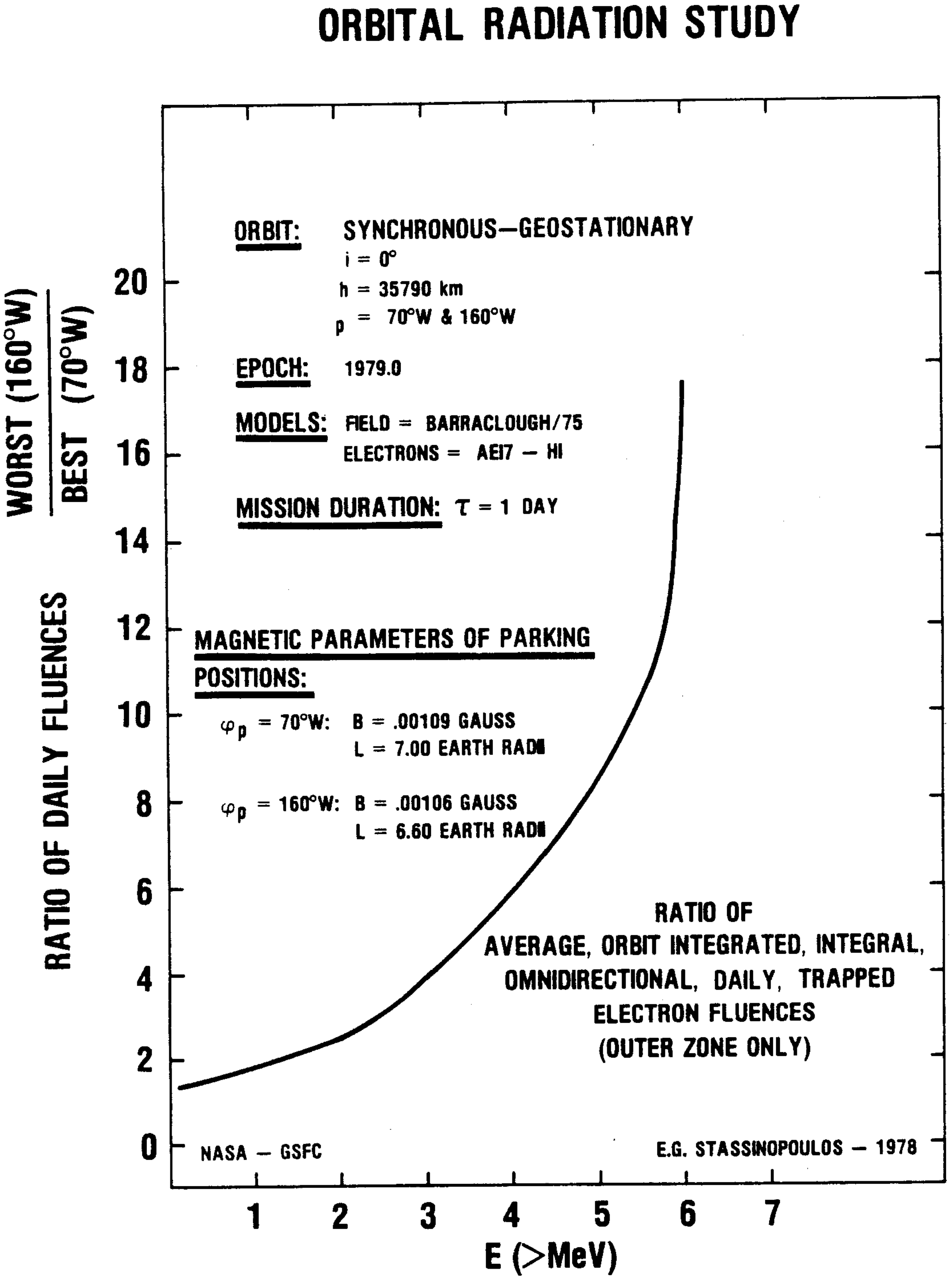

Figure 8. GEO: Ratio of worst to best case daily electron fluences.

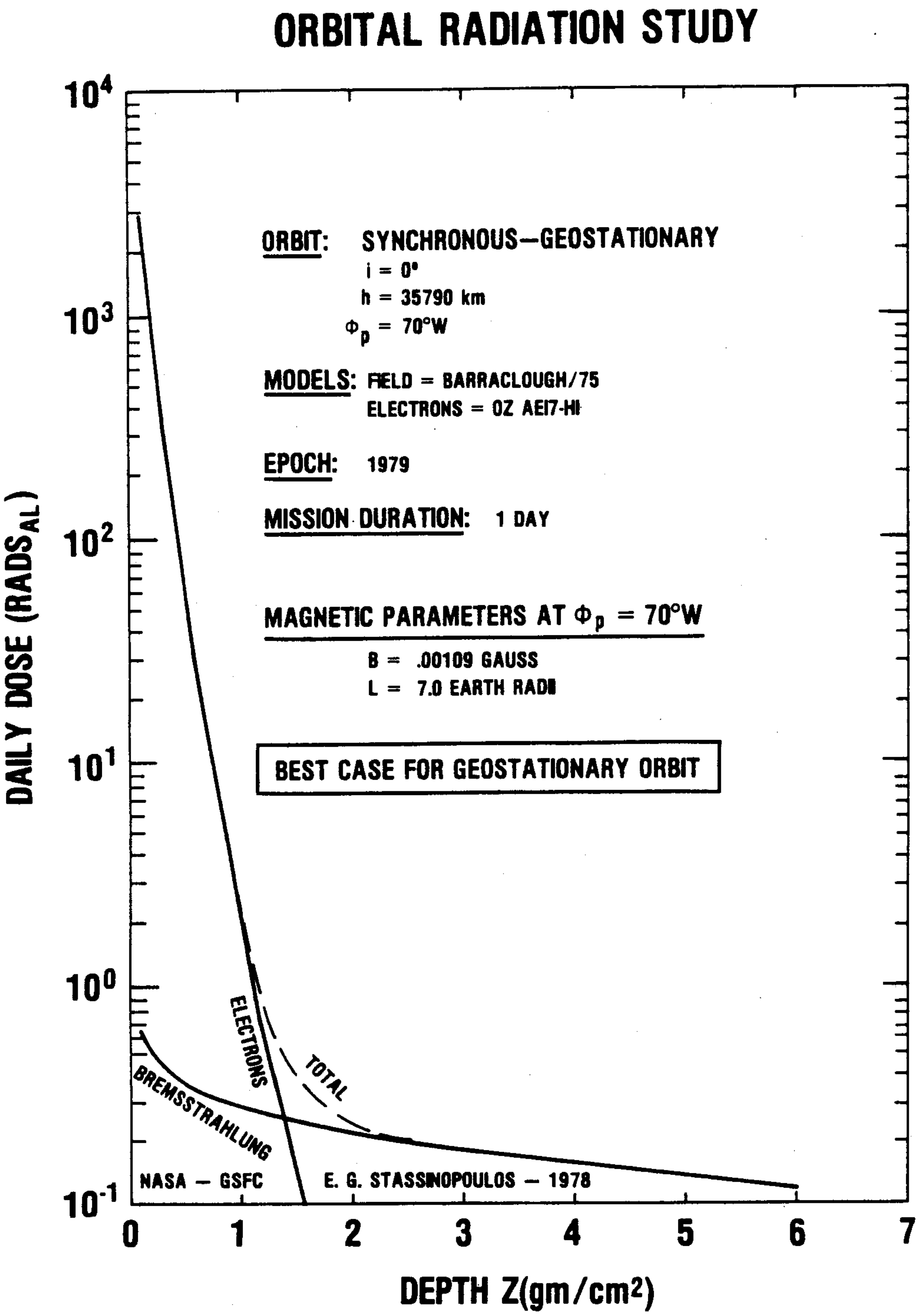

Figure 9. GEO: Dose-depth curves for best case in longitudinal parking position.

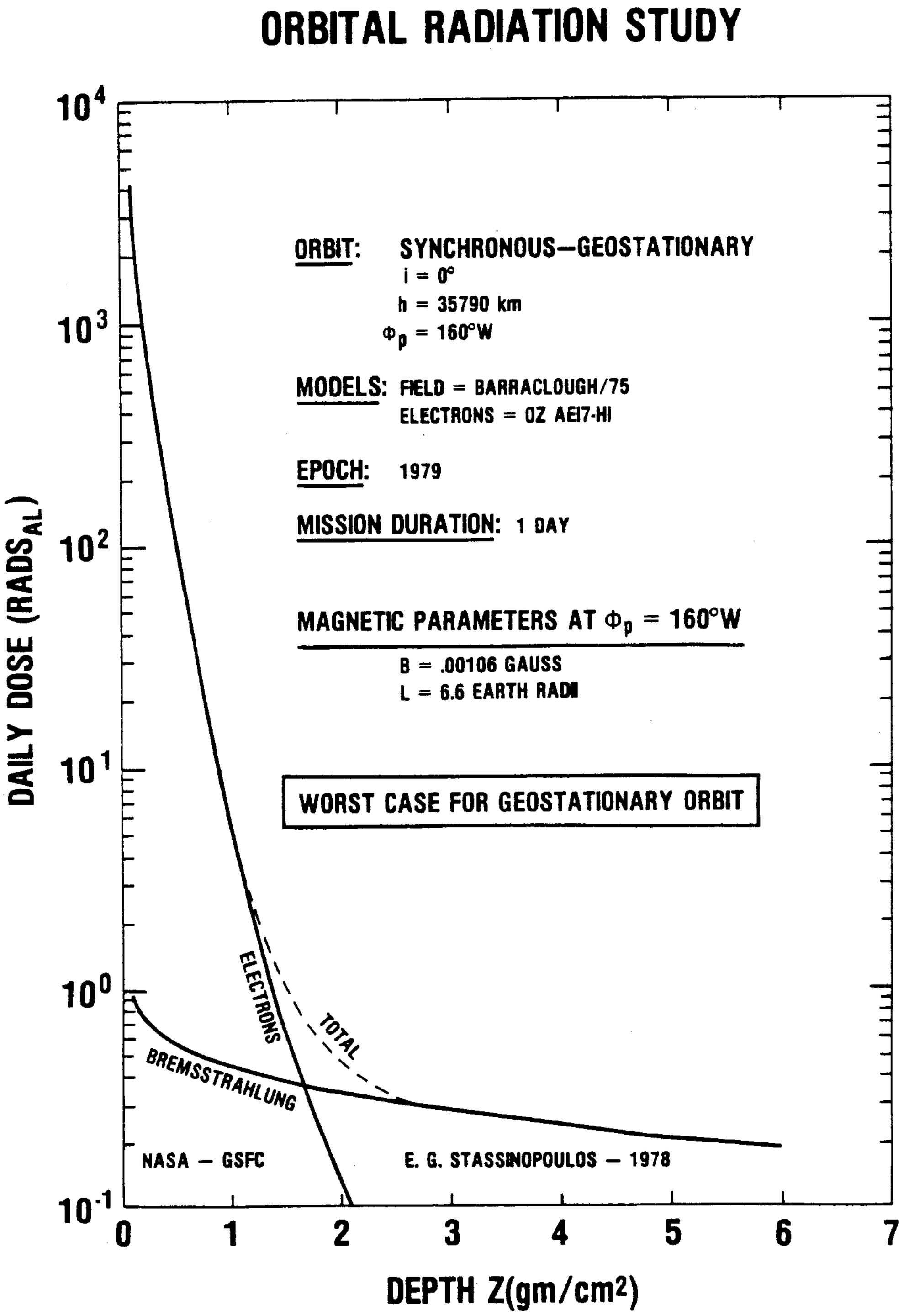

Figure 10. GEO: Dose-depth curves for worst case in longitudinal parking position.

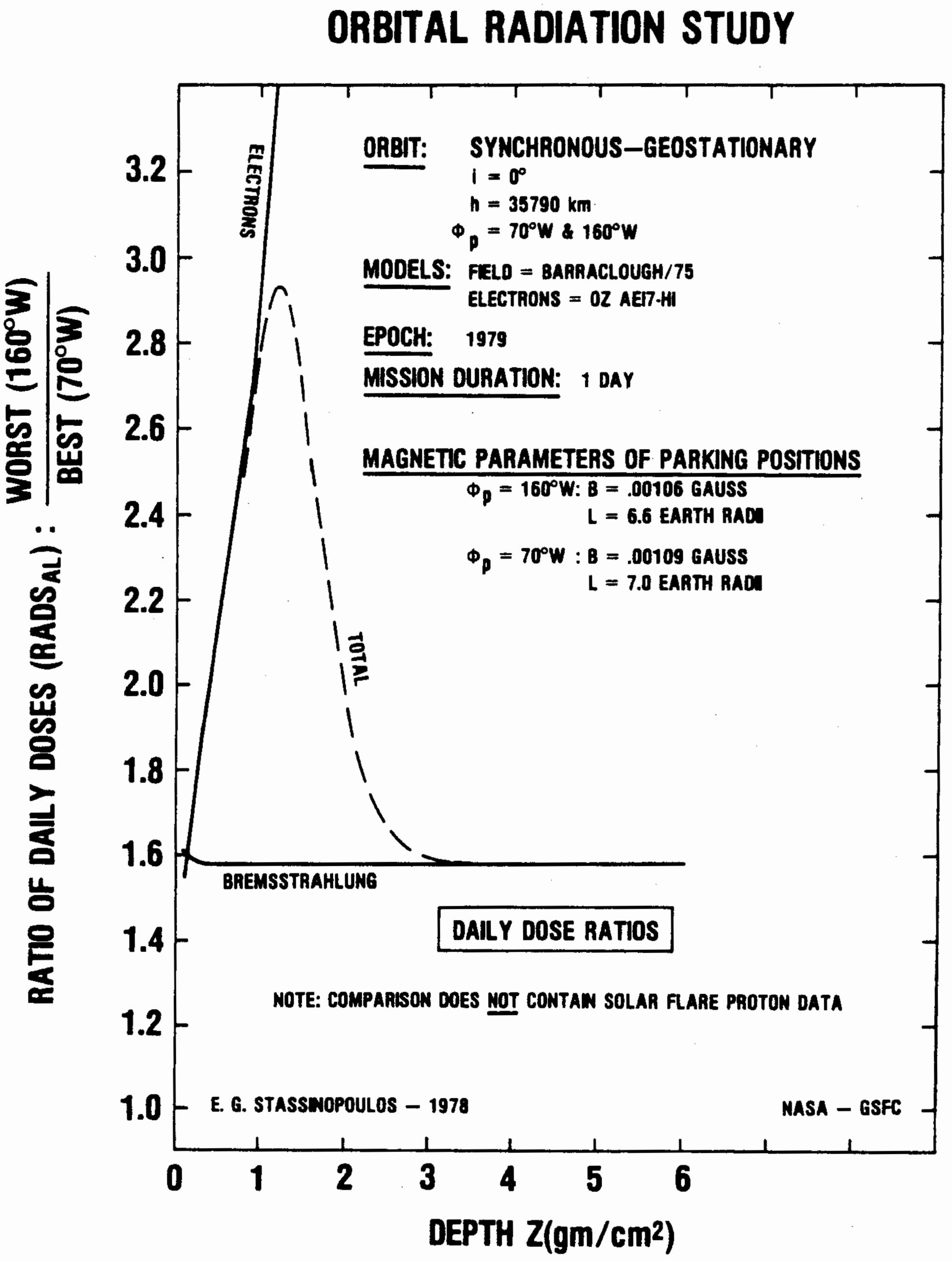

Figure 11. GEO: Ratio of worst to best case daily doses.

There is one other point of interest. The individual phases are not identically affected by variations in the environment, as summarized below.

	Substorm	Local Time	Solar Cycle
LEO	No	No	Yes
GEO	Yes	Yes	No
TE	Yes	Yes	Yes

Finally, LEO has only a partial and intermittent exposure to charged particle radiation (substantial amount of flux-free time), while TE and GEO have a continuous, uninterrupted exposure.

REFERENCES

Barraclough, D.R., Harwood, T.M., Leaton, B.R., and Malin, S.R.C. 1975. A model of the geomagnetic field at epoch 1975. Geophys. J. R. Astron. Soc. 43, 645-659.

Hassit, A., and McIlwain, C.E. March 1967. Computer programs for the computation of B and L (May 1966). Data User's Note NSSDC 67-27. National Space Science Data Center, Greenbelt, Maryland.

Hills, H.K., Chan, K.W., Teague, M.J., and Vette, J.I. 1979. Unpublished data.

Sawyer, D.M. and Vette, J.E. December 1976. AP8 trapped proton environment for solar maximum and solar minimum. NSSDC 76-06. National Space Science Data Center, Greenbelt, Maryland.

Stassinopoulos, E.G. 1979. The geostationary radiation environment. Submitted to J. Spacecr. Rockets.

Stassinopoulos, E.G. and Gregory, C.Z. 1979. UNIFLUX: A unified orbital flux integration and analysis system. To be published.

Stassinopoulos, E.G., Hebert, J.J., Butler, J.J. and Barth, J.L. May 1977. SOFIP: A short orbital flux integration program. NASA-GSFC Report X-601-77-114.

Stassinopoulos, E.G., Maale, K.A., and Hebert, J.J. December 1973. Trajectory computations with the NSSDC version of GEODYN and BLCONV programs, NSSDC 73-15. National Space Science Data Center, Greenbelt, Maryland.

Stassinopoulos, E.G. and Mead, G.D. February 1972. ALLMAG, GDMALG, LINTRA: Computer programs for geomagnetic field and field-line calculations. NSSDC 72-12. National Space Science Data Center, Greenbelt, Maryland.

Teague, M.J., Chan, K.W., and Vette, J.I. March, 1976. AE6: A model environment for trapped electrons for solar maximum. NSDDC/WDC-A-RES 76-04. National Space Science Data Center, Greenbelt, Maryland.

Teague, M.J., and Stassinopoulos, E.G. December, 1972. A model of the Starfish flux in the inner radiation zone. NASA-GSFC Report X-601-72-487.

Teague, M.J. and Vette, J.I. September 1972. The inner zone electron model AE-5. NSSDC 72-10. National Space Science Data Center, Greenbelt, Maryland.

Watts, J.W. and Burrell, M.O. June 1971. Electron and bremsstrahlung penetration and dose calculation. NASA TN D-6385.

A PRELIMINARY EVALUATION OF THE IONIZING-RADIATION ENVIRONMENT OF THE SATELLITE POWER SYSTEM

Richard Madey

Kent State University
Kent, Ohio 44242

SATELLITE POWER SYSTEM

A Satellite Power System (SPS) consists of many satellites in geostationary orbits. Each satellite generates electrical power from the sun, and then transmits that power to the earth by means of a microwave beam. Glaser (1968) first suggested this concept. Typically, each satellite provides 5,000 electrical megawatts (= 5 GW) of power at the utility interface on the ground. This power generation capacity is sufficient to meet the requirements of a major city such as Chicago or Los Angeles. An SPS program with a buildup rate to 300 GW would require 60 satellites with 5 GW capacity each.

Large solar cell arrays convert solar energy to dc electrical energy. Klystron power amplifiers, operating at a frequency of 2.45 GHz, perform the dc-to-rf conversion with an efficiency of 85% at a power level of 50 kW. A rectifying antenna (rectenna) on the ground collects and rectifies the rf energy with high efficiency (~ 80%) to dc electrical energy, which is then converted to 60 cycle ac for distribution by the utility system. The overall efficiency of the design in the current DOE/NASA Reference System Report (1979) is about 60%. At the earth's surface, the microwave beam has a maximum intensity of 23 mW/cm^2 (which is less than one-fourth of the solar constant) and an intensity of less than 1 mW/cm^2 outside the rectenna fenceline. The current U.S. exposure limit is 10 mW/cm^2.

Because of the large size and mass of each satellite, it is necessary to construct the satellites in orbit. A typical satellite has a solar collection area of about 55 km^2 and a mass of about 50-million kg. The most straightforward approach to the construction and installation of each satellite is to transport the flight hardware to a geostationary earth orbit and to construct the entire satellite there at the operational location. In this approach, orbit-transfer vehicles (OTVs) transport the necessary construction material from a low-earth orbit (LEO) to the geostationary-earth orbit (GEO). An alternative approach with potential cost savings is to construct the power generation modules for each satellite in the LEO and to use their power-generating capability to drive them to the GEO base by electric rocket propulsion. The trip time for electric rocket propulsion is 180 days. If the satellite is constructed only partially in LEO, the remainder of the material required to complete assembly and construction in GEO is transported to GEO with the power-generation modules. The LEO base is located[1] nominally in a 500-km circular orbit at the 28.5° inclination of the

---

[1] In the Boeing System Definition Study (1978), the LEO base has an altitude of 478 km and an inclination of 31°; the Rockwell International SPS Concept Definition Study (1978) treated a 500-km orbital altitude at approximately 28.5°; the Grumman Aerospace Corporation Study (1977) considered a 300 n mi (= 480 km) altitude and an inclination of 28.5°. The current concept in the Reference System Report (1979) developed jointly by DOE and NASA is largely a product of the two system definition studies conducted by Boeing (1978) and by Rockwell International (1978) combined with in-house efforts at the Johnson Space Center (JSC) and the Marshall Space Flight Center (MSFC), and several smaller contracted studies.

launch site at the Kennedy Space Center, and the GEO base in a geosynchronous (24-hour period) circular orbit at 0^0 inclination. The latter is presently the preferred inclination, although other inclinations are being considered (Reference Systems Report, 1979). A satellite in a circular geosynchronous orbit corotates with the geoid, as if rigidly attached, at an altitude of 35,800 km or about 5.6 earth radii. When the orbit lies in the equatorial plane, the satellite appears to be stationary to an earth observer at the equator in a meridian that is determined by conditions at injection. The satellite position at this meridian is called the parking longitude. Parking longitudes for an SPS program to meet U.S. power needs will be determined by the locations of the rectenna sites throughout the U.S. A report by Eberhardt (1977) discusses candidate locations for SPS rectifying antennas. The total crew size in orbit is about 700 at any one time, constructing two satellites simultaneously.[2] The construction crew works ten hours per day, six days per week. A personnel orbital transfer vehicle (POTV) delivers personnel and consummable supplies from LEO to GEO, and rotates personnel from GEO to LEO at 90-day intervals. A vehicle fueled with liquid oxygen and liquid hydrogen (LOX-LH_2) can make the trip in several hours.

RADIATION ENVIRONMENT

During the assembly, construction, operation, and maintenance of each SPS station, space workers will be exposed to the natural space radiation environments in LEO, in GEO, and in the region between

---

[2] The actual number of personnel in orbit will depend on options being evaluated (see Reference System Report, 1979).

these two orbits during orbital transfer. The penetrating radiations in space consist of protons and electrons in the geomagnetically trapped radiation, and energetic particles of solar and nonsolar origin.

The geomagnetically trapped radiation consists of two zones--an inner zone within about 2.8 earth radii and an outer zone beyond 2.8 earth radii. The region between 2 and 3 earth radii is sometimes called the electron "slot" because of a minimum in the electron intensity; there is no "slot" in the proton distribution. The average proton energy decreases continuously with increasing distance from the earth. The omnidirectional differential flux spectra of protons can be represented by an empirical exponential formula of the form

$$j(E) = C \exp(-E/E_0).$$

The characteristic proton energy E_0 varies approximately as the negative fifth power of the magnetic shell parameter L for the real geomagnetic field. For a perfect dipole field, L is the equatorial distance (measured in units of the earth's radius) to a particular magnetic field line. Time variations of the trapped proton spectrum occur as a result of atmospheric density changes with solar activity. A time-varying atmosphere causes time-varying losses since both the ionization-energy-loss rate and the nuclear-interaction-loss rate are proportional to the atmospheric density. The effect of the increase in the atmospheric density with increased solar activity is to reduce the trapped proton flux at the lower altitudes and lower energies.

The National Space Science Data Center at the NASA Goddard Space Flight Center prepares quantitative descriptions of the radiation environment in space from published data. As new data are compiled, existing models of the electron and proton radiation environments are revised and updated. The electron and proton models are referred to as the AE and AP series, respectively. Teague and Vette (1972) describe model AE-5 and Teague *et al*. (1976) describe model AE-6 for the electron environments in the inner zone during periods of minimum and maximum solar activity, respectively. Sawyer and Vette (1976) describe the AP-8 models for the trapped proton environment, which are designated AP-8 MIN and AP-8 MAX for periods of minimum and maximum solar activity. Based on the assimilation of new data, there has been a significant revision of the electron environment in the outer zone. The latest model is an interim model AEI-7 developed by Teague and Vette (1978) in two versions: AEI-7HI and AEI-7LO. The former model favors fits by Vampola to the data from the OVI-19 satellite; the latter is more representative of all data sets presently available to the National Space Science Data Center. Since measurements revealed more high-energy electrons than previously assumed, computed doses in the literature need to be revised upward.

Major solar particle events are more probable during a period of high solar activity than during the solar-quiet portion of the solar cycle; specifically, experience has shown that large events tend to occur on the ascending and descending portions of the solar cycle. Typically, only a few large events produce most of the total particle fluence during a solar cycle. The total fluence per steradian for solar cycle 20 from 1964 to 1975 is shown in the uppermost curve in Figure 1, which is based on data from King (1973). The fluence in this cycle was dominated by the three events occurring during the

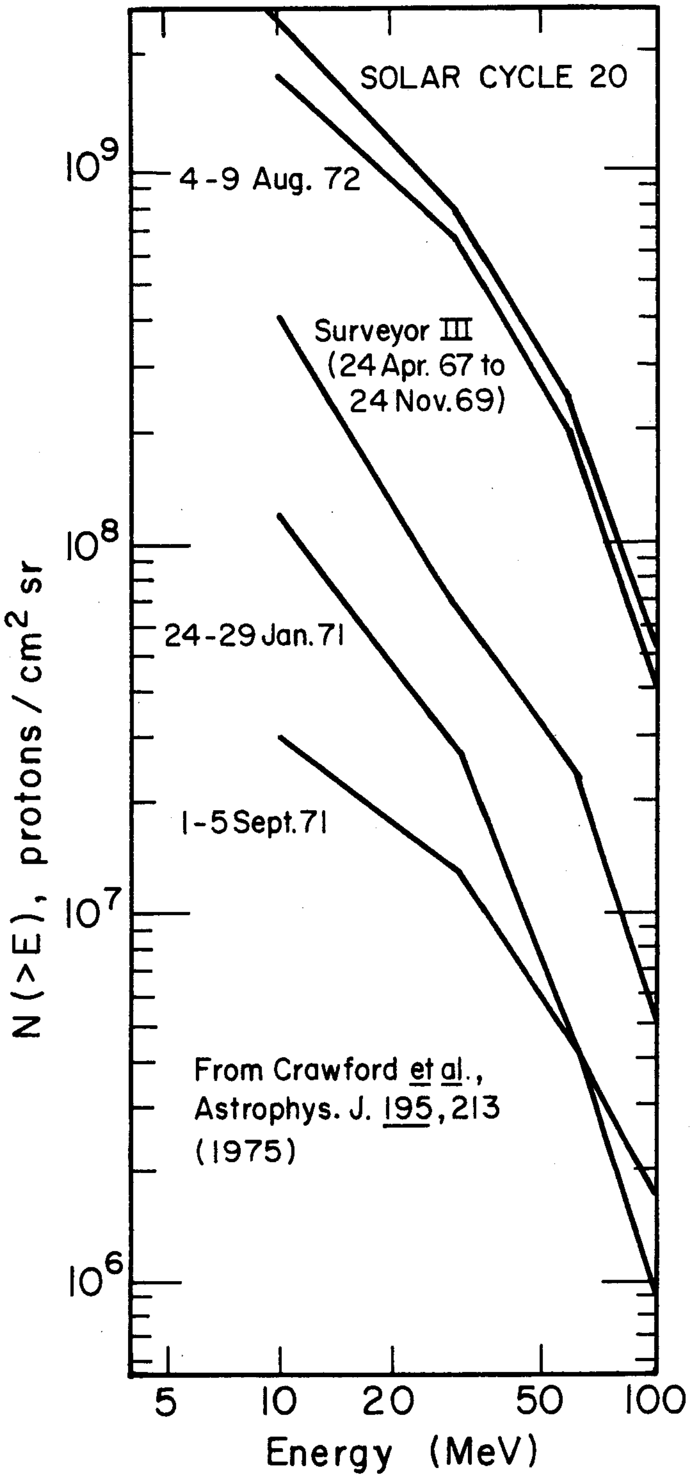

XBL759-4570

Figure 1. Integral proton fluences for solar particle events during solar cycle 20. (From King, 1973)

period from 4 to 9 August 1972. The curve labeled Surveyor III includes seven major events occurring during the period from 24 April 1967 to 24 November 1969. Fluences (or time-integrated flux densities) from the August 1972 events exceeded the accumulative total of all other cycle 20 events by about a factor of two for protons above 10 MeV and a factor of four for protons above 30 MeV. Integral fluence spectra for three major solar-particle events are shown in Figure 2, which is taken from Wilson and Denn (1976). This graph establishes the range of fluences from the largest events of solar cycles 19 and 20.

Comstock et al. (1966, 1969) measured the fluxes and energy spectra of the galactic cosmic-ray nuclei helium to iron at the time of minimum solar modulation (viz., October 1964 - November 1965). Based on the reported differential energy spectra of the various nuclei, Madey and McNulty (1969) represented the unidirectional differential flux spectra of nuclei by an inverse-power law in the total energy per nucleon E above E_1, and by a constant value in the kinetic energy per nucleon in the interval between T_0 and T_1:

$$n(E) = CE^{-\gamma} \qquad (E > E_1) \quad , \tag{1}$$

$$n(T) = C_1 \qquad (T_0 < T < T_1) \quad , \tag{2}$$

where

$$E(\text{GeV/nucleon}) = T\ (\text{GeV/nucleon}) + 0.9315 \quad . \tag{3}$$

The spectral exponent γ has an observed value of about 2.5. The representation in equation (2) is valid for a kinetic energy T_0 in the neighborhood of 100 MeV per nucleon. The value of the constant C_1 for oxygen, as reported by Comstock et al. (1966), is 5.4 nuclei/m^2-sec-sr-(GeV/nucleon) in the time interval from October to November 1964. The values of

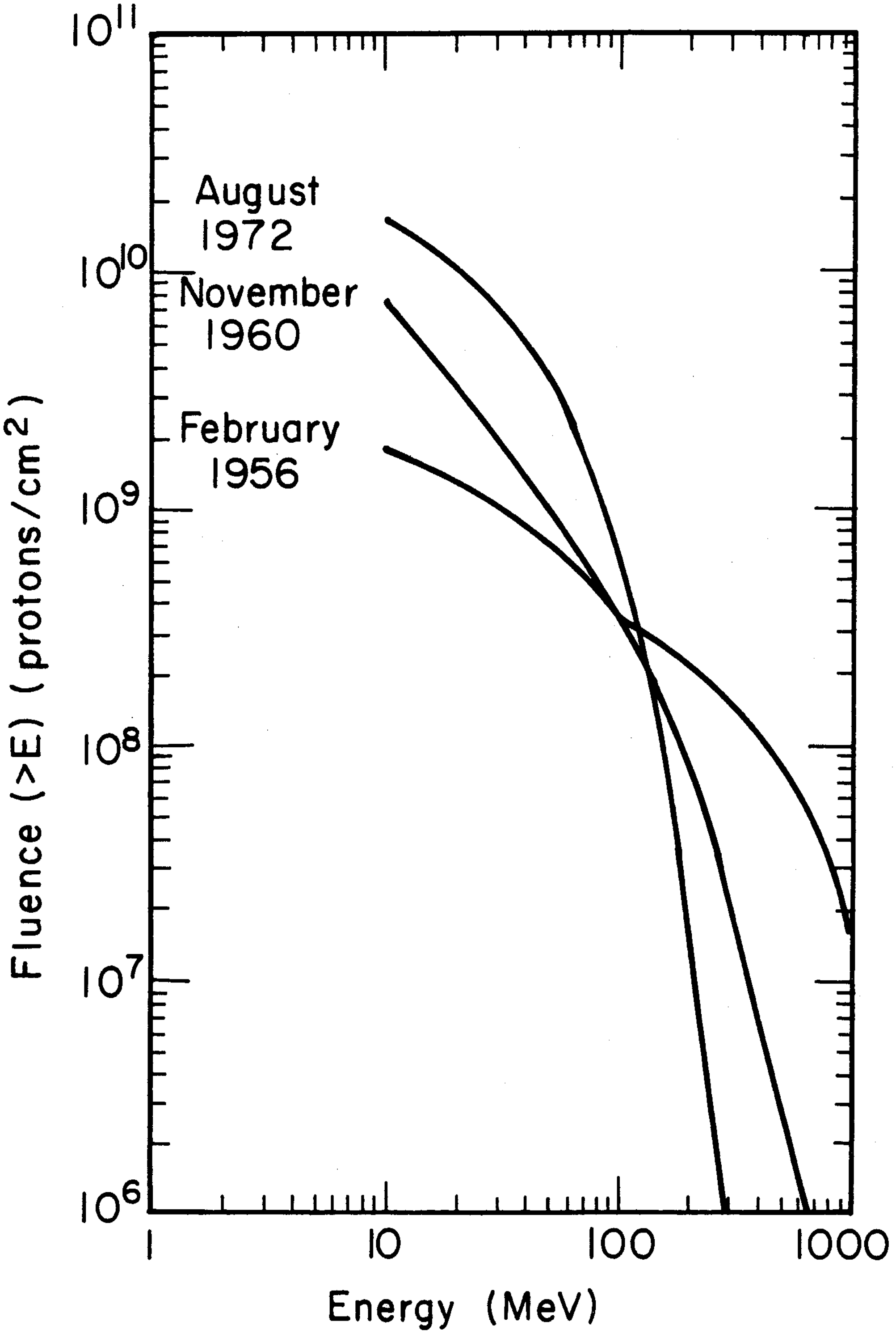

XBL7811-12343

Figure 2. Integral proton fluence spectra for the three solar particle events of February 1956, November 1960, and August 1972. (From Wilson and Denn, 1976)

C_1 for other nuclei come from measurements on the relative abundance of the elements in the cosmic radiation. There seems to be no significant change in the relative abundances with time even though the flux level changes with the solar cycle. Also, within the present experimental errors, the relative abundances appear to be independent of energy. The relative abundance of the nuclei in the cosmic radiation from the (IMP IV and OGO I) satellite measurements by the University of Chicago group are listed in Table 1 and plotted in Figure 3. The coefficient C in the high-energy portion of the differential flux equation (1) is given by Comstock _et al_. (1966) for some of the nuclei (namely, C, O, B, Ne, Mg, Si, and the Fe-Co-Ni group). These values for the coefficient C can be found in Table 1. For these nuclei, values for the total energy per nucleon E_1 can be found by equating equations (1) and (2):

$$E_1 = (C/C_1)^{1/\gamma} \qquad (4)$$

The values of E_1 are listed in Table 1. We have used equation (3) with $\gamma = 2.5$ to compute values for the coefficient C for the other nuclei for assumed (tabulated) values of E_1 and the measured values of C_1.

For $E > E_1$ (or $T > T_1$), the unidirectional integral flux spectra of the galactic cosmic-ray nuclei can be represented by the following power law:

$$N(>E) = \int_E^\infty n(E)dE = \frac{CE^{-(\gamma-1)}}{\gamma-1} \qquad (\text{for } E>E_1) \ . \qquad (5)$$

For $E_0 < E < E_1$ (or $T_0 < T < T_1$), the unidirectional integral flux

TABLE 1

Relative Abundance of Nuclei in the Cosmic Radiation and Parameters for Representing the Differential Flux Spectra at a Time of Minimum Solar Modulation.

Nucleus	Relative Abundance (× 10^3)	Coefficient C_1 [p/m^2-s-sr-(GeV-nuc^{-1})]	Coefficient C [p/m^2-s-sr(GeV-nuc^{-1})]	Total Energy E_1(GeV/nucleon)	Kinetic Energy T_1(GeV/nucleon)
${}_{2}\mathrm{He}$	4.2 ± 0.6	228 ± 32			
${}_{3}\mathrm{Li}$	19.5 ± 5	1.05 ± 0.03	2.8	1.485	.554
${}_{4}\mathrm{Be}$	6.5 ± 2.2	0.35 ± 0.12	0.94	1.485	.554
${}_{5}\mathrm{B}$	29 ± 6	1.6 ± 0.3	(4.3)	1.485	.554
${}_{6}\mathrm{C}$	100 ± 6	5.4 ± 0.3	(12)	1.376	.445
${}_{7}\mathrm{N}$	25.5 ± 2	1.4 ± 0.1	3.1	1.376	.445
${}_{8}\mathrm{O}$	100 ± 6	5.4 ± 0.3	(12)	1.376	.445
${}_{9}\mathrm{F}$	1.7 ± 0.2	0.092 ± 0.011	0.14	1.168	.236
${}_{10}\mathrm{Ne}$	17.5 ± 3	0.95 ± 0.16	(1.4)	1.168	.236
${}_{11}\mathrm{Na}$	4.1 ± 1.1	0.22 ± 0.06	0.25	1.064	.132
${}_{12}\mathrm{Mg}$	23 ± 1	1.2 ± 0.1	(1.4)	1.064	.132
${}_{13}\mathrm{Al}$	3.4 ± 0.4	0.18 ± 0.02	0.27	1.183	.251
${}_{14}\mathrm{Si}$	17 ± 3	0.92 ± 0.16	(1.4)	1.183	.251
${}_{15}\mathrm{P}$	1.95 ± 1.0	0.11 ± 0.06	0.16	1.170	.240
${}_{16}\mathrm{S}$	5.0 ± 1.3	0.27 ± 0.07	0.40	1.170	.240
${}_{17}\mathrm{Cl}$	1.01 ± 0.29	0.055 ± 0.016	0.081	1.170	.240
${}_{18}\mathrm{A}$	2.08	0.112	0.17	1.170	.240
${}_{19}\mathrm{K}$	1.37	0.074	0.11	1.170	.240
${}_{20}\mathrm{Ca}$	3.24 ± 0.65	0.17 ± 0.04	0.25	1.170	.240
${}_{21}\mathrm{Sc}$	1.25	0.068	0.10	1.170	.240
${}_{22}\mathrm{Ti}$	2.62	0.142	0.21	1.170	.240
${}_{23}\mathrm{V}$	2.38	0.129	0.19	1.170	.240
${}_{24}\mathrm{Cr}$	3.99 ± 1.25	0.215 ± 0.068	0.32	1.170	.240
${}_{25}\mathrm{Mn}$	2.65	0.143	0.21	1.170	.240
${}_{26}\mathrm{Fe}$-${}_{27}\mathrm{Co}$-${}_{28}\mathrm{Ni}$	8.15 ± 1.73	0.44 ± 0.09	(1.4)	1.589	.657

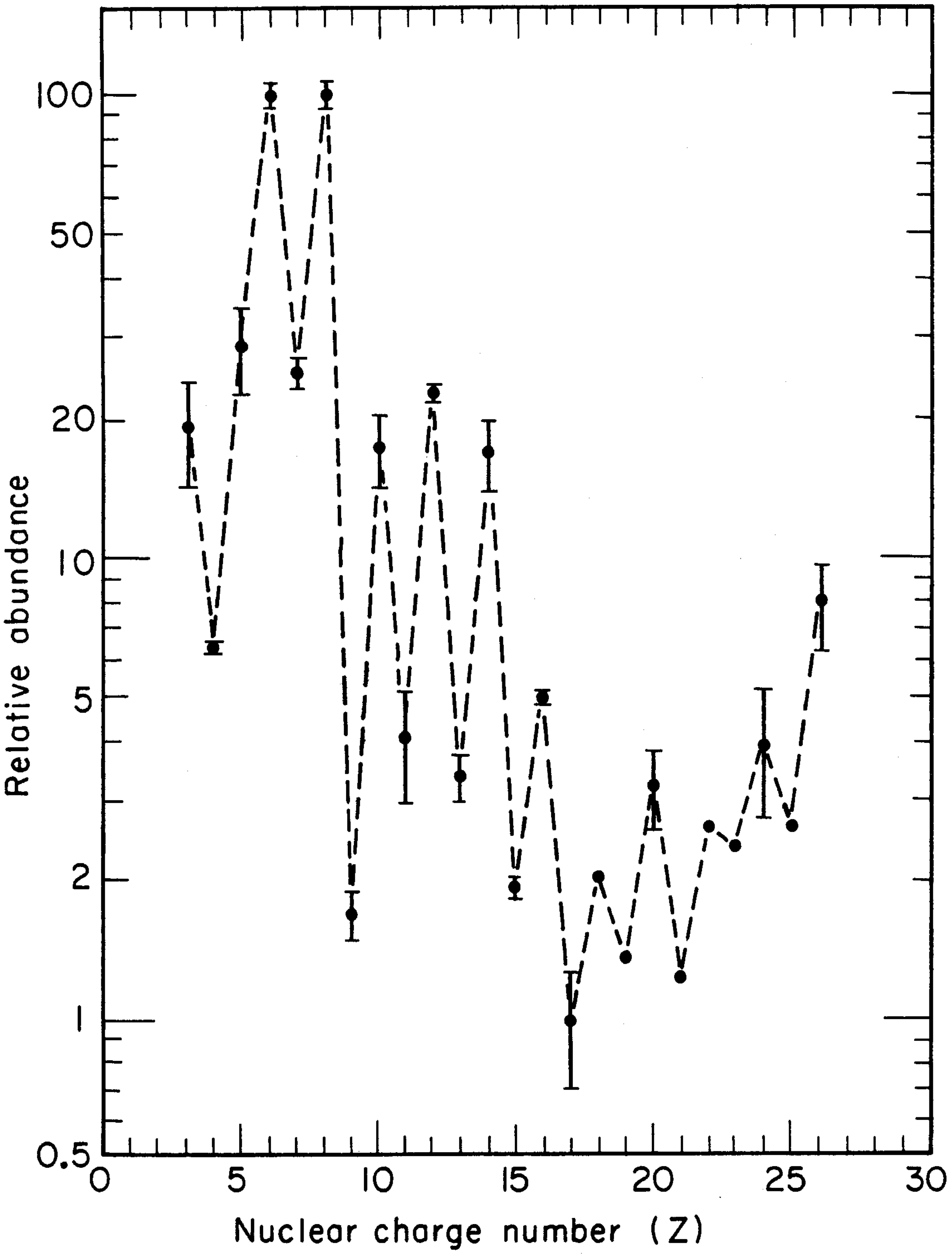

XBL7811-12344

Figure 3. The relative abundance of nuclei in the galactic cosmic radiation.

spectra of galactic cosmic-ray nuclei can be represented as follows:

$$N(>E) = \int_{E}^{E_1} n(E)\,dE + N(>E_1) = C_1(E_1-E) + \frac{C}{\gamma-1} E_1^{-(\gamma-1)}. \qquad (6)$$

Values of the coefficient $C/(\gamma-1)$ for integral flux spectra of galactic cosmic-ray nuclei for an integral spectral exponent $\gamma-1 = 1.5$ at a time of minimum solar modulation are listed in Table 2. Also listed in Table 2 are unidirectional integral fluxes above a total energy of 1.4 GeV per nucleon, which corresponds to a kinetic energy of 468 MeV per nucleon.

RADIATION DOSES

It is convenient to categorize radiation exposures of personnel in the SPS into two types: (1) predictable and (2) unpredictable. In the predictable category are exposures to the geomagnetically trapped protons, the geomagnetically trapped electrons and their associated bremsstrahlung, the proton and the helium fluxes in the galactic cosmic radiation, and radiations from isotopes or nuclear systems which may be carried aboard the SPS. Exposures from these sources are predictable in the sense that they can be calculated and measured. Control of exposures to these radiation sources involves tradeoffs between acceptable exposure levels and the weight of shielding. The unpredictable category includes exposures from solar-particle events, the high-charge ($Z > 2$) and high-energy (HZE) particle component of cosmic radiation, artificially trapped electrons and their associated bremsstrahlung, emergency extravehicular activities (EVA), and emergency repair of nuclear systems which may be carried aboard the SPS. The time of occurrence of solar particle

TABLE 2

Integral Flux Spectra of Galactic Cosmic-Ray Nuclei at a Time of Minimum Solar Modulation

Nucleus	Coefficient $C/(\gamma-1)$ p/m^2-s-sr-$(GeV/n)^{-(\gamma-1)}$	Flux Above Total Energy E $N(E > 1.40$ GeV/n) $(p/m^2$-s-sr)
${}_{3}$Li	1.88	1.04
${}_{4}$Be	0.627	.60
${}_{5}$B	2.87	1.58
${}_{6}$C	8.00	4.94
${}_{7}$N	2.07	1.28
${}_{8}$O	8.00	4.94
${}_{9}$F	0.091	.076
${}_{10}$Ne	0.933	.78
${}_{11}$Na	0.171	.43
${}_{12}$Mg	0.933	.97
${}_{13}$Al	0.183	.15
${}_{14}$Si	0.933	.77
${}_{15}$P	0.109	.091
${}_{16}$S	0.267	.22
${}_{17}$Cl	0.054	.045
${}_{18}$A	0.107	.090
${}_{19}$K	0.073	.061
${}_{20}$Ca	0.168	.14
${}_{21}$Sc	0.067	.056
${}_{22}$Ti	0.140	.17
${}_{23}$V	0.127	.11
${}_{24}$Cr	0.212	.18
${}_{25}$Mn	0.141	.18
${}_{26}$Fe-${}_{27}$Co ${}_{28}$Ni	0.933	.47
		19.37

events is unpredictable, and the biological effects of HZE particles are unknown. Also politically unpredictable are high-altitude nuclear detonations which inject copious numbers of electrons into the geomagnetic trapping region.

Several artificial radiation zones of trapped radiation were produced by the explosion of nuclear fission bombs at high altitudes during the period from 1958 through 1962. Electrons from the radioactive decay of fission fragments are the most important source of particles for artificial radiation zones. The Starfish explosion on 9 July 1962 produced an intense radiation zone which would not permit manned missions in low-earth orbits for months after the event (Hess, 1963). Since a nuclear explosion can produce an artificial radiation zone more intense than that produced by the Starfish explosion, the trapped radiation environment could be enhanced to the extent that the SPS mission would have to be aborted.

An estimate of the predictable radiation exposure from the natural radiation environment can be obtained by calculating the absorbed dose in aluminum behind a slab shield of aluminum versus the thickness of the shield. Figures 4 and 5 are the daily doses in aluminum computed for 2π geometry behind a semi-infinite slab shield by Stassinopoulos (1978) for LEO during periods of minimum and maximum solar activity, respectively, from trapped protons, trapped electrons and their associated bremsstrahlung. The dose in tissue is about 1.3 times that in aluminum. Note that the trapped protons constitute the dominant radiation hazard in LEO. The absorbed dose rate in tissue from trapped protons behind 300 mils ($=2$ g/cm^2) of aluminum is about 0.2 rad per day during

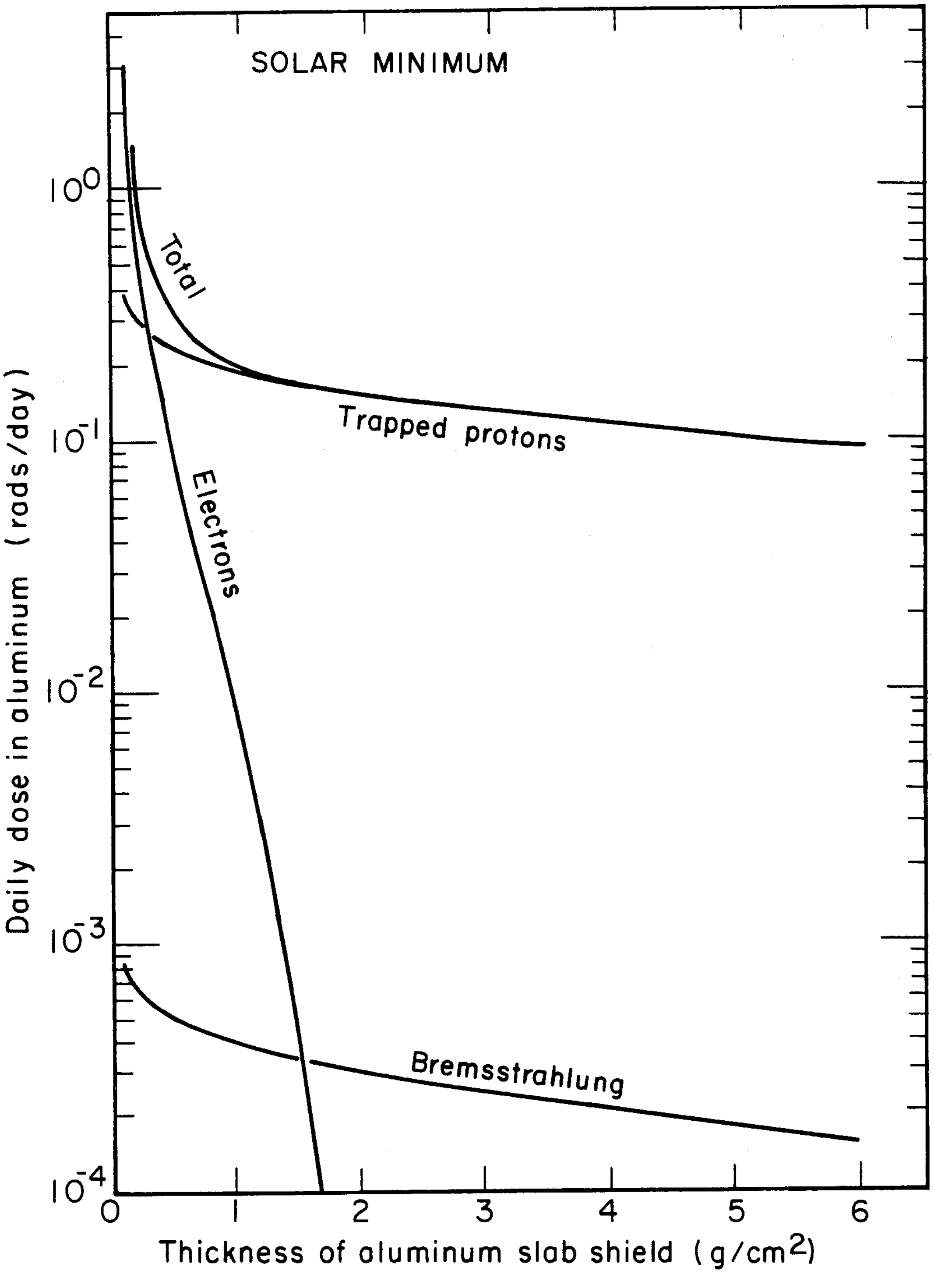

XBL 7811-12349

Figure 4. The dose in aluminum behind a slab shield of aluminum versus the aluminum shield thickness for a 500 km, 30° orbit during a period of minimum solar activity. (From Stassinopoulos, 1978)

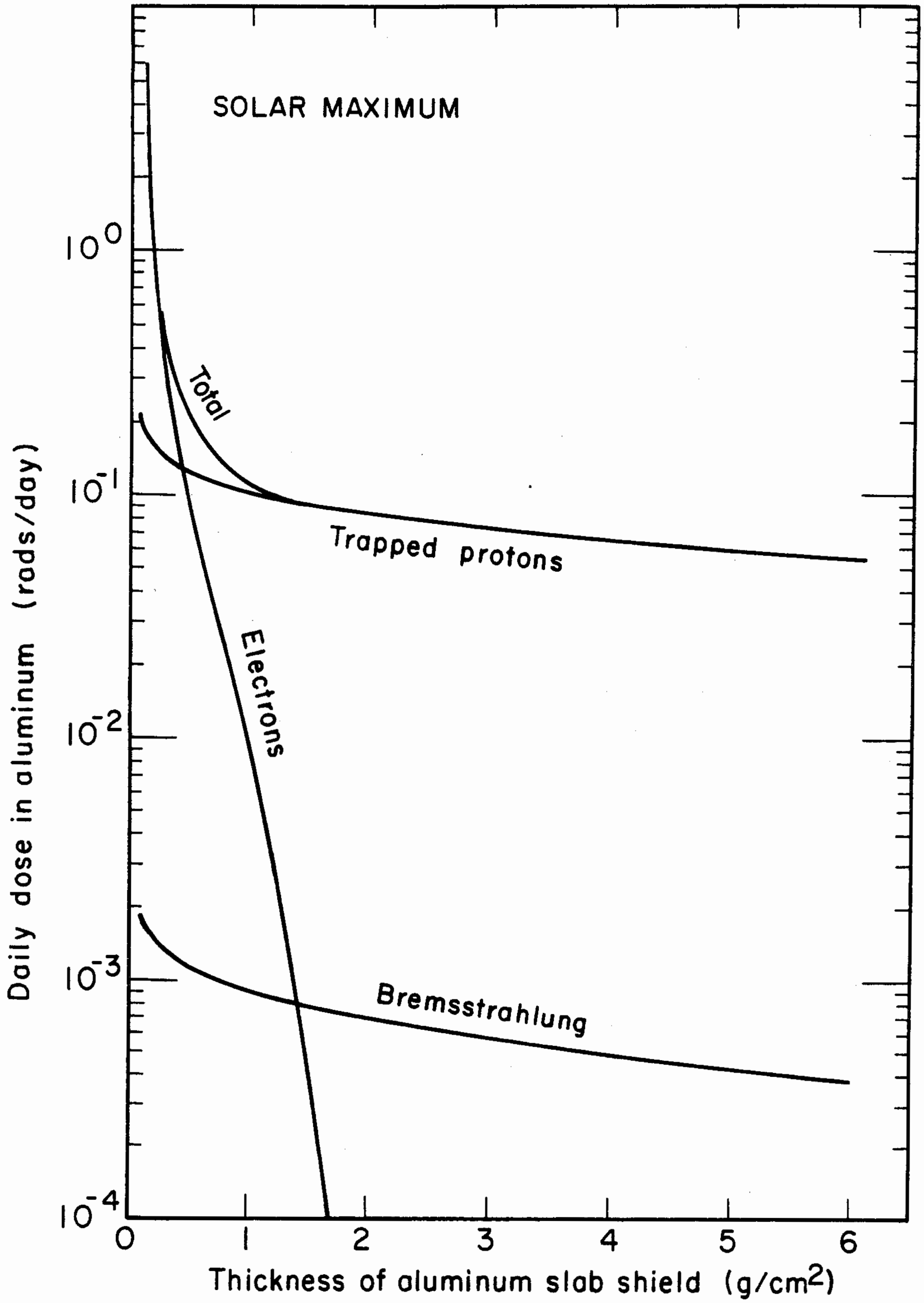

XBL7811-12350

Figure 5. The dose in aluminum behind a slab shield of aluminum versus the aluminum shield thickness for a 500 km, 30° orbit during a period of maximum solar activity. (From Stassinopoulos, 1978)

solar minimum and about 0.1 rad per day during solar maximum; the corresponding absorbed doses for a 90-day mission at the LEO base are about 20 rad during solar minimum, and about 10 rad during solar maximum.

For a 90-day mission at the LEO base, the dose from galactic cosmic radiation is less than 0.5 rad at any time during the solar cycle.

In Table 3, we summarize the daily dose rates and the 90-day mission doses behind 2 g/cm^2 (= 300 mils) of aluminum from predictable radiation sources in LEO.

TABLE 3

Daily Dose Rates and 90-day Mission Doses Behind 300 mils (= 2 g/cm^2) of Aluminum from Predictable Radiation Sources in a Low-Earth Orbit

Radiation Source	Dose Rate (rad/day)		Dose in 90 Days (rad)	
	solar min	solar max	solar min	solar max
Trapped electrons	$<10^{-3}$	$<10^{-3}$	<0.1	<0.1
Bremsstrahlung	$<10^{-3}$	$<10^{-3}$	<0.1	<0.1
Trapped protons	0.2	0.1	18	9
Galactic cosmic rays	0.004	0.003	0.4	0.3
TOTAL	0.2	0.1	18	9

Since the geomagnetic field diverts the paths of charged particles from the LEO satellite, exposure to energetic particles from solar flares is not of concern to space workers in the LEO satellite.

As a result of anomalously low values of the geomagnetic field in a region of the South Atlantic, the inner zone dips close to the earth in this region centered at 35^{o} west longitude and 35^{o} south latitude. Within the South Atlantic Anomaly (SAA), electrons and protons dip close enough to the earth to irradiate a satellite in LEO during portions of those orbit tracks that traverse the SAA. Each exposure in the SAA lasts a few minutes out of any single 90-minute orbital revolution. Since most LEO trajectories in a 24-hour period miss the SAA entirely, there is no exposure to inner-zone radiation for the majority of a 24-hour period. Thus, there is ample time during these exposure-free periods for space workers to undertake extra vehicular activity (EVA). If a space worker must engage in unscheduled EVA and passes through the SAA, then that worker would receive a skin dose of 0.3 rad behind a suit of thickness 0.2 g/cm^2 aluminum-equivalent for a "worst case" single traversal through the heart of the SAA. This dose estimate is about the same during periods of maximum and minimum solar activity because, from the data in Figures 4 and 5, the higher dose from trapped electrons during solar maximum compensates for the lower dose from trapped protons.

During the transfer from LEO to GEO, personnel will pass through the peak intensity regions of the inner and outer zones of the trapped radiation. Since the transit time of several hours for the SPS mission is relatively slow compared with several minutes for the Apollo mission, the potential exposure is great. Stassinopoulos (1979) calculated the fluence of trapped electrons and protons encountered during a

5.25-hour orbital transfer for specific initial and final positions on the orbital-transfer ellipse, and then calculated the absorbed dose behind a slab shield of aluminum versus the thickness of the shield. The absorbed dose for a round trip from LEO to GEO and back to LEO for the specified orbital-transfer ellipse is 3 rad behind 2 g/cm^2 aluminum and 0.2 rad behind 5 g/cm^2 aluminum. For a different orbital-transfer ellipse, the absorbed dose might be higher or lower by perhaps as much as several orders of magnitude. Trapped electrons contribute the major portion of the total dose behind 2 g/cm^2 aluminum, and electron bremsstrahlung dominates the dose behind shielding thicknesses greater than about 3 g/cm^2 aluminum.

At the altitude of geostationary orbits, the trapped electrons and the energetic particles from solar flares are the radiation components of major concern to space workers; trapped protons do not present a radiation hazard to personnel because the protons are not energetic enough to penetrate even the thinnest spacesuit. Trapped electron fluxes at geosynchronous altitude undergo large temporal fluctuations which can change by orders of magnitude in hours. For missions of extended duration in GEO, a local time-averaged energy-flux spectrum is appropriate for assessing the radiation exposure; however, the local time dependence of the ambient electron flux must be taken into account for short-term EVA. The short-term variations of the trapped electron fluxes constrain EVA and affect radiation shield requirements. It is necessary to take into account the maximum intensities of the trapped electrons in determining minimum requirements of the vehicle shield.

An important part of the radiation protection design for the GEO base involves the hazard from solar particle events. The geomagnetic field in GEO is too weak to afford shielding against energetic particles from solar flares. Protons above 10 MeV have direct access to this region of the geomagnetic field. While a time-averaged environment from solar particle events may be used for assessing the radiation damage to materials, personnel must be protected from the radiation effects of an individual, large solar-particle event such as that of August 1972. Rossi and Stauber (1977) calculated the dose-equivalent (in rem) in tissue received behind varying thicknesses of aluminum from the proton component of a model flare that approximates the integral flux and spectral shape of the August 1972 event. They used the flux spectrum from King (1973). Figure 6 is a plot of the total tissue dose-equivalent (in rem) versus the thickness of aluminum (in g/cm^2). This calculation indicates that about 40 g/cm^2 aluminum is needed to reduce the proton skin dose equivalent to 25 rem. The dose-equivalent includes contributions from secondary neutrons and protons produced in spallation and evaporation processes. The secondary particle contribution grows with increasing shield thickness and becomes greater than the primary proton dose behind 40 g/cm^2 aluminum.

Wilson and Denn (1976) calculated the dose and the dose-equivalent in a tissue sphere as a function of time during the solar particle event of 4 and 5 August 1972. Figure 7 is a plot of the fluence spectra from the August 1972 solar particle event as a function of energy for various times during the event. The lowest curve is the accumulated fluence approximately 40 minutes after the observation of the optical

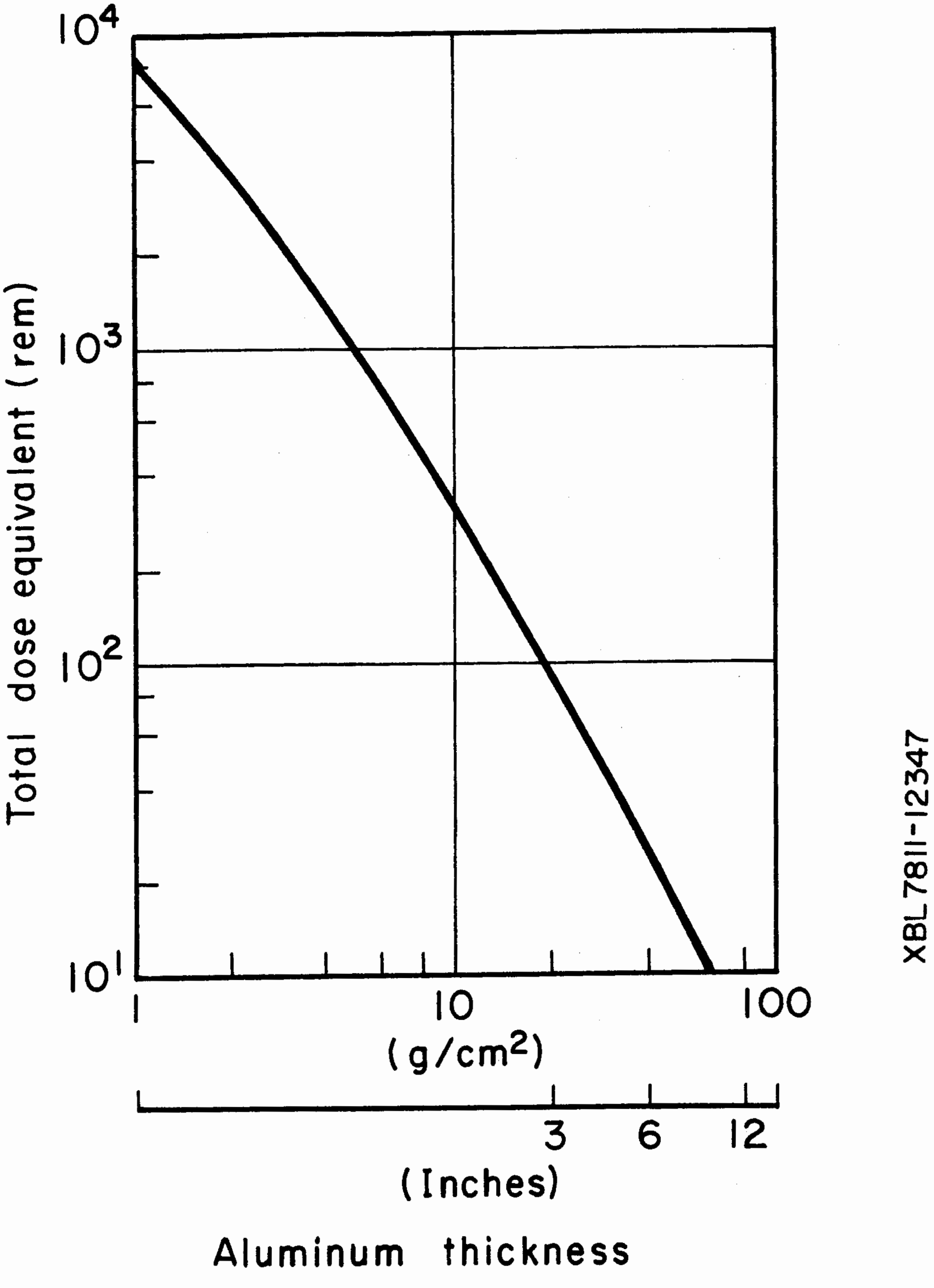

Figure 6. The total dose-equivalent in tissue from the solar proton event of August 1972 versus the thickness of aluminum shielding. (From Rossi and Stauber, 1977)

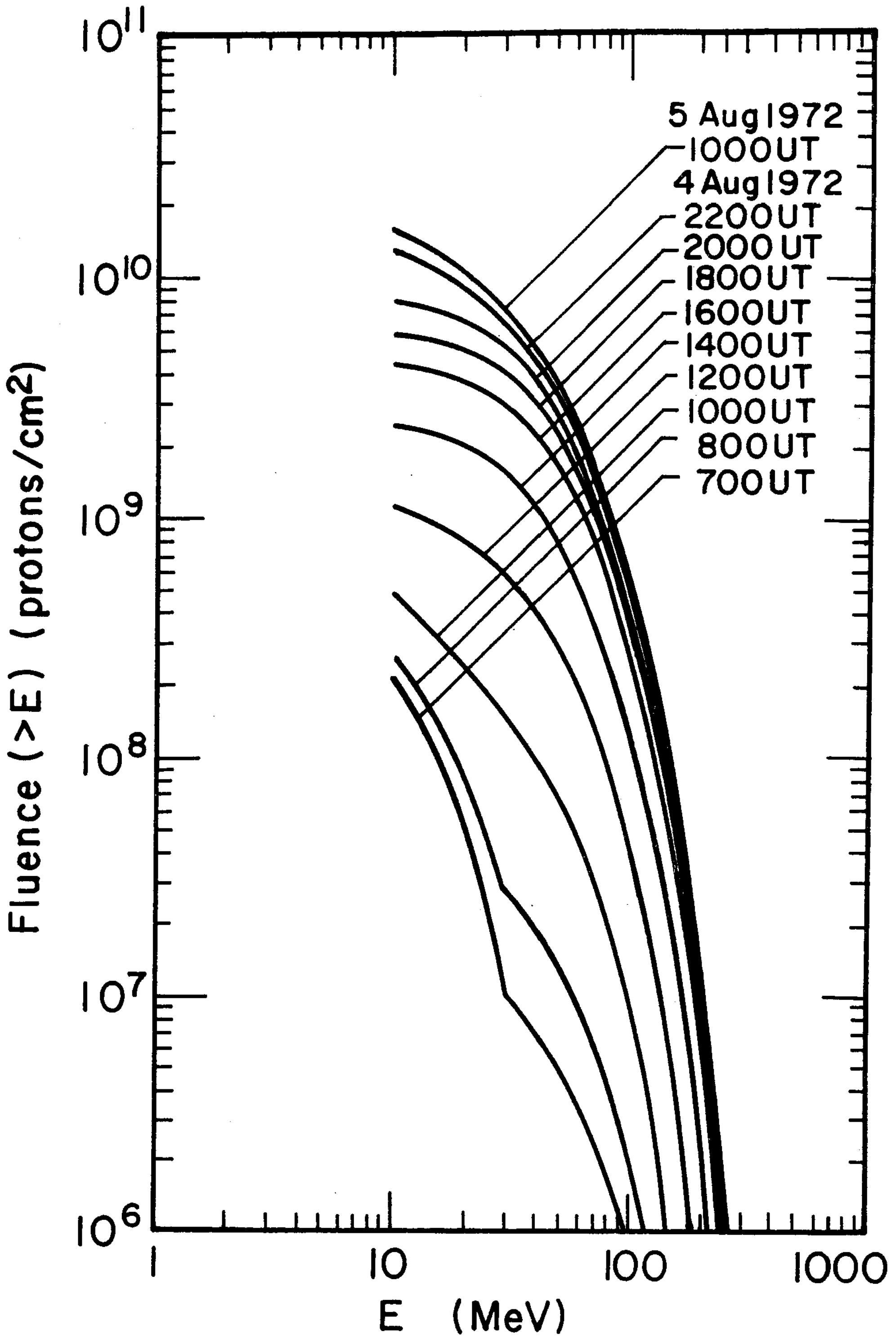

XBL 7811-12346

Figure 7. Fluence spectra from the August 1972 solar particle event as a function of time. (From Wilson and Denn, 1976)

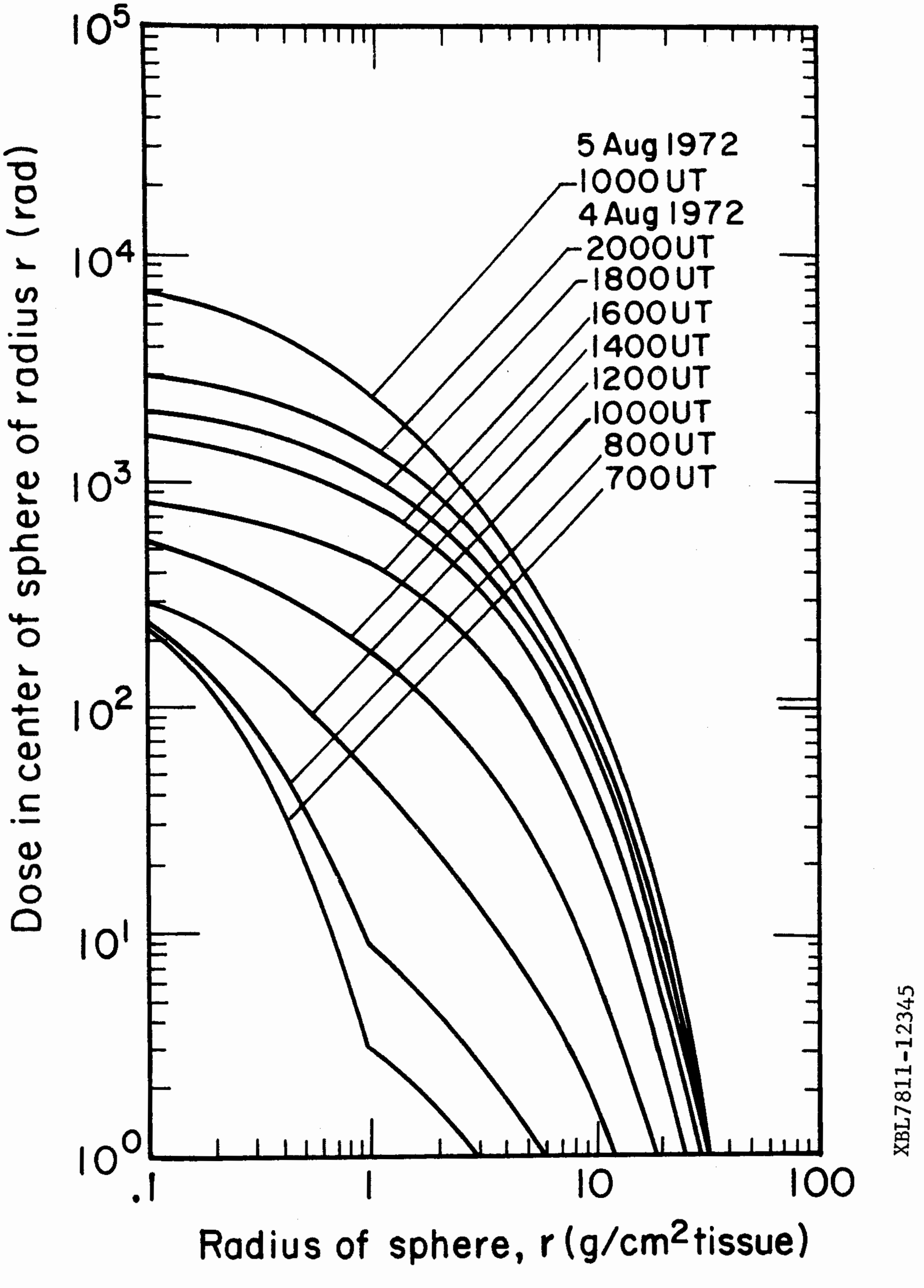

Figure 8. Absorbed dose at the center of a tissue sphere as a function of time during August 4 and 5, 1972, versus the radius of the sphere. (From Wilson and Denn, 1976)

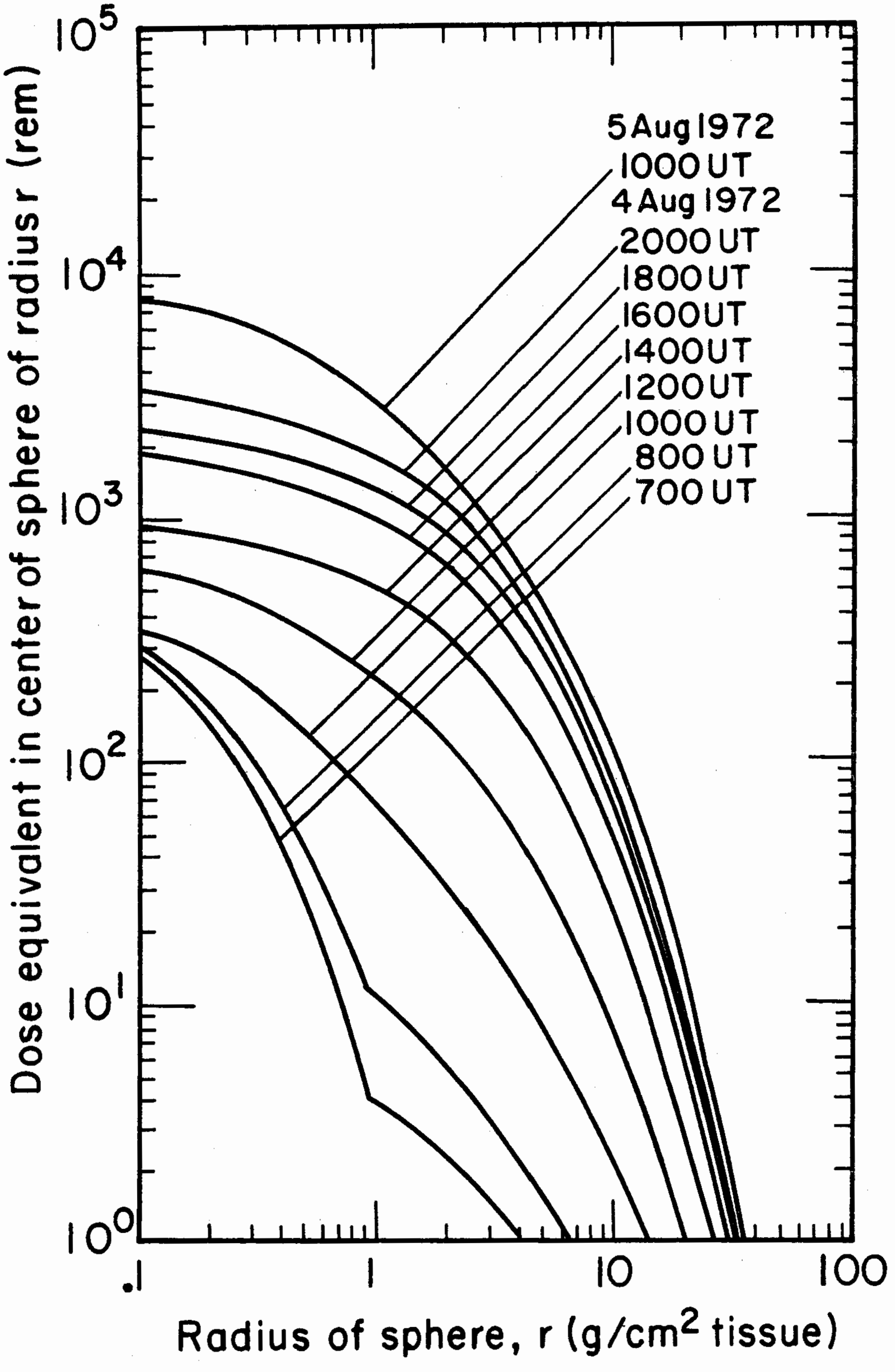

XBL7811-12348

Figure 9. Dose-equivalent at the center of a tissue sphere as a function of time during August 4 and 5, 1972, versus the radius of the sphere. (From Wilson and Denn, 1976)

flare on August 4. The source of the low-energy fluence above the break in the curve is protons from the earlier event on August 2. The high-energy shoulder in this curve indicates the onset of energetic particles from the event on August 4. The other curves show the fluence accumulated during the succeeding 15 hours of August 4 and the next 12 hours to 1000 UT on August 5 when the event was nearly over. These curves were based on IMP data below 60 MeV and an extrapolation according to exp (-E/28) above 60 MeV. This spectral extrapolation is consistent with the spectrum reported by King (1973) and the experimental measurement of Brazilevska *et al*. (1973). Figures 8 and 9 are the dose and the dose-equivalent, respectively, accumulated at the center of a tissue sphere versus the radius of the sphere for various times during August 4 and 5, 1972. These curves include the contributions from secondary neutrons and protons produced by the primary protons interacting with tissue. The dose-equivalent curve at 1000 UT on 5 August 1972 indicates that about 30 g/cm^2 tissue attenuates the dose-equivalent to 25 rem at the center of the tissue sphere. This result is consistent with that reported by Rossi and Stauber (1977) since tissue is more effective in stopping protons than aluminum; for example, a 220 MeV proton has a range of 30 g/cm^2 in tissue and 39 g/cm^2 in aluminum.

Wilson and Denn (1976) take into account self-shielding of marrow, skin, lens, and testes by body tissues. In Table 4 they calculate the time required to reach the 30-day exposure limits starting from the time of onset of energetic particles from the flare of 4 August 1972. With a shield thickness capable of stopping protons of about 120 MeV corresponding to an aluminum thickness of 13.7 g/cm^2, they find that the additional self-shielding is enough to keep the dose-equivalent below the 25-rem limit for the marrow and the 75-rem limit for the skin; however, the 37-rem limit for the eye lens and the 13- rem limit for the testes are reached in about 12 and 13 hours, respectively. Personal shielding in the form of goggles to protect the eye lens and lead undergarments to protect the testes would keep the weight of the storm shelter from increasing.

For the present workshop, Stassinopoulos (1979) updated his previous (1973) assessments of the radiation doses to personnel in synchronous satellites. His updated calculations for the electron environment in GEO are based on the model AEI-7, whereas his 1973 calculations used the AE-4 model. He calculated the daily doses and the 90-day mission doses behind a slab shield of aluminum versus the thickness

TABLE 4

Time Required to Reach Exposure Limits Starting from the Time of Onset of the August 4 Flare

Shield Thickness (g/cm^2 tissue)	Marrow (hr)	Skin (hr)	Lens (hr)	Testes* (hr)
0.2	6.0	3.0	1.9	4.4
0.4	6.1	3.5	2.4	4.9
1	6.3	4.7	3.6	5.2
5	8.9	8.0	6.5	7.3
10	∞	∞	11.7	12.7

*Values are overestimated since the testes dose is taken to be the same as the marrow dose.

of the shield. The results depend on the parking longitude because of the asymmetry of the geomagnetic field. The worst position is at 160° west longitude; the best, at 70° west longitude. Figure 10 is a plot of the daily doses in aluminum as a function of aluminum thickness for the worst position. In Table 5, we summarize the time-averaged daily dose rates and 90-day mission doses behind 300 mils (= 2 g/cm^2) of aluminum from predictable radiation sources for the best and worst parking longitudes in a geostationary orbit. More detailed information on the analysis of the radiation environment in GEO is contained in a companion paper by Stassinopoulos (1979).

There is a need to monitor and evaluate exposure to HZE particles during an extended mission in space because their biological effects are unknown. The dominant contribution to the fluence of HZE particles comes from the galactic cosmic radiation rather than from solar-particle events. Since the conventional absorbed dose is the integral of the product of the differential (in energy) flux spectrum and the energy deposition rate, the conventional absorbed dose is small. Curtis (1976) estimated the absorbed dose rates from galactic cosmic rays at roughly 10 rad per year with 35% coming from particles with $Z > 2$, and 10% from particles with $Z > 20$.

RADIATION EXPOSURE LIMITS

Radiation exposure limits in current use for the SPS mission are listed in Table 6. The Space Science Board of the National Academy of Sciences (1970) proposed these exposure limits to serve as radiation-protection guides and constraints for vehicle-design studies and mission planning. The recommended exposure limits assume that the space mission

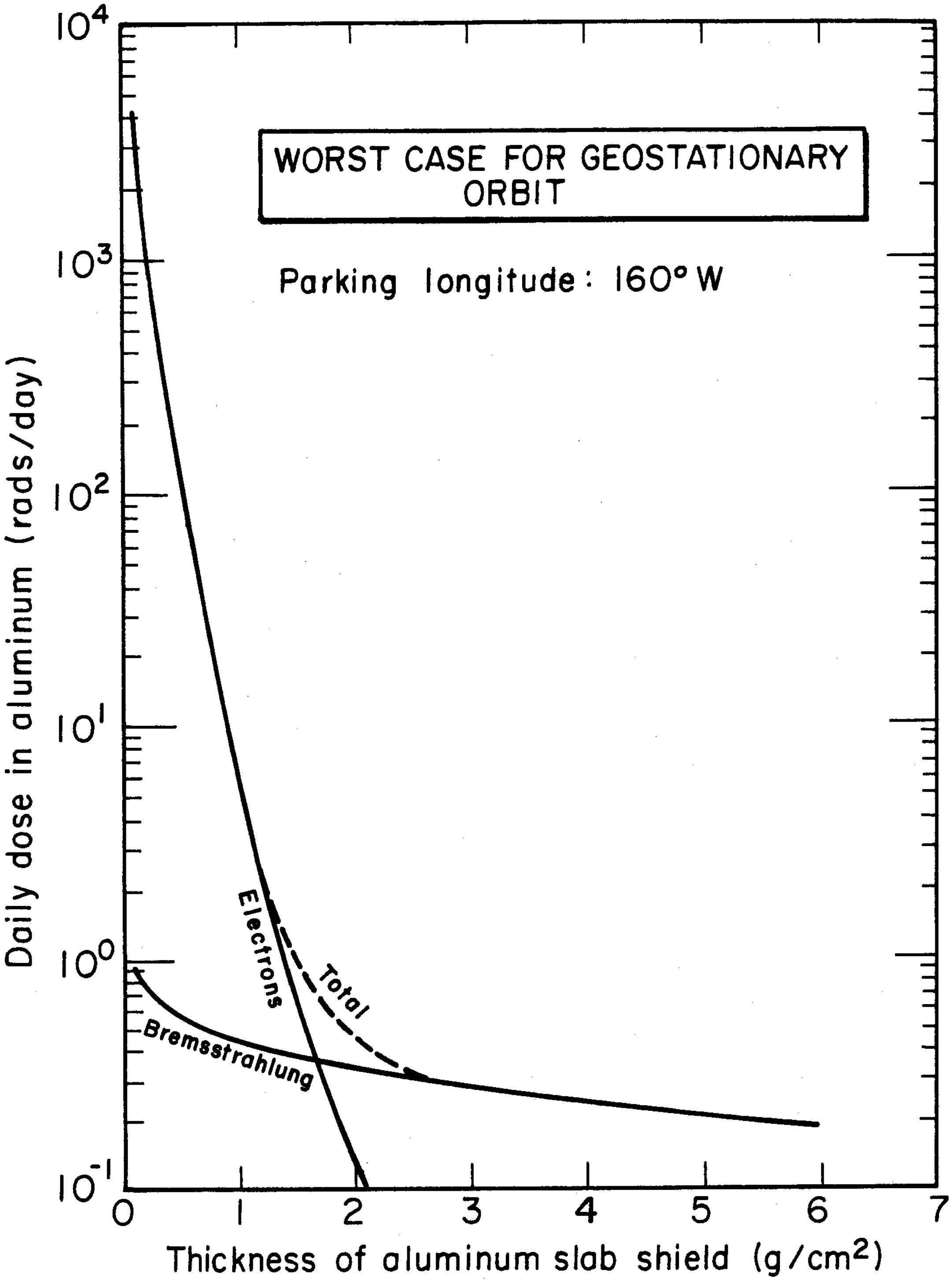

XBL7812-12355

Figure 10. Daily dose in aluminum behind a slab shield of aluminum versus the aluminum shield thickness for the worst (160°) parking longitude in a geostationary orbit. (From Stassinopoulos, 1978)

TABLE 5

Average Daily Dose Rates and 90-day Mission Doses Behind 300 mils (= 2 g/cm^2) of Aluminum from Predictable Radiation Sources for the Best and Worst Parking Longitudes in a Geostationary Earth Orbit

Radiation Source	Worst Position (160° West longitude) (rad/day)	(rad)	Best Position (70° West longitude) (rad/day)	(rad)
Trapped electrons	0.16	14	0.026	2.37
Bremsstrahlung	0.44	40	0.28	25
Trapped protons	-	-	-	-
Galactic cosmic rays	0.02	1.8	0.02	1.8
TOTAL	0.60	56	0.30	29

is a high-risk operation requiring realistic consideration of the radiation hazard in perspective with other risks. Accordingly, the radiation exposure limits for space workers are higher than the conventional standards for professional radiation workers. If the much lower exposure limits listed in Table 7 for professional radiation workers were applied to personnel in space, the feasibility of the SPS mission would be challenged severely. The 90-day mission doses in LEO (Table 3) and GEO (Table 4) exceed the exposure limits in Table 7. One of the recommendations in the 1970 report of the National Academy of Sciences is that the proposed exposure limits be reviewed and revised "as additional pertinent information becomes available and before application to actual operations." Because of the impact of the exposure limits on the feasibility of the SPS mission, the recommended review of the

TABLE 6

Mission Radiation Exposure Limits in Dose-Equivalents (REM)

	Daily*	30 Days	90 Days**	Yearly	Career
Bone marrow (5 cm)	0.2	25	35	75	400
Skin (0.1 mm)	0.6	75	105	225	1200
Eye lens (3 mm)	0.3	37	52	112	600
Testes[+] (3 cm)	0.1	13	18	38	200

*Averaged over one year.

**Permissible for two consecutive quarters provided restriction from further exposure maintains yearly limits.

[+] Applicable only if avoidance of psychological effects of possible oligospermia and temporary infertility is deemed important.

TABLE 7

Occupational Radiation Exposure Limits in Dose-Equivalent (rem)

	Daily*	90 days	Yearly	Career**
Blood-forming organs	0.014	3	5	5(N-18)
Skin	0.082	7.5	30	
Eye lens	0.014	3	5	
Gonads	0.014	3	5	

*Averaged over one year.

**The accumulated occupational dose to the whole body shall not exceed 5(N-18) rem, where N is the individual's age in years.

exposure limits needs to be accomplished at an early date.

The radiation exposure limits in Table 6 are based on the primary reference risk recommended by the Radiobiological Advisory Panel of the Committee on Space Medicine of the Space Science Board. The primary reference risk corresponds to an added probability of radiation-induced leukemia and other neoplastic diseases over a period of about 20 years that is equal to the natural probability for the specific population at risk. The panel recommended also that the primary reference risk exposure be taken as a dose-equivalent of 400 rem at the mean (5 cm) depth of the bone marrow irrespective of the exposure rate.

The exposure limits in Table 6 are dose-equivalents in rem at the specified mean depth of interest, where the dose-equivalent is the product of the absorbed dose D in rads and a quality factor Q. The quality factor takes into account differences in biological effectiveness of radiation of different quality, which is measured by the linear energy transfer (LET) or rate of dissipation of energy along the path of the charged particle. The purpose of introducing the quality factor in radiation protection is to ensure that the risk from a specified maximum permissible dose of high-LET radiation does not exceed that from a maximum permissible dose of low-LET radiation. The relationship between Q and LET recommended by the International Commission on Radiological Protection (1966) assumes that Q has a constant value of 20 beyond an LET of 175 keV/μm. Barendsen _et al_. (1963) and Todd (1967) reported that the relative biological effectiveness (RBE) for killing cultured dividing mammalian cells reaches a maximum of 6 to 8 in the LET range of 100 to 200 keV/μm, and decreases to unity at 1000 keV/μm. Thus, the Q-LET relationship may overestimate the dose-equivalent for production of neoplastic, skin, testicular, and possibly occular lens responses by very densely ionizing radiation. On the other hand, it is known that RBE increases as the dose decreases, so that the large value of Q may not be unreasonable for the doses considered here.

The establishment of exposure limits that are less restrictive than those for conventional occupational exposure requires quantitatively reliable information on the levels of human response as a function of dose and conditions of exposure. The quantity and nature of existing data are inadequate to derive confidence limits for space conditions. One uncertainty arises because of the lack of information on the interaction of radiation exposure with exposure to other stresses such as weightlessness in the space environment. Other uncertainties arise because of inadequate information on biological effects of the HZE particle component of cosmic radiation. These very highly ionizing particles produce a unique type of biological damage which normally cannot be produced by other types of radiation. An HZE particle damages many contiguous cells along the particle track, and produces a microscopic lesion. Malachowski _et_ _al_. (1978) observed this type of injury in recent laboratory studies. The radiation exposure limits in Table 6 are not applicable to biological effects such as this microlesion type of injury which can be produced only by HZE particles and not by other radiations of different quality. Also, the concept of quality factor breaks down when the biological effect cannot be produced by the low-LET reference radiation. To assess the damage from HZE particles, it is necessary to acquire radiobiological information that will permit the prediction of dose-response relationships for the HZE particles. Measurements are needed of the probability for inactivation by HZE particles of nondividing cells that compose the primary functional portion of the central nervous system. It is necessary also to determine the degree of redundancy in the brain and the possible consequences of progressive destruction of nondividing nerve cells during space missions of extended duration. There is a need also to introduce a new physical parameter other than the conventional absorbed dose in order to quantify the exposure. In the National Academy of Sciences (1973) report entitled "HZE-Particle Effects in Manned Spaceflight," it was suggested as a first approximation that a critical or threshold ionization level may be required to inactivate or impair cells. Below the threshold, the biological effect does not occur; and above the threshold, the biological effect occurs with probability of 100%. The threshold-LET concept resulted in the introduction of a physical quantity called the specific track length (or track length per unit mass) for specifying the exposure to HZE particles. The specific track length (in units of cm/g) is the fluence of particles above the threshold ionization level in the organ divided by the density of the organ. Calculation of the specific track length must take into account the slowing down and nuclear fragmentation of the incident HZE particles in the material shielding the organ of interest. Figure 11 is a plot of the integral-number LET spectrum for the major components of HZE particles at solar minimum under no shielding (Curtis, 1973). The ordinate is the flux density (in particles/cm^2-year) above a given LET, and the abscissa is LET (in keV/μm of tissue).

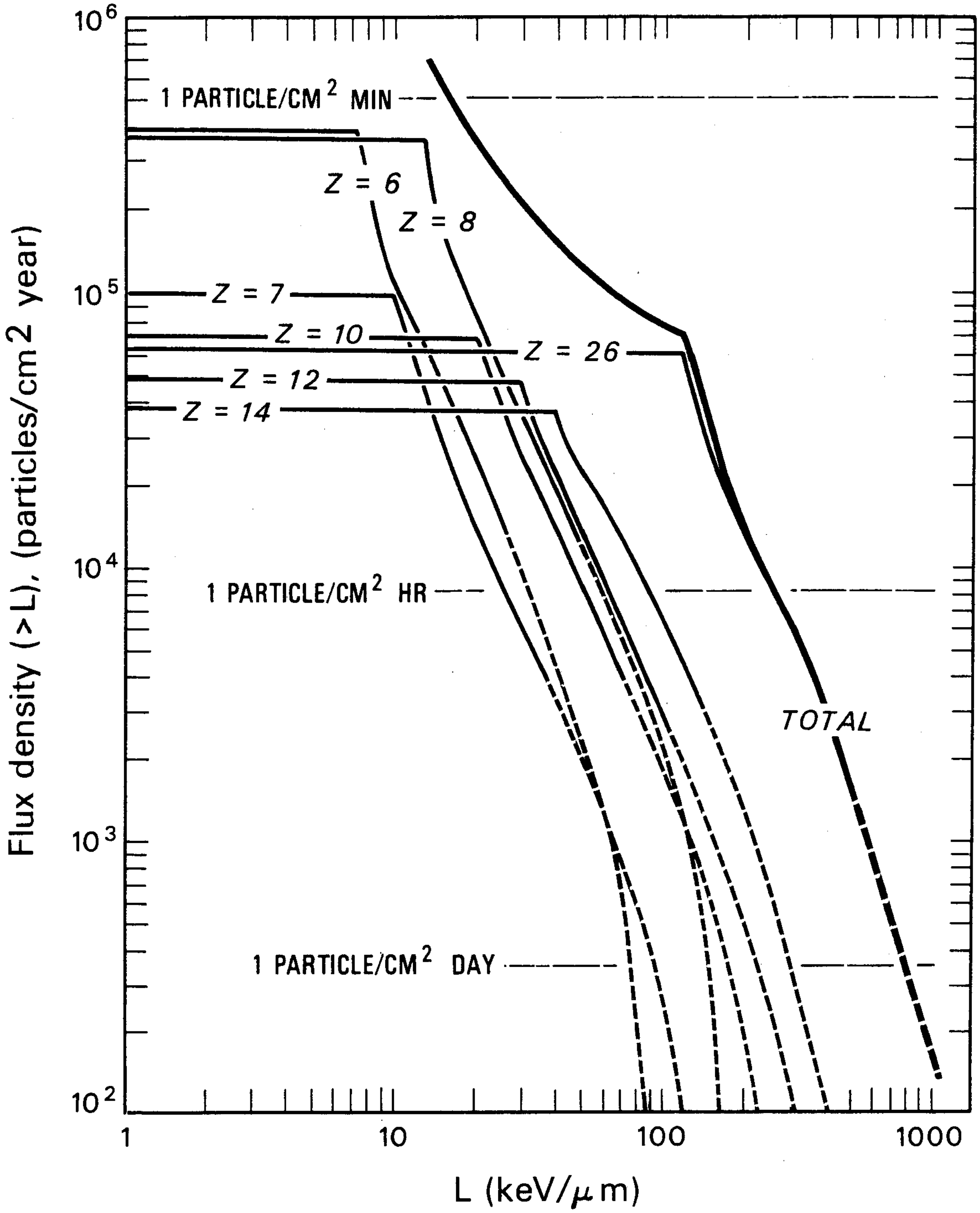

XBL7811-12342

Figure 11. Integral number LET spectrum for the major components of HZE particles at solar minimum under no shielding. (From Curtis, 1973)

RADIATION DOSIMETRY

Both passive and active dosimeters are needed for monitoring radiation exposures. If each worker wears two passive dosimeters at all times with one located behind some shielding (e.g., perhaps strapped to a leg), then it will be possible to make some assessment of protection from self-shielding by body tissues. The passive dosimeters should be rugged, reliable, and simple enough to be read by the individual and the medical officer. In addition to passive dosimeters for each individual, real-time monitoring of solar particle events and also of other short-term fluctuations of the trapped electron fluxes is needed in GEO. Both sources of radiation can produce exposures in excess of allowable limits. Space workers in GEO need to be warned to move to areas affording greater protection if, for any reason, radiation levels exceed established limits. There is a need also to monitor exposure to HZE particles because of the unknown biological effects from the unique type of radiaton injuries produced by these particles.

Table 4 from Wilson and Denn (1976) estimates the time to reach exposure limits to the marrow, skin, eye lens, and testes for the solar particle events of August 1972 as a function of the thickness of a shield. These estimates include the self-shielding of these organs by the body. For a space worker in a space suit with a typical tissue-equivalent thickness of 0.3 g/cm^2, the results of Table 4 indicate that dose-equivalent limit to the skin would be reached in about three hours. The space suit helmet would give the eyes protection for a longer time. This three-hour period is more than adequate for such space workers to move either inside the vehicle with a tissue-equivalent thickness between one and five g/cm^2 or inside the storm shelter.

Paulikas and Blake (1971) report that trapped electron intensities in GEO during intense magnetic storms increase by more than two orders of magnitude in a few hours followed by decay with mean lifetime of several days. When the peak intensity is reached, exposures in excess of allowable limits can be accumulated in about 30 minutes or less. Here again the period of a few hours before reaching peak intensities is more than adequate for space workers in space suits to move within the vehicle for protection.

From an operations point of view, a radiation monitoring system is necessary to warn space workers when radiation levels expect to become excessive. On-board active dosimetry with rate and integration capabilities appears to be an attractive monitoring means. The dosimetry system should indicate both surface and depth doses and dose rates in all appropriate areas. It appears also that the dosimetry system could be adapted by modifying instrument systems which have been designed and used aboard spacecraft. Greiner et al. (1978) are flying a satellite-born multidetector cosmic-ray telescope which identifies the charge and mass of incident cosmic-ray nuclei over the energy range from about 20 to 500 MeV per nucleon. Particle identification is based on the multiple energy loss technique.

The instrument described by Althouse et al. (1978) measures the isotopic composition of solar and galactic cosmic rays for the elements Li through Ni in the energy range from about 5 to 250 MeV per nucleon. The instrument described by von Rosenvinge et al. (1978) measures the charge composition of energetic particles over wide regions in energy (from about 1 to 500 MeV per nucleon) and in charge (from Z = 1 to 28). Individual isotopes are resolvable for Z = 1 through 7 over a restricted energy range. This instrument measures electrons also from 2 to 10 MeV.

At this workshop, Wefel (1979) reviewed the rapid evolution of instrumentation for charged particle measurements in space that has taken place over the last decade. While present technology is sufficient to monitor the ionizing-radiation environment of the SPS, the continued rapid development anticipated in the coming years implies that techniques superior to those now in use may be available before SPS construction begins.

The development of the latest generation of space radiation instrument systems was accelerated greatly because of the availability of heavy ions (HZE particles) at the Bevalac. The heavy-ion beams permitted testing, modification, retesting, and calibration of the instruments to ensure before launch that all components functioned as designed. During this process, unexpected effects in both the detectors and electronics were discovered and corrected. Corrective action would have been impossible if these effects had been discovered after launch.

In addition to real-time monitoring of the relevant components of the radiation environment, there is interest in including an entire complement of charged-particle instruments, perhaps orbiting in a satellite in the vicinity of the SPS, to produce a complete data base on the radiation environment. Although the quantity of information would be too large to be assimilated in real-time, the recorded data will permit reconstruction of the radiation environment for use in connection with unanticipated radiation problems.

CONCLUSIONS

To conclude this evaluation of the ionizing-radiation environment of the satellite power system, we summarize the preliminary assessment of the radiation doses and highlight some potential problem areas. As presently conceived, the SPS mission might involve 270 thousand space workers over a period of 30 years.[3]

1. In LEO, nearly all of the radiation dose comes from the geomagnetically trapped protons in the South Atlantic Anomaly. A preliminary estimate indicates that the 90- day mission dose behind 300 mils ($\approx$ 2 g/cm^2) of aluminum is about 20 rads at solar minimum; the dose at solar maximum is about one-half that at solar minimum.

2. In the orbital transfer from LEO to GEO, the trapped electron fluence is responsible for the major portion of the total dose, with trapped electrons dominating behind a shield thickness less than about 2 g/cm^2 aluminum and electron bremsstrahlung dominating behind thicker shields. A preliminary estimate of the dose for a round trip from LEO to GEO and back to GEO for a one-way transfer time of 5.25 hours[4] is typically 3 rad behind 2 g/cm^2 aluminum and 0.2 rad behind 5 g/cm^2 aluminum.

---

[3] Tentatively, there will be about 350 construction workers rotated every 90 days for each of 60 satellites during an eighteen month construction phase, and about twenty maintenance workers rotated every 90 days for each of 60 satellites during the thirty-year operational phase. The actual numbers of space workers will depend on options still under evaluation (see Reference System Report, 1979).

[4] This transfer time was that assumed by Stassinopolis (1979). Longer transfer times would, of course, increase the absorbed doses.

3. In GEO, the dose from predictable radiation sources comes from penetrating electrons and the associated bremsstrahlung. A preliminary estimate based on the interim model (AEI-7) for the electron environment indicates that the 90-day mission dose behind 300 mils (= 2 g/cm^2) of aluminum varies from about 29 rad for the best parking longitude of 70^o west to about 56 rad for the worst parking longitude of 160^o west. Since the major contribution comes from electron bremsstrahlung, it is possible to reduce these doses significantly by designing the walls of the work areas with an additional layer of heavy metal, such as tantalum or lead, to attenuate the electron bremsstrahlung more effectively.

4. A critical question affecting the design and possibly the feasibility of the SPS is whether or not the radiation exposure limits in current use will be reduced. In order to introduce stability into the planning for the SPS mission, it is necessary to settle this question at an early date.

5. There is a major uncertainty in the assessment of the radiation hazards because of the lack of information on the biological effects of the HZE particles. There is a need to generate this information with HZE particle beams from the Bevalac. The need to monitor exposure to HZE particles will remain as long as there are unknown biological effects from the unique type of radiation injuries produced by these particles.

6. High-altitude nuclear detonations represent a politically unpredictable source of radiation. The injection of copious numbers of high-intensity electrons into the geomagnetic trapping region will

require plans for returning all personnel to earth until radiation levels have decreased to lower values.

7. An important part of the radiation protection design for the GEO base involves the hazard to personnel from solar particle events. A heavily-shielded shelter is necessary to protect personnel from large solar particle events such as those of August 1972. To minimize the design weight of the storm shelter, it is necessary to take into account self-shielding of critical organs by body tissues and to use personal shielding such as goggles to protect the eye lens and lead undergarments to protect the testes and ovaries. While self-shielding by body tissues provides time for space workers to move to the protective shelter before reaching the mission exposure limits, an early warning system is desirable to minimize the exposure.

8. Both passive and active dosimeters are needed for monitoring radiation exposures. In addition to rugged, reliable, and simple passive dosimeters for each individual, real-time monitoring is needed of unpredictable radiation sources, such as nuclear detonations, solar particle events, and short-term fluctuations of trapped electron fluxes in GEO. Space workers in GEO must be warned to move to areas affording greater protection whenever exposures from unpredictable radiations may exceed established limits. There is a need also to monitor exposure to HZE particles because of the unknown biological effects from the unique type of injuries produced by these particles. The design of appropriate active dosimeters can be based on the technology of existing space-operational instruments.

9. The radiation requirements for each portion of the SPS mission

must be determined from the combined exposures for the total mission; for example, the allowable exposure within the vehicle at GEO depends on the exposures in LEO, during orbital transfer, during scheduled and unscheduled EVA, and as anticipated from solar particle events. It is necessary to re-evaluate the radiation shielding requirements in terms of the exposure budget for each portion of the mission. Since there are large uncertainties in the existing models of the space radiation environment, re-evaluation of the shielding requirements must be updated as the models are improved; for example, an important improvement needed in the model of the electron environment for GEO is the dependence on the solar cycle. The numbers quoted above for the preliminary estimates of doses do not take into account the uncertainties in models.

RECOMMENDATIONS FOR CONTINUING RESEARCH EFFORT

It is clear from the foregoing analysis that several unanswered questions should be attacked without delay. The recommendations made below emerge from these considerations, and would seem to constitute the minimum activity that must be supported, based on our present knowledge of the problems involved.

1. One of the major unresolved questions is the extent of the hazard from the HZE component of the radiation in GEO. Two types of studies are recommended in this regard:

   a. Early initiation of appropriate studies of the biological effects of HZE particles on critical organs. This question was not addressed in the present study. It is recommended that a committee be constituted to examine this question, and to arrive at a series of experiments to be conducted with available heavy-ion beams to assess the biological effects of the critical body organs assumed to be the most vulnerable to the accumulation of damage from the HZE component.

b. Realistic calculations of 90-day HZE exposure for a "typical" space worker as a function of shielding thickness. For an adequate evaluation of the hazards to be made, it is recommended that reasonable estimates be obtained of the fluences of the HZE component expected in the various critical organs determined in (a) above. Although the number of variables involved precludes a precise determination, it is important that the spacecraft designer is aware of the consequences of increasing the thickness of materials available for shielding. Although the absolute magnitude of the fluences may not be determinable with accuracy, the relative variation of fluence with thickness could give valuable information on the effects of a given increase in thickness. This could impact the risk vs. cost analysis for the ultimate design chosen.

2. Re-evaluation of the radiation exposure limits to be used in spacecraft design. It is clear that the radiation doses expected to be encountered by a space worker during a 90-day SPS mission may exceed the limits recommended by the NCRP and ICRP for radiation workers. Since there will be a large number of workers who will potentially receive a significant radiation exposure, the career limits established by the NAS committee for astronauts may not be appropriate. In any case, this question should be examined in detail. It is recommended

that an appropriate committee be constituted to study the question of what the appropriate exposure limits should be for workers involved with the construction and maintenance of SPS.

On the basis of the limits determined by this committee, estimations of doses throughout an entire 90-day mission must be recalculated, using realistic shielding configurations, so that the spacecraft designer will have guidance in supplying sufficient shielding to appropriately limit radiation exposure from predictable sources. In addition, strategies for dealing with the unpredictable sources must be developed at an early stage, as these may have significant impact on the final design.

ACKNOWLEDGMENTS

This preliminary evaluation of the ionizing-radiation environment of the satellite power system was carried out in conjunction with the Workshop on "The Radiation Environment of the Satellite Power System" held at the Lawrence Berkeley Laboratory on 15 September 1978. The author gratefully acknowledges Dr. Walter Schimmerling, Dr. John W. Wilson, and particularly Dr. Stanley Curtis for reading and commenting on this report.

REFERENCES

Althouse, W.E., Cummings, A.C., Gurrard, T.L., McWaldt, R.A., Stone, E.C., and Vogt, R.E. 1978. A cosmic ray isotope spectrometer. *IEEE Trans. Geosci. Electron.* *GE-16*, 163-165.

Barendsen, G.W., Walter, H.M.D., Fowler, J.F., and Bewley, D.K. 1963. Effects of different ionizing radiations on human cells in tissue culture. *Radiat. Res.* *18*, 106-119.

Bazilevskaya, G.A., Stozhkov, Y.J., Charakhchyan, A.N., and Charakhehan, T.N. 1973. The energy spectra for the conditions of propagation in the interplanetary space for solar protons during the cosmic ray events of August 4 to 9, 1972. Proceedings of the 13th International Cosmic Ray Conference at Denver, Colorado, pp. 1702-1707.

Boeing Aerospace Company and the General Electric Company. 1978. Solar power satellite system definition study, part III. D180-24071-1 Preferred Concept System Definition. Report prepared under contract NAS 9-15196 to NASA/JSC.

Curtis, S.B. 1973. Frequency of heavy ions in space and their biologically important characteristics. *Life Sci. Space Res.* *11*, 209-214.

Curtis, S.B. 1976. Radiation fields in spacecraft. *IEEE Trans. Nucl. Sci.* *NS-23*, 1355.

Eberhardt, A.W. 1977. Candidate locations for SPS rectifying antennas. NASA MSFC Technical Memorandum, *NASA TM-78146*.

Glaser, P.E. 1968. Power from the sun: its future. *Science* *162*, 857-861.

Greiner, D.E., Beiser, F.S., and Heckman, H.H. 1978. ISEE-C HKH high energy cosmic rays. *IEEE Trans. Geosci. Electron.* *GE-16*, 163-165.

Grumman Aerospace Corporation. 1977. Space-based solar power conversion and delivery systems study; analysis of orbital systems. Report prepared in fulfillment of ECON Agreement E-100 as part of Contract NAS8-31308 to NASA/MSFC.

Hess, W.N., ed. 1963. Collected papers on the artificial radiation belts from the July 9, 1962 nuclear detonation. *J. Geophys. Res.* *68*, 605-758.

International Commission on Radiological Protection (ICRP). 1966. Recommendations of the International Commission on Radiological Protection. *ICRP Publication No. 9*. London: Pergamon Press.

King. J. 1973. Solar proton fluences for 1977 to 1983 space missions. J. Spacecr. Rockets 11(6), 401-408.

Malachowski, M., Yang, T.C.H., and Tobias, C.A. 1978. Private communication.

National Academy of Sciences. 1970. Radiation protection guides and constraints for space-mission and vehicle-design studies involving nuclear systems. Report of the Radiobiological Advisory Panel of the Committee on Space Medicine, Space Sciences Board.

National Academy of Sciences. 1973. HZE-particle effects in manned spaceflight. Report of the Radiobiological Advisory Panel of the Committee on Space Biology and Medicine Space Science Board, edited by D. Grahn.

Paulikas, G.A. and Blake, J.B. 1971. The particle environment of the synchronous altitude. Models of the trapped radiation environment. Long Term Time Variations (vol. III). NASA SP-3024, pp 51-67.

Reference System Report. January 1979. Satellite power system concept development and evaluation program, October, 1978. Report DOE/ER-0023, U.S. Department of Energy and NASA.

Rockwell International. 1978. Satellite power systems (SPS) concept definition study, SD 78-AP-0023. Report prepared under Contract NAS 8-32475 to NASA/MSFC.

Rossi, M. and Stauber, M. 1977. Radiation protection design considerations for man in geosynchronous orbit. IEEE Trans.Nucl.Sci. NS-24(6).

Sawyer, D.M. and Vette, J.I. 1976. AP-8 trapped proton environment for solar maximum and solar minimum. NSSDC/WDC-A-R&S. 70-06. National Space Science and Data Center. Greenbelt, Maryland.

Stassinopoulos, E.G. 1973. Radiation hazards to synchronous satellites: the IUE (SAS-D) mission. NASA Goddard Space FLight Center Report X-601-73-330.

Stassinopoulos, E.G. 1978. The geostationary radiation environ ment. NASA GSFC, Preprint Report X-601-78-34. November 1978. (Submitted to J. Spacecr. Rockets.)

Stassinopoulos, E.G. 1979. A preliminary study of the charged particle radiation for the satellite power system. Proceedings, Workshop on the Radiation Environment of the Satellite Power System. Lawrence Berkeley Laboratory. 15 September 1978. LBL-8581. (These proceedings.)

Teague, M., Chan, K.W., and Vette, J.I. 1976. AE6: A model environment of trapped electrons for solar maximum. DSSDC/WDC-A-R&S 76-04. National Space Science Data Center. Greenbelt, Maryland.

Teague, M. and Vette, J.I. 1972. The inner zone electron model AE-5. NSSDC 72-10. National Space Science Data Center. Greenbelt, Maryland.

Teague, M. and Vette, J.I. 1978. Preliminary communication from Michael Teague.

Todd, P. 1967. Heavy-ion irradiation of cultured human cells. Radiat. Res. Suppl. 7, 196-207.

Von Rosenvinge, T.T., McDonald, F.B., Trainor, J.H., Van Hollenbeke, M.A.I., and Fisk, L.A. 1978. The medium energy cosmic ray experiment for ISEE-C. IEEE Trans. Geosci. Electron. GE-16(3), 208-212.

Wefel, J.P. 1979. Instrumentation for radiation measurements in space. Proceedings, Workshop on the Radiation Environment of the Satellite Power System. Lawrence Berkeley Laboratory, 15 September 1978. LBL-8581. (These proceedings.)

Wilson, J.W., and Denn, F.M. 1976. Preliminary analysis of the implications of natural radiations on geostationary operations. NASA Technical Note. NASA/TN D-8290.

U.S.GPO:1979-689-058(F)38

TECHNICAL INFORMATION DEPARTMENT
LAWRENCE BERKELEY LABORATORY
UNIVERSITY OF CALIFORNIA
BERKELEY, CALIFORNIA 94720